SMART CHEMICAL SENSING MICROSYSTEM: TOWARDS A NOSE-ON-A-CHIP

by
Su-Lim Tan
School of Engineering
University of Warwick

A thesis submitted to the University of Warwick
for the degree of Doctor of Philosophy
December 2005

Contents

Heading	Page
Contents	*ii*
List of Figures	*vii*
List of Tables	*xii*
Summary	*xiii*
Acknowledgements	*xiv*
Declaration	*xv*
Selected Abbreviations and Acronyms	*xvii*
Selected Symbol Reference	*xix*
CHAPTER 1: Introduction	**1**
1.1 Mammalian olfactory system	*1*
1.2 Electronic noses	*6*
1.2.1 Sensor-based electronic noses	*7*
1.2.2 Instrument-based electronic noses	*10*
1.2.3 Combined approach electronic noses	*11*
1.3 Applications of electronic noses	*14*
1.4 Research objectives	*16*
1.5 Outline of thesis	*17*
1.6 References	*18*
CHAPTER 2: Project evolution and system description	**23**
2.1 Introduction	*23*
2.2 Mimicking the biological olfactory system	*23*
2.2.1 Spatio-temporal signal	*25*
2.3 Microfabrication	*26*
2.3.1 Micro gas sensor array	*26*
2.3.2 Microchannel fabrication review	*27*
2.4 Project description	*30*
2.5 Conclusions	*31*
2.6 References	*31*

CHAPTER 3: Design and simulation of microchannels and microsensors 37

3.1 Introduction 37

3.2 Microchannels and microchambers design and simulation 37

3.2.1 Microchannel geometrical models 38

3.2.2 Microchamber geometrical models 41

3.2.3 Mathematical models and boundary conditions 42

3.2.4 Band-broadening effect 44

3.2.5 Simulation results for microchannels and microchambers 45

3.3 Gas chromatographic column simulations 48

3.3.1 Gas chromatographic column geometrical models 48

3.3.2 Mathematical models and boundary conditions 50

3.3.3 Band-broadening effect 52

3.3.4 Retention effect 54

3.3.5 HETP and separation factor 55

3.3.6 Spatio-temporal signals generation 58

3.4 Polymer-composite sensor response model 61

3.4.1 Dynamic sensor response model 63

3.4.2 Velocity effect on sensor response 65

3.5 Conclusions 66

3.6 References 67

CHAPTER 4: Design and fabrication of microsensors and microsensor arrays 70

4.1 Introduction 70

4.2 Proto-nose discrete sensors 70

4.2.1 Discrete sensors design and fabrication 70

4.2.2 Micropositioning alignment system 72

4.2.3 Discrete sensors polymers deposition 73

4.3 Hybrid-nose sensor arrays 75

4.3.1 Hybrid-nose sensor arrays design and fabrication 75

4.3.2 Micromasks design and fabrication 77

4.3.3 Hybrid-nose polymers deposition 77

4.4 aVLSI-nose smart sensor arrays 79

4.4.1 Combined chemoResistive/FET sensor design 81

4.4.2 DC-offset cancellation circuit for offset removal 85

4.4.3 Smart sensor cell and sensor array 88
4.4.4 aVLSI-nose post-procesing and polymers deposition 91
4.5 Conclusions 92
4.6 References 93

CHAPTER 5: Design and fabrication of microfluidic packages **95**

5.1 Introduction 95
5.2 Stereolithography and microstereolithography fabrication 96
5.3 Stereolithography and microstereolithography systems 100
5.3.1 System setup 103
5.3.2 Support structures generation 104
5.3.3 Design and fabrication process 107
5.3.4 Resin properties 110
5.4 Micropackages design and fabrication 110
5.4.1 Simple micropackages with single continuous microchannel 111
5.4.2 Complex micropackges with multiple microchannel segments 113
5.4.2.1 Preliminary designs 114
5.4.2.2 Updated designs for resolving post-processing complication 116
5.5 Micropackages and Perfactory system characterisation 119
5.5.1 Mechanical properties: surface roughness and hardness 119
5.5.2 Perfactory system resolution, repeatability and build accuracy 121
5.6 Conclusions 124
5.7 References 125

CHAPTER 6: Nose-on-a-chip: Integration **128**

6.1 Introduction 128
6.2 Proto-nose microsystems 128
6.2.1 Proto-nose I microsystem 129
6.2.2 Fast-nose microsystem 133
6.2.3 Proto-nose II microsystem 133
6.3 Nose-on-a-chip microsystems 136
6.3.1 Microchamber design and fabrication 136
6.3.2 Microchannel package and microsensor array alignment 138
6.3.3 Sealing 139

6.4 Stationary phase deposition 141
6.5 Conclusions 146
6.6 References 146

CHAPTER 7: Micro gas test station for device characterisation **149**

7.1 Introduction 149
7.2 Vapour test station 149
7.2.1 System setup 150
7.2.2 Electronic interfaces and controls 152
7.3 Data acquisition system 156
7.3.1 Data acquisition electronics 158
7.3.2 Discrete sensor array interfaces for fast-nose and proto-noses 160
7.3.3 Microsensor array interface for hybrid-nose 161
7.3.4 Microsensor array interface for aVLSI-nose 163
7.4 Software control system 164
7.4.1 Modular hierarchical design 164
7.4.2 Fast-nose, proto-nose and hybrid-nose software interfaces 167
7.4.3 aVLSI-nose software interface 170
7.4.4 Automated test cyles and data logging 171
7.5 Conclusions 173
7.6 References 173

CHAPTER 8: Microsystems characterisation and experimental results **175**

8.1 Introduction 175
8.2 Proto-nose microsystems characterisation 175
8.2.1 Discrete sensor characterisation using fast-nose microsystem 176
8.2.2 Proto-nose I and II characterisation 181
8.2.2.1 Comparison between uncoated and coated microchannel 182
8.2.2.2 Spatio-temporal signals 183
8.3 Hybrid-nose characterisation 188
8.3.1 Hybrid-nose characterisation with microchamber 188
8.3.2 Discrimination analysis using olfactory imaging 190
8.3.3 Nose-on-a-chip characterisation 195
8.3.3.1 Microchannel package MSL101 (5 cm long microchannel) 195

8.3.3.2 Microchannel package MSL112 (32 cm long microchannel) 198
8.3.3.3 Microchannel package MSL115 (240 cm long microchannel) 200
8.4 aVLSI-nose characterisation 203
8.4.1 Smart sensor cell 203
8.4.2 DC-offset cancellation circuit for offset removal 206
8.5 Conclusions 208
8.6 References 209

CHAPTER 9: Conclusions and further work 211

9.1 Overview 211
9.2 Project objectives 212
9.3 The development of artificial olfactory systems 213
9.4 Characterisation and performance of the nose-on-a-chip systems 216
9.5 Further work 223
9.6 References 224

APPENDIX A: Finite element simulation of microchannel GC using FEMLAB 226

APPENDIX B: Estimation of partition coefficient using linear solvation energy relationship (LSER) equations 235

APPENDIX C: Stereolithography and microstereolithography resin properties 239

APPENDIX D: Schematic diagrams 243

List of Figures

Heading	Page
Figure 1.1: The anatomy of the human olfactory system.	*2*
Figure 1.2: Operation range of gas sensing systems and mammalian olfactory system.	*3*
Figure 1.3: Schematic diagram illustrating the axonal connectivity pattern between the nose and the main olfactory bulb.	*4*
Figure 1.4: A comparison between the processing in an e-nose and a biological olfactory system.	*7*
Figure 1.5: Discrete gas sensors and sensor arrays.	*8*
Figure 1.6: Sensing techniques and materials employed to produce gas sensor.	*8*
Figure 1.7: Sensor-based electronic noses.	*9*
Figure 1.8: Instrument-based electronic noses.	*11*
Figure 1.9: Combined approach electronic nose system with multi sensor array system (SAS) and fingerprint mass spectrometry (FMS), Prometheus, Alpha-MOS.	*12*
Figure 1.10: Schematic layout of silicon implementation of the olfactory system.	*13*
Figure 1.11: Comparison of the probability of error versus analysis time for various systems.	*14*
Figure 2.1: Microchannels fabricated by fusion and anodic bonding.	*28*
Figure 2.2: Microchannels fabricated using various micromachining techniques and materials.	*28*
Figure 3.1: 2-D parabolic velocity profile of microchannel.	*38*
Figure 3.2: Geometrical model of a scaled proto-nose II.	*39*
Figure 3.3: MSL101 geometry.	*40*
Figure 3.4: MSL113 geometrical model with surface profile of a travelling ethanol vapour pulse.	*40*
Figure 3.5: FEM simulation of microchamber fluid flow.	*41*
Figure 3.6: Microchannel boundary conditions and symmetry axis.	*42*
Figure 3.7: Simulation of pulse delivered to sensor surface and actual sensor response at two different flow velocities.	*44*
Figure 3.8: Broadening effect of delivered pulse as a function of flow velocity.	*45*
Figure 3.9: Profiles of analyte delivered to sensor S1, S2, S3, S4 and S5 for proto-nose I.	*46*
Figure 3.10: Profiles of ethanol vapour delivered to sensor S1, S20, S36, S37, S38, S39 and S40 for proto-nose II.	*46*
Figure 3.11: MSL101 delivered ethanol vapour profile near inlet and outlet.	*47*
Figure 3.12: Comparison of different microchamber designs.	*47*
Figure 3.13: Proto-nose I geometrical model.	*49*
Figure 3.14: MSL113 geometrical model.	*49*
Figure 3.15: Microchannel GC boundary conditions and symmetry axis.	*51*
Figure 3.16: Representation of GC output defining retention time and peak broadening width.	*52*
Figure 3.17: Broadening of ethanol vapour pulse at sensor S1 and S20.	*53*
Figure 3.18: Broadening of toluene vapour pulse at sensor S1 and S20.	*53*

Figure 3.19: Comparison of separation factor between analytical and finite element model. 57
Figure 3.20: HETP against average velocity for microchannel GC. 57
Figure 3.21: Spatio-temporal signals, 59
Figure 3.22: Proto-nose I sensor responses to ethanol vapour. 60
Figure 3.23: Proto-nose I sensor responses to toluene vapour. 61
Figure 3.24: Geometrical model and boundary conditions for FE simulation of sensor response. 62
Figure 3.25: Finite element simulation of polymer-composite sensor response. 63
Figure 3.26: Fitted response of PSB, PEVA, PEG, PCL and PVPH sensor. 65
Figure 3.27: Effect of flow velocity on sensor response. 66
Figure 4.1: Microsensor design. 71
Figure 4.2: Discrete sensor masks. 72
Figure 4.3: Microsensor and mask alignment. 72
Figure 4.4: Micropositioning alignment system setup. 73
Figure 4.5: Photograph of polymer-composite deposition system. 74
Figure 4.6: Deposited discrete sensors. 75
Figure 4.7: Hybrid-nose sensor array. 76
Figure 4.8: Hybrid-nose packaging and wafer. 76
Figure 4.9: Mechanical micromasks for polymer deposition. 77
Figure 4.10: Hybrid-nose resistance monitoring PCB for polymer deposition. 78
Figure 4.11: Polymer deposition scheme. 78
Figure 4.12: Photographs of deposited hybrid-noses. 79
Figure 4.13: Block diagram of a sensor cell design. 80
Figure 4.14: Combined resistive/FET sensor design. 81
Figure 4.15: Relationship between aspect ratio and sensor resistance. 82
Figure 4.16: Combined resistive/FET sensor. 83
Figure 4.17: Capacitive equivalent circuit. 84
Figure 4.18: Example of a polymer sensor response to various pulses of ethanol and toluene vapour in air with baseline voltage. 85
Figure 4.19: Pspice simulation result of the DC-offset cancellation circuit. 87
Figure 4.20: Detailed circuit implementation of a sensor cell. 88
Figure 4.21: Data format for sensor cell operational parameters. 89
Figure 4.22: Timing diagram for initialisation phase of aVLSI sensor array. 89
Figure 4.23: Smart sensor cell. 90
Figure 4.24: aVLSI sensor array. 90
Figure 4.25: Gold deposition of aluminium electrodes. 91
Figure 4.26: Deposited aVLSI sensor array. 92
Figure 5.1: Basic principle of microstereolithography fabrication. 96
Figure 5.2: Theoretical intensity profile of the UV laser beam (approximately Gaussian) and the resultant spot cured within the resin. 97
Figure 5.3: Classical MSL system using the vector-by-vector scanning process. 98
Figure 5.4: Freely movable objects fabricated by super-IH process. 98
Figure 5.5: Stereolithography and microstereolithography systems. 100
Figure 5.6: Microchannel package fabricated using Viper si2 system. 101
Figure 5.7: Microchannel package fabricated using Proform MSL system. 101
Figure 5.8: Photographs of Perfactory MSL system. 102
Figure 5.9: Setup of the Perfactory MSL system. 103
Figure 5.10: Support structure generation. 105

Figure 5.11: Support structure for fabrication of objects with freely movable parts. *106*
Figure 5.12: Fabricated objects with supporting structure. *106*
Figure 5.13: Four layer masks for complex microchannel package. *108*
Figure 5.14: Perfactory machine parameter. *109*
Figure 5.15: 7-step MSL fabrication process. *109*
Figure 5.16: Exposure time versus layer thickness for Perfactory Mini material at 400 mW dm^{-2}. *110*
Figure 5.17: Simple microchannel package designs and assembly. *112*
Figure 5.18: Simple microchannel packages fabricated by the Perfactory MSL system. *113*
Figure 5.19: Complex microchannel packages earlier designs. *115*
Figure 5.20: First generation complex microchannel packages. *116*
Figure 5.21: Strategy to resolve blockage by uncured resin for complex microchannel package. *116*
Figure 5.22: Complex microchannel package designs. *117*
Figure 5.23: Fabricated complex microchannel packages. *118*
Figure 5.24: Complex microchannel packages with lid assembly. *119*
Figure 5.25: Surface roughness of MSL115. *120*
Figure 5.26: Effect of pixel and placement error. *122*
Figure 5.27: Effects of stairs-stepping as a function of layer thickness. *124*
Figure 6.1: PCB base of proto-nose I. *129*
Figure 6.2: Perspex lid of proto-nose I. *130*
Figure 6.3: Fully assembled proto-nose I system. *131*
Figure 6.4: Detailed schematic of proto-nose I design. *132*
Figure 6.5: Fast-nose microsystem. *133*
Figure 6.6: Detailed schematic of proto-nose II design. *134*
Figure 6.7: Proto-nose II system. *136*
Figure 6.8: Microchamber design. *137*
Figure 6.9: Microchamber assembled with hybrid-nose microsensor array. *137*
Figure 6.10: Microchannel package vertical alignment markers. *138*
Figure 6.11: Microchannel package base designs for horizontal alignment. *139*
Figure 6.12: Microchannel package sealing. *139*
Figure 6.13: Fully assembled nose-on-a-chip microsystems. *140*
Figure 6.14: Deposition of stationary phase using static coating. *143*
Figure 6.15: Parylene deposition. *144*
Figure 6.16: Parylene C coated proto-noses and microchannel packages. *145*
Figure 7.1: Schematic of vapour test station setup. *150*
Figure 7.2: Photographs of the vapour test station. *152*
Figure 7.3: Schematics of interface electronics to microvalve and mass flow meter. *153*
Figure 7.4: Micropump programmable operating voltage. *154*
Figure 7.5: Micropump interface electronics with current sensing ADC. *155*
Figure 7.6: Temperature and humidity sensmitter (AH31, Sensirion) interface and timing protocol. *156*
Figure 7.7: Overview of system setup. *157*
Figure 7.8: Multiple resistive sensors multiplexing and sensing circuit. *159*
Figure 7.9: Programmable amplifier and 16-bit ADC circuit. *159*
Figure 7.10: Data acquisition interface for fast-nose and proto-nose systems. *161*

Figure 7.11: Hybrid-nose second level multiplexing circuitries to support 80 sensors. *162*
Figure 7.12: aVLSI-nose control signal level shifting. *163*
Figure 7.13: Proto-nose software hierarchy. *165*
Figure 7.14: Sub-VI example, temperature and humidity sensor interface (AH31). *166*
Figure 7.15: Proto-nose control software and data-logging hierarchy menus. *168*
Figure 7.16: Fast-nose data acquisition software. *169*
Figure 7.17: aVLSI-nose configuration menu sub-VI. *171*
Figure 7.18: Data logging main-VI. *172*
Figure 8.1: Discrete sensor response magnitudes characterisation at room temperature. *176*
Figure 8.2: Sensor resistance variations. *177*
Figure 8.3: Effect of velocity on sensor response. *178*
Figure 8.4: Effect of flow velocity on sensor response magnitude and response time. *179*
Figure 8.5: Analyte absorption along microchannel. *181*
Figure 8.6: Sensor responses along a coated and uncoated microchannel. *183*
Figure 8.7: Spatial signal of different types of sensors responding to simple analytes. *184*
Figure 8.8: Spatial signal of different types of sensors responding to complex analytes. *184*
Figure 8.9: Temporal signals of sensors responding to simple and complex analytes. *186*
Figure 8.10: PCA plots with spatio-temporal data of 5 sensors (S2, S12, S19, S28, and S39) on proto-nose II. *187*
Figure 8.11: Hybrid-nose sensor array response to simple analytes. *189*
Figure 8.12: Typical sensor responses to different analytes with varying pulse widths and flow rates. *189*
Figure 8.13: 3D and 2D fingerprint of cream vapour and peppermint oil vapour. *190*
Figure 8.14: Effect of varying pulse widths and flow rates. *191*
Figure 8.15: PCA plots of seven analytes at various pulse widths and flow rates. *192*
Figure 8.16: Comparison between mono and stereolfactory images. *194*
Figure 8.17: Bidirectional hybrid-nose responses to ethanol vapour in air. *195*
Figure 8.18: PVPD sensor responses to vanilla. *196*
Figure 8.19: Ultra-fast sensor responses. *196*
Figure 8.20: Temporal signals of sensors along MSL101 microchannel. *197*
Figure 8.21: 10 different types of sensors responding to 10 s pulses of simple (toluene and ethanol vapour in air) and complex (peppermint and vanilla essence vapour in air) analytes in air at 30 ml min^{-1}. *197*
Figure 8.22: Temporal signals of sensors along MSL112 microchannel. *199*
Figure 8.23: Difference in temporal signal between toluene and ethanol vapour in air on MSL112 microchannel. *199*
Figure 8.24: Hybrid-nose temporal signals when assembled with MSL115 microchannel package. *200*
Figure 8.25: Varying temporal signals for simple analytes on hybrid-nose when assembled with MSL115 microchannel package. *201*

Figure 8.26: PCA plots with spatiotemporal data of 5 sensors (S34 (30 mm from inlet), S38 (1060 mm from inlet), S57 (2100 mm from inlet), S27 (2160 mm from inlet), and S30 (2200 mm from inlet)) for hybrid-nose with MSL115 microchannel package. *202*
Figure 8.27: Driving current and sensor response stability. *204*
Figure 8.28: Effect of varying drive current on sensor response to simple analytes. *205*
Figure 8.29: Sensor response magnitudes characterisation. *206*
Figure 8.30: Sensor responses to simple analytes for direct and interface mode of operation. *207*

List of Tables

Heading	Page
Table 1.1: Some reported applications of electronic nose systems.	*15*
Table 2.1: Bonding techniques for various material combinations and their requirements.	*29*
Table 3.1: Stationary phase materials and their commercial acronyms.	*55*
Table 3.2: Retention time for ethanol and toluene vapour with 5 stationary phase materials.	*55*
Table 3.3: Sensing materials for 5 sensor types and their acronyms.	*64*
Table 3.4: Experimental results of PSB, PEVA, PEG, PCL and PVPH composite sensor responses to ethanol and toluene vapour fitted to a first-order exponential equation.	*64*
Table 4.1: Polymer-composite sensing material recipes for 5 sensing materials.	*74*
Table 4.2: Polymer-composite sensing material recipes for 5 new sensor types.	*74*
Table 5.1: Major SL and MSL processes developed between 1993 and 2004.	*99*
Table 5.2: Resolution and build envelope of the two variant of Perfactory MSL systems.	*104*
Table 5.3: Polymerised resin properties.	*120*
Table 6.1: Sensor placements on the proto-nose I.	*131*
Table 6.2: Sensor placements on the proto-nose II.	*135*
Table 7.1: Hardware components of the VTS system.	*151*
Table 8.1: Effect of temperature on the response magnitude of PEVA sensor to ethanol vapour in air.	*179*
Table 8.2: Average Euclidean distance between any two odorant clusters.	*193*
Table 9.1: Major components of various systems and the technologies used for their fabrication.	*215*
Table 9.2: Nose-on-a-chip systems description and analyte tested.	*216*
Table 9.3: Summary of the characterisation results.	*221*

Summary

The electronic nose is a rudimentary replica of the human olfactory system. However there has been considerable commercial interest in the use of electronic nose systems in application areas such as environmental, medical, security and food industry. In many ways the existing electronic nose systems are considerable inferior when compared to their biological counterparts, lacking in terms of discrimination capability, processing time and environmental adaptation. Here, the aim is to extract biological principles from the mammalian olfactory systems to create a new architecture in order to aid the implementation of a nose-on-a-chip system. The primary feature identified in this study was the nasal chromatography phenomena which may provide significant improvement by producing discriminatory spatio-temporal signals for electronic nose systems.

In this project, two different but complimentary groups of systems have been designed and fabricated to investigate the feasibility of generating spatio-temporal signals. The first group of systems include the fast-nose (channel 10 cm × 500 μm^2), proto-nose I (channel 1.2 m × 500 μm^2) and II (channel 2.4 m × 500 μm^2) systems that were build using discrete components. The fast-nose system was used to characterise the discrete sensors prior to use. The proto-nose systems, in many ways, resembles gas chromatography systems. Each proto-nose system consists of two microchannels (with and without coating) and 40 polymer-composite sensors of 10 different materials placed along it. The second group of systems include the hybrid-nose and the aVLSI-nose microsensor arrays assembled with microchannel packages of various lengths (5 cm, 32 cm, 71cm, 240 cm) to form nose-on-a-chip systems. The hybrid-nose sensor array consists of 80 microsensors built on a 10 mm × 10 mm silicon substrate while the aVLSI-nose sensor array consists of 70 microsensors built on a 10 mm × 5 mm silicon substrate using standard CMOS process with smart integrated circuitries. The microchannel packages were fabricated using the Perfactory microstereolithography system. The most advanced microchannel package contains a 2.4 m × 500 μm^2 microchannel with an external size of only 36 mm × 27 mm × 7 mm. The nose-on-a-chip system achieved miniaturisation and eliminates the need for any external processing circuitries while achieving the same capability of producing spatio-temporal signals.

Using a custom-designed vapour test station and data acquisition electronics, these systems were evaluated with simple analytes and complex odours. The experimental results were in-line with the simulation results. On the coated proto-nose II system, a 25 s temporal delay was observed on the toluene vapour pulse compared to ethanol vapour pulse; this is significant compared to the uncoated system where no delay difference was obtained. Further testing with 8 analyte mixtures substantiated that spatio-temporal signals can be extracted from both the coated proto-nose and nose-on-a-chip (hybrid-nose sensor array with 2.4 m long microchannel) systems. This clearly demonstrates that these systems were capable of imitating certain characteristics of the biological olfactory system. Using only the temporal data, classification was performed with principal components analysis. The results reinforced that these additional temporal signals were useful to improve discrimination analysis which is not possible with any existing sensor-based electronic nose system. In addition, fast responding polymer-composite sensors were achieved exhibiting response times of less than 100 ms. Other biological characteristics relating to stereolfaction (two nostrils sniffing at different rates), sniffing rate (flow velocity) and duration (pulse width) were also investigated. The results converge with the biological observations that stereolfaction and sniffing at higher rate and duration improve discrimination. Last but not least, the characterisation of the smart circuitries on the aVLSI-nose show that it is possible to achieve better performance through the use of smart processing circuitries incorporating a novel DC-offset cancellation technique to amplify small sensor response with large baseline voltage. The results and theories presented in this study should provide useful contribution for designing a higher-performance electronic nose incorporating biological principles.

Acknowledgements

I would like to thank my academic supervisor Prof. Julian Gardner for generously allowing me the opportunity of studying in this field, and for his constant guidance and support during my PhD. I would also like to acknowledge the Engineering and Physical Science Research Council (EPSRC) for their financial support of the project and Nanyang Technological University (Singapore) for their financial support to the author during the three years of study. I am also grateful to all of my friends and colleagues for their constant support and encouragement during the course of this study. For practical work associated with my PhD. I would particularly like to thank the members of the *Sensors Research Laboratory, School of Engineering, University of Warwick,* including, Mr F. T. Courtney for his assistance in mechanical matters and to Dr James Covington, Mr I. Griffiths, Mr Jesus Garcia-Guzman, Ms Irina Leonte and to Dr M.V. Cole for their help in technical matters.

I would also like to acknowledge our collaborators Dr Tim Pearce and Dr Carlo Fulvi-Mari from *Department of Engineering, University of Leicester UK* for their contribution in neuromorphic modelling of the biological olfactory system. My utmost acclamation also goes to our other collaborators Dr Alister Hamilton and Dr Thomas Koickal from the *School of Engineering and Electronics, University of Edinburgh UK* for their outstanding contribution in the design of the aVLSI chips.

Last but not least, I would like to acknowledge everyone who has help me in one way or the another, without which this would not have been possible.

Declaration

The work described in this thesis is entirely original and my own, except where otherwise indicated.

Parts of this work have been presented at international conferences and published in the scientific literature listed below:

1. Journal Paper

[1] S.L. Tan, J.A. Covington, J.W. Gardner, ***Velocity-optimised diffusion for ultra-fast polymer-based resistive gas sensors***, Accepted for publication on IEE-Science, Measurement and Technology, October 2005.

2. Conference Papers

[1] J.A. Covington, S.L. Tan, J.W. Gardner, A. Hamilton, T.J. Koickal, T.C. Pearce, ***Combined smart chemFET/resistive sensor array***, IEEE Sensors Conference, Toronto, Canada, 22-24 October, 2003.

[2] S.L. Tan, J.A. Covington, J.W. Gardner, ***Ultra-fast chemical sensing microsystem employing resistive nanomaterials***, SPIE 11th International Symposium on Smart Structures and Materials, San Diego, USA, 14-18 March, 2004.

[3] S.L. Tan, J.A. Covington, J.W. Gardner, P.J. Hesketh, ***Ultra-fast/low volume odour delivery package for chemical microsystems***, IEEE Sensors Conference, Vienna, Austria, 24-27 October, 2004.

[4] T.C. Pearce, T.J. Koickal, C.F. Mari, J.A. Covington, S.L. Tan, J.W. Gardner, A. Hamilton, ***Silicon-based neuromorphic olfactory pathway implementation***, Brain Inspired Cognitive Systems Conference, Scotland, UK, 29 August – 1 September, 2004.

[5] T.C. Pearce, C.F. Mari, J.A. Covington, S.L. Tan, J.W. Garner, T.J. Koickal, A. Hamilton, ***Silicon-based neuromorphic implementation of the olfactory pathway***, The 2nd International IEEE EMBS Conference on Neural Engineering, Washington D.C., USA, 16-19 March, 2005.

[6] T.J. Koickal, S.L. Tan, A. Hamilton, J.A. Covington, J.W. Gardner, T.C. Pearce, ***A smart interface circuit to ameliorate loss of measurement range in chemical microsensor arrays***, IEEE Instrumentation and Measurement Technology conference, Ottawa, Ontario, Canada, 17-19 May, 2005.

Selected Abbreviations and Acronyms

TERM	DEFINITION
ADC	Analogue to Digital Conversion
AOB	Accessory Olfactory Bulb
aVLSI	Analogue Very Large Scale Integration
BCB	Benzocyclobutene
CAD	Computer Aided Design
CD	Conduction and Diffusion
CLK	Clock
CFLEX	Tygon 3350 silicone
CMOS	Complementary Metal Oxide Semiconductor
DAC	Digital to Analogue Conversion
DC	Direct Current
DI	Diffusion
DIO	Digital Input/Output
DLP	Digital Light Processing
DMD	Digital Micromirror Device
DVD	Digital Versatile Disk
E-nose	Electronic Nose
F	Flow Rate
FE	Finite Element
FEM	Finite Element Method
FET	Field Effect Transistor
FID	Flame Ionisation Detector
GC	Gas Chromatography
GI	Glass
GR	Granule Cell
HETP	Height Equivalent to Theoretical Plates
Hi-RES	High Resolution
I/O	Input/Output
IFN	Integrated Firing Neuron
IH	Integrated Harden
LAN	Local Area Network
LCD	Liquid Crystal Display
LIGA	Lithography Galvonoforming Abforming
LSER	Linear Solvation Energy Relationship
M/T	Mitral/Tufted Cell
MEMS	Micro-Electro-Mechanical-System
MOB	Main Olfactory Bulb
MOS	Metal Oxide Semiconductor
MPEG	Motion Picture Expert Group
MRSA	Methicillin Resistant Staphylococcus Aureus
MS	Mass Spectrometry
MSL	Microstereolithography
NC	Neocortex
NOC	Nose-On-a-Chip
NS	Navier-Stokes
OB	Olfactory Bulb

OE	Olfactory Epithelium
OS	Operating System
OR	Olfactory Receptor
ORN	Olfactory Receptor Neuron
Paralyene C	Poly (mono-chloro-para-xylylene C)
PARC	Pattern Recognition
PBA	Poly (bisphenol A carbonate)
PC	Personal Computer
PC	Principal Component
PCA	Principal Component Analysis
PCB	Printed Circuit Board
PCL	Poly (caprolactone)
PCX	Poly (chloro P xylylene)
PDE	Partial Differential Equation
PDMS	Poly (dimethylsiloxane)
PEG	Poly (ethylene glycol)
PEVA	Poly (ethylene-co-vinyl acetate)
PG	Periglomerulus Cell
PSB	Poly (stylene-co-butadiene)
PSF	Poly (sulfane)
PTFE	Poly (tetrafluoroethylene)
PVC	Poly (9-vinylcarbazole)
PVPD	Poly (vinyl pyrrolidone)
PVPH	Poly (4-vinyl phenol)
PW	Pulse Width
QCM	Quartz Crystal Microbalance
R.H.	Relative Humidity
RIE	Reactive Ion Etching
SAW	Surface Acoustic Wave
SF	Separation Factor
Si	Silicon
SL (or STL)	Stereolithography
SPI	Serial Peripheral Interface
TB	Tuberculosis
TTL	Transistor-Transistor Logic
UV	Ultra-Violet
VAP	Ventilator Acquired Pneumonia
VI	Virtual Instrument
VLSI	Very Large Scale Integration
VTS	Vapour Test Station
SE-30	Poly (dimethylsiloxane)
OV-11	Poly (dimethylmethylphenyl-siloxane) 35% mol phenyl groups
EGAD	Poly (ethylene glycol adipate)
H10	Bis (3-allyl-4-hydroxyphenyl) sulfone
QF1	Poly (trifluoropropylmethyl-siloxane)

Selected Symbol Reference

TERM	DEFINITION
∇	Vector different operator $\left(\frac{\partial}{\partial x_1},\ldots,\frac{\partial}{\partial x_n}\right)$
ΔR	Change in resistance
ΔV	Change in voltage
ΔV_{max}	Maximum change in voltage
μ	Viscosity
μC	Microchannel
A	Cross Sectional Area (Area)
C	Concentration
c	Partition coefficient
C_{GATE}	Gate capacitance
C_M	Concentration in mobile phase
$C_{PARASITIC}$	Parasitic capacitance
C_S	Concentration in stationary phase
C_{SENSOR}	Sensor capacitance
C_{SUB}	Substrate capacitance
D	Diffusion coefficient
D_0	Diffusion coefficient at zero velocity (static diffusion)
D_M	Diffusion in mobile phase
D_S	Diffusion in stationary phase
I (I_{SENS})	Constant driving current of sensor
K	Retention factor
L	Length
M	Constant (i.e. 10,000)
N	Normal vector
P	Pressure
Q	Activation energy
R	Resistance
R	Gas constant
R^2	Goodness of fit to first-order exponential equation
R_a	Mean surface roughness
R_i	Fixed reference resistor
R_{ON}	On resistance of analogue multiplexer
R_{ON} (R_{OFF})	Base resistance
R_{ON1}	Level 1 on resistance of analogue multiplexer
R_{ON2}	Level 2 on resistance of analogue multiplexer
R_s	Sensor resistance
Sym	Symmetry
SP	Stationary Phase
t	Time
t	Thickness
T	Absolute temperature
t'_R	Adjusted retention time
t_d	Relative retention time
t_{PW}	Pulse width duration
t_R	Retention time

v_c	Velocity of carrier gas
v_0	First-order velocity coefficient
V	Velocity
V_{BIAS1}	Biasing voltage 1
V_{BIAS2}	Biasing voltage 2
V_{GATE}	Gate voltage
V_{GS}	Gate-source voltage
V_{REF}	Reference voltage
V_S	Output voltage of sensor
w	Stationary phase coating thickness
W	Peak Basewidth
W	Width
z_0	Column half height
ρ	Density
ρ	Resistivity
σ	Half mid-basewidth
τ_{OFF}	Decay time coefficient
τ_{ON}	Response time coefficient
Ω	Boundary
∂	Derivative operator

To my wife May, our families and friends

for their timeless support and encouragement

Chapter 1

Introduction

This chapter introduces the mammalian olfactory system and the electronic nose system, discussing both the strengths and weaknesses of these systems. In addition, the aims and objectives of the research performed here are described. Lastly, an outline of the thesis is presented.

1.1 Mammalian olfactory system

The sense of smell is the most enigmatic among the five human senses (sight, hearing, touch, smell and taste). Olfaction is extremely important in the lives of many species since it is often their primary window to the environment [1.1]. Many animals such as dogs are classified as macrosmatic (having a keen sense of smell that is important to their survival) whereas human are considered microsmatic (have little or no olfactory sensitivity) [1.2]. Although the human sense of smell has degraded due to their evolution over the past 5 million years or more [1.2-1.3], it is still strongly linked with our emotions and aesthetics [1.4]. For many animal species, the sense of smell is crucial to their survival. It is used for navigation, food sourcing, sexual reproduction and also as a sign of impending danger [1.2, 1.4].

To allow an in-depth discussion of the various components of the biological olfactory system, an anatomy of the human olfactory system is shown in Figure 1.1 [1.2]. The smelling process begins with the inhalation of air through the nostrils, drawing odorant molecules towards the olfactory mucosa. A study has shown that 90 % of the inspired air is not sampled for olfactory content [1.5]. Nevertheless, the remaining content is savoured by the 10 million (5 millions in each nostril) or so olfactory receptors (ORs). The ORs are embedded inside a thin mucus layer and are connected to the olfactory receptor neuron (ORN). These are subsequently connected to the glomeruli nodes (approximately 1000-2000 in numbers) in the olfactory bulb. There are approximately 1000 different types of ORs (3 % of total genes in the human body), enabling us to recognise approximately 10,000 different odours [1.2, 1.6-1.7]. What is

more complex is the constant renewal of the ORs (the process is known as neurogenesis) over a 5-7 weeks period; yet the olfactory system is still robust enough to enable us to remember 'smell' even though a completely new set of ORs are in use [1.2, 1.6].

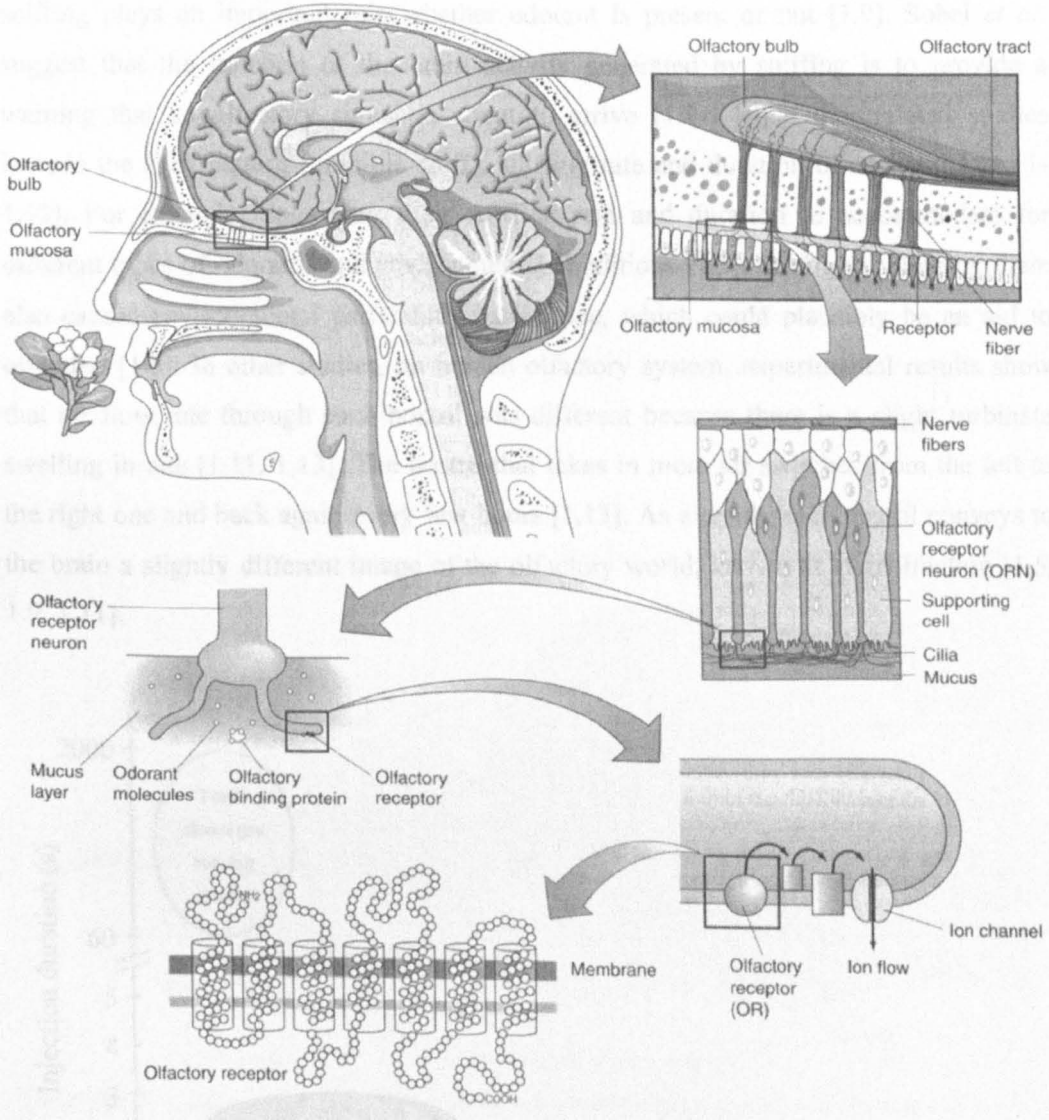

Figure 1.1: The anatomy of the human olfactory system [1.2].

Comparing the olfactory system of human with other animals, such as rats and dogs, rats are 8 to 50 times more sensitive to odour than humans whilst dogs are 300 to 10,000 times more sensitive, depending upon the odorant [1.8]. Rats have about 10 million ORs while dogs have about 1 billion ORs. However, the sensitivity of an OR, in all 3

mammals, is similar [1.2]. As such, the improvement in discrimination capability is not likely from just the number of ORs but other factors must play a vital role.

Various other studies have focused on identifying the techniques or features employed in mammalian olfactory system that affect discrimination. For example, sniffing plays an important role whether odorant is present or not [1.9]. Sobel *et al.* suggest that the function of the brain activity generated by sniffing is to provide a warning that an olfactory signal is about to arrive [1.9-1.10]. Other related studies include the sniff pattern (multiple sniff), sniffing rate and duration of each sniff [1.11-1.12]. For example, dogs vary their sniffing rate and duration to accommodate for different types of odorants and environmental conditions [1.5]. Strong exhaling by them also causes environmental particulate disturbance, which could plausibly be an aid to olfaction [1.5]. In other studies, on human olfactory system, experimental results show that air flow rate through each nostril was different because there is a slight turbinate swelling in one [1.11, 1.13]. The nostril that takes in more air switches from the left to the right one and back again every few hours [1.13]. As a result, each nostril conveys to the brain a slightly different image of the olfactory world, known as stereolfaction [1.5, 1.9, 1.11].

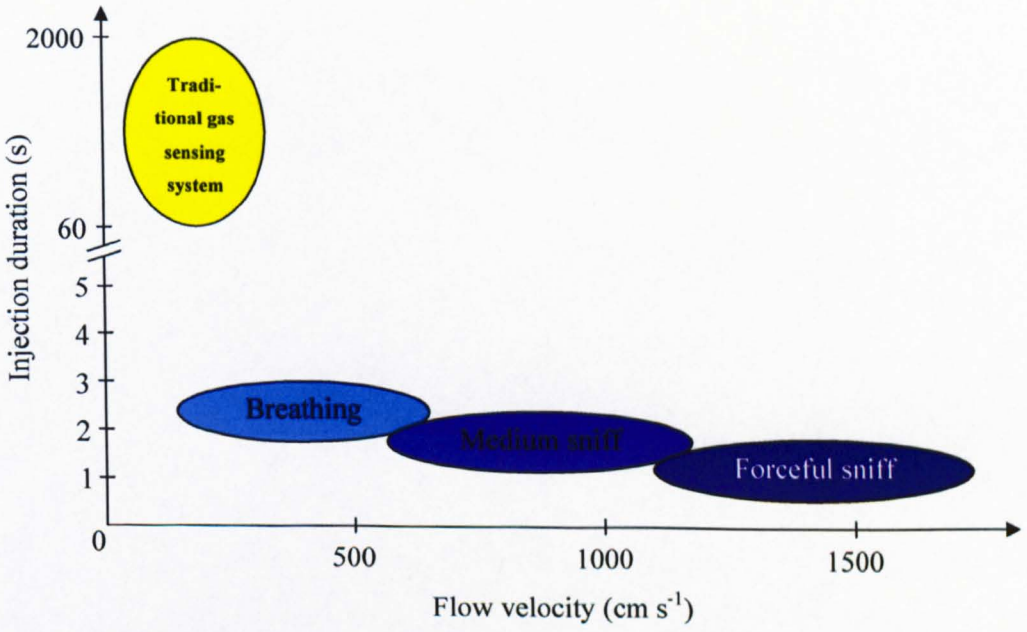

Figure 1.2: Operation range of gas sensing systems and mammalian olfactory system

Traditionally, gas sensor systems are operated with a relatively low flow rate, because it is generally believed that the response time is reaction-rate limited. Typical gas velocities across the sensors are anywhere between 20 and 200 cm s^{-1} [1.11, 1.14-1.16]. It is interesting that these gas sensors flow rates are considerable slower than the biological system. The human olfactory system operates at flow rates of between 180 and 1100 ml s^{-1}, i.e. 300 – 1540 cm s^{-1} across the olfactory epithelium [1.11, 1.17-1.19] as shown in Figure 1.2. This range can be conveniently classified according to three categories: a normal intake of breath, typically 300 cm s^{-1}, a medium sniff at 880 cm s^{-1}, and a forceful sniff at 1540 cm s^{-1}. The duration of the intake of air also varies with the three types of sniffing. Studies have shown that, as expected, increasing the sniffing velocity is usually accompanied with a reduced sniffing duration associated with the fixed capacity of the lungs, where the duration of a sniff varies anywhere from 100 ms to 3 s [1.11]. Figure 1.2 shows the range of operation for traditional gas sampling systems and three biological operations.

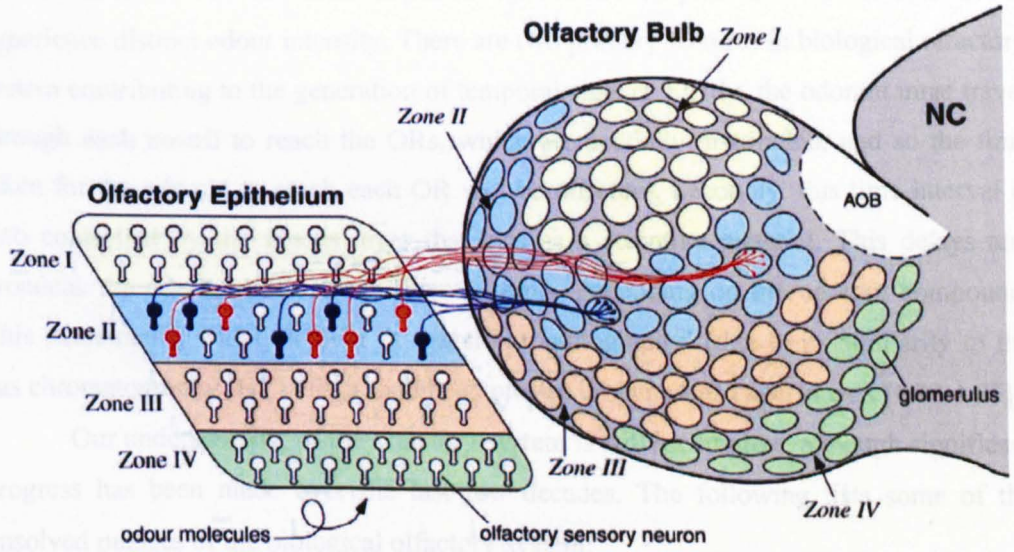

Figure 1.3: Schematic diagram illustrating the axonal connectivity pattern between the nose and the main olfactory bulb (MOB). The olfactory epithelium (OE) in mice is divided into four zones (zones *I* through *IV*) that are defined by the expression of odorant receptors. Olfactory sensory neurons in a given zone of the epithelium project to glomeruli located in a corresponding zone (zones *I* through *IV*) of the MOB. Axons of sensory neurons expressing the same odorant receptor (red or dark blue) converge to only a few defined glomeruli. Neocortex (NC); accessory olfactory bulb (AOB) [1.20].

Another recent discovery is the segregation of the ORs into 4 zones on the glomerular sheet of the main olfactory bulb (MOB) as shown in Figure 1.3 [1.20]. Each zone

contains about 250 different types of ORs onto which the same types of ORs are mapped onto the same glomerulus. As the ORs are spatially distributed across the olfactory bulb (OB) and that the OB has a varying cross-sectional geometry, the ORs will produce a spatio-temporal response map. There is also suggestion that the olfactory system may employ spatial segregation of sensory input to encode the quality of an odour [1.3].

In separate experiments conducted with rats, it has been shown that subtle differences in spatial representation can provide enough information for nearly perfect discrimination [1.11]. Slow temporal evolution has also been shown to enhance the differences in neuron firing patterns [1.12]. Others suggest that the position of the activated neurons could plausibly define the quality of odours [1.21].

These spatio-temporal data generated by the olfactory system are beginning to receive interest from researchers, although it is unclear at this point how this information is used [1.2-1.3, 1.9, 1.10-1.13, 1.22]. The spatial information is perceived from two perspectives. There are 1000 different types of ORs which are spatially distributed on the glomerular sheet. The difference in selectivity and in their placement causes each OR to experience distinct odour intensity. There are two primary features in biological olfactory system contributing to the generation of temporal signals. Firstly, the odorant must travel through each nostril to reach the ORs, which are spatially distributed, and so the time taken for the odorant to reach each OR will be different. Secondly, this time interval is also controlled by the mucus layer that acts as a retentive material. This delays and broadens the odorant pulse by different extents, depending on the odorant compound. This phenomena, widely known as 'nasal chromatography' (due to its similarity to the gas chromatography (GC) effect) had been proven in numerous experiments [1.22-1.25].

Our understanding of the olfactory system is still incomplete, although significant progress has been made over the last few decades. The following lists some of the unsolved puzzles of the biological olfactory system:

- It is not known how the signals derived from different ORs are represented in the olfactory cortex and other areas of the brain [1.6];
- How are the individual components of an odour code deciphered to yield the perception of an odour [1.6]?
- There are 4 zones within the glomerular sheet but the function of each zone is unknown [1.2];

- How can only 1000 different types of ORs enable the nose and brain of mammals to distinguish more than 10,000 different odours [1.26]?
- How does the central olfactory system combine or compare signals among 1000 types of ORs [1.27]?

The recent award of Nobel prizes in medicine or physiology (2004) to Richard Axel and Linda Buck for their work in unravelling the complexity of smell published in 1991 shows that some of the mysteries are beginning to unfold [1.7]. With many mysteries of smell and the biological olfactory system starting to be solved, it is likely that the answers to these questions will soon be known.

1.2 Electronic noses

Machine olfaction began early in the 20th century although the first conceptualisation of e-nose was made only years later in 1982 at the Warwick University in UK by Persaud and Dodd [1.28]. The term electronic-nose first appears in 1988 [1.29]; it was subsequently defined formally by Gardner *et al.* [1.4] as follows

"*An electronic nose is an instrument which comprises an array of electronic chemical sensors with partial specificity and an appropriate pattern recognition system, capable of recognising simple or complex odours.*"

Figure 1.4 shows a comparison between the processing in an electronic nose and the biological olfactory system [1.30]. With the aid of a mass flow control system, the odorant is drawn across an array of sensors, which convert odorant molecules into some form of electrical signals. These signals are then conditioned and processed prior to digitalisation. A pattern recognition (PARC) engine (usually implemented in software) is then used to classify the current odour with respect to a known odorant databases.

This type of e-nose architecture works well for simple discrimination analysis where the odorant classes are highly dissimilar. For complex odorants where the differences are subtle, it is still a very challenging task for an e-nose system to solve. Although the e-nose system has its concept abstracted from the biological olfactory system, the details differ significantly at various stages of implementation.

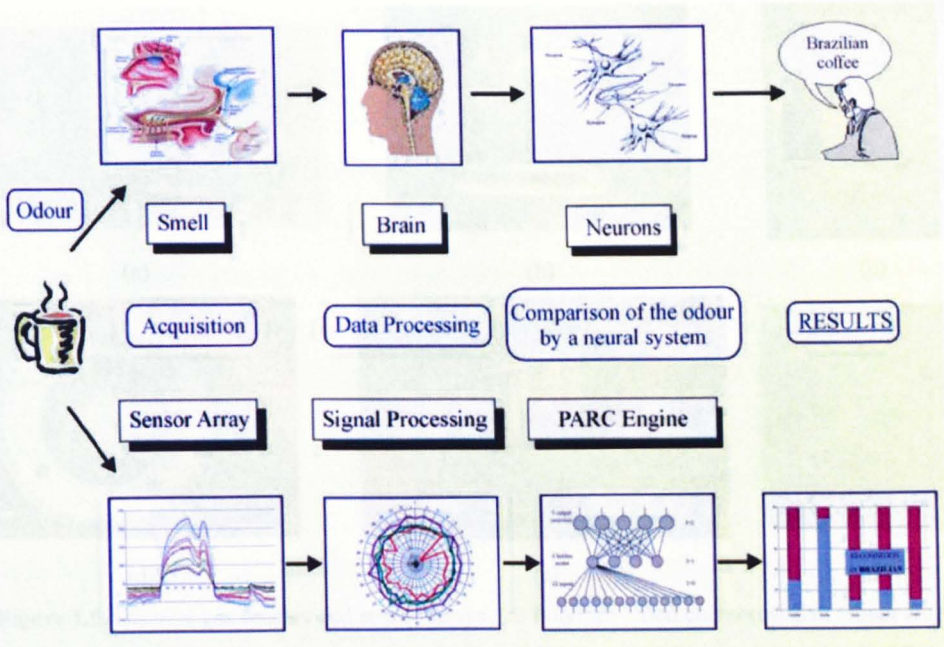

Figure 1.4: A comparison between the processing in an e-nose and a biological olfactory system [1.30].

1.2.1 Sensor-based electronic noses

A sensor-based e-nose typically consists of a flow system connected to a pump and some switching valves with a sensor array residing in a sampling chamber. The sensors are interfaced to some form of signal conditioning and data acquisition electronics, where the sensors responses are collected whenever the system is triggered. The data acquired are usually analysed using a software implemented pattern recognition algorithm, which compares the present data set to some previously trained data and thus classify them under one of the learned classes (e.g. a supervised pattern recognition system).

Central to the system are the sensors used to detect odorants. Usually sensors are either employed in a discrete fashion, i.e. individual or integrated together, by either putting discrete devices together or integrating many sensors onto a single device, to form an array. Most e-nose systems employ a discrete sensor array since it allows individual sensors to be replaced easily, for example if poisoned. The fabrication process is also less complex since there is no risk of cross-contamination when depositing multiple sensing materials. On the other hand, combining sensors onto one array device allows on-chip integration of processing circuitry; hence it enables miniaturisation at a lower cost, making it attractive for portable implementation. A few examples of both types of sensors are shown in Figure 1.5.

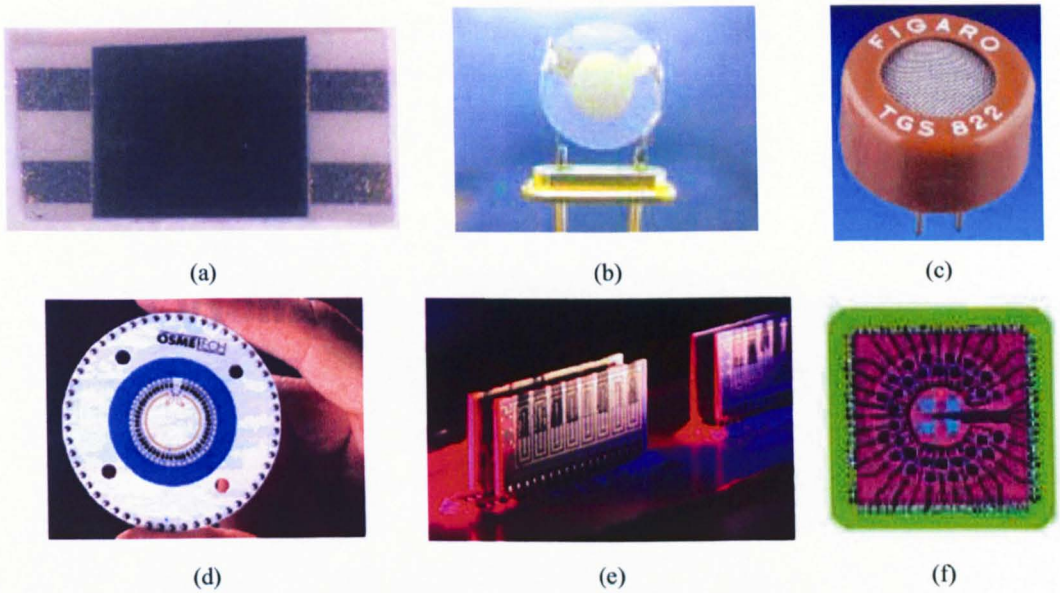

(a) (b) (c)

(d) (e) (f)

Figure 1.5: Discrete gas sensors and sensor arrays. (a) Polymer-based chemoresistive sensor from Osmetech [1.31]. (b) Polymer-based quartz crystal microbalance (QCM) sensor from Applied Sensor [1.32]. (c) Figaro TGS822 tin dioxide (SnO_2) sensor [1.33]. (d) Osmetech 48-sensor discrete sensor array [1.31]. (e) NASA 32-sensor integrated sensor array [1.34]. (f) Smiths Detection (previously known as Cyrano Sciences) 32-sensor integrated array [1.35]. (Not to scale)

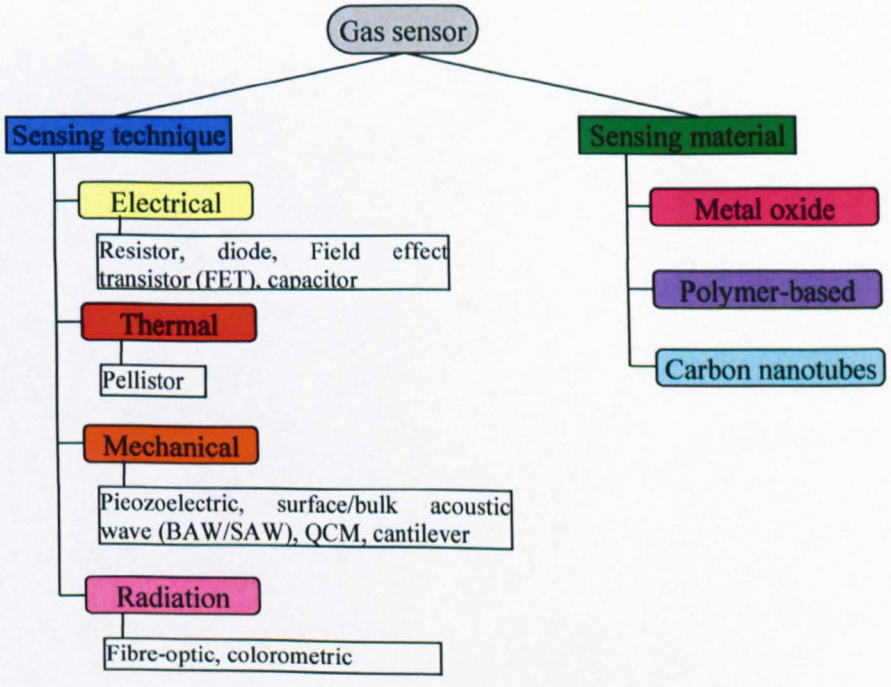

Figure 1.6: Sensing techniques and materials employed to produce gas sensor.

The right sensing technique with an appropriate sensing material can produce a gas sensor. Many possible techniques and materials have been demonstrated as listed in Figure 1.6. In summary, four commonly used transduction techniques are electrical, thermal, mechanical and radiation, while the 3 regular classes of sensing materials are metal oxide, polymer-based and carbon nanotube materials.

The most prevalent gas sensor employed in commercial electronic noses system is the chemoresistor. This is because they are cheap and can be easily interfaced to data acquisition electronics. The first-generation of commercial electronic nose, based on these types of sensors, were bench-top machines that were bulky and expensive. Today, portable hand-held units are available due to the improvement in sensor technology.

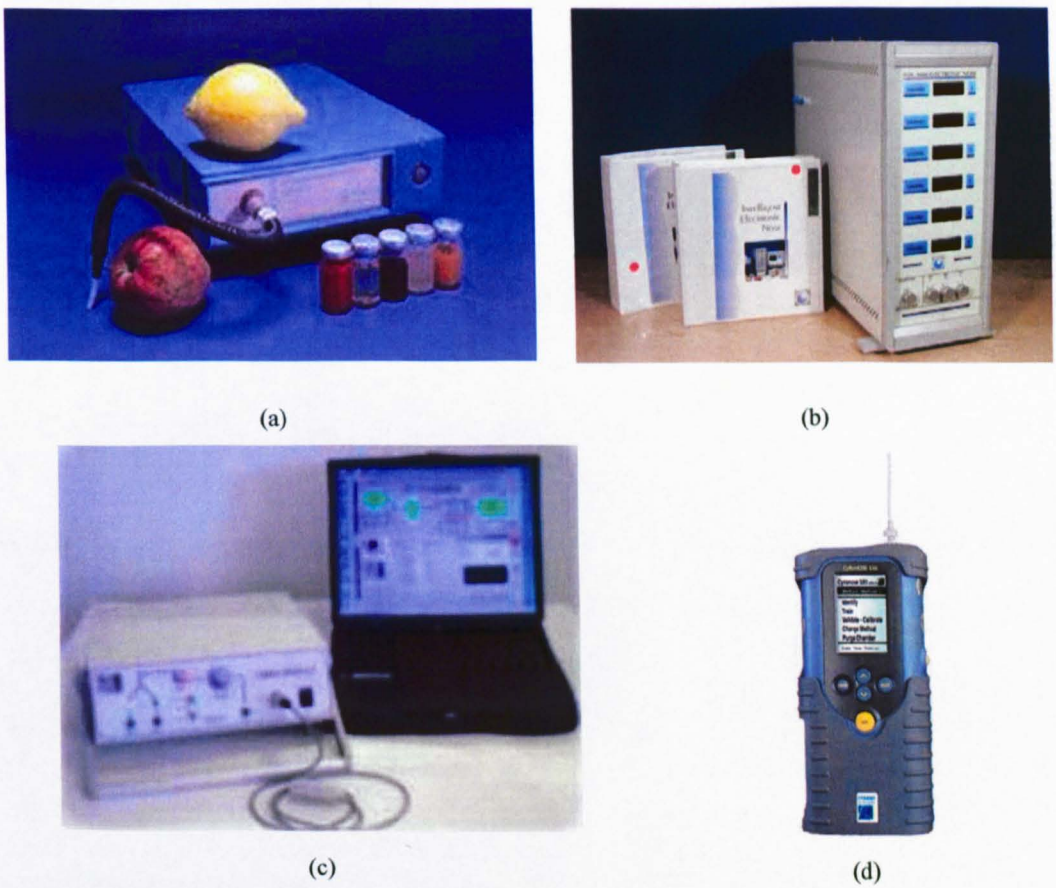

Figure 1.7: Sensor-based electronic noses. (a) PEN (portable electronic nose) from WMA Airsense using 10 MOS sensors [1.36]. (b) FOX 3000 from Alpha-MOS using 12 MOS sensors [1.37]. (c) LibraNOSE 3 from Technobiochip Scarl using 8 QCM sensors [1.38]. (d) Cyranose 320 portable electronic nose from Smiths Detection using 32 polymer-composite sensors [1.35]. (Not to scale)

Figure 1.7 shows some examples of the commercially available sensor-based electronic nose systems. Figure 1.7(a)-(c) are bench-top units requiring a PC connection to the e-noses for operation. Portable hand-held units, such as the Cyranose 320 from Smiths Detection, are available. However, these systems are lacking in terms of functionality (especially in PARC) due to the limited processing power of their embedded processor and the power available in battery-operated portable units.

1.2.2 Instrument-based electronic noses

Conventionally, chemical composition is analysed using instrumental techniques such as GC and mass spectrometry (MS). Chromatographic techniques are based principally on the partition of compounds between a stationary phase and a mobile phase, so that molecules are separated on the basis of the different strengths of their interactions with the stationary phase [1.4]. A strong interaction causes the molecule to remain in the stationary phase considerable longer than a molecule with a weak interaction, hence the molecules are separated. Using a long micro-column (usually longer than 10 m with typical cross-section < 1 mm^2) coated with a retentive material on its inner surface, the compound to be analysed is injected into the column at an optimum velocity, using an inert carrier gas, e.g. He. Towards the outlet of the column, a series of peaks begin to elute, representing various components of the composition. The time taken for the molecules to elute is a function of the phase/odorant interaction. A flame ionisation detector (FID) or surface acoustic wave (SAW) sensor is normally placed at the end of the column and is used to capture these eluted peaks. Other studies have shown that it is possible to employ gas sensors, used in electronic noses, for such detection purposes [1.40-1.41].

Another analytical method for detecting odorant compounds is to use mass spectrometry. This technique separates molecules by ionisation and then separating the ions in the mass spectrometer according to the mass-to-charge ratio of the ion [1.4]. A combination of the two techniques, called GC-MS, is a popular technique for identifying volatile compounds. However, all these three techniques are costly, requiring a complex system and would usually take a long time to complete each analysis. Nevertheless, they are still attractive for those applications where high resolution and sensitivity are required for off-line analysis. Some of these instrument-based electronic nose systems are available on the market as shown in Figure 1.8. Figure 1.8(a) shows an MS-based e-nose

system from Smart Nose while Figures 1.8(b)-(d) show three GC-based e-nose systems from Agilent Technologies, Electronic Sensor Technology and Alpha-MOS respectively.

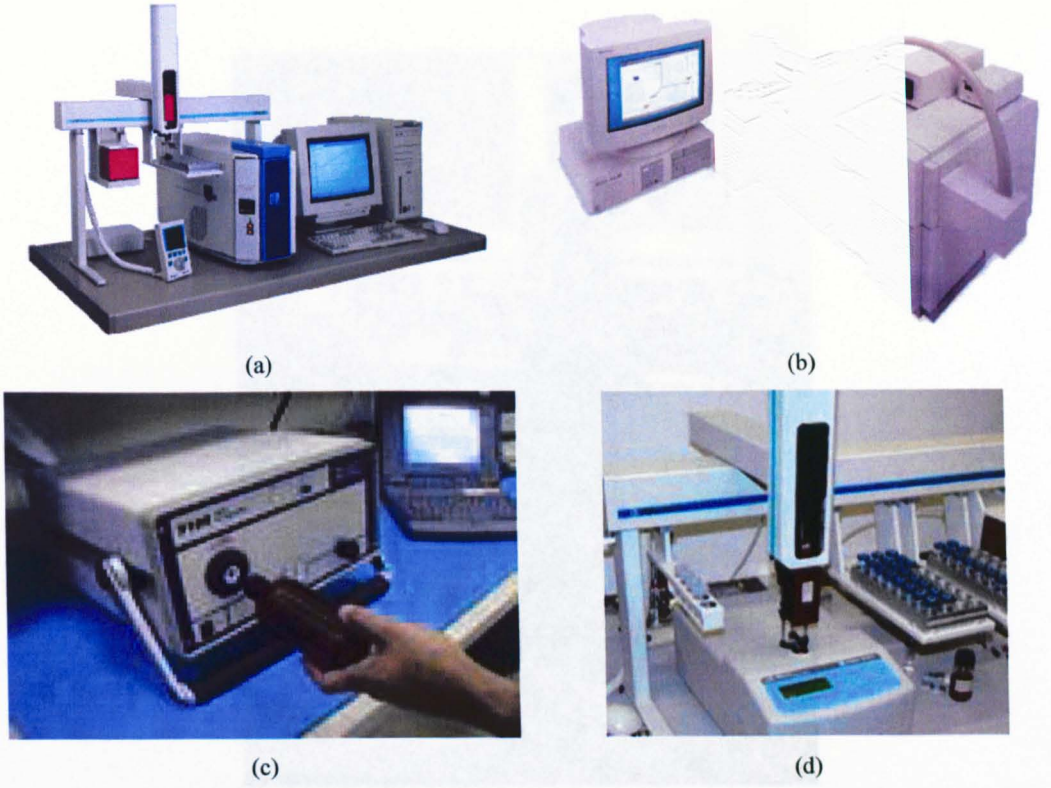

Figure 1.8: Instrument-based electronic noses. (a) Smart-nose, a MS-based e-nose from Smart-nose Ltd. [1.41]. (b) HP 4440 A, a GC-based e-nose from Agilent Technologies [1.42]. (c) z-nose, a GC-based e-nose from Electronic Sensor Technology [1.43]. (d) Heracles, a GC-based e-nose from Alpha-MOS [1.37]. (Not to scale)

1.2.3 Combined approach to electronic noses

To harness the advantages of both traditional e-nose sensor based systems and analytical instrument-based systems, it is useful to combine them to create a new architecture platform for the electronic nose. The Prometheus e-nose system [1.37] from Alpha-MOS is one such example as shown in Figure 1.9. It combines the KRONOS (fingerprint mass spectrometer) and the FOX 4000 (18-sensor traditional e-nose) system to create an integrated platform where both techniques (MS and traditional e-nose) are employed simultaneously.

The pitfall of this system is that the two techniques are loosely combined with multiple sensors used to replace the one detector MS system. The sensitivity of the

system certainly is improved; however, the analysis time remains similar. These systems are also expensive due to the need to include two sets of components instead of one. In addition, the original MS system architecture is still used, except with multiple sensors.

Figure 1.9: Combined approach electronic nose system with multi sensor array system (SAS) and fingerprint mass spectrometry (FMS), Prometheus, Alpha-MOS [1.37].

A possible method to reduce the analysis time is to make partial results available before the whole separation process is complete. By merging the features found in biological olfactory system with the know-how of the traditional electronic nose system, a new combined e-nose architecture shown in Figure 1.10 [1.44] has been proposed. The idea behind this system is to emulate the 'nasal chromatography' effect observed in the biological olfactory system, combined with the spatio-temporal signal extraction and processing of these signals using silicon implemented olfactory bulb model. The front-end of the system will consist of a gas chromatography column with an array of sensors placed along it. The project is a collaborative effort between University of Leicester, University of Edinburgh and University of Warwick.

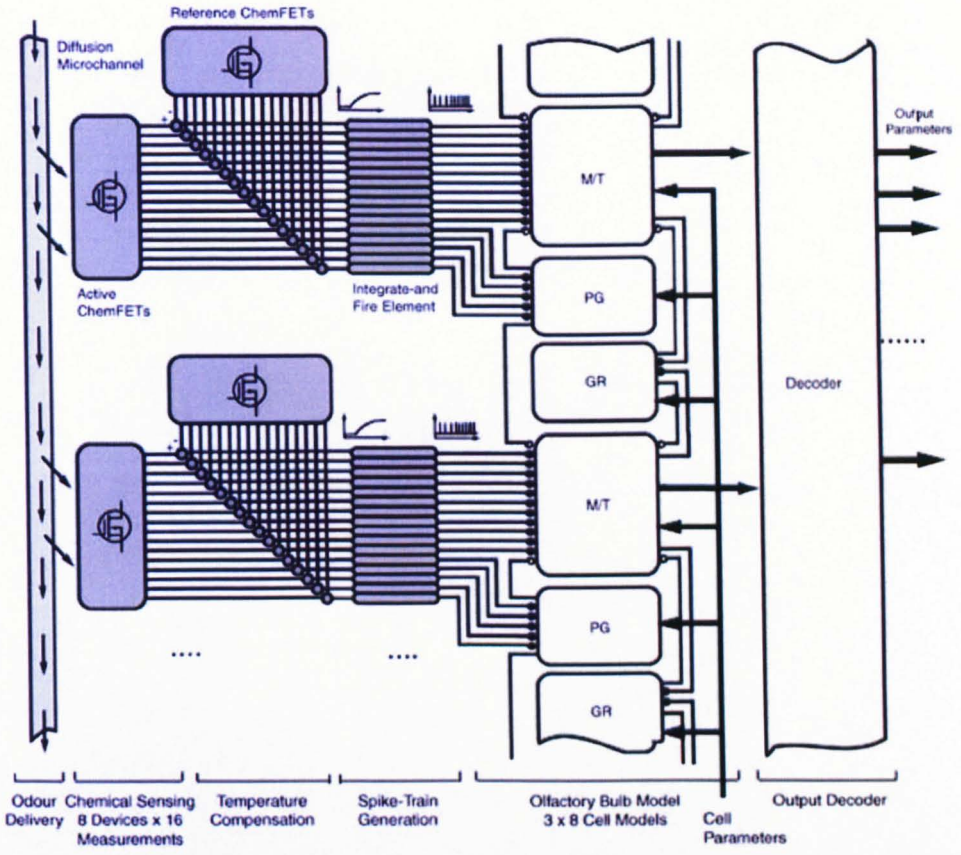

Figure 1.10: Schematic layout of the proposed silicon implementation of the olfactory system, showing the odour delivery, chemFET (field effect transistor) array, integrate and fire elements, olfactory bulb model and output decoder. Peri-glomerulus (PG) cell model, granule (GR) cell model, mitral/tufted (M/T) cell model. Excitatory connections shown as filled circles. Inhibitory connections shown as empty circles [1.44].

Figure 1.11 shows a plot comparing the analysis time versus the probability of error between a GC system and a traditional e-nose system. For the GC system, there will be a minimum time before which the first component of the compound starts to elute. From that time onwards, various peaks representing the remaining components will elute, decreasing the error rate of the system. In traditional e-nose systems, all sensors are exposed to the compound/odorant simultaneously. The sensors start to respond as soon as the analyte is injected. However it will require a finite amount of time to settle down due to the differences in response time of the diverse sensor array and the need to perform pattern recognition. In general, the effective discrimination is not as favourable when compared to the GC system; however it is capable of providing a fast response time. The nose-on-a-chip system proposed here (Figure 1.10) harnesses the strength of both

systems; it is expected to out-perform its predecessors. For the nose-on-chip (NOC) system proposed here, the two effects will combine to generate an initial set of results from the sensors that are placed closer to the inlet. As the analytes traverse along the microchannel GC, they will be delayed (retained) by differing amount depending on their strength of interaction with the stationary phase material. This will be picked-up by the sensors toward the end of the microchannel when the analysis time is extended. The effective result is expected to outstrip the GC system because it has an array of sensors probing along the microchannel GC instead of just one sensor towards the end of the GC system.

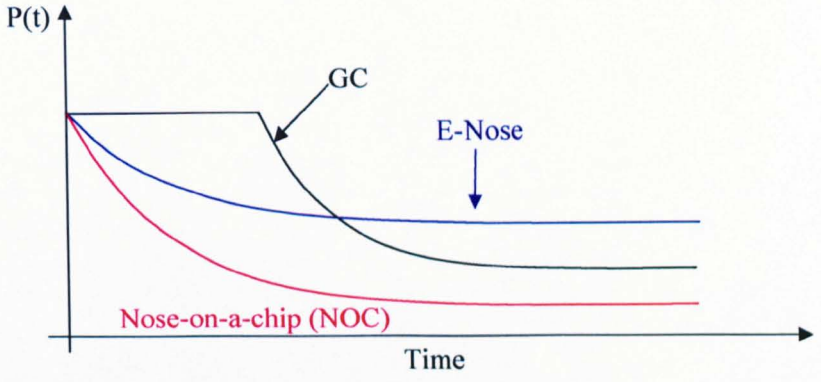

Figure 1.11: Comparison of the probability of error versus analysis time for various systems.

1.3 Applications of electronic noses

The scope for deploying e-nose systems has been increasing due to its improved capability to distinguish odours over recent years. When the first commercial e-nose was introduced in 1993 (Fox 2000, Alpha-MOS, France), the main application areas were in the food and related industries. Environmental monitoring is also a growing application area for the e-nose. Other emerging areas include the use of e-nose for medical diagnostic applications especially in the area of health monitoring. Security related applications is another area of huge potential for growth, and include explosives and drug detection and biometric identification among many others. Table 1.1 tabulates some of the reported applications of e-nose classified under these four broad categories.

In the food and related industries, e-noses are normally used to monitor the food quality at various stages of processing [1.45-1.46]. They have the potential to provide consistent quality assurance, replacing the human counterparts, who are subjective and

easily fatigued. The demands on e-nose systems for environmental monitoring applications are far more challenging due to the varying background conditions. The e-nose provides a practical solution, as it is capable of offering round the clock monitoring. There is also potential interest from the automotive industries, where these systems could be used to monitor the air quality inside the car cabin and the exhaust gases of a car to determine the combustion efficiency and pollution index [1.50]. This will certainly accelerate the development of low cost sensors due to their potentially huge demand.

Table 1.1: Some reported applications of electronic nose systems.

Category	Application	E-nose used	Reference
Food and related industries	Classification of vegetable oils	Fox 2000, Alpha-MOS	[1.45]
	Characterisation of commercial Cheddar cheese flavour	eNose 5000, Marconi Applied Technologies	[1.46]
	Perfume identification	Tokyo Inst. Tech. in-house QCM-based e-nose	[1.47]
Environmental monitoring and automotive related	Contaminating residues of insecticides	MOSES II by Lennartz Electronic/MoTech	[1.48]
	Characterisation of wastewater	NOSE (model D), Neotronics Scientific	[1.49]
	Cabin air analyser for automotive	Warwick in-house e-nose	[1.50]
Medical diagnostic and health monitoring	Detection of Mycobacterium tuberculosis (TB)	Bloodhound e-nose Model BH114	[1.51]
	Methicillin Resistant Staphylococcus Aureus (MRSA) detection	Osmetech e-nose	[1.52]
	Early Traces of Lung Cancer	Cyranose 320 from Smiths Detection	[1.53]
Security	Explosive detection	zNose 7100 from Electronic Sensor Technology	[1.54]
	Nerve agent detection	zNose 4100 from Electronic Sensor Technology	[1.55]
	Body odour (hand) for biometric identification	Scentinel e-nose from Mastiff Electronic System	[1.56]

Another emerging area for e-noses is in medical diagnostics. Many diseases can be detected by the odour they emit, including Escherichia coli (E-coli), Tuberculosis (TB) [1.51], Methicillin Resistant Staphylococcus Aureus (MRSA) [1.52], lung cancer [1.53], fungal growth and Ventilator Acquired Pneumonia (VAP). The e-nose is an attractive option for diagnostic as it is non-intrusive and provides fast analysis. In the area of security related applications, e-noses can be employed for various tasks including the detection of explosives, nerve agents and toxic gases [1.54-1.55]. It has also been reported that the human body odour of the hand can be detected for biometric identification [1.56].

1.4 Research objectives

The primary focus of the project is to extract the engineering design principles underpinning the mammalian olfactory system and apply them to an artificial nose. The deficiency in the discrimination capability of the current e-nose systems when compared to the biological olfactory systems has highlighted the need to re-think its architectural implementation. The nasal chromatography effect, which generates spatio-temporal signal generation, could well be playing considerable effect, providing significant improvements in discrimination. Beside the performance factor, the cost and size of commercially available e-nose systems is still expensive (€10,000 to €100,000) and bulky in size. To address these issues, new microfabrication techniques will be investigated to create a miniaturised nose-on-a-chip microsystem with integrated smart circuitry.

The biologically emulated nose-on-a-chip system requires two essential components; these are the smart sensor array and the microchannel package. The semiconductor wafer fabrication processes provide an ideal platform for implementing the smart sensor array, where signal conditioning and processing circuitry can be integrated. The cost will be significantly reduced through volume production while its small feature size ensures optimum miniaturisation. The microchannel package is vital for producing the spatio-temporal signals. Various micromachining techniques will be investigated to facilitate cost-size-performance optimisation. In short, the main research objectives are summarised as follows:

- The development of finite element simulation models for the sensors, microchannels and GC microchannels to aid the design and development process.
- The design and development of discrete gas sensors, sensor arrays and CMOS compatible smart sensor arrays.
- The design and development of novel mass transport limited microchannels and microchannel packages that mimics the properties of the olfactory epithelium.
- The integration of the discrete sensors, sensor arrays and microchannel packages to create novel biological emulated prototype systems and nose-on-a-chip microsystems.
- The characterisation of the various microsystems to demonstrate the generation of spatio-temporal signals.

1.5 Outline of thesis

The thesis describes the design, development and characterisation of various e-nose microsystems. Chapter 1 reviews the biological olfactory system and the electronic nose system to highlight their differences. It also discusses the main application areas of the electronic nose system. The aims and objectives of the thesis are then presented.

Chapter 2 describes the project evolution, examines the key enabling technologies and gives a brief description of the various components developed in this project.

Chapter 3 discusses new finite element simulation models for the biologically emulated microchannels performed as part of this project. Two major classes of microchannels are described, they are the uncoated microchannels and those microchannels coated with a thin layer of retentive materials (known as stationary phase). A sensor model for the polymer-composite sensor is also developed to facilitate the complete system to be simulated. In addition, other variables such as flow velocity and pulse width are studied using these models.

Chapters 4 and 5 cover new works in the design and development of two of the important components, the sensors and the microchannel packages. The fabrication of three different types of sensors and sensor arrays are discussed in Chapter 4. In Chapter 5, the design and fabrication of the microchannel packages will be given.

Chapter 6 describes the integration process of the discrete sensors and the nose-on-a-chip microsystem based on the sensor arrays and microchannel packages. The deposition process for the microchannel GC is presented.

Chapter 7 details the components of the support systems for characterising all the above systems. They include the vapour test station and data acquisition circuit as well as the custom-designed software interfaces to enable automated testing and data logging.

Chapter 8 reports the characterisation results of the fabricated microsystems to evaluate their performance. The focus here has been geared towards obtaining spatio-temporal signals from these systems and the use of these signals to aid discrimination.

Chapter 9 concludes the research discussing the results and how the objectives of the project are fulfilled. Last but not least, the latest developments are presented to highlight the possible future enhancements.

1.6 References

[1.1] B.W. Ache, ***Phylogeny of smell and taste***, Smell and Taste in Health and Disease, T. V. Getchell, R. L. Doty, L. M. Bartoshuk, and J. B. Snow, Jr., eds. Raven Press, 1991, New York.

[1.2] E.B. Goldstein, ***Sensation and perception***, Sixth Edition, Wadsworth Inc Fulfilment, 2002.

[1.3] R. Axel, ***Representations of olfactory information in the brain***, Howard Hughes Medical Institute (HHMI), http://www.hhmi.org/research/investigators/axel.html, March 2002.

[1.4] J.W. Gardner, P.N. Bartlett, ***Electronic noses: principles and applications***, Oxford University Press, Inc, New York, 1999.

[1.5] G.S. Settles, ***Sniffers: Fluid-dynamic sampling for olfactory trace detection in nature and homeland security***, The 2004 Freeman Scholar Lecture, Journal of Fluids Engineering, March 2005.

[1.6] B. Malnic, J. Hirono, T. Sato, L.B. Buck, ***Combinatorial receptor codes for odours***, Cell, Vol. 96, pp. 713-723, 1999.

[1.7] L. Buck, R. Axel, ***A novel multigene family may encode odorant receptors: a molecular basis for odor recognition***, Cell, Vol. 65, pp. 175-187, 1991.

[1.8] D.D. Laing, R.L. Doty, W. Breipohl, ***The human sense of smell***, New York: Springer, 1991.

[1.9] N. Sobel, V. Prabhakaran, J.E. Desmond, G.H. Glover, R.L. Gode, E.V. Sullivan, J.D.E. Garbrieli, ***Sniffing and smelling: separate subsystems in the human olfactory cortex***, Nature, Vol. 392, March 1998.

[1.10] N. Sobel, V. Prabhakaran, Z. Zhao, J.E. Desmond, G.H. Glover, E.V. Sullivan, J.D.E. Garbrieli, ***Time course of odorant-induced activation in the human primary olfactory cortex***, Journal of Neurophysiology, 83, pp. 537-551, 2000.

[1.11] N. Sobel, R.M. Khan, C.A. Hartley, E.V. Sullivan, J.D.E. Garbrieli, ***Sniffing longer rather than stronger to maintain olfactory detection threshold***, Chem. Senses 25, pp. 1-8, 2000.

[1.12] N. Uchida, Z.F. Mainen, ***Speed and accuracy of olfactory discrimination in the rat***, Nature Neuroscience, Vol. 6, November 2003.

[1.13] N. Sobel, R.M. Khan, A. Saltman, E.V. Sullivan, J.D.E. Garbrieli, ***Olfaction: The world smells different to each nostril***, Nature, Vol. 402, November 1999.

[1.14] A. Meckes, J. Behrens, ***Microfluidic system for the integration and cyclic operation of gas sensors***, Sensors and Actuators, 76, pp. 478-483, 1999.

[1.15] T. Eklov, I. Lundstrom, ***Gas mixture analysis using a distributed chemical sensor system***, Sensors and Actuators, B 57, pp. 274-282, 1999.

[1.16] S-J. Liu, H-X. Shen, J-X. Feng, ***Effects of gas flow-rates on a Clark-type oxygen gas sensor***, Analytica Chimica Acta 313, pp. 89-92, 1995.

[1.17] M.S. Nieuwenhuizen, J.L.N. Harteveld, ***An automated SAW gas sensor testing system***, Sensors and Actuators A, pp. 219-229, 1994.

[1.18] I. Hahn, P.W. Scherer, M.M. Mozell, ***Velocity profiles measured for airflow through a large-scale model of the human nasal cavity***, J. of Applied Physiology, 75, pp. 2273-2287, 1993.

[1.19] K. Keyhani, P.W. Scherer, M.M. Mozell, ***A numerical model of nasal odorant transport for the analysis of human olfaction***, J. Theoretical Biology, 186, 1997.

[1.20] K. Mori, H. Nagao, Y. Yoshihara, ***The olfactory bulb: coding and processing of odour molecule information***, Science, Vol. 286, 22nd October 1999.

[1.21] R. Axel, L.B. Buck, ***The mystery of smell: Finding the odorant receptors***, Howard Hughes Medical Institute (HHMI), http://www.hhmi.org/senses/d120.html, March 2002.

[1.22] M.M. Mozell, M. Jagodowicz, ***Mechanisms underlying the analysis of odorant quality at the level of the olfactory mucosa, I: Spatiotemporal sorption patterns***, Annual New York Academy of Sciences, 237, pp. 76-90, 1974.

[1.23] M.M. Mozell, ***Evidence for a chromatographic model of olfaction***, The Journal of General Physiology, Vol. 56, pp. 46-63, 1970.

[1.24] M.M. Mozell, M. Jagodowicz, ***Chromatographic separation of odorants by the nose: Retention times measured across in vivo olfactory mucosa***, Science, Vol. 181, pp. 1247-1249, 1973.

[1.25] R. Axel, L.B. Buck, C. Dulac, ***Sensing smell***, Howard Hughes Medical Institute (HHMI), http://www.hhmi.org/annual99/a243.html, March 2002.

[1.26] L.K. Altman, ***Unravelling enigma of smell wins Nobel for 2 Americans***, http://www.nytimes.com/2004/10/05/science/05nobel.html?ex=1254715200&en=1ff9b1667815f2cb&ei=5088&partner=rssnyt, The New York Times, 5th October 2004.

[1.27] D.E. Hornung, R.D. Lansing, M.M. Mozell, ***Distribution of butanol molecules along bull frog olfactory mucosa***, Nature, Vol. 254, Apr 17, pp. 617-618, 1975.

[1.28] K.C. Persaud, G.H. Dodd, ***Analysis of discrimination mechanisms of the mammalian olfactory system using a model nose***, Nature 299, pp. 352-355, 1982.

[1.29] J.W. Gardner, ***Pattern recognition in the Warwick electronic nose***, 8th International Congress of the European Chemoreception Research Organisation, Coventry, UK, 1988.

[1.30] J.A. Covington, J.W. Gardner, ***A nose on a chip? High temperature electronic odour sensors***, Eurosensors XVIII Conference, Italy, September 2004.

[1.31] Osmetech plc, http://www.osmetech.co.uk/, March 2003.

[1.32] AppliedSensor GmbH, ***Polymer-based QMB (quartz microbalance)***, http://www.appliedsensor.com/qmb_sensors_%28as-qhv%29/, Reutlingen, 72770 Germany, March 2003.

[1.33] Figaro gas sensor manufacturer, http://www.figarosensor.com/products/822pdf.pdf, Figaro USA Inc., Glenview, IL 60026 USA, March 2003.

[1.34] Jet Propulsion Laboratory, NASA, http://mix.msfc.nasa.gov/ABSTRACTS/MSFC-0300200.html, March 2004.

[1.35] Smiths Detection, http://www.devicelink.com/ivdt/archive/00/01/004.html, March 2003.

[1.36] WMA Airsense Analysentechnik GmbH, ***PEN (portable electronic nose) using 10 MOS sensors***, http://www.airsense.com/english/index5.html, Schwerin 19061, Germany, March 2004.

[1.37] Alpha-MOS France, ***FOX 3000 electronic nose system using 10 MOS sensors***, http://www.alpha-mos.com/en/products/profox.php, Toulouse 31400, France, March 2004.

[1.38] Technobiochip Scarl, ***LibraNOSE 3 using 8 QCM sensors***, http://www.technobiochip.com/, 57033 Marciana Marina (LI), Isle of Elba – Italy, March 2004.

[1.39] S. Beling, G. Bläser, J. Bock, L. Heinert, M. Traxler, D. Kohl, ***Signal conditioning for semiconductor gas sensors being used as detectors in gas-chromatographs and similar applications***, Sensors and Actuators B: Chemical, Vol. 52, pp. 15-22, 1998.

[1.40] P.W. Ash, N.W. Barnett, L. Ebdon, S.J. Rowley, ***Configuration and optimisation of semiconductor gas sensors as gas chromatographic detectors***, Analytica Chimica Acta, 216, pp. 147-161, 1989.

[1.41] Smart-nose Ltd, ***Smart-nose, a MS-based e-nose system***, http://www.smartnose.com/, Marin-Epagnier, Switzerland, March 2004.

[1.42] Agilent Tecnologies Inc, ***HP 4440 A, a GC-based e-nose system***, http://www.chem.agilent.com/cag/peak/peak1-00/article01.html, Palo Alto, CA 94306, USA, March 2004.

[1.43] Electronic Sensor Technology, ***zNose 7100, a GC-based e-nose system***, http://www.znose.com/7100.htm, Newbury Park, CA 91320, March 2004.

[1.44] J.W. Gardner V.K. Varadan, O.O. Awadelkarim, ***Microsensors, MEMS and smart devices***, John Wiley & Sons, Ltd, 2001.

[1.45] Y.G. Martín, J.L.P. Pavón, B.M. Cordero, C.G. Pinto, ***Classification of vegetable oils by linear discriminant analysis of electronic nose data***, Analytica Chimica Acta 384, pp. 83-94, 1999.

[1.46] P.J.O. Riordan, C.M. Delahunty, ***Characterisation of commercial Cheddar cheese flavour.1: traditional and electronic nose approach to quality assessment and market classification***, International Dairy Journal 13, pp. 355–370, 2003.

[1.47] T. Nakamoto, A. Fukuda and T. Moriizumi, ***Perfume and flavour identification by odour-sensing system using quartz-resonator sensor array and neural-network pattern recognition***, Sensors and Actuators B: Chemical, Vol. 10, pp. 85- 90, 1993.

[1.48] R.E. Baby, M. Cabezas, E.N.W. de Reca, ***Electronic nose: a useful tool for monitoring environmental contamination***, Sensors and Actuators B: Chemical, Vol. 69, pp. 214-218. 2000.

[1.49] R.M. Stuetz, R.A. Fenner, G. Engin, ***Characterisation of wastewater using an electronic nose***, Water Research, Vol. 33, pp. 442-452, 1999.

[1.50] R. Tamadoni, J.W. Gardner, D.C. Dyer, A. Krauss, U. Weimar, I. Besnard, P.N. Bartlett, L. Gier,C. Stefano, D. Briand, B. van der Schoot, H. Sundgren, F. Davide, ***A cabin air analyser for automotive application***, 8th Int. Conf. on Chemical Sensors, Basel, Switzerland, 3-5 July 2000.

[1.51] A.K. Pavlou, N. Magan, J.M. Jones, J. Brown, P. Klatser, A.P.F. Turner, ***Detection of Mycobacterium tuberculosis (TB) in vitro and in situ using an electronic nose in combination with a neural network system***, Biosensors and Bioelectronics 20, pp. 538–544, 2004.

[1.52] Osmetech plc, ***E-Nose Healthcare Applications, Methicillin Resistant Staphylococcus Aureus (MRSA) detection***, http://www.osmetech.com/enose.htm, March 2004.

[1.53] The Cleveland Clinic, ***Electronic nose capable of sniffing out early traces of lung cancer***, http://www.clevelandclinic.org/media/media.htm, April 13, 2005.

[1.54] E.J. Staples, ***Nerve gas detection using a SAW/GC***, http://www.znose.com/tech_papers/papers/GeneralAnalysis/ACS_99.pdf, Electronic Sensor Technology, EST Internal Report, May 2002.

[1.55] G.W. Watson, D.S. McGuire, ***Detection of explosives in soil and water with electronic nose***, http://www.znose.com/tech_papers/papers/Security/NERVE.pdf, American Chemical Society Meeting, Ontario, California, October 5-7, 1999.

[1.56] Mastiff Electronic Systems, ***Future biometric technologies***, http://et.wcu.edu/aidc/BioWebPages/Biometrics_Future.html, Hampshire, UK, March 2004.

Chapter 2

Project evolution and system description

2.1 Introduction

It is not uncommon for our increased understanding of biological systems to be followed by significant technological advances. One good example is the colour filter masks used in colour television, which were created based on study of the human vision system [2.1]. In the evolution of electronic noses, there have been many milestones in the areas of sensor design, sensing material and packaging. However, the improvement in performance has been more limited; considering the advancements in technology and biological discoveries achieved over the recent years. In an attempt to bridge this limitation, radical hypothesis are investigated by emulating the discoveries observed in the biological olfactory system [2.2].

In this chapter, the abstraction of one specific primary feature that could govern the superiority of biological noses will be discussed. This is the 'spatio-temporal' feature that is found in many biological systems and is applied in many real-world applications (such as digital video compression). In order to demonstrate this key feature, two prototype systems have been built to study the technique of spatio-temporal signals generation. At the same time, extensive investigations have been conducted to determine the optimum method for constructing a nose-on-a-chip (NOC) system, using the latest microfabrication techniques. In addition, this chapter also serves as an introduction to discuss various sub-systems developed throughout the project. This should enable readers to have a better understanding of the proposed final system before the components are examined in detail.

2.2 Mimicking the biological olfactory system

Among the five human senses, the sense of smell is the least understood. Although the study on mammalian olfactory system has been equivalent with respect to other human

senses, it has only yielded many of its secrets in the last two decades. Recently, Richard Axel and Linda Buck were awarded with Nobel Prize (2004) for their discovery of a gene pool that contains the blueprint for receptors or sensors within the nose which identify odours [2.3]. The range of animals used for various studies of olfactory systems is vast, ranging from fish [2.4], salamander [2.5], rat [2.6], and dog [2.7] to human [2.3, 2.8-2.10], amongst many others.

The study of the human vision system has led to the discovery of the fact that only three primary types of colour photoreceptors (rods and cones, i.e. sensors) are used to distinguish among all the colours we perceive [2.1, 2.10]. Other researchers working on hearing have made many discoveries which have led to many improvements for those with hearing disabilities, and more notably the creation of stereo sound. These are just some of the well known examples where the study of biological systems can be used to aid technological development.

The concept of electronic nose was mooted in 1982 [2.11] at the University of Warwick and later formally defined by Gardner [2.12]. Although the e-nose systems have existed for some time, their performance still falls far behind their biological counterparts. The general perception for this deficiency is due to the lack of sensor numbers (10 million olfactory receptors (ORs) in human and 1 billion ORs in dog as compared to the current highest density sensor array of 1,000) and tunings (sensor diversity, approximately 1,000 different types of receptor proteins expressed by the human genome, diversity in electronic nose is usually less than 50). Moreover, most e-nose systems do not inherit any enhanced architectural feature of their biological counterpart.

Here, the aim is to investigate any distinct biological features that could be exploited to enhance odour discrimination. The relevant feature can be described through the following facts. The nasal system has a thin layer of mucus that has been shown to exhibit a gas chromatographic effect. Together with the spatial distribution of the vast amount of receptors cells, a spatio-temporal map of the odorant is conveyed to the brain [2.13-2.16]. Further research by olfactologists is required to show how the brain makes use of these information to aid discrimination or to provide evidence that it is capable of providing compensation to offset the time differences (temporal signals) [2.17-2.18]. Exploiting this distinct feature could yield significant improvement in terms of odour

discrimination. The challenge is how to harness this feature by combining it with modern fabrication technologies to create a new architecture for e-nose systems.

2.2.1 Spatio-temporal signal

Once this spatio-temporal feature was identified, the focus of the research shifted towards the interpretation of what constitutes spatio-temporal signals and how these can be replicated and exploited. The use of spatio-temporal information is not new and the best analogy is its application on digital video compression. The analogue video tape has been replaced with high definition digital video or versatile disc (DVD). A motion video consists of a minimum of 25 static picture frames arranged in sequence every second. The compression technique (MPEG-1/2/4) can reduce vast amount of data by using images that are similar (spatio-temporal picture sequence). Consider a video clip with blue sky background with a man parachuting. If you analyse each static picture, most of the data are similar because the background is the same, so data can be compressed easily due to the spatial similarity. Comparing across different frame sequences, only the man on parachute is different; hence temporal similarities are abundant as well.

Mozell *et al.* published extensively in the 1960s and 1970s on their study of various mammalian olfactory systems. Their work focused on collecting evidence of different biological olfactory systems to demonstrate that they exhibit a 'chromatographic alike' effect which results in the creation of an odorant's 'spatio-temporal map' [2.17-2.23]. Many other researchers have also published similar observations [2.8-2.10, 2.13-2.25]. Mozell *et al.*'s basic concept is known as 'nasal chromatography' that is analogous to the gas chromatographic effect. The mucus layer of the biological olfactory system acts in the same way as the retentive stationary phase of a gas chromatography (GC) column [2.20-2.21, 2.25]. They argued that this chromatographic effect is one of the mechanisms basic to odorant discrimination and spatio-temporal information is likely to be of central importance to the understanding of both quality and intensity of discrimination [2.22]. Due to the differing retentive nature of the mucus on different odorants and the physical distance between receptor cells, there will be time lag (temporal) information between various analytes reaching different receptor cells. The spatial signals can be viewed from two perspectives. Due to the relative positioning of different receptor cells on the receptor sheet, their signals will be

different. Secondly, as various groups of receptor cells are selectively tuned to different odorants, they will response distinctively to a particular odorant.

Having identified the underlying basic mechanism of nasal chromatography, an advance electronic nose-on-a-chip system will be designed based on this biologically inspired concept. The NOC system will be built using microfabrication technologies incorporating room temperature sensor elements with a micro-GC column. A sensor array will be placed along the microchannel to capture spatio-temporal signals. In the next section, the microfabrication technologies for realising the system will be investigated.

2.3 Microfabrication

Recent technological advances in microelectronics have led to a trend towards creating integrated miniaturised devices or microsystems (moving towards nanosystems). One exemplary paradigm is the semiconductor industry. Since the creation of the first planar integrated circuit in 1961, the technology has progressed tremendously in terms of resolution (currently, the minimum feature size is 65 nm) and cost. Moore observed in 1965 an exponential growth in the number of transistors per integrated circuit and predicted that this trend would continue. His prediction remains accurate until today and is commonly described as the Moore's law [2.26]. Over the last two decades, novel techniques have emerged to build on the success of microlithography-based semiconductor fabrication (primarily due to mass reproducibility and cost) to extend their reach into the area of Micro-Electro-Mechanical-Systems (MEMS), and more recently into microfluidic systems (sometimes described as lab-on-a-chip). These hybrid systems have proven to be attractive due to the 'cost-feature-size-power' aspects. Taking into account such technological advantages, the feasibility of implementing the proposed system on such a platform is investigated.

2.3.1 Micro gas sensor array

The fabrication of gas sensor arrays using silicon microfabrication techniques is not new. Numerous researchers, including Lewis *et al.* [2.27-2.28], Goodman *et al.* [2.28-2.29], Lundström *et al.* [2.30] and many others [2.31-2.32], have fabricated such arrays, some of them with over 1000 sensors. However the sensor diversity is still limited (< 20). Although these sensor arrays offer high-density integration, they suffer in terms of

having to deposit large groups of sensors with the same sensing material, resulting in low reproducibility. Lower density arrays are preferred in some scenarios [2.1, 2.12] as the distances between sensors are further apart, allowing each sensor to be deposited with a different sensing material. The fabrication of micro gas sensor arrays is highly dependent upon the type of deposition technique. Those requiring the whole sensor array to be dipped into some form of solution (such as electro-chemical deposition [2.33] and microlithography deposition [2.34]) will limit the diversity because the deposited sensors will be contaminated if they are exposed to other solutions. On the other hand, those sensor arrays that offer wider diversity usually employ spraying technique through a mechanical mask [2.27-2.29]. Hence, the sensors need farther physical separation.

The ability to integrate driving and conditioning circuitries within the sensor array substrate provides an attractive solution for larger arrays. This is consistent with the trend to produce smart sensor arrays [2.35]. However, it is difficult to incorporate large numbers of integrated circuits into high density sensor arrays, due to space constraints. These arrays usually combine the driving circuitries with some form of multiplexing to provide access to each sensor by scanning them sequentially [2.28-2.29]. Others provide highly intelligent sensors at the expense of lower sensor count [2.36]. Nevertheless, as the technology progresses, higher density smart sensor arrays are becoming more feasible and a logical step towards circuit integration.

2.3.2 Microchannel fabrication review

Microchannels can be fabricated using various techniques such as the etching of a silicon wafer or glass and subsequently bonding them together. Traditional micromachining techniques performed on bulk silicon material produce high-quality microchannels with high-aspect ratio such as those shown in Figure 2.1(a) which was fabricated using fusion bonding [2.37-2.38], and Figure 2.1(b) which was fabricated using anodic bonding [2.39-2.42]. However, these bonding techniques usually require high temperature/voltage/pressure, which are not compatible with polymer-based gas sensors that only can tolerate temperatures less than 100 °C.

Other techniques using photo-patterned materials to create microchannels have also been investigated [2.43-2.49]. The advantages of using such techniques include the relative ease of fabrication, the use of low temperature, and the fabrication of microchannels on silicon (with integrated circuitries) after processing. Poly

(dimethylsiloxane) (PDMS) [2.43], benzocyclobutene (BCB) [2.44], SU-8 [2.45-2.46] (Figure 2.2(a)) and poly (mono-chloro-para-xylylene) (Parylene) [2.47] (Figure 2.2(b)) have been proposed by various researchers. These materials have been traditionally used as photoresists with the primary advantages of being photo-patternable, low fabrication temperature, and ease of processing. In particular, SU-8 has recently gained much attention due to its ability to create high-aspect ratio MEMS, its ease of thickness control and its high mechanical strength.

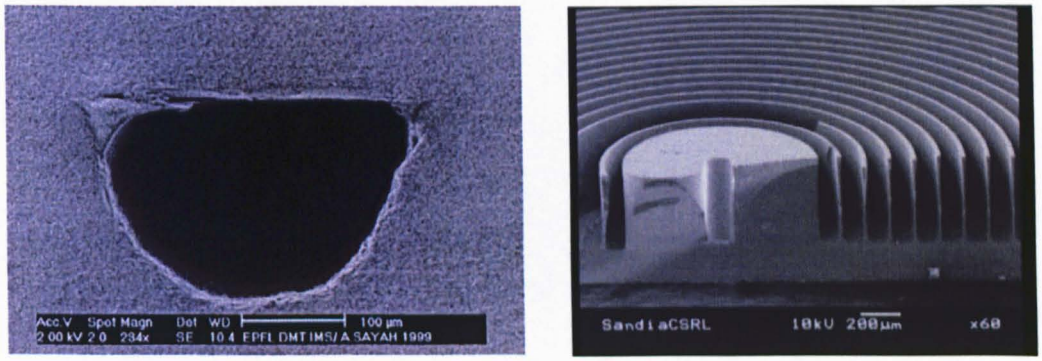

(a) (b)

Figure 2.1: Microchannels fabricated by fusion and anodic bonding. (a) Fusion bonded microchannel [2.38]. (b) Anodicaly bonded GC microchannel [2.41].

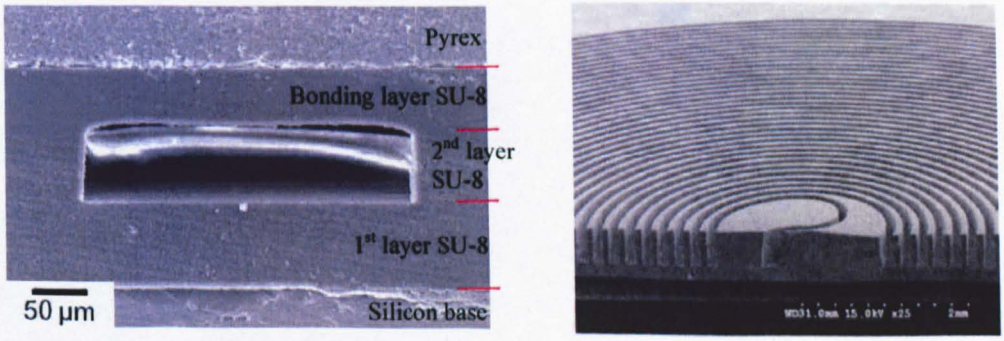

(a) (b)

Figure 2.2: Microchannels fabricated using various micromachining techniques and materials. (a) Microchannel fabricated with multilayers SU-8 with silicon base and pyrex lid [2.45]. (b) Microchannel GC fabricated with parylene [2.47].

Other bonding techniques have also been investigated using different base materials to create microchannels. Table 2.1 summarises a survey of some of the available techniques.

Table 2.1: Bonding techniques for various material combinations and their requirements.

	Si-Si				Si-Gl			Gl-Gl			Si-Pl	Gl-Pl	Pl-Pl
Adhesive													
Eutectic													
Anodic													
Fusion													
Surface Roughness * (μm)	< 3	< 50	< 1	< 1	< 5	< 50	< 1	< 5	< 50	< 1	< 5		
Intermediate Layer & Thickness (μm)	BCB 1-12	Au + Ti 0.15	S_iO_2 0.5-5	N	PD MS 5-30	N	N	PD MS 5-30	Poly-S_i 0.16-2	Y 2-5	Y (epoxy) 5-30		
Temp. (°C)	65	370	450	1000	50	450	450 (100)	50	50	250	< 100 (depends on epoxy used)		
Pressure (MPa)	0.17	Vac	-	-	-	-	- (50)	-	Vac	-	-		
Bond Strength (MPa)	30	0.5	30	200	-	-	9 (6)	-	H	H	-		
Trench Filling	N	Y	Y	N	N	-	N	N	Y	-	Y		
Voltage (V)	0	0	100	0	0	700	0	0	500	0	-		
Void (%)	0	>10	L	0	L	L	L	L	L	L	L		

* Unprocessed wafer has a surface roughness of 0.2 nm. (Y-Yes, N-No, Vac-Vacuum, H-High, L-Low)

Adhesive bonding: Use an intermediate glue or polymer layer for adhesion.

Eutectic bonding: Form silicides with silicon and metal (e.g. platinum silicide).

Anodic bonding: Technique for bonding silicon to glass.

Fusion bonding: Annealing at high temperature to form silicon-oxide-silicon bond.

For traditional micromachining techniques working with either silicon or glass, trenches are created on one-side of the silicon prior to bonding with a flat surface base to form the microchannel. The micromachining techniques usually employ deep-Reactive Ion Etching (RIE) [2.49-2.50], Lithography Galvonoforming Abforming (LIGA) [2.51], power blasting [2.52] or others which are complex and expensive.

Another emerging area of active development is the rapid prototyping industries. Conventional stereolithography fabrication techniques used to fabricate industrial prototypes have low resolution (typically > 250 μm). Recently, these systems have been developed to create high resolution processes employing fine dual lasers to fabricate components with nanometer resolution. The new Microsystems Laboratory at the University of Warwick [2.53] is pioneering many new initiatives using this technology. In particular, this technology has been employed to fabricate microchannel packages that are compatible for integration with gas sensor arrays. This technique will be discussed in detail in Chapter 5.

2.4 Project description

There are several issues to address towards the development of the NOC system. Having reviewed the evolution of electronic nose and the biological olfactory system, it was established that the superiority of the biological counterpart is not solely based on the number and diversity of ORs, but it is also a combination with other features. Although it is still unclear at this point which is the main feature providing this superiority, the existence of spatio-temporal information in biological nose is expected to play a significant role. To achieve optimal performance for the NOC system, biological principles are incorporated as basis of the design. Furthermore, an in-depth study on the current trend and available technologies is conducted to ensure state-of-the-art platforms are chosen to address performance, cost and size issues for low to medium volume production.

The project is separated into two main groups of systems progressing in parallel. The first group of systems consist of fast-nose and proto-nose systems which are built using discrete components to explore the feasibility of generating spatio-temporal signals. Inheriting the nasal chromatography concept, a microchannel (with and without coating to experiment the retention effect of stationary phase) with diverse discrete sensors placed along it is built. The initial design (proto-nose I) yielded significant results. This design was superseded with proto-nose II with improved sensor and microchannel configuration.

The second group of systems comprised NOC microsystems which were designed to operate based on the same biological principle as the proto-nose. The NOC was intended to offer a huge reduction in size with complete smart integrated circuitry. Two sensor arrays have been fabricated within this work based on resistive polymer-composite sensors and FET devices. The hybrid-nose is a low-cost sensor array test-bed dedicated for experimentation. It was fabricated in-house to capture the essence of sensor placements without integrated circuitry. Designed in tandem was a aVLSI-nose fabricated using a standard CMOS process. This sensor array has integrated drive and conditioning circuits to remove the need for an external processing circuit. The sensor array itself was insufficient without a media to deliver the analytes to the sensors for generating spatio-temporal signals. Hence for the NOC, a microchannel package was fitted over the sensor array to deliver the analytes. Having discussed various microchannel fabrication techniques in Section 2.3.2, many trials using different

materials (such as SU-8) were conducted. The complications and high-cost involved for low-volume fabrication using these techniques directed the research to focus on a new emerging technique employing microstereolithography. This technique will be examined in details in Chapter 5.

Prior to the design and fabrication of the proposed systems, there are many uncertainties considering the integration of the microchannel packaging with the sensor array and the performance of the systems. To reduce the cost and time required to redesign the system, finite element simulations were conducted to predict the performance of various designs of the system components. These simulations (Chapter 3) include microchannels of different dimensions, lengths and coatings combined with sensors of different diversities and placements.

2.5 Conclusions

In this chapter, the rationale for embarking on the project was presented. Initially, the recent discoveries made in biological olfactory system were examined. It was identified that the spatio-temporal signals generated by the nasal chromatography effect may well be the main feature resulting in the superior performance of biological olfactory system. Having understood this phenomenon, a review on the current trends in microsystems technologies, especially those related to microchannel and microsensor array fabrication, was conducted. After careful considerations of the design issues (such as cost, process availability, size and the requirements of generating spatio-temporal signals) involved to build the systems, the processes used to fabricate the main components were briefly discussed. This outline serves as an overview of the work carried out towards building a nose-on-a-chip.

2.6 References

[2.1] J.E. Crouch, ***Functional human anatomy***, Williams & Wilkins, Fourth edition, Philadelphia, 1984.

[2.2] T.C. Pearce, S.S. Schiffman, H.T. Nagle, J.W. Gardner, ***Handbook of machine olfaction: Electronic Nose Technology***, Wiley-VCH Verlag GmbH & Co, Weinheim, Germany, 2003.

[2.3] L. Buck, R. Axel, ***A novel multigene family may encode odorant receptors: a molecular basis for odor recognition***, Cell, Vol. 65, pp. 175-187, 1991.

[2.4] W.C. Michel, M.J. Sanderson, J.K. Olson, D.L. Lipschitz, ***Evidence of a novel transduction pathway mediating detection of polyamines by the zebra fish olfactory system,*** The Journal of Experimental Biology 206, pp. 1697-1706, 2003.

[2.5] J.S. Kauer, ***On the scents of smell in the salamander***, Nature Vol. 417, pp. 336-342, 2002.

[2.6] J.W. Scott, T. Brierley, ***A functional map in rat olfactory epithelium***, Chemical Senses, 24, pp. 679-690, 1999.

[2.7] E.H. Ashton, J.T. Eayrs, D.G. Moulton, ***Olfactory acuity in the dog***, Nature 179, pp. 1069–1070, 1957.

[2.8] K. Mori, H. Nagao, Y. Yoshihara, ***The olfactory bulb: Coding and processing of odor molecule information***, Science, Vol. 286, 1999.

[2.9] I. Hahn, P.W. Scherer, M.M. Mozell, ***Velocity profiles measured for airflow through a large-scale model of the human nasal cavity***, The American Physiology Society, pp. 2273-2287, 1993.

[2.10] R. Alex, L. Buck, ***The mystery of smell: How rats and mice - and probably humans - recognise odours***, Howard Hughes Medical Institute, http://www.hhmi.org/senses/, December 2003.

[2.11] K. Persaud, G.H. Dodd, ***Analysis of discrimination mechanisms of the mammalian olfactory system using a model nose***, Nature 299, pp. 352-355, 1982.

[2.12] J.W. Gardner, P.N. Bartlett, ***Electronic noses: Principles and applications***, Oxford University Press, Inc, New York, 1999.

[2.13] M. Lysetskiy, A. Lozowski, J.M. Zurada, ***Invariant recognition of spatio-temporal in the olfactory system model***, Neural Processing Letters 15, pp. 225–234, 2002.

[2.14] S. Sachse, C.G. Galizia, ***Role of inhibition for temporal and spatial odor representation in olfactory output neurons: A calcium imaging study***, Journal of Neurophysiology 87, pp. 1106–1117, 2002.

[2.15] B. Quenet, D. Horn, G. Dreyfus, ***Temporal coding in an olfactory oscillatory model***, Neurocomputing 38-40, pp. 831-836, 2001.

[2.16] W.J. Freeman, ***Spatial divergence and temporal dispersion in primary olfactory nerve of cat***, Journal of Neurophysiology 35, pp. 733 – 744, 1972.

[2.17] M.M. Mozell, M. Jagodowicz, ***Mechanisms underlying the analysis of odorant quality at the level of the olfactory mucosa, I: Spatiotemporal sorption patterns***, Annal New York Academy of Sciences, 237, pp. 76-90, 1974.

[2.18] D.E. Hornung, M.M. Mozell, ***Factors influencing the differential sorption of odorant molecules across the olfactory mucosa***, The Journal of General Physiology, Vol. 69, pp. 343-361, 1977.

[2.19] M.M. Mozell, ***The spatiotemporal analysis of odorants at the level of the olfactory receptor sheet***, Journal of General Physiology 50, pp. 25-41, 1966.

[2.20] M.M. Mozell, ***Evidence for a chromatographic model of olfaction***, The Journal of General Physiology, Vol. 56, pp. 46-63, 1970.

[2.21] M.M. Mozell, M. Jagodowicz, ***Chromatographic separation of odorants by the nose: Retention times measured across in vivo olfactory mucosa***, Science, Vol. 181, pp. 1247-1249, 1973.

[2.22] D.E. Hornung, R.D. Lansing, M.M. Mozell, ***Distribution of butanol molecules along bull frog olfactory mucosa***, Nature, Vol. 254, Apr 17, pp. 617-618, 1975.

[2.23] D.E. Hornung, S.L. Youngentob, M.M. Mozell, ***Olfactory mucosa/air partitioning of odorants***, Brain Research, 413, pp. 147-154, 1987.

[2.24] G.S. Settles, ***Sniffers: Fluid-dynamic sampling for olfactory trace detection in nature and homeland security- The 2004 freeman scholar lecture***, The journal of fluids engineering, Vol. 127, pp. 189-218, 2005.

[2.25] R.B. Nachbar, T.H. Morton, ***A gas chromatographic (GLPC) model for the sense of smell: Variation of olfactory sensitivity with conditions of stimulation***, Journal of Theoretical Biology 89, pp. 387-407, 1981.

[2.26] G.E. Moore, ***Cramming more components onto integrated circuits***, Electronics, Vol. 38, pp. 114-117, April 1965.

[2.27] N.S. Lewis's Research Group, ***High density gas sensor array***, California Institute of Technology, Division of Chemistry and Chemical Engineering, http://www.its.caltech.edu/~mmrc/nsl/default.htm, January 2004.

[2.28] J.A. Dickson, M.S. Freund, N.S. Lewis, R.M. Goodman, ***An integrated chemical sensor array using carbon black polymers and a standard CMOS process***, Technical Digest of the Solid-State Sensor and Actuator Workshop, pp. 162-165, 2000.

[2.29] J.A. Dickson, R.M. Goodman, ***Integrated chemical sensors based on carbon black and polymer films using a standard CMOS process and post-processing,*** ISCAS 2000, IEEE International Symposium on Circuits and Systems, May 28-31, Geneva, Switzerland, 2000.

[2.30] I. Lundström, R. Erlandsson, U. Frykman, E. Hedborg, A. Spetz, H. Sundgren, S. Welin, F. Winquist, ***Artificial 'olfactory' images from a chemical sensor using a light-pulse technique,*** Nature 352, pp. 47-50, 1991.

[2.31] J. Mizsei, ***Olfactory images by scanning Kelvin method,*** Sensors and Actuators B 48, pp. 300-304, 1998.

[2.32] N.A. Rakow, K.S. Suslick, ***A colorimetric sensor array for odour visualization,*** Nature, Vol. 406, pp. 710 – 713, August 2000.

[2.33] P.N. Bartlett, P.B.M. Archer, S.K. Ling-Chung, ***Conducting polymer gas sensors part I: fabrication and characterization,*** Sensors and Actuators, Vol. 19, pp. 125-140, 1989.

[2.34] S.G. Wang, Q. Zhang , D.J. Yang , P.J. Sellin , G.F. Zhong, ***Multi-walled carbon nanotube-based gas sensors for NH_3 detection,*** Diamond and Related Materials 13, pp. 1327–1332, 2004.

[2.35] J.W. Gardner, V.K. Varadan, O.O. Awadelkarim, ***Microsensors, MEMS and smart devices,*** John Wiley & Sons Ltd, Chicester, 2001.

[2.36] C. Hagleitner, A. Hierlemann, D. Lange, A. Kummer, N. Kerness, O. Brand, H. Baltes, ***Smart single-chip gas sensor microsystem,*** Nature, Vol. 414, pp. 293-296, Nov 2001.

[2.37] R.W. Tjerkstra, M. de Boer, E. Berenschot, J.G.E. Gardeniers, A. van den Berg, M.C. Elwenspoek, ***Etching technology for chromatography microchannels,*** Electrochimica Acta., Vol. 42, pp. 3399-3406, 1997.

[2.38] A. Sayah, D. Solignac, T. Cueni, M.A.M. Gijs, ***Development of novel low temperature bonding technologies for microchip chemical analysis applications,*** Sensors and Actuators, 84, pp. 103–108, 2000.

[2.39] S.C. Terry, J.H. Jerman, J.B. Angeli, ***A gas chromatographic air analyzer fabricated on a silicon wafer,*** IEEE Transaction on Electron Devices, Vol. 26, pp. 1880-1886, 1979.

[2.40] G. Wiranto, N.D. Samaan, D.E. Mulcahy, D.E. Davey, ***Microfabrication of capillary columns on silicon***, Proc. of SPIE, Int. Society for Optical Engineering – SMART electronic and MEMS, Vol. 3242, pp. 59-64, 1997.

[2.41] C.M. Matzke, R.J. Kottenstette, S.A. Casalnuovo, G.C. Frye-Mason, M.L. Hudsin, D.Y. Sasaki, R.P. Manginell, C.C. Wong, ***Microfabricated silicon gas chromatographic microchannels: fabrication and performance***, SPIE Int. Society of Optical Engineering. Proc. of SPIE: micromachining and microfabrication process and technology IV, Santa Clara, California, Vol. 3511, Sep 1998.

[2.42] A. Berthold, ***Low temperature wafer-to-wafer bonding for microchemical systems***, Deltch Uitgevers, The Netherlands, Feb 2001.

[2.43] G. C. López, A.J. Rosenbloom, V.W. Weedn, K.J. Gabriel, ***In Situ Fabricated Microchannels using Porous Polymer and Xenon Difluoride Etchant***, Micro Total Analysis System (μTAS), Nara, Japan. November 3-7, 2002.

[2.44] T. Glinsner, V. Dragoi, C. Thanner, G. Mittendorfer, P. Lindner, C. Schaefer, ***Wafer bonding using BCB and SU-8 intermediate layers for MEMS applications***, SEMICON Taiwan 2002, Sep 16-18, 2002.

[2.45] R. Jackman, ***Soft Lithography, Lecture Notes for 10.491***, MIT, Feb 2001.

[2.46] MicroChem Corp. (MCC), supplier of SU-8 photoresist, SU-8 datasheets, http://www.microchem.com/products/su_eight.htm, viewed on 28th October 2002.

[2.47] H-S Noh, P.J. Hesketh, G.C. Fyre-Mason, ***Parylene gas chromatographic column for rapid thermal cycling***, Journal of Microelectromechanical Systems, Vol. 11, pp. 718-725, 2002.

[2.48] R.J. Jackman, T.M. Floyd, R. Ghodssi, M.A. Schmidt, K.F. Jensen, ***Microfluidic systems with on-line UV detection fabricated in photodefinable epoxy***, Journal of Micromech. Microeng., 11, pp. 263–269, 2001.

[2.49] C-T Pan, H. Yang, S-C Shen, M-C Chou, H-P Chou, ***A low-temperature wafer bonding technique using patternable materials***, Journal of Micromech. Microeng., 12, pp. 611-615, 2002.

[2.50] V.N. Hung, T. Abe, P.N. Minh, M. Esashi, ***High-frequency one-chip multichannel quartz crystal microbalance fabricated by deep RIE***, Sensors and Actuators A: Physical, Vol. 108, pp. 91-96, 2003.

[2.51] R.K. Kupka, F. Bouamrane, C. Cremers, S. Megtert, ***Microfabrication: LIGA-X and applications***, Applied Surface Science, Vol. 164, pp. 97-110, 2000.

[2.52] D. Solignac, A. Sayah, S. Constantin, R. Freitag, M.A.M. Gijs, ***Powder blasting for the realisation of microchips for bio-analytic applications***, Sensors and Actuators A 92, pp. 388-393, 2001.

[2.53] Microsystems Laboratory, School of Engineering, http://www2.warwick.ac.uk/fac/sci/eng/eed/research/srl/, University of Warwick, Oct 2004.

Chapter 3

Design and simulation of microchannels and microsensors

3.1 Introduction

This chapter describes the design and simulation of a range of microchannels, microchambers and microsensors for various microsystems. Two types of microchannel are described, namely: the uncoated microchannel; and the gas chromatography (GC) microchannel. The uncoated microchannel will be used in proto-nose while the GC microchannel will be used in both the proto-nose and NOC systems. Here, the primary goal is to predict the analyte transport behaviour within a long, narrow microchannel coated with a thin inner absorbent coating (i.e. a basic GC column). These columns exhibit a distinct retentive characteristic for different analytes. A commercial finite element (FE) simulation package (FEMLAB, Comsol Inc UK) is used for simulating and optimising different geometrical models, while an analytical model was employed to predict the dynamic behaviour of the microsensors. Two important characteristics of the predicted analyte profile were examined, namely: the diffusion broadening effect as an ideal square pulse travels along the microchannel; and the retention delay, either due to the offsetted positional placement of the sensor or the retentive nature of the coating.

3.2 Microchannels and microchambers design and simulation

The microchannel delivery concept has recently attracted considerable attention [3.1-3.2]. It is driven by a desire to create a highly portable, miniaturised, disposable and power efficient integrated system. This is made possible with improvement in technologies such as micromachining, and rapid prototyping techniques. With many of these systems moving towards microscale and nanoscale, it is necessary to investigate many established theories to determine their validity at microscale size, as discussed in details in Section 3.2.3.

Within the scope of this project, two different but complementary approaches have been taken to create the final nose-on-a-chip (NOC) microsystem. Firstly, prototype systems (proto-noses) were built, based on large discrete components, to explore and study various aspects of the proposed system. Developed concurrently were the miniaturised NOC systems used to investigate various microfabrication techniques to create microfluidic packages and integrating it with silicon-based microsensor arrays. In the next section, the microchannels used for both systems will be described.

3.2.1 Microchannel geometrical models

The microchannel is the main component of a microfluidic system used to deliver analytes to the sensor array. Two microchannel geometries were studied, namely the circular and rectangular cross-sectional microchannel. The rectangular microchannel was preferred for 3 important reasons. Firstly, it was easier to fabricate using micromachining techniques. Secondly, it was easier to integrate within a microsensor array. The integration introduced many complications due to the need for the sensors to be placed at various locations along the microchannel. Thirdy, it offered higher performance in the case of gas chromatographic columns (described in Section 3.3). The simulations for gas flow in four different microchannels are discussed here. Two microchannels were used in proto-nose I and proto-nose II, respectively, the other two were the microchannels embedded in the microchannel packages MSL101 and MSL113.

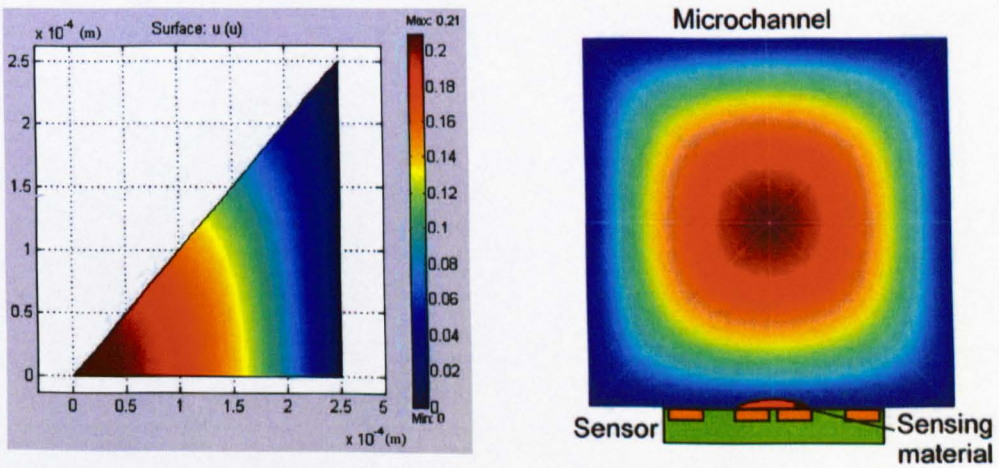

(a) (b)

Figure 3.1: 2-D parabolic velocity profile of microchannel. (a) 1/8 cross-sectional velocity profile. (b) Complete microchannel velocity profile with sensor placement.

The microchannels designed for the two proto-nose systems have the same cross sectional geometry of 0.5 mm × 0.5 mm. Proto-nose I had a microchannel length of approximately 1.2 m whereas proto-nose II was about 2.4 m. As the microchannel cross-section was square, it exhibited 8-fold symmetry along its central axis, as shown in Figure 3.1(b). Therefore, only 1/8 of the microchannel has to be simulated. This provides an 8 fold saving in computational time without any compromise in accuracy. Figure 3.1(a) shows one-eight cross-sectional velocity profile of the microchannel. Figure 3.1(b) shows how they are combined to form the complete microchannel and the location of the sensor.

As the cross-section of the microchannel was uniform, the computational complexity was further reduced by performing a 2-D simulation of the transport phenomena and couple the results to the 3-D microchannel. Figure 3.2(a) shows the microchannel geometry for proto-nose II and Figure 3.2(b) shows the mesh of the microchannel. The only difference for proto-nose I (not shown here) is the length of the microchannel.

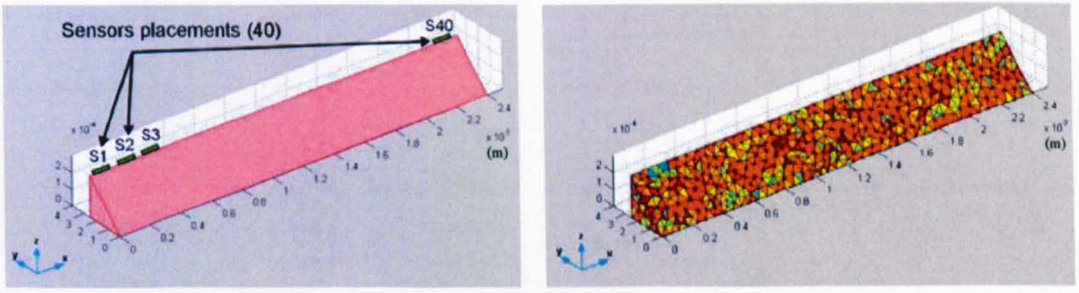

(a) (b)

Figure 3.2: Geometrical model of a scaled proto-nose II. (a) Scaled microchannel geometry with sensors placements. (b) Microchannel mesh (computational nodes).

A limitation of the simulation software prevents geometry with large scaled differences (> 100) to be created due to the huge computational complexity (computational nodes) required. To overcome this limitation, a scaled geometry was created. The dimensions for Y and Z axes shown in Figure 3.2 are in actual sizes, but the X-axis dimension was scaled by 1000 times. To compensate for the effect of scaling, the diffusion coefficient in the X-axis was scaled accordingly. It is conveniently provided in the software as an anisotropic coefficient (Appendix A). This is possible because a linear diffusion model has been assumed.

Two miniaturised micropackages, to be used with the microsensor array, were designed and simulated. A simple microfluidic package (MSL101) and a complex microfluidic package (MSL113) were designed to assemble with a silicon microsensor array. The MSL101 has a single continuous microchannel of 50 mm in length with a cross-section of 200 μm × 200 μm. The geometrical design of the microchannel, as shown in Figure 3.3, was intended to be flip-mounted onto the silicon microsensor array with the microchannel traversing across all the sensors. The micropackage sat on top of the microsensor array.

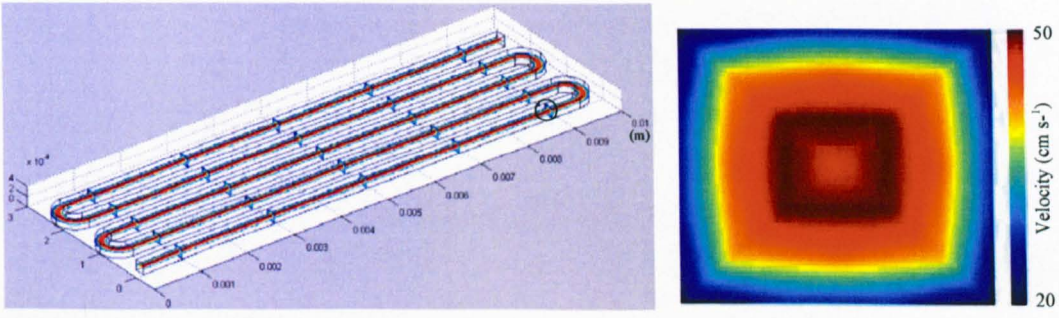

(a) (b)

Figure 3.3: MSL101 geometry. (a) Geometrical model. (b) Cross-section velocity profile.

The MSL113 package has a 71 cm × 0.5 mm × 0.5 mm microchannel. A similar technique of exploiting symmetry axes and scaling as shown in Figure 3.1 and Figure 3.2 was used. Figure 3.4 shows the surface concentration profile of MSL113 when a 5 s pulse of ethanol vapour is injected into the microchannel.

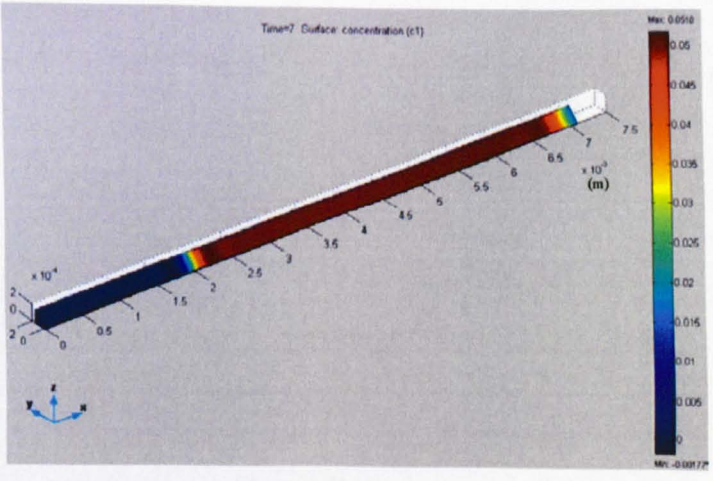

Figure 3.4: MSL113 geometrical model with surface profile of a travelling ethanol vapour pulse.

The MSL115 has a much longer microchannel (2.4 m × 0.5 mm × 0.5 mm). The simulation for MSL113 can be reused by specifying a different scaling factor. In the next section, the model for various microchamber designs will be discussed. This microchamber is necessary for the testing of the microsensor array.

3.2.2 Microchamber geometrical models

In addition to the microfluidic packages, a microchamber was designed and built to enable rapid testing of the microsensor array without the need for a complicated integration process. The microchamber featured a 10 mm × 4 mm × 1 mm box rectangular enclosure with a volume of 40 µl. The main design consideration was to ensure simultaneous uniform concentration distribution across the whole microsensor array. Figure 3.5 shows 3 proposed geometrical models for the microchamber.

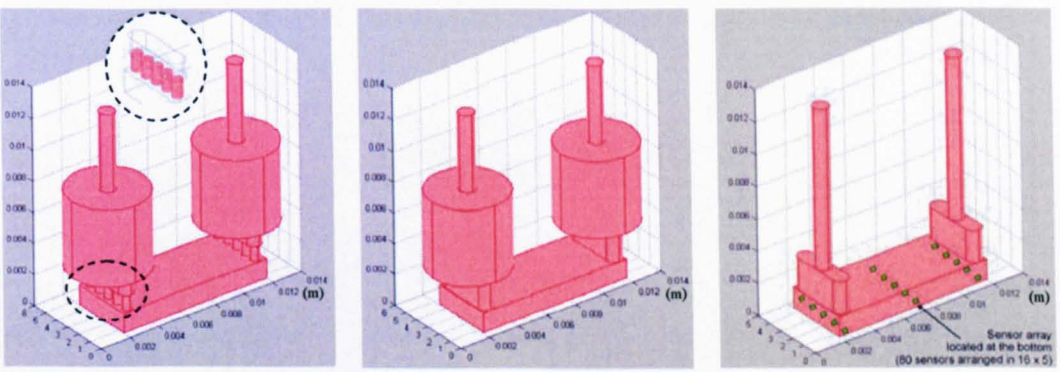

(a) (b) (c)

Figure 3.5: FEM simulation of microchamber fluid flow. (a) Final microchamber design. (b) Microchamber design 1. (c) Microchamber design 2.

Circular tubing originating from vapour test station connected to the microchamber has the geometry shown in the top portion of the microchamber (Figure 3.5(a)). As the microsensor array was spatially distributed in a rectangular manner (Figure 3.5(c)), connecting the circular source to the rectangular outlet resulted in a non-uniform analyte distribution. Parabolic flow profile worsens the concentration distribution. Hence, five small holes were used to re-distribute the analyte vapour, providing a more uniform distribution across the sensor array. The other important aspect was the time delay (temporal signal) between the same vapour pulses when it reached the different sensors

(Section 3.2.5). Fortunately, no significant time variations were observed in the final design.

3.2.3 Mathematical models and boundary conditions

Fluid flow and transport in a microchannel are usually studied using the classical Navier-Stokes (*NS*) equation [3.3-3.5]. However, experimental research has shown that *NS* fails to hold when the cross-sectional area is reduced to less than 80 μm^2 [3.3, 3.6]. All microchannels used for study are outside within this limit, and hence *NS* can still apply. A second important criterion on the usage of *NS* is to limit it within the laminar flow regime [3.3, 3.7]. By keeping the Reynold's number (Re) below 2000, it can be ensured that the flow was laminar [3.3]. In addition to the transport of analyte along the microchannel, the analyte will also be susceptible to dispersion and broadening. This can be accounted for using a Convection and Diffusion (*CD*) equation [3.7]. The convective term has often been neglected [3.8], but is included here to account for the small amount of broadening due to convection.

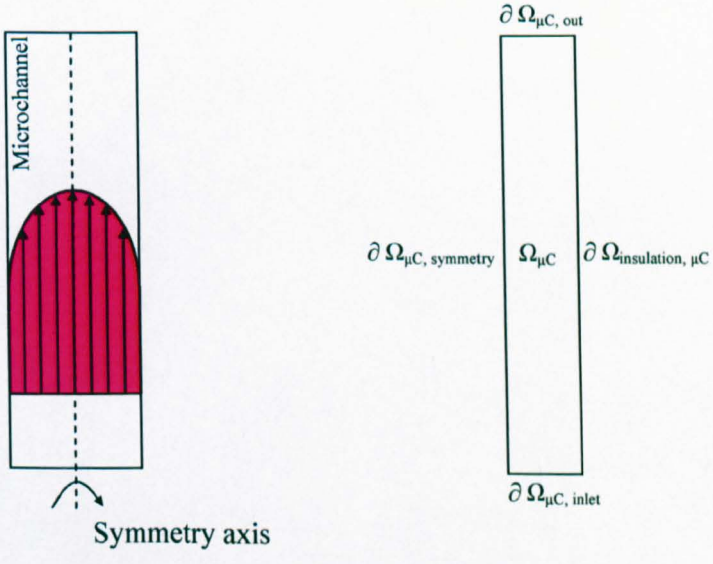

Figure 3.6: Microchannel boundary conditions and symmetry axis.

FEMLAB operates on a system of partial differential equations (PDEs) when attempting to solve geometrical model by applying a finite element method (FEM). Many real-world applications involve the simultaneous application of PDEs from several areas of sciences

or engineering; this type of analysis is referred as multi-physics modelling [3.9]. A multi-physics model incorporating *NS* and *CD* were used to model the analyte transport. *NS* was used to simulate the laminar transport of carrier gas and test analyte along the microchannel, while *CD* accounts for the flux transport and dispersion of the moving analyte pulse. Figure 3.6 shows the boundary conditions and Equations (3-1) to (3-5) state the PDEs and the associated assumptions.

Navier-Stokes (NS) equation

$$\mu\nabla^2 V + \rho(V.\nabla)V + \nabla P = 0 \qquad (3\text{-}1)$$

where μ is the viscosity, ρ is the density, P is the pressure and V is the velocity,

∇ (the vector differential operator) is the operator $\left(\frac{\partial}{\partial x_1},...,\frac{\partial}{\partial x_n}\right)$ where n = 1, 2, or 3.

Convection and Diffusion (CD) equation

$$\frac{\partial C}{\partial t} + \nabla.(-D\nabla C + CV) = 0 \qquad (3\text{-}2)$$

where D is the diffusion coefficient, C is the concentration.

At the inlet, the concentration boundary conditions are:

$$C = C_i \ (t < t_{PW}) \qquad \text{at} \quad \partial\,\Omega_{\mu C,inlet} \qquad (3\text{-}3)$$

where C_i is the injected concentration for a duration of t_{PW}.

At the outlet, it is assumed that the convective contribution to the mass transport is much larger than the diffusive contribution.

$$(-D\nabla C + CV).n = (CV).n \qquad \text{at} \quad \partial\,\Omega_{\mu C,out} \qquad (3\text{-}4)$$

where n is the normal vector to the respective boundary.

Further, it is assumed that there is no transport over the symmetry boundaries.

$$(-D\nabla C + CV).n = 0 \qquad \text{at} \quad \partial\,\Omega_{\mu C,symmetry} \qquad (3\text{-}5)$$

3.2.4 Band-broadening effect

When an analyte pulse is delivered to a sensor, the analyte vapour temporal profile presented to the sensor determines its response. It is hence important to study the amount of broadening (refer to Figure 3.16) and any other effects as the analyte travels along a microchannel or microchamber. Due to the diffusion and dispersion of the test analyte pulse, the fronts of the pulse broaden out with time inside the microchannel. It is important to know the rate of broadening at different velocities as this will determine the ultimate time-dependent sensor response. For example, consider the perfect model of a square vapour pulse being presented to a sensor at a flow velocity of 500 cm s^{-1}. If a basic first-order exponential model of the sensor response is assumed, the expected sensor response is as shown in Figure 3.7(a). However, if the velocity is reduced down to 10 cm s^{-1}, the delivered pulse broadens out into a bell-like curve and the magnitude of the response will also be reduced. So a sensor with the same response model will respond differently as illustrated in Figure 3.7(b). In addition to the response time and magnitude, the pulse is clearly delayed, i.e. there is a time lag between the moment the analyte is injected to the time it reaches the sensor. This problem is compounded by long inlet tubes, poor chamber design, and a low velocity at which the analyte is delivered.

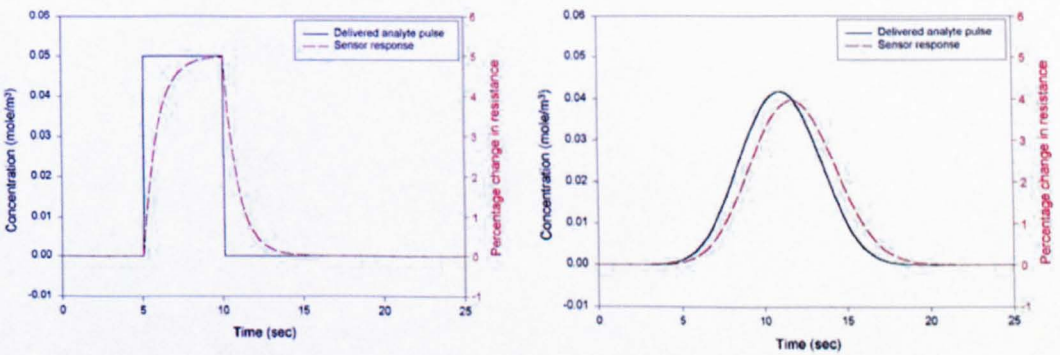

(a) (b)

Figure 3.7: Simulation of pulse delivered to sensor surface and actual sensor response at two different flow velocities. (a) Velocity = 500 cm s^{-1}. (b) Velocity = 10 cm s^{-1}.

The simulation results shown in Figure 3.8 demonstrate that significant broadening of an ethanol vapour pulse in air occurring near the outlet of a 10 cm × 0.5 mm × 0.5 mm microchannel, when the flow velocity is below a value of 20 cm s^{-1}. At a velocity above 50 cm s^{-1}, negligible broadening is observed. Simulations with different test analytes have shown similar trends with the precise broadening depending upon the diffusion

coefficient of the analyte in the carrier gas (i.e. air). An example of the simulation parameters is included in Appendix A. When the flow velocity is reduced, it approaches a static diffusion function. On the other hand, as the velocity is increased, there will be no broadening effect. However, operating beyond the laminar flow regime (Re > 2000) will result in turbulent and unwanted mixing effect.

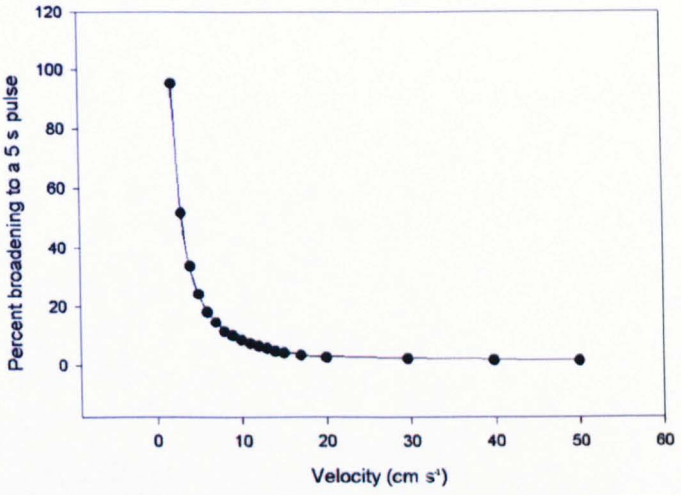

Figure 3.8: Broadening effect of delivered pulse as a function of flow velocity.

3.2.5 Simulation results for microchannels and microchambers

The two proto-nose simulation results show that similar and predictable analyte profiles can be delivered to the sensors. This is clearly a result of only the length being different. 40 sensors were placed along the microchannel on both proto-noses, their detail placements will be discussed in Chapter 5. Due to their offset locations, each profile is time-shifted but otherwise appears identical except for a slight broadening as the sensors are placed further down the microchannel. Figure 3.9(a) shows the ethanol vapour profiles as they appear to the first 5 sensors along the microchannel, of proto-nose I, at a flow velocity of 50 cm s^{-1}. In this scenario, a 5 s analyte pulse is injected at time t = 0 s. The time delay between each profile depends on the physical distance between the sensors. Due to their close proximity in distance, the profiles are similar.

The toluene vapour profiles for the same sensor are shown in Figure 3.9(b). They are similar to the profile for ethanol vapour as these two analytes only differ in diffusion coefficient in the carrier gas (i.e. air). The slight difference in diffusion coefficient does not result in any significant changes in the delivered analyte profiles as it is dominated by the flow transport.

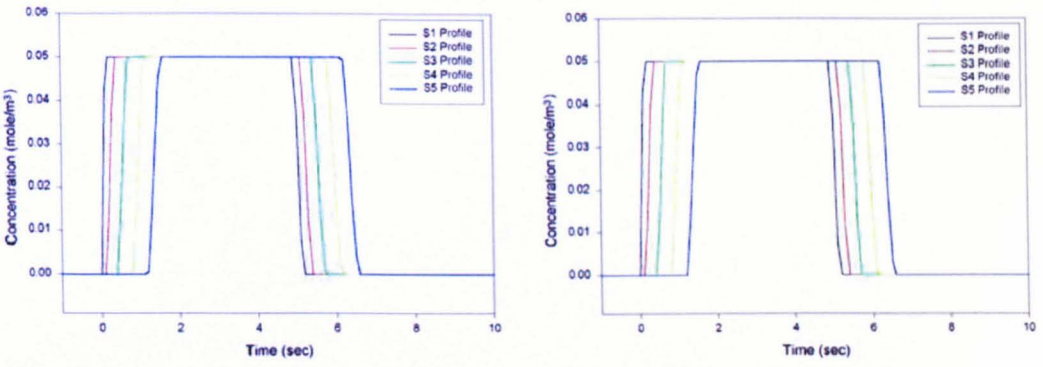

Figure 3.9: Profiles of analyte delivered to sensor S1, S2, S3, S4 and S5 for proto-nose I. (a) Ethanol vapour in air. (b) Toluene vapour in air.

As the pulse travels further down the microchannel, more broadening occurs. This broadening is insignificant when compared to the time delay between each profile. Figure 3.10 shows a comparison between the delivered profiles to sensor S1, S20, S36, S37, S38, S39 and S40 for proto-nose II. Due to the close proximity of S36-S40, there is little time delay between these profiles. Comparing between the analyte profiles of S1, S20 and S36, the time delays are significant (7 s between S1 and S20, 5 s between S20 and S36). Towards the end of the microchannel, the analyte pulse is clearly broadened when compared to the pulse near the inlet.

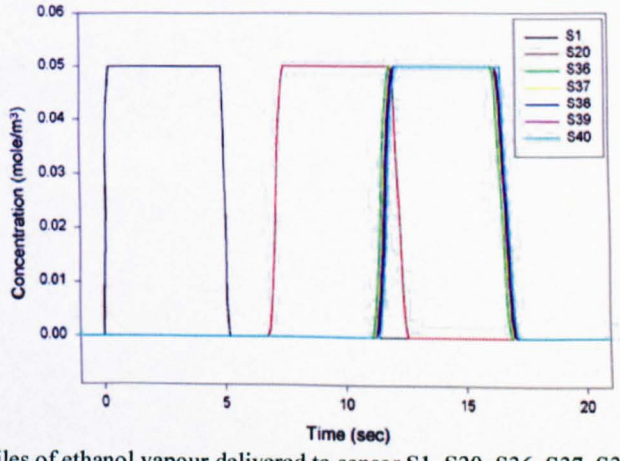

Figure 3.10: Profiles of ethanol vapour delivered to sensor S1, S20, S36, S37, S38, S39 and S40 for proto-nose II.

For smaller microchannels, their profiles are also similar. One such example is shown in Figure 3.11 for the delivered profiles to MSL101 microchannel at velocity of 30 cm s^{-1}.

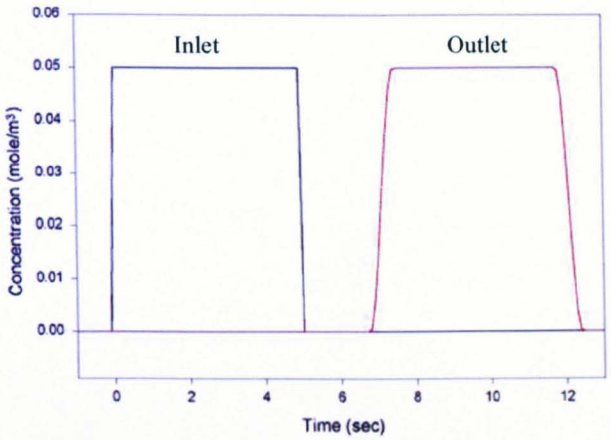

Figure 3.11: MSL101 delivered ethanol vapour profile near inlet and outlet.

In the case of microchannel delivery, although all sensors are placed at different locations along the microchannel, their positions relative to the cross-section of the microchannel are always consistent (Figure 3.1(b)). This ensures the effect of the parabolic flow on the analyte profile stays the same across all the sensors. For the microchamber intended to be used with the microsensor array, this is not observed due to the mismatch in delivery channel (interconnect tubing) and measurement chamber dimension. Therefore, it is important to perform design iterations to overcome the non-uniform concentration distribution across the microsensor array.

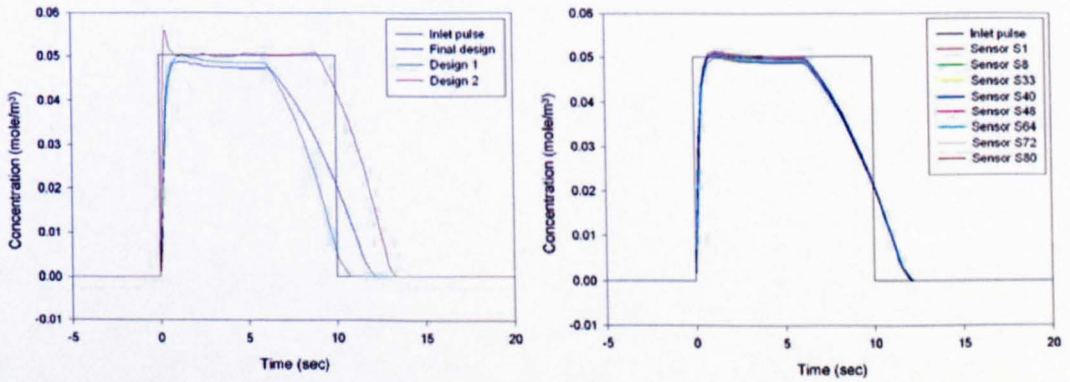

(a) (b)

Figure 3.12: Comparison of different microchamber designs. (a) Comparison between delivered profiles of different microchamber designs. (b) Comparison between delivered profiles to different sensors within the sensor array of final microchamber design (refer to Chapter 4 for the sensor locations).

Figure 3.5 shows three of the many iterated designs and Figure 3.12 shows their corresponding simulation results. Figure 3.12(a) shows three different analyte profiles of

the same sensor when a different microchamber is used. The final microchamber design provides the best resemblance to the injected analyte pulse. Figure 3.12(b) shows a comparison between the analyte profiles at different locations within the sensor array for the final microchamber design (Figure 3.5(a)). These sensor locations are chosen at all extreme corners and middle to determine the maximum possible differences in the delivered analyte profiles. The simulation results show that there is no difference in terms of temporal delay, but there is a small but negligible variation (< 1 %) in terms of response magnitude.

3.3 Gas chromatographic column simulations

The basic principle of gas chromatographic (GC) separation operates on a layer of retentive material (known as a stationary phase) around the inner surface of a column. When a pulse of compound analyte is injected into the column with a carrier gas (known as the mobile phase, usually an inert gas such as nitrogen or helium is used), each component within the compound analyte travels along the column at a different velocity, depending upon their affinity with the stationary phase. Hence, towards the end of the column, a sequence of pulses will elute representing the separated components.

Various numerical techniques [3.8, 3.10-3.11] are available although each differs slightly in terms of their mathematical formulations. Commercial softwares such as ChromWIN [3.12] and GC-SOS [3.13] are also readily available to predict and fine-tune various design parameters for performance enhancement. There are two main reasons for creating a finite element model instead of using one of the many techniques available. Firstly, those available techniques only allow the response at the end of the column to be predicted. Here, the responses at various locations along the column are required. Secondly, the column design does not conform to the standard GC column. In the case of the proto-nose designs, only 3 sidewalls are coated with retentive materials instead of all 4 for practical reasons. For this design, only two-fold symmetry can be achieved as shown in Figure 3.13.

3.3.1 Gas chromatographic column geometrical models

Here the two main geometrical models will be discussed. The first relates to the proto-nose geometry while the second relates to the geometry for the microchannel delivery package. The geometrical models for the GC microchannel are the same as the previous

microchannels except for an additional retentive layer on its inner surface. The same technique of optimising the computational efficiency is used by performing a 2-D simulation on the analyte transport and exploiting any symmetrical plane. Figure 3.13 shows the cross-section of the GC microchannel for proto-nose I and it complete 3-D geometry. There is symmetry along the centre of the microchannel as the GC microchannel has only 3 coated surfaces. The same technique has been used to create the geometrical model for the proto-nose II, details are not shown here as they only differs in their length (or scaling factor).

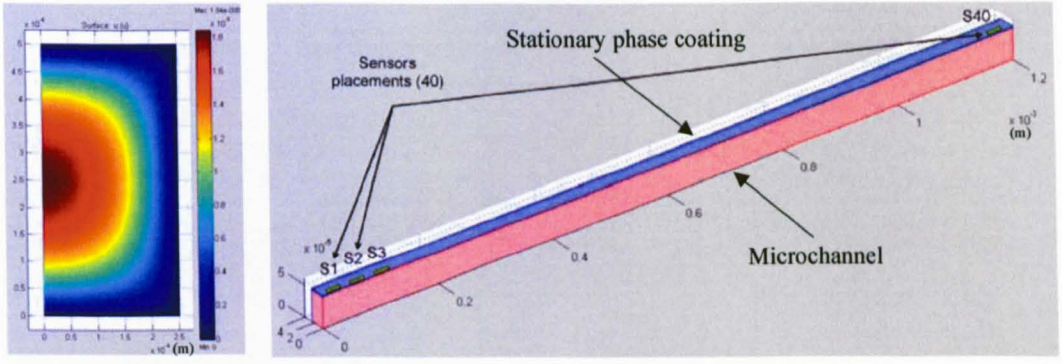

(a) (b)

Figure 3.13: Proto-nose I geometrical model. (a) 2D velocity profile. (b) Scaled 3D geometrical model.

For a standard GC microchannel, the geometry is similar to the uncoated microchannel except that all the inner surfaces are coated with a thin layer of stationary phase material. Figure 3.14 shows the geometrical model for this GC microchannel. As this channel is coated on all 4 side walls, more symmetrical planes can be exploited (refer to Figure 3.1(b)).

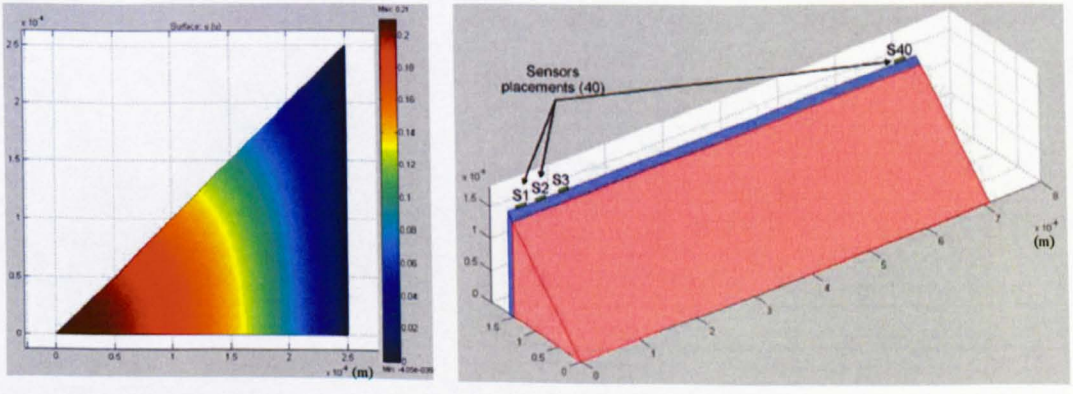

(a) (b)

Figure 3.14: MSL113 geometrical model. (a) 2D velocity profile. (b) Scaled 3D geometrical model.

By extending it length (or using a different scaling factor), the geometry (not shown here) for MSL115 microchannel GC can be obtained.

3.3.2 Mathematical models and boundary conditions

Numerous researches have identified the physical phenomena dominating the separation process of a GC column. This is pre-dominantly a laminar flow with convection and diffusion occurring within the column. Only diffusion occurs within the stationary phase coating [3.7, 3.14]. A 2-D Navier-Stokes (*NS*) model is used to simulate the laminar transport and the result of this parabolic velocity profile is then exported to the inlet of the column. Within the column, a multi-physics mode with Convection and Diffusion (*CD*) and Diffusion (*DI*) is used. The *NS* simulates the laminar transport of carrier gas and test analyte along the column, while *CD* accounts for the flux transport and dispersion of the injected pulse. A separate *DI* mode is required to simulate diffusion within the stationary phase. The PDEs for *NS* and *CD* are the same as those discussed in Section 3.2.3. The PDE for *DI* is given in Equation (3-6). The retentive characteristic of the stationary phase material for the analyte is incorporated by modifying boundary conditions as described next.

Diffusion (DI) equation

$$\frac{\partial C}{\partial t} + \nabla.(-D\nabla C) = 0 \qquad (3\text{-}6)$$

To account for the partition coefficient, *c*, which measures the equilibrium distribution of analyte molecules between the mobile (gas) phase and the stationary phase, the boundary conditions are modified as follows [3.9].

$$\left[\frac{\partial C_M}{\partial t} + \nabla.(-D\nabla C_M + C_M V)\right].n = M.(C_S - cC_M) \quad \text{at } \partial\,\Omega_{\mu C,SP} \qquad (3\text{-}7)$$

$$\left[\frac{\partial C_S}{\partial t} + \nabla.(-D\nabla C_S + C_S V)\right].n = M.(cC_M - C_S) \quad \text{at } \partial\,\Omega_{SP,\mu C} \qquad (3\text{-}8)$$

where *n* is the normal vector to the respective boundary.

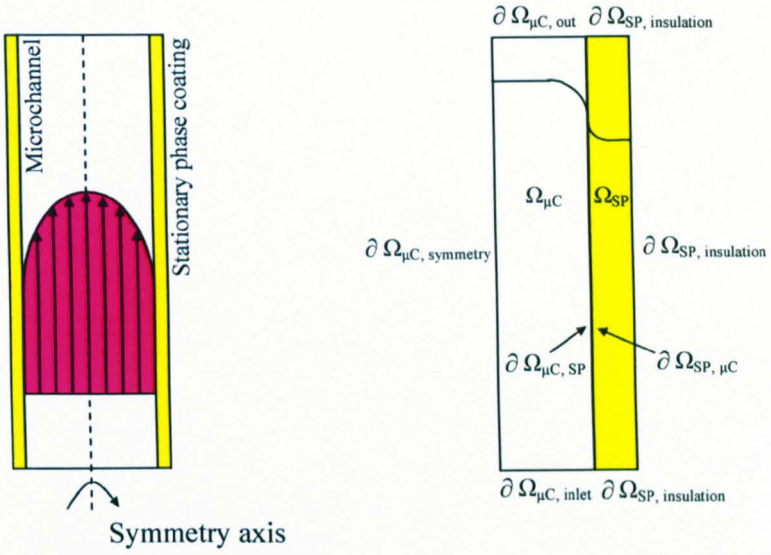

Figure 3.15: Microchannel GC boundary conditions and symmetry axis.

c is the partition coefficient define as

$$c = \frac{C_S}{C_M} \tag{3-9}$$

where C_S is the concentration in stationary phase and C_M is the concentration in the mobile phase.

As there will be discontinuities in the concentration profile at the boundaries between mobile and stationary phases, two separate variables, C_M and C_S are used to describe the concentration in each of the respective phases. In order to obtain continuous flux over the phase boundaries, a special type of boundary condition, using the stiff-spring method is employed [3.9]. Instead of defining Dirichlet concentration condition (Appendix A) according to the partition coefficient, c which would destroy the continuity of the flux, a continuous flux condition is defined [3.9]. At the same time, the concentration is forced to the desired values. M is a large number (i.e. 10,000) to ensure the concentration differences in the brackets (Equation (3-7) and (3-8)) on the right approaches zero [3.9]. Note that these boundary conditions also give continuity in flux, provided M is sufficiently large [3.9]. Other boundary conditions and assumptions for the microchannel GC are the same as the uncoated microchannel (refer to Section 3.2.3).

3.3.3 Band-broadening effect

The microchannel GC suffers from band-broadening similar to any other traditional microchannels due to the diffusion and dispersion effect of a moving pulse. In fact, a pulse travelling along a GC microchannel has increasing broadening under the same operating conditions when compared to a uncoated microchannel, as the retentive material prolongs the duration the analyte stays within the microchannel. The amount of broadening affects the performance of the GC column because separated peaks overlap with each other, giving less information about the components of the compound analytes at the outlet of the column. The velocity of the carrier gas affects the amount of broadening as discussed in Section 3.2.4. However, for a GC column, increasing the velocity will not always improve the system performance, as less retention occurs within stationary phase, hence giving less separation. Therefore the optimum operating point is a compromise between the broadening and retention effects.

From the sketch of an ideal chromatogram shown in Figure 3.16 [3.15], the parameters which characterise an output peak can be defined. The amount of broadening is defined by the peak basewidth as $W = 4\sigma$ while the retention time is defined by t_R.

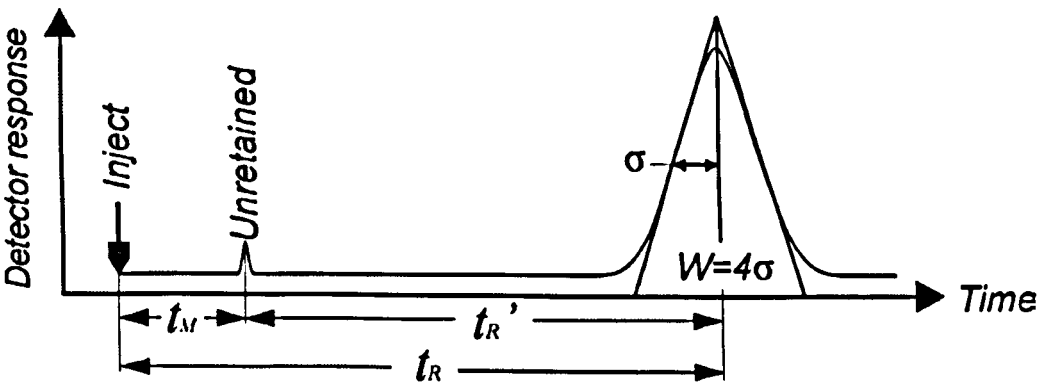

Figure 3.16: Representation of GC output defining retention time and peak broadening width.

Considering the case for proto-nose I microchannel GC, a 5 s ethanol vapour pulse will slowly broaden as it travels along the column. Figure 3.17 shows the injected ethanol vapour pulse near the inlet and the pulse at the middle of the microchannel GC. Under the same flow velocity of 50 cm s^{-1}, a toluene vapour pulse will give a different response as shown in Figure 3.18. Two effects can be observed. The first relates to the broadening of analyte pulse while the second relates to the retention time (delay) of the analyte.

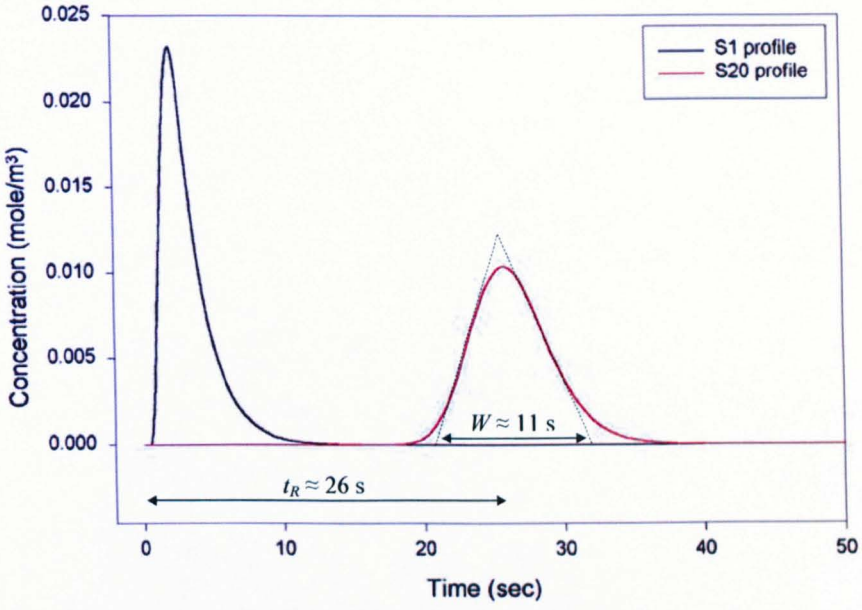

Figure 3.17: Broadening of ethanol vapour pulse at sensor S1 and S20.

Comparing the two ethanol vapour profiles for the two sensors, the latter sensor's (S20) profile broadens and its magnitude reduced as it travels down the microchannel GC. Comparing the two analytes (ethanol and toluene vapour), the amount of broadening is different, at the same sensor position, due to the different retentive property of the stationary phase acting on each analyte.

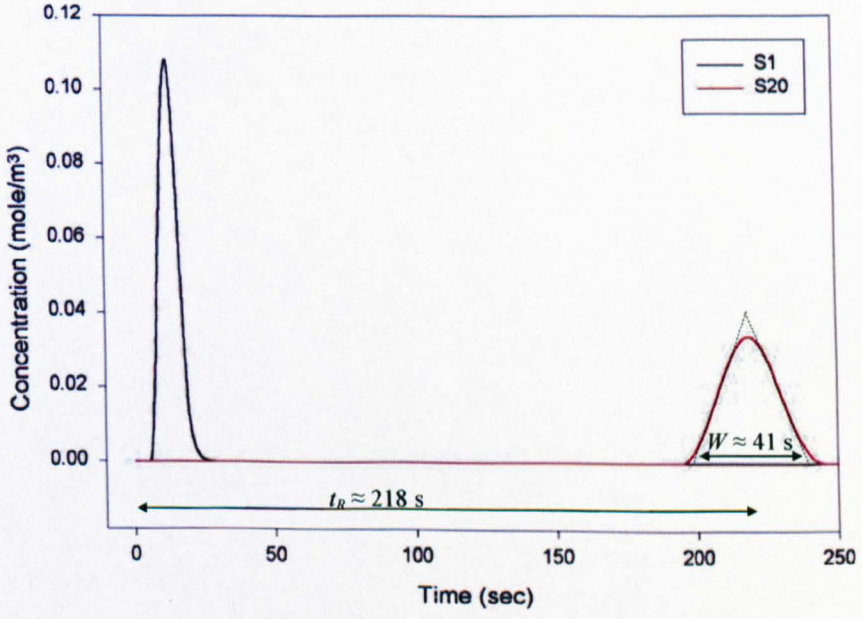

Figure 3.18: Broadening of toluene vapour pulse at sensor S1 and S20.

3.3.4 Retention effect

The time shifting depends on the affinity of each individual component within a compound analyte to a stationary phase. This is usually termed as the retention time (t_R) as given in Figure 3.16. The degree of affinity of an analyte to the stationary phase is defined by the partition coefficient. Using the linear solvation energy relationship (LSER) equations, the partition coefficient can be estimated [3.16]. Details relating to these estimations can be found in Appendix B.

The retention times for ethanol and toluene vapour for sensor S1 and S20 are shown in Figure 3.17 and 3.18 respectively. In addition to the finite element simulation, a well established analytical model can also be use to determine the retention time for standard GC column. The retention time is a function of the column geometry, flow velocity and the partition coefficient between the analyte and stationary phase. The retention factor, k, is a function of the column geometry, partition coefficient and stationary phase coating thickness as given in Equation (3-10).

$$k = \frac{Cross-sectional\ \ Perimeter}{Cross-sectional\ \ Area} \times cw = \frac{8z_0cw}{4z_0^2} = \frac{2cw}{z_0} \qquad (3\text{-}10)$$

where z_0 is the column half height and w is the stationary phase coating thickness.

At a particular flow velocity of the carrier gas, the analyte will travel at a different velocity depending upon k, as shown in Equation (3-11).

$$Vel_{ave} = \frac{1}{1+k} \times v_c \qquad (3\text{-}11)$$

where v_c is the velocity of the carrier gas.

Hence the retention time will be related to the ratio of the length (distance between the sensor location to the inlet of the microchannel GC) to the average velocity of the analyte, as given in Equation (3-12).

$$t_R = \frac{L}{Vel_{ave}} = \frac{L(z_0+2cw)}{v_c \times z_0} \qquad (3\text{-}12)$$

Table 3.1: Stationary phase materials and their commercial acronyms.

Stationary phase material	Acronym
Poly (dimethylsiloxane)	SE-30
Poly (dimethylmethylphenyl-siloxane) 35% mol phenyl groups	OV-11
Poly (ethylene glycol adipate)	EGAD
Bis (3-allyl-4-hydroxyphenyl) sulfone	H10
Poly (trifluoropropylmethyl-siloxane)	QF1

Table 3.2: Retention time for ethanol and toluene vapour with 5 stationary phase materials.

		Ethanol vapour		
	c	Analytical	Numeric	Error
SE-30	4.76	18.9 s	19.0 s	0.53 %
OV-11	6.03	21.4 s	21.6 s	0.93 %
EGAD	14.97	38.7 s	39.5 s	1.96 %
H10	58.03	122.3 s	125.0 s	2.22 %
QF1	6.28	21.9 s	22.0 s	0.55 %

		Toluene vapour		
	c	Analytical	Numeric	Error
SE-30	37.59	82.6 s	84.5 s	2.28 %
OV-11	56.74	119.8 s	123.0 s	2.69 %
EGAD	170.7	340.9 s	349.0 s	2.39 %
H10	48.21	103.2 s	106.0 s	2.68 %
QF1	28.57	65.1 s	66.5 s	2.10 %

To determine the accuracy of the finite element model, the retention time is cross-validated with the solution given by the analytical model. As the analytical model only applies to a standard GC column, the MSL114 (120 cm × 0.5 mm × 0.5 mm GC microchannel) will be used for comparison. Two test analytes, ethanol and toluene vapours and 5 commercially available stationary phase materials were used. The 5 stationary phase materials are listed in Table 3.1. Table 3.2 shows a comparison of the retention time between the finite element model and the analytical model. The finite element model produces accurate estimation of the retention time with an error of less than 3 % when compared to the numerical method.

3.3.5 HETP and separation factor

The height equivalent to the theoretical plates (HETP) is the usual performance measurement guideline to determine the efficiency of a GC column. The HETP determines the efficiency per unit length, while a more complete measurement known as the separation factor (SF) can compare an overall column. The HETP is first defined by Golay in 1958 where he combined theories on Poiseuille flow, static and dynamic diffusion and partition coefficient [3.10]. Since then it has been slightly modified by

Gidding [3.17], and more recently by Spangler [3.8] to remove some inaccurate assumptions. These include the use of *NS* equations (as oppose to Poiseuille flow) and the inclusion of the convection term (on top of diffusion).

$$HETP_{Spangler} = 2\frac{D_m}{v_c} + \frac{0.9 + 2k + 35k^2}{96(1+k)^2}\frac{v_c z_0^2}{D_m} + \frac{2k}{3(1+k)^2}\frac{v_c w^2}{D_s} \qquad (3\text{-}13)$$

$$SF = \frac{L}{HETP}\left(\frac{k}{1+k}\right)^2 \qquad (3\text{-}14)$$

In Section 3.3.4, the retention time of the finite element model was compared with that of the analytical model and it was found to be similar. To further establish the accuracy of the finite element model, the separation factor will be compared to the solutions obtained from the analytical model. The HETP and separation factor for the analytical model proposed by Spangler are shown in Equation (3-13) and (3-14), respectively. For the finite element model, the broadening parameters of the pulse at the outlet, as shown in Figure 3.16, will be used to estimate the separation factor.

$$SF = 16\left(\frac{t_R'}{W}\right)^2 = 5.545\left(\frac{t_R'}{\sigma}\right)^2 \qquad (3\text{-}15)$$

where t_R' is the adjusted retention time (refer to Figure 3.16).

Equation (3-15) provides an estimate of the separation factor by physically measuring the broadening and retention time of the eluted peak at the outlet. The adjusted retention time is the time difference between the unretained peak (in the case of traditional GC, the peak of the carrier gas) and the delayed analyte pulse.

The same analytes and stationary phase materials given in Table 3.1 and Table 3.2 will be used for comparison between these two models. Figure 3.19 shows the result of the comparison for (a) ethanol vapour and (b) toluene vapour in air. The finite element model prediction has an error of 9 % or less; this appears to be higher at larger partition coefficients. A few possible sources of these errors are associated with the separation factor. These include the physical measurement technique (referring to Figure 3.17 and Figure 3.18, t_R' and W in Equation (3-15) are estimated by physically drawing the anchoring lines over the pulse) used to estimate the separation factor. The geometry

scaling technique used may also contribute some percentage of error as each computation point along the scaling axis has been stretched (by an amount proportional to the scaling coefficient). As for the higher error at larger partition coefficients, it is possibly caused by the precision of the computation time step used. As the retention time is a strong function of the partition coefficient, the peak at the outlet will take a longer time to elute. The higher the precision used for the time step, the longer it will take to complete the simulation. Hence, to improve the simulation efficiency, the time steps are scaled according to the estimated retention time.

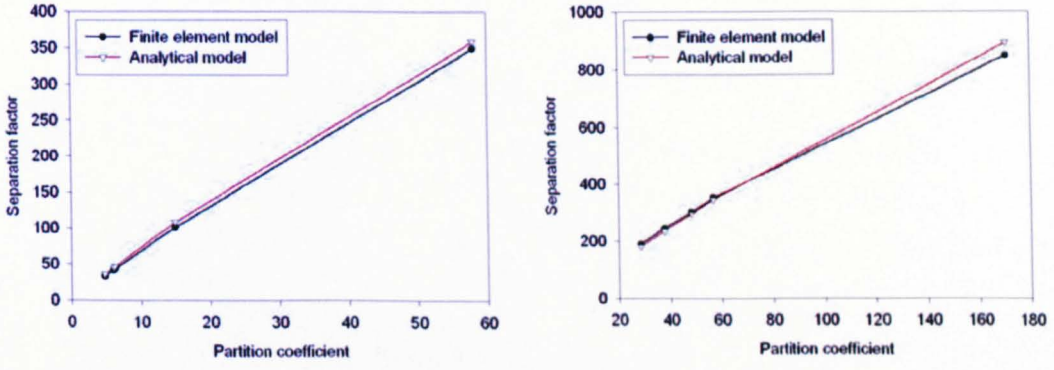

(a) (b)

Figure 3.19: Comparison of separation factor between analytical and finite element model. (a) Separation factor for ethanol vapour. (b) Separation factor for toluene vapour.

As the finite element model provides a similar estimation of the separation factor for a GC microchannel when compared to the analytical solutions, it is possible to show with a high degree of confidence that the simulation results for other unknown but similar models is likely to be reasonable.

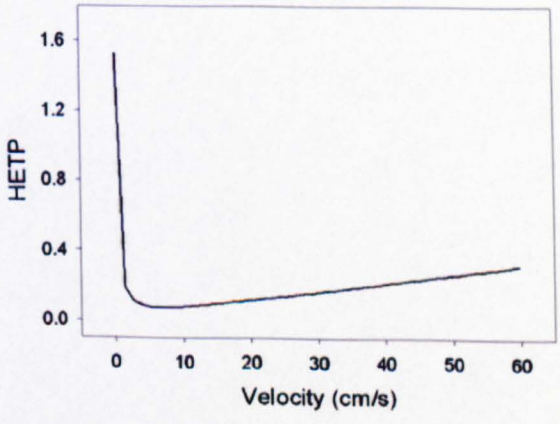

Figure 3.20: HETP against average velocity for microchannel GC.

In addition to calculating the column efficiency, the HETP is always used to determine the optimum operating velocity of a column. Typically, a classical V-shaped curve (shown in Figure 3.20) can be obtained by plotting the velocity against HETP where the minimum HETP (max SF) corresponds to the optimum operating point. For the GC microchannel, the optimum operating point is at a velocity of around 7 cm s^{-1}. However, it is more favourable to operate the sensors at a higher velocity (> 50 cm s^{-1}) due to their improved response times that are desirable for a low-cost analogue VLSI chip [3.17]. The effect of operating at a higher velocity does not appear to affect significantly the efficiency of the microchannel GC (refer to Figure 3.20).

3.3.6 Spatio-temporal signals generation

The spatio-temporal information can be viewed from two perspectives as introduced in Chapter 2. In the first case, consider a microchannel coated with stationary phase SP1 with multiple sensors of the same type S_a being placed along it. The spatial information can be obtained by comparing the sensor responses to other responses in a microchannel coated with a different stationary phase SP2. The temporal information corresponds to the time-shifting of the sensors as they are placed at different locations along the microchannel. Hence the relative time of the sensor response is dependent upon the flow rate pulse of the analyte travelling along the channel. In the second scenario, there is only one coated GC microchannel, but with sensors of different types (S_a, S_b, ..., S_c) placed along the microchannel. Other variations are possible but these two novel configurations will be studied in the simulations described to generate spatio-temporal information.

In the former configuration, a set of 5 GC microchannels, each coated with a different stationary phase material (as given in Table 3.1) was studied. In addition, each microchannel has the same number of sensors (of the same type) placed along it. In this system, it was possible to generate spatio-temporal signals. Figure 3.21 shows the simulation results of the spatio-temporal signals generated by these 5 set systems. Only 3 sensor responses are depicted in Figure 3.21; one near the inlet (S1), one at the middle (S20) and one near the outlet (S40) of the proto-nose I system.

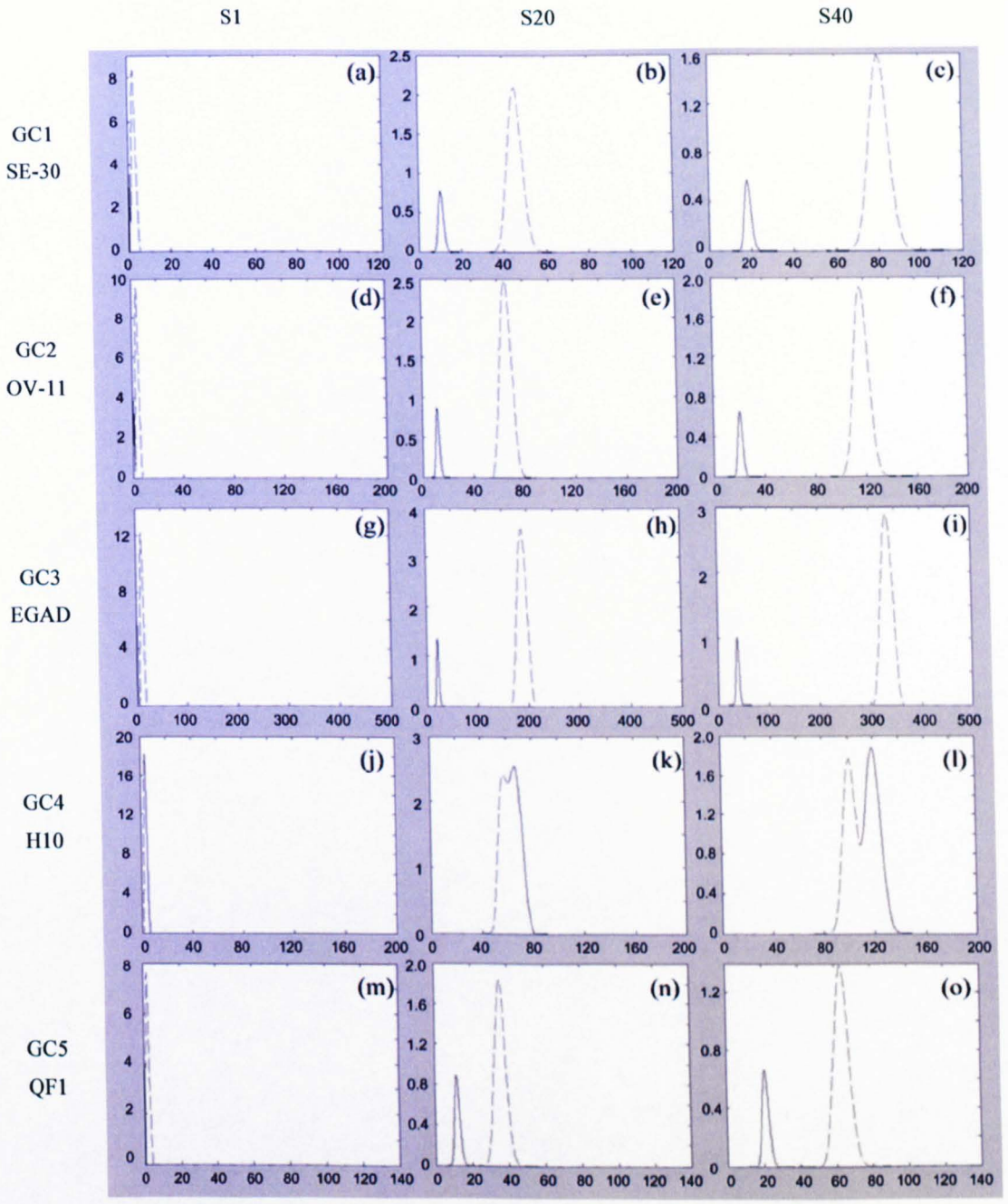

Figure 3.21: Spatio-temporal signals, (a)-(c) Sensor responses to ethanol (blue) and toluene vapour (green) pulses in air at three locations (near inlet (S1), middle (S20) and near outlet (S40)) along a SE-30 coated column, (d)-(f) Sensor responses under the same condition with a column coated with OV-11, (g)-(i) Sensor responses under the same condition with a column coated with EGAD, (j)-(l) Sensor responses under the same condition with a column coated with H10, and (m)-(o) Sensor responses under the same condition with a column coated with QF1. (Plotted in percentage change in resistance versus time (s)).

Comparing the sensor responses to ethanol and toluene vapour, the time delay (temporal signal) increased when moving towards the outlet of the microchannel. Comparing across different GC microchannels, the sensor responses at the same location are distinctive due to the disparity in retention behaviour of each stationary phase coating acting on the same analyte, thus giving spatial signals. The advantages of using this configuration are that only one type of sensor is needed and a better discrimination is achieved due to the higher diversity of operating 5 different GC microchannels simultaneously. However, this is at the expense of using 5 GC microchannels each coated with a different stationary phase materials.

In addition to the spatio-temporal signal, when a complex analyte is used (such as a binary ethanol/toluene mixture), a sequence of separated pulses will elute towards the end of the GC microchannel, as would normally be expected for a GC column. The advantage of this feature is the ability to provide extra discrimination since the nominally identical sensors towards the end of the microchannel will be capable of providing information on both the type of analyte and also its quantity.

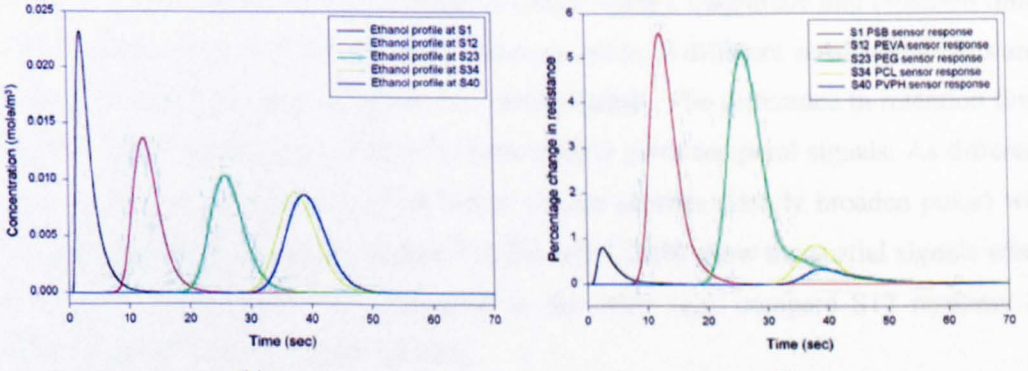

(a) (b)

Figure 3.22: Proto-nose I sensor responses to ethanol vapour. (a) Ethanol vapour profiles at 5 sensor locations along the GC microchannel. (b) 5 different types of sensors responding to ethanol vapour at these locations.

In the second scenario, a single GC microchannel with 5 different types of sensors (10 different types of sensors for proto-nose II) was considered. The temporal signals were generated in the same manner while the spatial signals were extracted using the response profiles of different types of sensors. Due to the disparity in partition coefficient, the response magnitudes and profiles were different. Details pertaining to the

characterisation of these sensors and their response time and profile to ethanol and toluene vapour in air are given Section 3.4.

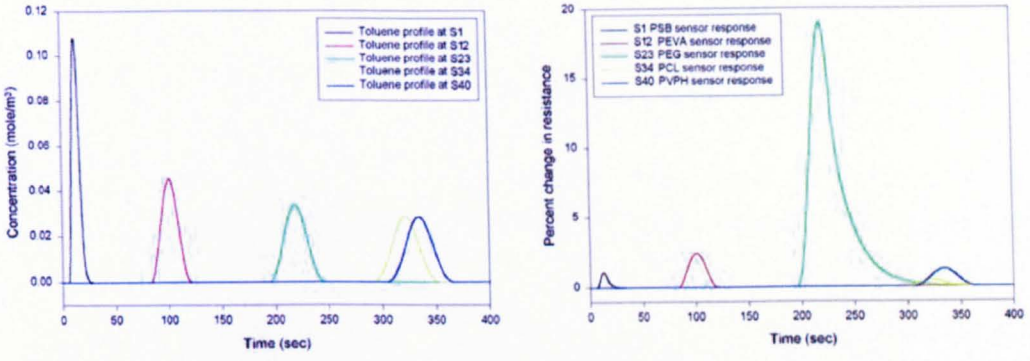

(a) (b)

Figure 3.23: Proto-nose I sensor responses to toluene vapour. (a) Toluene vapour profiles at 5 sensor locations along the microchannel GC. (b) 5 different types of sensors responding to toluene vapour at these locations.

Referring to Figures 3.22 and 3.23, the analyte profiles for ethanol and toluene vapour, as presented to the sensors, differs in duration (pulse width), magnitude and retention time. Only 5 sensors are shown for simplicity; they are made of different sensing materials and placed at various locations along the GC microchannel. The difference in retention time (Figure 3.22(a) and Figure 3.23(b)) for each analyte gives temporal signals. As different types of sensors are being used, the highly similar profiles (slowly broaden pulse) will produce contrasting responses. Figure 3.22(b) and 3.23(b) show the spatial signals when the corresponding sensors are compared to the other (e.g. compare S12 response in Figure 3.22(b) to S12 in Figure 3.23(b)).

This technique is perhaps preferable because it requires only one GC microchannel. The expense of increasing the number of sensor types can be easily overcome as there are many different types of polymer sensors available. The only complication is in the fabrication of the sensor array, as multiple types of sensing materials have to be deposited onto a single array in close proximity. This issue will be discussed in Chapter 4.

3.4 Polymer-composite sensor response model

It is desirable to be able to understand and then predict the dynamic behaviour of different resistive polymer-composite sensors to different analytes. The mechanism underlying the interaction between the polymer and the gas molecules, and the manner in which this generates a change in the properties of the polymer is still a matter of scientific debate [3.18]. Several possible modes of interaction can be envisaged, which include swelling effect of the polymer, interaction between gas molecules and charge carrier on the polymer chain, interaction between the gas molecules and the counter ions within the polymer and oxidation or reduction of the polymer by the gas [3.18]. Nevertheless, numerous studies on modelling the behaviour of these sensors have suggested that this dynamic response can be approximated with a first-order exponential response model [3.18-3.20]. A Pspice model [3.19] and more recently a Cadence model [3.20] have become available. However, they are not suitable because these models are not simulated in an MATLAB environment. A finite element model has also been proposed using similar method, and its geometrical model is shown in Figure 3.24.

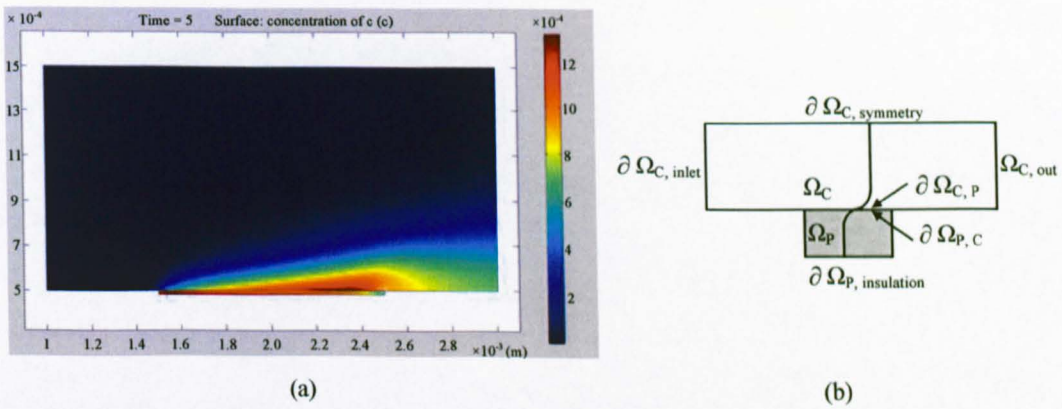

(a) (b)

Figure 3.24: Geometrical model and boundary conditions for FE simulation of sensor response. (a) Geometrical model of microchannel with polymer sensor. (b) Boundary conditions.

The mathematical PDEs and boundary conditions are exactly the same as the GC microchannel, and hence are not repeated here (available in [3.21]). Results of the finite element simulation confirmed the first-order exponential response behaviour of this type of sensor. Figure 3.25 shows the simulation result of an injection of 5 s ethanol vapour pulse to the inlet of the microchannel. The sensor response follows a first-order exponential model.

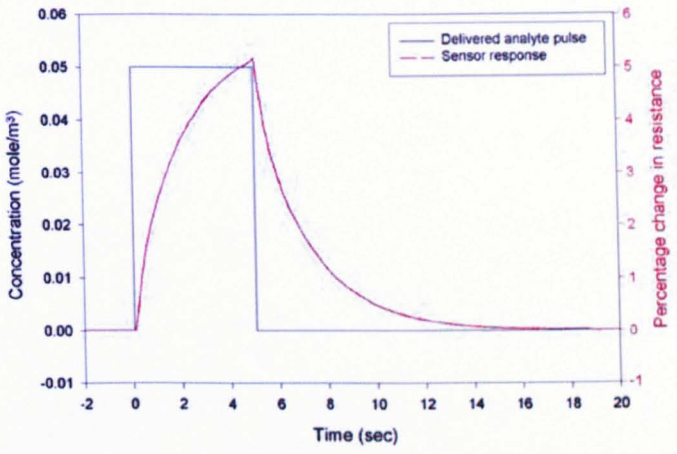

Figure 3.25: Finite element simulation of polymer-composite sensor response.

In order to realise the full system response, the analyte profiles simulated in Sections 3.2 and 3.3 have to be coupled together with the sensor response model. Two techniques can be used here. The first technique requires the geometrical model of the microchannel to be modified to include a layer of sensing material below the microchannel. In the proposed second technique, the analyte profiles are extracted from the finite element model and the sensor responses are coupled by applying first-order exponential response model numerically. Since FEMLAB is an extension package running on top of MATLAB, the finite element solutions are readily available in MATLAB. Hence, this makes the second technique attractive. In addition, the second technique is less complex to perform compared to adding geometries that complicates the existing model as more computational nodes are created. Furthermore, extra multiphysics modes have to be included to the original model, making it less computational efficient. Also, many simulation parameters such as partition coefficient, diffusion coefficient between the test analytes and polymer materials are not readily available. Although using the numerical first-order exponential approximation still requires the coefficients for the equation, they can be easily extracted by fitting their responses obtained experimentally to the first-order exponential equation.

3.4.1 Dynamic sensor response model

The dynamic sensor responses are polymer and analyte pair specific. The response determines both the response magnitude and response time. Ethanol and toluene vapour are the primary analytes, and PSB, PEVA, PEG, PCL and PVPH (Table 3.3) are the

polymer-composite (with carbon black nanosphere particles) sensing materials used. Using the first-order exponential model, the "on transient" is given by Equation (3-16).

$$R = R_{ON}\left(1-e^{-\tau_{ON}t}\right) \qquad (3\text{-}16)$$

where R_{ON} is the base resistance and τ_{ON} is the response time coefficient.

while the "off transient" is given by Equation (3-17).

$$R = R_{OFF}\, e^{-\tau_{OFF}t} \qquad (3\text{-}17)$$

where R_{OFF} is the base resistance and τ_{OFF} is the decay time coefficient.

For simplicity, the "off transient" is estimated to be about 20 % lower based on experimental results. This is due to the slower desorption process [3.18-3.20].

Table 3.3: Sensing materials for 5 sensor types and their acronyms.

No.	Polymer material	Acronyms
1	Poly (stylene-co-butadiene)	PSB
2	Poly (ethylene-co-vinyl acetate)	PEVA
3	Poly (ethylene glycol)	PEG
4	Poly (caprolactone)	PCL
5	Poly (4-vinyl phenol)	PVPH

Table 3.4 gives the fitted "on transient" of the experimental results to the first-order exponential equation. In general, the sensors responded much faster to ethanol vapour when compared to toluene vapour with a higher percentage change in resistance. This is likely due to smaller molecule size of ethanol vapour which resulted in a more rapid absorption. It is this difference in both response time and magnitude that provides a better selectivity, giving a larger difference in the spatial signal.

Table 3.4: Experimental results of PSB, PEVA, PEG, PCL and PVPH composite sensor responses to ethanol and toluene vapour fitted to a first-order exponential equation (Equation (3-16)).

Sensor	Toluene			Ethanol		
type	R_{ON}	τ_{ON}	R^2	R_{ON}	τ_{ON}	R^2
PSB	0.5346	0.3568	0.8638	3.3282	0.4062	0.9902
PEVA	2.6793	0.7229	0.9626	20.9653	0.5349	0.9870
PEG	35.1677	0.0630	0.9945	32.5009	0.1445	0.9948
PCL	0.8580	0.103	0.9477	7.7427	0.0807	0.9964
PVPH	2.1748	0.1887	0.9928	2.1630	0.1881	0.9950

**For R_{ON} and τ_{ON}, refer to Equation (3-16), R^2 is the goodness of fit to the first-order exponential equation.*

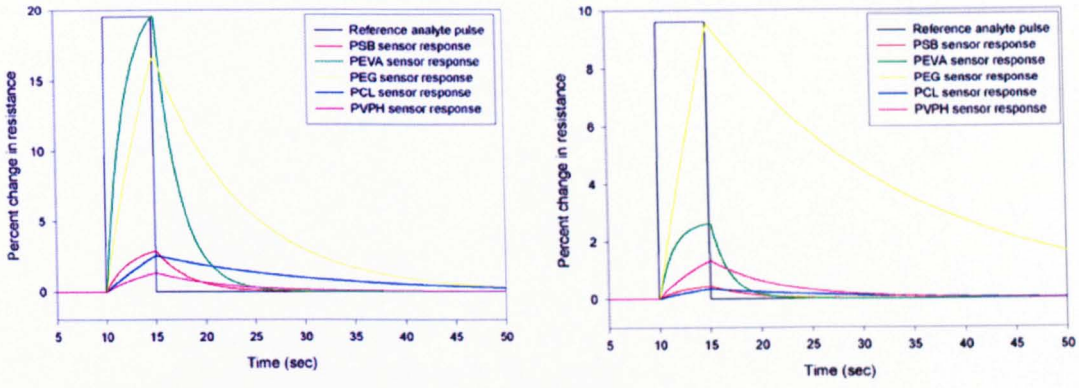

Figure 3.26: Fitted response of PSB, PEVA, PEG, PCL and PVPH sensor. (a) Sensor response to ethanol vapour. (b) Sensor response to toluene vapour.

Figure 3.26(a) and (b) show the fitted responses of PSB, PEVA, PEG, PCL and PVPH sensors to ethanol and toluene vapour respectively.

3.4.2 Velocity effect on sensor response

Liu *et al.* first reported the effect of flow rate on gas sensor sensitivity in 1995 [3.22]. More recently Eklov *et al.* [3.23] showed that an increase in flow rate could improve the response time of their sensor array. However, they choose to operate at a lower flow rate (10 ml min^{-1}) to give differential response to their type of sensor array. The sensors with different response profiles (spatial signals) are desired in their case for its ability to provide a larger diversity of responses to improve their pattern recognition algorithm (rather than redundant responses). Yoshigoe *et al.* [3.24] simply reported an influence of flow rate on their sensor response, but did not elaborate upon their investigation. Finally, fast resistive polymer gas sensors were reported by Briglin *et al.* in 2003. Fast sensor responses (< 10 ms) were obtained by operating the chamber at flow rates in excess of 5.9 L min^{-1} (1500 cm s^{-1}). However, they did not investigate the effect of flow rate on the sensor response time.

To study the effect of velocity on sensor response, the diffusion coefficient of the analyte within the polymer sensing material has to be modified. The effective diffusion coefficient of the polymer has been modelled for the sake of simplicity with a linear term as follows

$$D = D_o (1 + v_o V) \tag{3-18}$$

where v_o is a first order velocity coefficient and D_o is the diffusion coefficient at zero velocity (static diffusion).

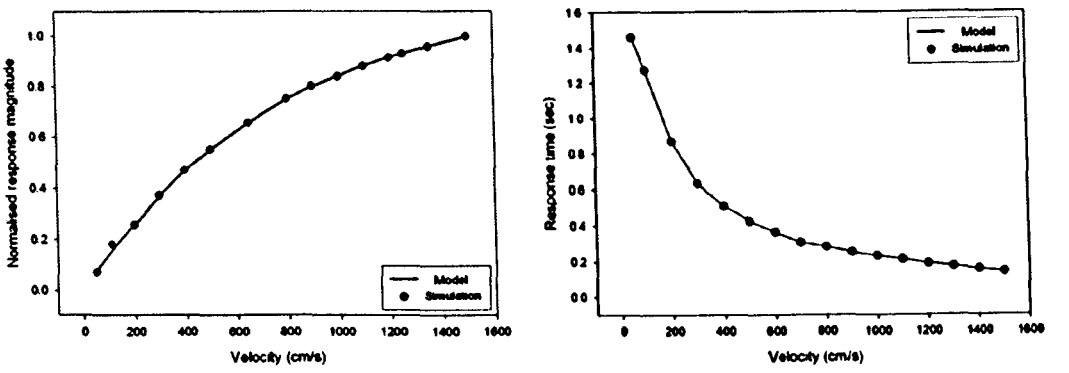

(a) (b)

Figure 3.27: Effect of flow velocity on sensor response. (a) Effect of flow velocity on sensor response magnitude. (b) Effect of flow velocity on sensor growth coefficient (reciprocal of response time).

The effective diffusion coefficient as defined in Equation (3-18) is applied to the model given in Figure 3.24. Figure 3.27 shows the effect of velocity on the sensor response magnitude and response time. A 5 s toluene vapour pulse was injected at the inlet and the effect of the sensor response is monitored. Figure 3.27(a) shows the normalised response magnitude against flow velocity. As the velocity was increased, the response magnitude increased. Similarly, as the velocity increased, the response time decreases as shown in Figure 3.27(b), giving a faster responding sensor. Both parameters approach saturation when the velocity is increase further, resembling an exponential function.

3.5 Conclusions

This Chapter reports on the simulation of the transport of a vapour pulse down a microchannel, microchamber and GC microchannel to an array of polymer-composite sensors. For microchannel vapour delivery, the most important variable was the flow velocity of the carrier gas. It has been shown that a slow flow velocity leads to undesirable broadening, producing varying analyte profiles for different sensors placed along the microchannel, causing inconsistent sensor response for a same analyte. The

geometry of the microchannel has less direct impact on the delivered analyte profile. However, it will affect the pressure drop across the microchannel and the amount of analyte required.

For the microchamber, the main design consideration has been focused on creating a geometry that is capable of delivering a uniform concentration profile to all sensors within the sensor array simultaneously.

In the case of GC microchannel, the aim of generating spatio-temporal signals has been demonstrated. Two different strategies have been discussed; one using multiple GC microchannel with different coating materials, and the other using a single GC microchannel with a diverse sensing array of multiple sensing materials. Although both configurations were capable of generating spatio-temporal signals, the latter configuration was selected for its simplicity. When the performance matrix (separation factor) for a GC microchannel using a finite element model was compared to the analytical solution, it was found to be accurate in predicting the response behaviour of the system.

Finally, the dynamic response behaviours of 5 different types of polymer-composite sensors have been modelled against their responses to toluene and ethanol vapours using the first-order exponential response model. Using measured response data, the profiles were fitted to the exponential equations to obtain the coefficients. These equations were subsequently used to couple to the analyte delivery profiles to obtain the final sensor responses. The velocity effect on the sensor response behaviour was also studied to determine the impact of adjusting the flow velocity on the sensors. These design considerations on the microchannel geometry, together with practical manufacturing constraints, will be discussed in Chapter 5 and 6. The simulation results will be compared to the experimental results in Chapter 8.

3.6 References

[3.1] D. Bhusari, H.A. Reed, M. Wedlake, A.M. Padovani, S.A.B. Allen, P.A. Kohl, ***Fabrication of air-channel structures for microfluidic, microelectromechanical, and microelectronic applications***, Journal of Microelectromechanical Systems, Vol. 10, No. 3, Sep 2001.

[3.2] A. Rasmussen, M. Gaitan, L.E. Locascio, M.E. Zaghloul, ***Fabrication techniques to realize CMOS-compatible microfluidic microchannels***, Journal of Microelectromechanical Systems, Vol. 10, No. 2, Jun 2001.

[3.3] J. Pfahler, J. Harley, H. Bau, J. Zemel, ***Liquid transport in micro and submicron channels***, Sensors and Actuators A 21-23, pp. 431-434, 1990.

[3.4] C. Aubert, S. Colin, R. Caen, ***Unsteady gaseous flows in tapered microchannels***, Technical Proc. 1998, Int. Conf. on Modeling and Simulation of Microsystems, Santa Clara, California, USA, Apr 6-8, 1998.

[3.5] F. Sharipov, ***Non-isothermal gas flow through a rectangular microchannels***, Technical Proc., Int. Conf. on Modeling and Simulation of Microsystems, San Juan, Puerto Rico, USA, Apr 19-21, 1999.

[3.6] A. Meckes, J. Behrens, O. Kayser, W. Beneckem, T. Becker, G. Müller, ***Microfluidic system for the integration and cyclic operation of gas sensors***, Sensors and Actuators 76, pp. 478-483, 1999.

[3.7] K. Keyhani, P.W. Scherer, M.M. Mozell, ***A numerical model of nasal odorant transport for the analysis of human olfaction***, Journal of Theoretical Biology, pp. 279-301, 1997.

[3.8] G.E. Spangler, ***Relationships for modelling the performance of rectangular gas chromatographic columns***, Journal of Microcolumn Separation, 13(7), pp. 285-292, 2001.

[3.9] E. Fontes, P. Byrne, J. Sundqvist, P. Bosander, M. Marklund, ***FEMLAB chemical engineering user manual (version 2.1)***, Comsol, Inc, March 2001.

[3.10] M.J.E. Golay, ***Gas Chromatography: Theory of chromatography in open and coated tubular columns with round and rectangular cross-sections***, D. H. Desty, Ed., *(1958 Amsterdam Symposium)*, (Butterworths, London), pp. 36-55, 1958.

[3.11] M.J.E. Golay, ***The height equivalent to a theoretical plate of retentionless rectangular tubes***, Journal of Chromatography A, Vol. 216, 1981, pp. 1-8.

[3.12] O. Trapp, V. Schurig, ***ChromWIN - A computer program for the determination of enantiomerization barriers in dynamic chromatography***, Computer and Chemistry, 25, pp. 187-195, 2001.

[3.13] GC-SOS, http://www.chemsw.com/, ***Gas Chromatography Simulation and Optimization Software***, Viewed on 20/12/2002.

[3.14] I. Hahn, P.W. Scherer, M.M. Mozell, ***A Mass Transport Model of Olfaction***, Journal of Theoretical Biology, 167, pp. 115-128, 1994.

[3.15] S.C. Terry, J.H. Jerman, J.B. Angeli, ***A gas chromatographic air analyzer fabricated on a silicon wafer***, IEEE Transaction on Electron Devices, 1979.

[3.16] M.H. Abraham, C.F. Poole, S.K. Poole, ***Classifications of stationary phases and other materials by gas chromatography***, Journal of Chromatography A, 842, pp. 79-114, 1999.0

[3.17] P.W. Ash, N.W. Barnett, L. Ebdon, S.J. Rowley, ***Configuration and optimisation of semiconductor gas sensors as gas chromatographic detectors***, Analytica Chimica Acta, 216, pp. 147-161, 1989.

[3.18] K.J. Albert, N.S. Lewis, C.L. Schauer, G.A. Sotzing, S.E. Stitzel, T.P. Vaid, D.R. Walt, ***Cross-reactive chemical sensor arrays***, American Chemical Society, Chemical Review, Vol. 100, No. 7, pp. 2595-2625, 2000.

[3.19] J.W. Gardner, E. Llobet, E.L. Hines, ***PSPICE model for resistive gas and odour sensors***, IEE Proc.-Circuits Devices Syst. Vol. 146, No. 3, pp. 101-104, 1999.

[3.20] M. Cole, N. Ulivieri, J. Garcia-Guzman, J.W. Gardner, ***Parametric model of a polymeric chemoresistor for use in smart sensor design and simulation***, Microelectronics Journal, 34, pp. 865-875, 2003.

[3.21] S.L. Tan, J.A. Covington, J.W. Gardner, ***Velocity-optimised diffusion for ultra-fast polymer-based resistive gas sensors***, IEE- Science, Measurement and Technology, at press.

[3.22] S-J Liu, H-X Shen, J-X Feng, ***Effects of gas flow-rates on a Clark-type oxygen gas sensor***, Analytica Chimica Acta 313, pp. 89-92, 1995.

[3.23] T. Eklov, I. Lundstrom, ***Gas mixture analysis using a distributed chemical sensor system***, Sensors and Actuators, B 57, pp. 274-282, 1999.

[3.24] T. Yoshigoe, T. Nishina, S. Sato, K. Yamaki, M. Endo, ***Development of gas sensors for volatile organic compounds by using solid polymer electrolyte membrane electrodes***, Analytical Sciences, Vol. 17, pp. 1023-1025, 2001.

[3.25] S.W. Briglin, N.S. Lewis, ***Characterization of the temporal response profile of carbon black – polymer composite detectors to volatile organic vapours***, Journal of Physical Chemistry B, Vol.107, pp. 11031-11042, 2003.

Chapter 4

Design and fabrication of microsensors and microsensor arrays

4.1 Introduction

This chapter describes the design and fabrication of three types of sensor chips. The first type of sensor chip is discrete, fabricated in-house for the proto-nose microsystems. The second type is a 10 mm × 10 mm silicon sensor array with 80 chemoresistive microsensors arranged in 5 rows of 16 elements. The last type is an extension of the second type, fabricated using standard silicon CMOS process in collaboration with University of Edinburgh. It consists of 70 microsensors arranged in 5 rows of 14 elements. Each microsensor has its own programmable drive, gain and offset cancellation circuits.

In general, chemoresistive microsensor consists of 2 electrodes across which the polymer-composite sensing material has to be deposited. Details about the polymer materials, their mix recipes, preparation and deposition process are given here.

4.2 Proto-nose discrete sensors

The discrete sensors have been designed for the proto-nose microsystem. Due to their simplicity, they can be easily fabricated and deposited with different sensing materials. The basic design consists of two electrodes with a sensing material deposited across an inter-electrode gap.

4.2.1 Discrete sensors design and fabrication

The silicon-based substrate for the chemoresistors has been fabricated at University of Warwick using UV lithography techniques in a 3" batch process. Each device is 2.5 mm × 4 mm in size and consists of a pair of thin gold electrodes on a SiO_2/Si substrate with an electrode length of 1 mm and an inter-electrode gap of 75 μm. Figure 4.1(a) shows the design and dimension of the microsensor and Figure 4.1(b) shows a fabricated sensor

after wafer dicing. Although the aspect ratio (length of the electrode / inter-electrode gap) of the sensor does not have significant impact on the sensor response [4.1-4.2], it is desirable to have a high aspect ratio as it is easier to achieve the desirable resistance for the recipes listed in Table 4.1 and Table 4.2. The effective aspect ratio for this sensor is 13.3 (1 mm / 75 μm).

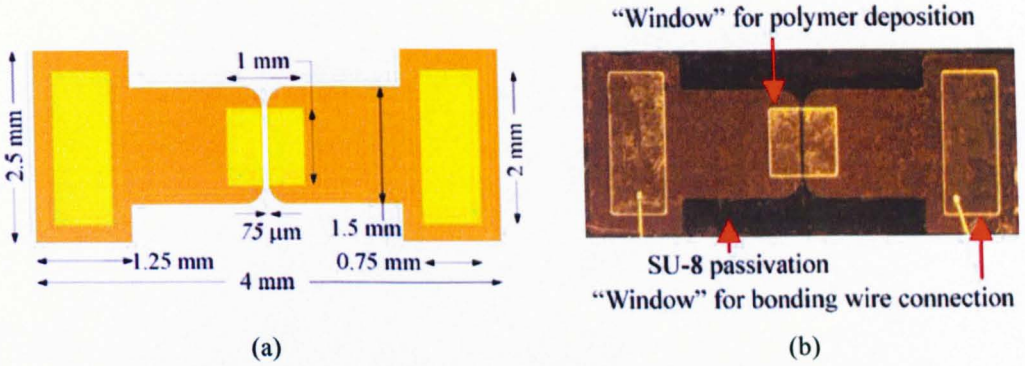

Figure 4.1: Microsensor design. (a) Microsensor design and dimension. (b) Photograph of fabricated microsensor.

A 450 μm thick, 3" silicon wafer with silicon oxide (1 μm) is used as the based substrate. A 20 nm adhesion layer of chrome was thermally evaporated, followed by 250 nm of gold. These metals layers were deposited using the Auto306 thermal evaporation system (Edwards, UK). Next, a layer of photoresist (Microposit S1818, Shipley) was spin-coated and the wafer was soft baked at 100 °C for 90 s. The mask for the sensor pattern (shown in Figure 4.2(a)) was aligned with the wafer using a double-sided mask aligner system (Karl Suss, MJB21) and exposed to UV light for 7 s. The wafer was then developed in a photoresist developer (Microposit 351) for 1 minute and etched to define the electrodes using a gold etchant (2 g KI, 1 g I_2, 50 ml H_2O) followed by a chrome etchant (8 g ceric suplate, 12 ml nitric acid, 80 ml H_2O). The photoresist was removed using acetone before a layer of SU-8 10 (Micro Chem, UK) was deposited and patterned using the mask shown in Figure 4.2(b). This layer acts as a protective film and it also defines the "windows" for sensing materials deposition and bonding wires for electrical connection. The processing steps for SU-8 10 can be found in [4.3].

The masks for the discrete microsensors shown in Figure 4.2 consist of 177 sensors on each wafer. Due to the low resolution required, these masks were fabricated in-house using high-resolution laser printer (1600 dpi) by direct printing onto an acetate

sheet. The resolution of this system gives a minimum feature size of approximately 10 μm.

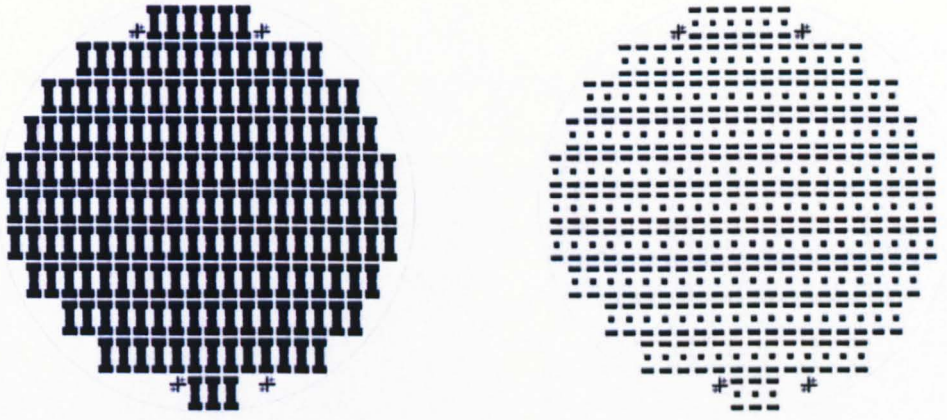

(a) (b)

Figure 4.2: Discrete sensor masks. (a) Sensor electrode mask. (b) Sensor passivation layer mask.

Lastly, the wafer was diced using a dicing saw (Tempress Model 602) and each sensor was bonded onto a 4-pin PCB header shown in Figure 4.3(a), ready for sensing material deposition. The microsensor mounted on a 4-pin header was placed onto a micropositioning alignment system (Figure 4.4(a)) and aligned to a mechanical micromask (bronze sheet, 250 μm thick) shown in Figure 4.3(b).

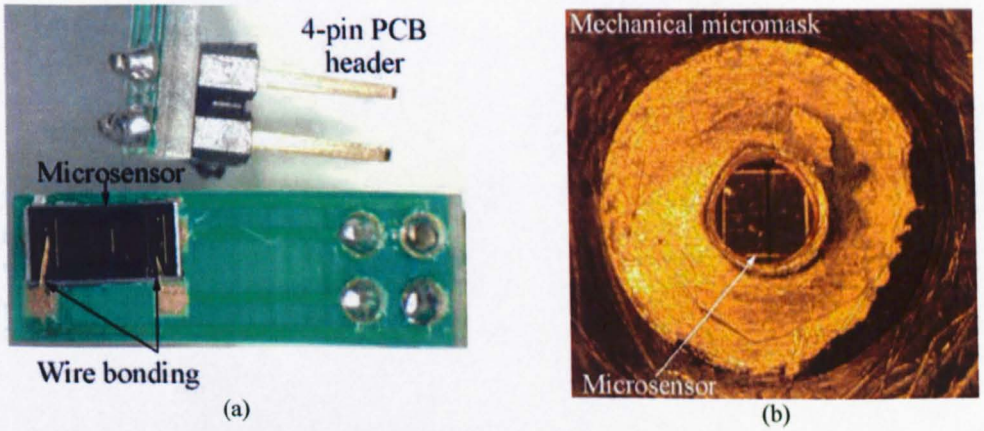

(a) (b)

Figure 4.3: Microsensor and mask alignment. (a) Microsensor bonded onto a 4-pin PCB header. (b) Microsensor alignment to a mechanical micromask.

4.2.2 Micropositioning alignment system

The micropositioning alignment system shown in Figure 4.4(a) allows the microsensor to be attached. A micromask plate (Figure 4.3(b)) with a hole of 1.2 mm in diameter was

fixed to 4 supporting pillars. The X-Y adjust provided an easy means of moving the microsensor horizontally and vertically such that the hole on the mask aligns directly on top of the inter-electrode gap (Figure 4.3(b)). The two pins bonded to the microsensor were connected to a multimeter to monitor the resistance during sensing material deposition. The side-view of the alignment setup is shown in Figure 4.4(b).

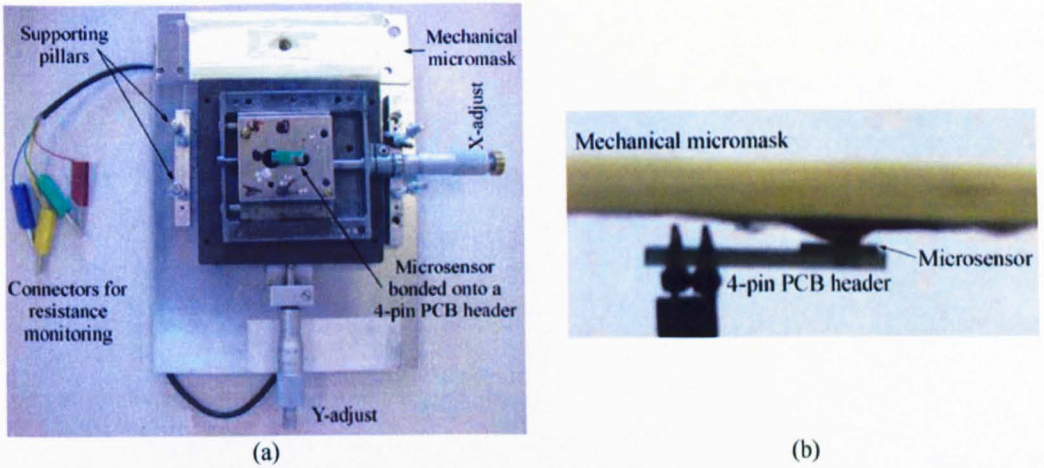

Figure 4.4: Micropositioning alignment system setup. (a) Micropositioning alignment system. (b) Side-view of mask and microsensor alignment.

4.2.3 Discrete sensors polymers deposition

The five recipes used to create the sensing materials are given in Table 4.1. The polymers materials were supplied by Sigma Aldrich (UK) and the carbon black (Black Pearls 2000) material was supplied by Cabot Corporation (USA). The polymers were either in powder form or small crystals while the carbon black contains nanospheres with diameter of typically 50 - 80 nm. The polymer was firstly dissolved in their respective solvent overnight with the aid of a magnetic stirrer (See hotplate magnetic stirrer, UK) at an elevated temperature (50 °C). Next, carbon black was added and the mixture was sonicated for 10 minutes using a flask shaker (Griffin and George, UK). The mixture was then ready for deposition onto the sensors using an airbrush (HP-BC Iwata, Japan) controlled with micro spraying system (RS precision liquid dispenser, UK) as shown in Figure 4.5. The airbrush was held 10 - 15 cm away from the mask and several passes were sprayed depending on the desired thickness (or resistance). This gives a circular coating typically 1.5 mm in diameter. The electrical resistances of the polymer sensors

were controlled through the deposition process to a value between 2 kΩ to 8 kΩ with a typical film thickness of about 20 μm (± 25 %).

Table 4.1: Polymer-composite sensing material recipes for 5 sensing materials.

No.	Polymer material	Carbon black	Solvent
1	PSB, 0.7 g	0.175 g	Toluene, 20 ml
2	PEVA, 1.2 g	0.3 g	Toluene, 20 ml
3	PEG, 1.2 g	0.3 g	Ethanol, 20 ml
4	PCL, 1.2 g	0.3 g	Toluene, 20 ml
5	PVPH, 1.2 g	0.3 g	Ethanol, 20 ml

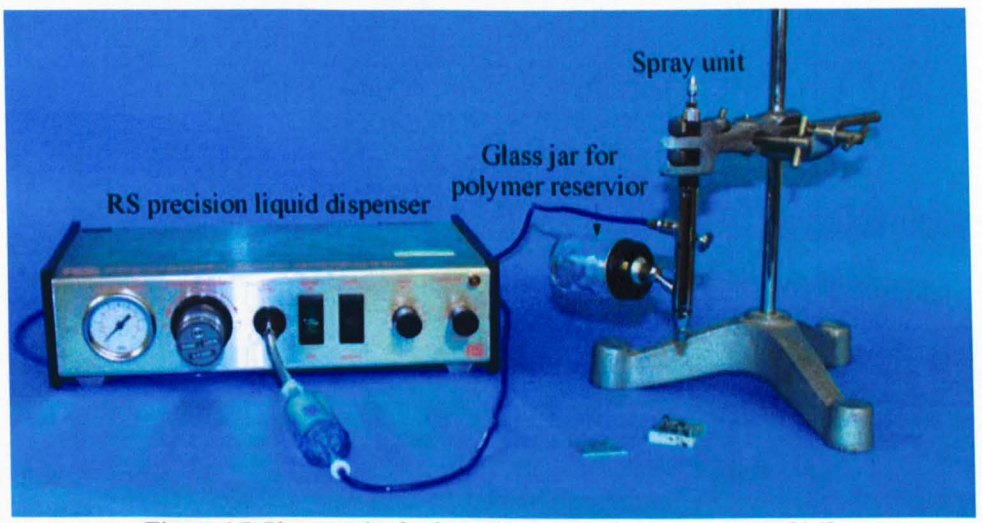

Figure 4.5: Photograph of polymer-composite deposition system [4.4].

In addition to the 5 types of polymer materials listed in Table 4.1, 5 new types of sensors based on different polymer-composite materials were used as shown in Table 4.2. The original five types are used in the proto-nose I while the combined 10 different materials are used for proto-nose II. The increase in sensor diversity is important especially for the classification of complex analytes. The decision of increasing the sensor diversity was made after proto-nose I was completed and the analysis showed the need to increase the sensor diversity. The use of these materials for various chemical detections has been demonstrated previously [4.5-4.6].

Table 4.2: Polymer-composite sensing material recipes for 5 new sensor types.

No.	Polymer material	Carbon black	Solvent
1	Poly (9-vinylcarbazole) (PVC), 0.3 g	0.3 g	Toluene, 20 ml
2	Poly (vinyl pyrrolidone) (PVPD), 0.3 g	0.3 g	Ethanol, 20 ml
3	Poly (bisphenol A carbonate) (PBA), 0.7 g	0.175 g	Dichromethane, 20 ml
4	Poly (sulfane) (PSF), 0.7 g	0.175 g	Dichromethane, 20 ml
5	Poly (chloro P xylylene) (PCX), 1.2 g	0.3 g	Toluene, 20 ml

Figure 4.6 shows two examples of the deposited discrete sensors. Figure 4.6(a) shows a PBA sensor and Figure 4.6(b) shows a PSB sensor. Finally, all sensors were exposed to a temperature post-treatment at 40 °C for 24 hours to stabilise the resistance prior to use.

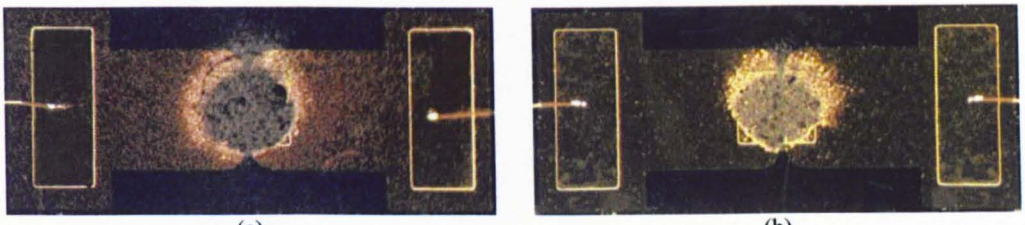

(a) (b)

Figure 4.6: Deposited discrete sensors. (a) Discrete sensor deposited with PBA. (b) Discrete sensor deposited with PSB.

4.3 Hybrid-nose sensor arrays

The hybrid-nose is an in-house fabricated version with similar dimension as the final analogue very large scale integration (aVLSI) nose sensor array. The aim here was to create an interim solution (while waiting for the design and fabrication of aVLSI-nose) to prepare for other subsystems including the micromasks, microchannel packaging, etc. The other important reason for building the hybrid-nose is the high-cost associated with fabricating low volume aVLSI chips using standard industrial process. Large amount of chips will be required for the initial polymer deposition and packaging integration trials, making the hybrid-nose a highly cost-effective solution for these trials.

4.3.1 Hybrid-nose sensor arrays design and fabrication

The silicon-based substrates for the sensor array have been fabricated at the University of Warwick. Each device was 10 mm × 10 mm in size and consisted of 80 pairs of thin gold electrodes on a SiO_2/Si substrate as shown in Figure 4.7(a). Figure 4.7(b) shows the dimension between each sensor and Figure 4.7(c) shows each sensor has two electrodes of 220 μm × 200 μm with an inter-electrode gap of 20 μm. The sensor arrays were passivated with a 10 μm thick protective layer of SU-8 with a "window" defined over the electrodes for sensing material deposition and I/O pads for electrical connections. The effective aspect ratio of each sensor is 9 (180 μm / 20 μm) after SU-8 deposition.

The sensors were arranged in 5 rows of 16 elements. To reduce the number of I/O pad connections, such that the sensor array design will fit into a single mask (for the

electrodes), some electrodes are commoned together. One electrode of each sensor in row 1 is commoned with one electrode of the sensor in row 4 of the same column. The same applies to the sensors in row 2 and row 5 as shown in Figure 4.7(b). This scheme reduced the I/O pads by 20 % without any compromise in the sensor performance. However, there is a limitation in terms of the connectivity to the data acquisition circuitries; this will be discussed in Section 7.3.3.

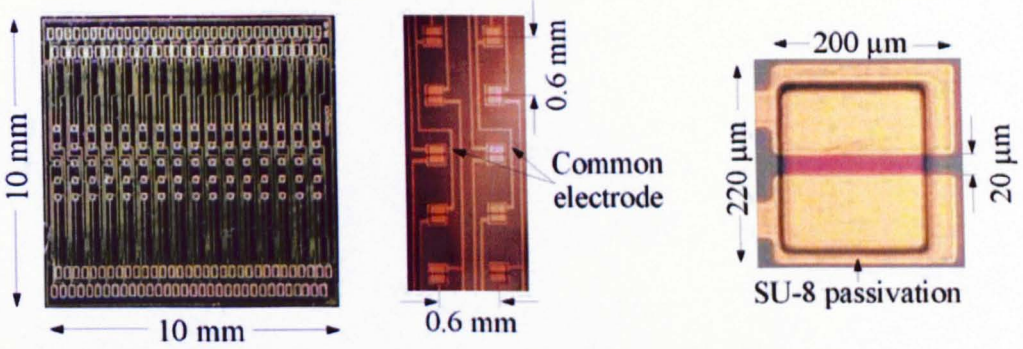

Figure 4.7: Hybrid-nose sensor array. (a) Hybrid-nose sensor array. (b) Sensor array connectivity. (c) Dimension of sensor cell.

The devices were packaged into a PGA256 semiconductor specific socket for easy interconnection, as shown in Figure 4.8(a). The fabrication process for the sensor array was exactly the same as the discrete sensor array and hence will not be discussed here. A fabricated wafer which consists of 26 devices before dicing is shown in Figure 4.8(b).

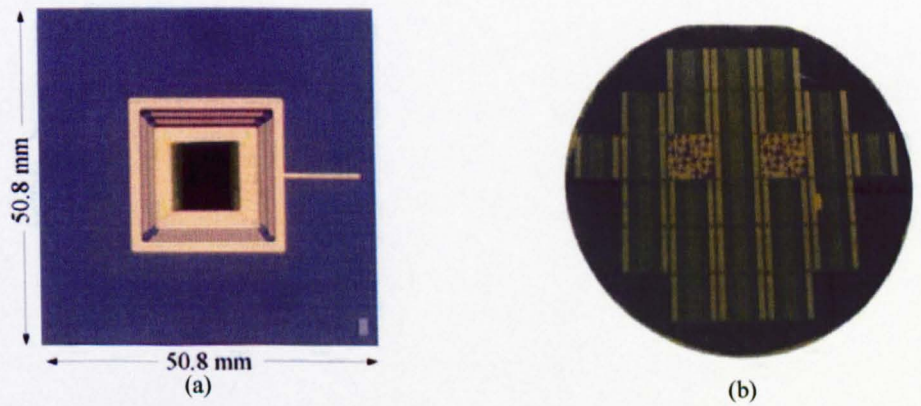

Figure 4.8: Hybrid-nose packaging and wafer. (a) Hybrid-nose packaged on a PGA256 socket. (b) 3" wafer with 26 hybrid-noses.

4.3.2 Micromasks design and fabrication

The micromasks are fabricated from a 50 μm thick copper/beryllium foil (Goodfellow Cambridge Ltd, UK) with each aperture being 300 μm in diameter. Using standard lithography techniques, the copper foil was etched with copper etchant (40 g ferric chloride hexahydrate granule (Mega Electronics Ltd, UK), 100 ml H_2O) for 60 s. Figure 4.9(a) shows a 16-hole single row micromask fabricated using this technique. Figure 4.9(b) shows the alignment of an 80-hole micromask with the hybrid-nose sensor array, and Figure 4.9(c) shows the dimension of the micromask and alignment with the hybrid-nose microsensors.

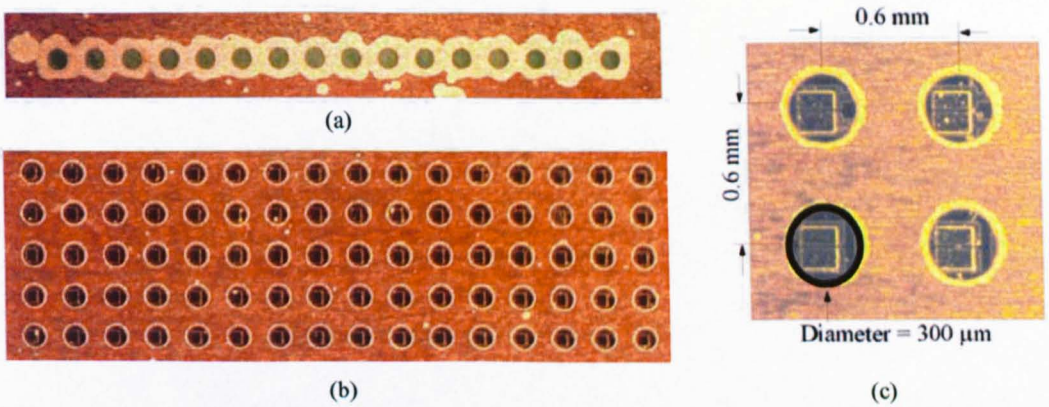

Figure 4.9: Mechanical micromasks for polymer deposition. (a) Single row 16-sensor micromask. (b) 80-sensor micromask aligned on hybrid-nose. (c) Magnified view of sensor array to micromask alignment.

4.3.3 Hybrid-nose polymers deposition

The same polymer composite materials as described in Section 4.2.3 were deposited onto the hybrid-nose microsensor array. To enable the resistance of each sensor to be monitored during the deposition process, a printed circuit board (PCB) as shown in Figure 4.10 was used. The same alignment system as shown in Figure 4.4 was used to align the micromask on the hybrid-nose microsensor arrays. The deposition process resulted in a circular polymer coating typically 350 μm in diameter. The electrical resistance of the deposited polymer sensors can be controlled through the deposition process to a value of about 1 kΩ to 20 kΩ with a typical film thickness of about 20 μm (± 50 %). Higher resistance variations were observed due to the sensors being deposited in bank (sensors with the same polymer are deposited simultaneously).

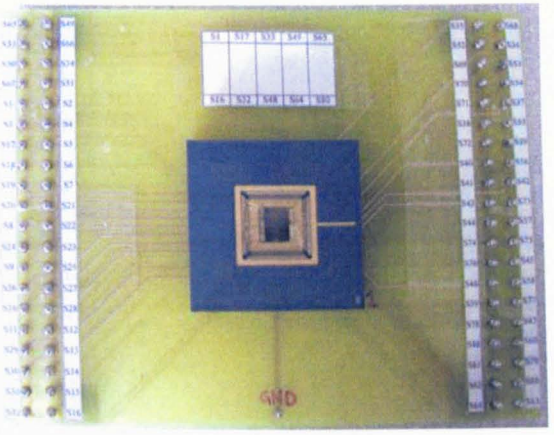

Figure 4.10: Hybrid-nose resistance monitoring PCB for polymer deposition.

Again, two variations of hybrid-noses with different polymer materials were fabricated. The first type (hybrid-nose I) consisted of 5 different types of sensing materials, as shown in Table 4.1, while hybrid-nose II consisted of 10 different types of polymer composite materials. There was no specific scheme on the grouping of different sensor types as this was dictated by the design of the microchannel packaging. The sensors were grouped in 8 or 16's, deposited with the same sensing material due to their close proximity. The two deposition schemes for the hybrid-noses are shown in Figure 4.11(a) and Figure 4.11(b) respectively. Hybrid-nose I consists of 5 different sensing materials each deposited on 16 sensors across each row. For hybrid-nose II, 8 sensors are deposited with the same sensing material, with two types of materials across each row.

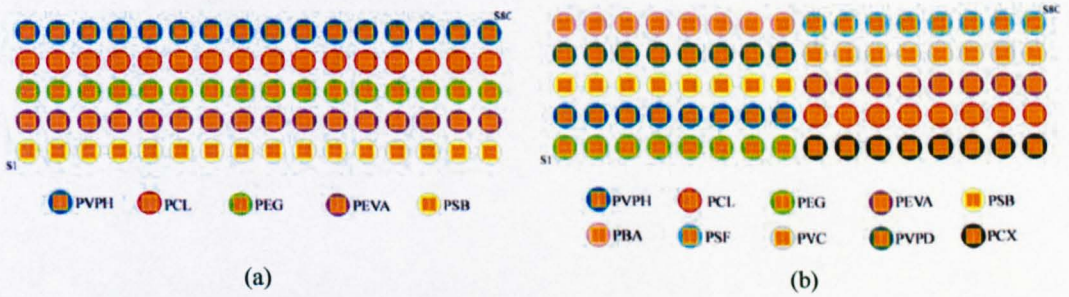

(a) (b)

Figure 4.11: Polymer deposition scheme. (a) Hybrid-nose I with 5 different types of polymers. (b) Hybrid-nose II with 10 different types of polymers.

These two generations of deposited hybrid-noses are shown in Figure 4.12. Figure 4.12(a) shows hybrid-nose I and Figure 4.12(b) shows hybrid-nose II. These devices were exposed to the same temperature treatment prior to use.

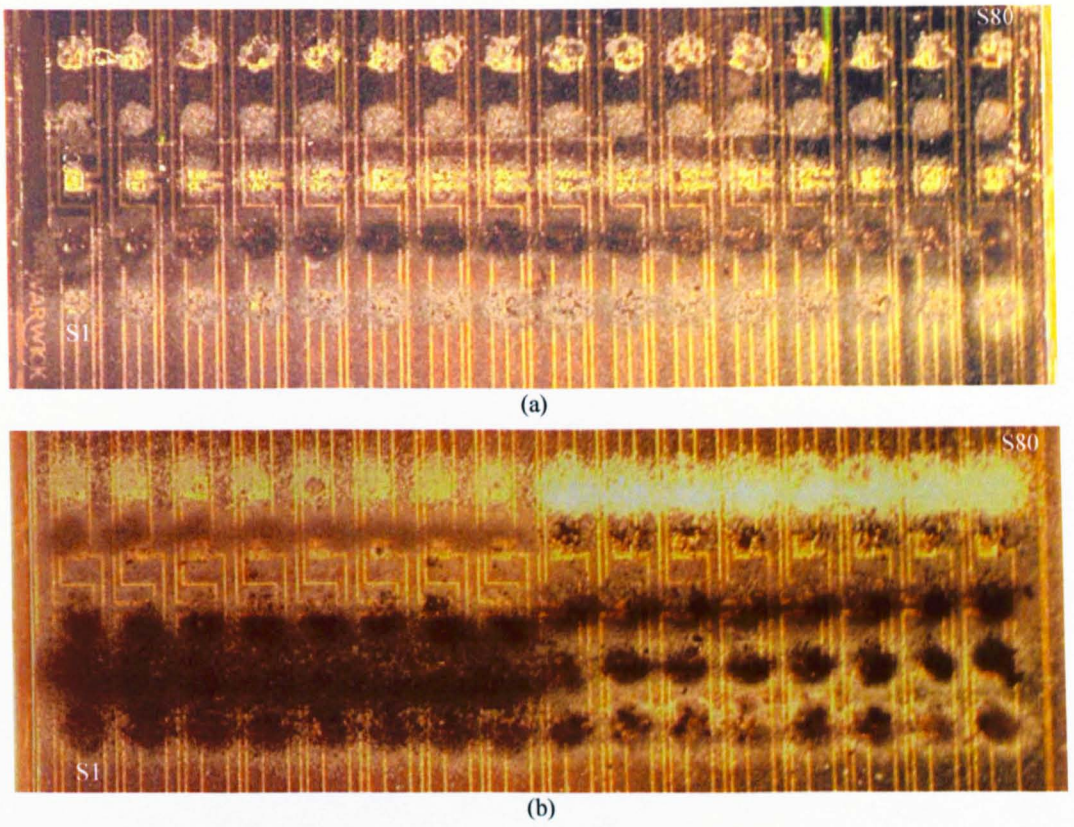

Figure 4.12: Photographs of deposited hybrid-noses. (a) Hybrid-nose I with 5 different sensing materials. (b) Hybrid-nose II with 10 different sensing materials.

4.4 aVLSI-nose smart sensor arrays

The aVLSI-nose is an advance smart sensor array fabricated using standard Austria Microsystems (AMS, AG, Austria) Complementary Metal Oxide Semiconductor (CMOS) 0.6 μm CUP process through the Europractice [4.7]. This chip was 10 mm × 5 mm in size and was designed using aVLSI in collaboration with the University of Edinburgh (sensors were designed by the University of Warwick, analogue circuits were designed by the University of Edinburgh). This sensor chip contains 70 sensor cells arranged in 5 rows of 14 elements. Each sensor has it own programmable current drive, DC-offset cancellation, amplification and low pass filtering circuits. Within each sensor, the sensing mode of operation was either as a resistive or Field Effect Transistor (FET) sensor, which is also programmable. The basic design for each sensor cell is shown in Figure 4.13. Some additional test circuits are also included in this chip for integrated firing neuron and synapses; these will not be covered here.

The AMS 0.6 μm CUP is a 2-poly/3-metal CMOS process with a minimum gate length of 0.6 μm. As the cost is directly proportional to the area of each device, it is extremely important to limit the size without any compromise in functionality. The relative distances between each sensor have been maintained to be the same as the hybrid-nose to ensure the same microchannel packages can be used. One sensor on the front and end of each row was removed to ensure the system will fit into a 10 mm × 5 mm die area.

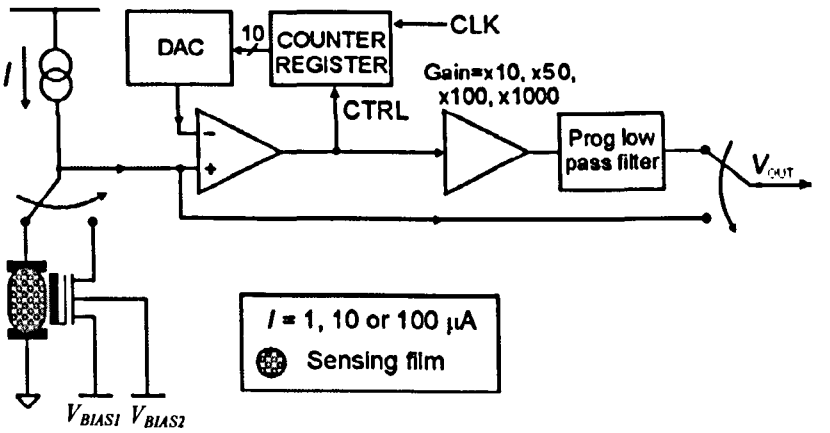

Figure 4.13: Block diagram of a sensor cell design.

Figure 4.13 shows the block diagram of a sensor cell design. The circuits can be separated into 3 parts, the driving, sensor and signal conditioning blocks. There are 3 constant current sources programmable via a software interface. On the sensor mode selector, a multiplexer selects between the resistive or FET mode of sensing. These two components form a minimal working sensor where the output signal can be selectable to be outputted directly or signal conditioned. On the signal conditioning route, the signal baseline (offset) was compared to a ramp voltage generated by a counter and digital-to-analogue converter (DAC) pair. The counter is clocked externally to increase the count, thereby increasing the DAC output voltage. This ramping signal was compared with the sensor baseline voltage, and upon exceeding the baseline voltage of the sensor, the comparator toggles to stop the counter from counting. This difference signal (sensor output minus baseline) will be amplified with a selectable gain and low-pass filter. The exact programming sequence will be described in details in Section 4.4.3.

4.4.1 Combined chemoResistive/FET sensor design

The basic design strategy for the aVLSI-nose resistive sensor array is the same as hybrid-nose except that it conforms to the design rules of the CMOS fabrication process. Figure 4.14(a) shows the design and dimension for the combined sensor. The two black squares on each side are the electrodes for the resistive sensor, while the long rectangular strip in the middle is the capacitive sensing plate for the FET sensor, as shown in Figure 4.14(b). The different colours of Figure 4.14(a) represent the different layers of the process. Although not all the layers are required for the resistive sensor electrodes, many have to be included to conform to the design rules [4.8]. These design rules include the minimum feature sizes of all layers, as well as the minimum distance between each layer. Conformance to these design rules does not guarantee the sensor will be functional, as these rules are meant to ensure the fabrication limitations are obeyed. It is possible to break the design rules if the designer is aware of the consequence as the manufacturer will not guarantee these designs. In addition to the resistive sensor, a FET test sensor is also included in each test cell. This FET sensor uses the same sensing material as the resistive sensor, so that it does not require additional post-processing. The design of the FET sensor is based on a floating gate, which is capacitively coupled to the sensing material.

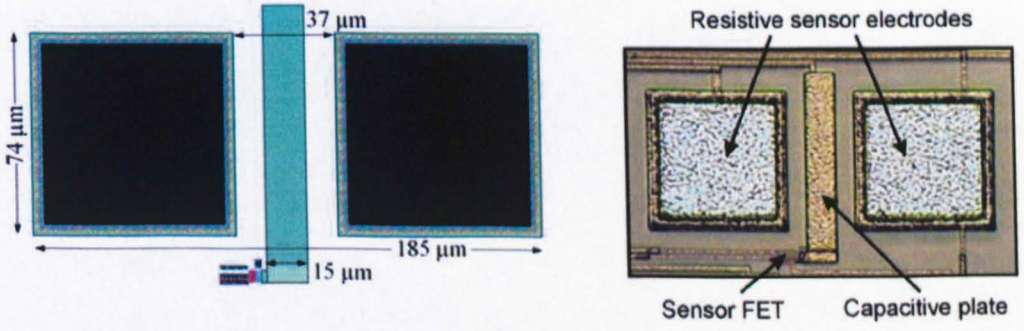

Figure 4.14: Combined resistive/FET sensor design. (a) Sensor design and dimension. (b) Fabricated sensor footprint.

The aspect ratio of the sensor is 2 which is defined by the length (74 µm) over the inter-electrode gap (37 µm). A clearer illustration is shown in Figure 4.15. In Figure 4.15(a), a pictorial view of a deposited sensor is shown. The circular mask has resulted in circular shape for the deposited sensing material. However, only the rectangular block across the

closer edges of the two electrodes needs to be considered. Figure 4.15(b) shows the model for the sensor resistance.

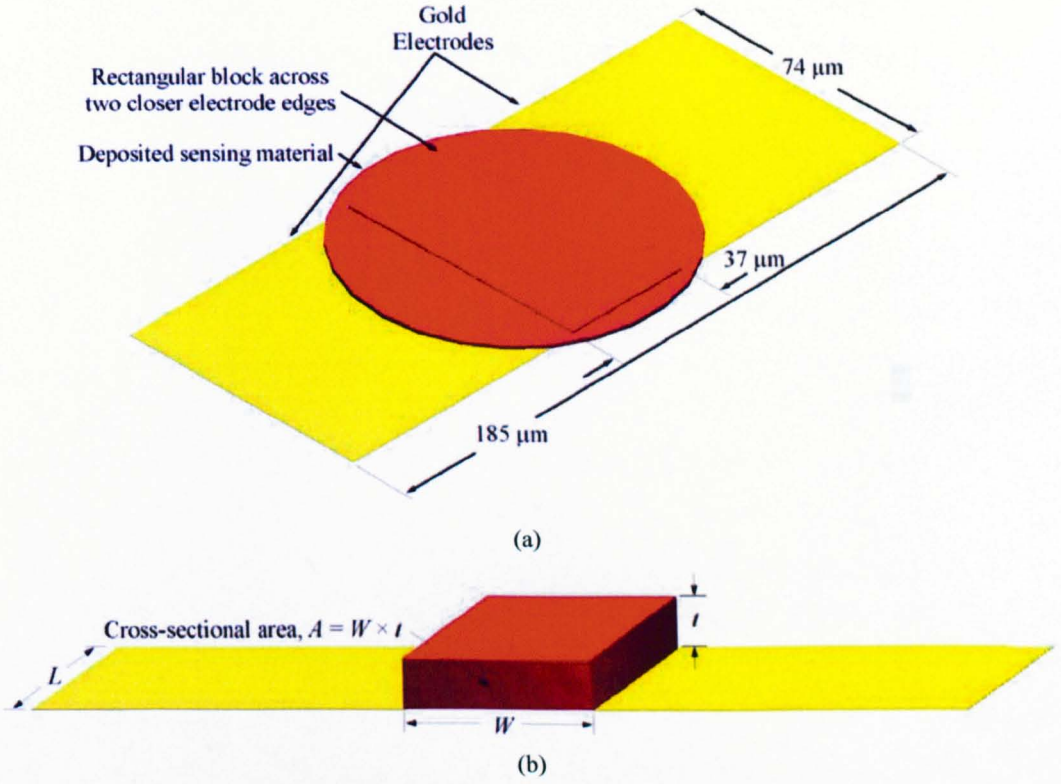

Figure 4.15: Relationship between aspect ratio and sensor resistance. (a) Pictorial view of a deposited sensor. (b) Model relating sensor resistance to the aspect ratio of sensor electrodes.

Assuming that the rectangular block of sensing material has a length, L, thickness, t, and inter-electrode gap (width), W. Equation (4-1) can be used to estimate the sensor resistance.

$$R_S = \frac{\rho \times L}{A} = \frac{\rho \times L}{W \times t} \qquad (4\text{-}1)$$

where ρ is the resistivity of the sensing material, L is the length and A is the cross-sectional area.

Assuming that the thickness, t, is uniform and therefore constant

$$R_S \ \alpha \ \frac{L}{W} \qquad (4\text{-}2)$$

where L / W is the aspect ratio.

As such, the resistance of the sensor is directly proportional to the aspect ratio of the electrodes.

The main limitation of many previously fabricated FET chemical sensors is their incompatibility with standard foundries fabrication processes [4.9-4.11]. The gate of this FET sensor is connected to a capacitive sensing plate which is left floating. Any potential created through the sensing material interaction (working function change) with a target gas or vapour appears, due to capacitive coupling, on the gate of the FET. However, there is a constraint requiring that sufficient potential at the gate is achieved to ensure the transistor turns on. As the gate is floating, it will have a potential subject to the variation in the fabrication process. This value can vary anywhere between -500 mV to +2 V [4.9]. Therefore, it is possible that if the gate potential is at -500 mV, any small modulation of the gate potential created by the sensing material will be lost. A double strategy is employed to ensure the transistor will be turned on. Firstly, the source voltage (V_{BIAS1} shown in Figure 4.13) can be biased to operate in the negative region to allow V_{GS} to be greater than 0.7 V, hence in the conduction region. Alternatively, or by employing both techniques simultaneously, a second capacitive plate placed below the sensing plate can be used to capacitively inject a biasing voltage (V_{BIAS2} shown in Figure 4.13) to turn on the FET.

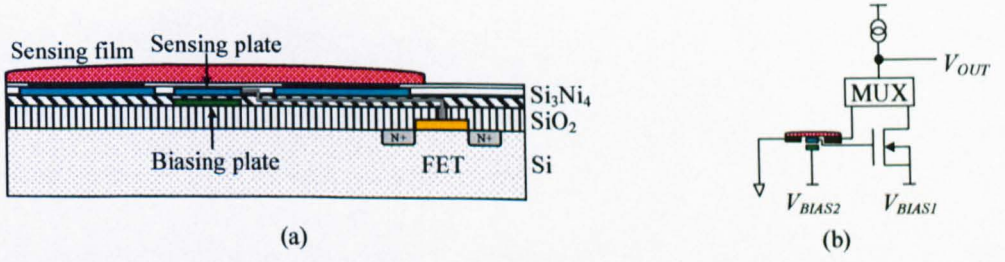

Figure 4.16: Combined resistive/FET sensor. (a) Cross-sectional view of sensor. (b) Schematic diagram of sensor.

Figure 4.16(a) shows the cross-sectional view of the sensor and (b) shows the schematic diagram of the sensor. The capacitive sensing plate is implemented on metal layer 3 which is directly below the silicon nitride passivation layer under the sensing film. The biasing plate was implemented on metal layer 2. In this design, the sensing mechanism was achieved by charge redistribution from the floating gate to the FET gate. It is thought that when the polymer is exposed to a reactive gas or vapour, the work function of the

polymer changes [4.9-4.11]. This results in a change of the potential of the polymer above the floating electrode. This in turn induces a charge movement, between the floating gate and the FET gate, so altering the operating point of the FET. Similar designs have been reported using a suspended gate FET where the sensing material is deposited on the underside of a top plate [4.9]. This top plate is suspended from the lower plate by an air gap, which channels the sample gas. A limitation of this design is that as the FET is enhanced, it will require a certain minimum voltage before becoming active. Hence, a charge will have to be induced on the gate sufficient enough for conduction to occur so that the FET is turned on.

As the design is based on capacitors, it is useful to examine at the capacitive equivalent circuit for this design. Figure 4.17(a) shows the circuit schematic of the FET sensor. V_S is the potential developed by the sensing material and I_{SEN} is the current through the FET. Figure 4.17(b) shows the capacitive equivalent circuit where C_{SENSOR} is the sensor capacitance, C_{SUB} is the substrate capacitance, C_{GATE} is the gate capacitance and V_{GATE} is the gate voltage.

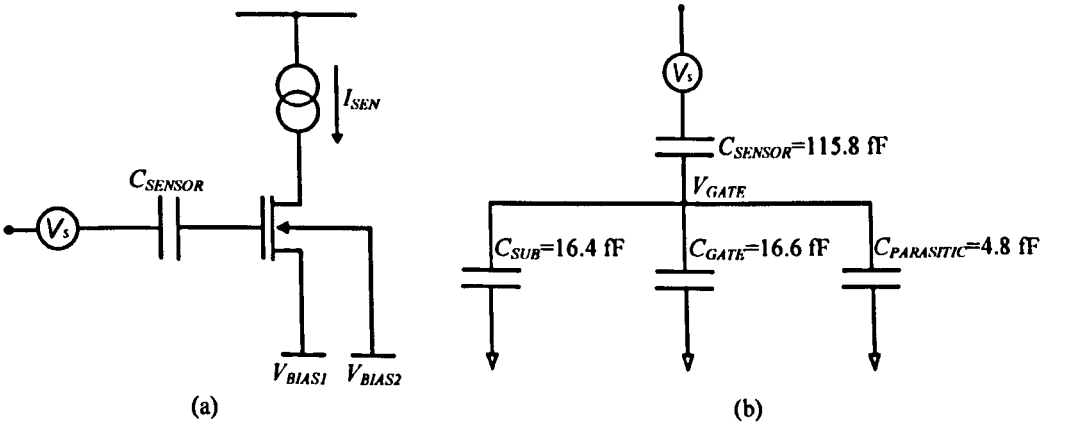

Figure 4.17: Capacitive equivalent circuit. (a) Circuit schematic of FET sensor. (b) Capacitive diagram with capacitance values.

It is possible to calculate these capacitance values as the dimensions of the capacitance plates and the materials between each layer are known. The length of the centre electrode will be extended to 114 μm, which is the extension of the pad structure following the design rules. The parasitic capacitance includes the track capacitance calculated from the track length (6 μm × 8 μm of metal 2, 5 μm × 6 μm of metal 1 and 9 μm × 1.5 μm of poly 1) and values from the AMS process parameter data sheet [4.12]. The parasitic resistance

is in the order of $\approx 10^{16}$ Ω. Transistor dimensions of 0.6 μm × 10 μm (channel length / width) have been used in these calculations.

$$V'_{GATE} = \frac{C_{SENSOR}}{C_{SUB} + C_{GATE} + C_{PARASITIC} + C_{SENSOR}} \times V_S \qquad (4\text{-}3)$$

Using these values, the gate voltage can be calculated as a ratio of the capacitance as shown in Equation (4-3) where V'_{GATE} is the gate voltage from only the sensing potential. From these values the loss of signal by capacitive coupling from the voltage source is calculated to be 24.6 %.

4.4.2 DC-offset cancellation circuit for offset removal

The primary function of the DC-offset cancellation circuit was to remove the DC baseline voltage of the sensor, allowing the small sensor response signal to be amplified. Given in Equation (4-4), the sensor output voltage (V_S) has a nominal value, commonly known as the baseline or offset voltage. This offset voltage typically sits at around 2.5 V (for CMOS, it is desirable to have an offset voltage in the middle of the operating voltage range to allow maximum positive and negative voltage variation).

$$V_S = I_{SEN} \times R_S \qquad (4\text{-}4)$$

where I_{SEN} is the constant current drive and R_S is the nominal resistance of the sensor.

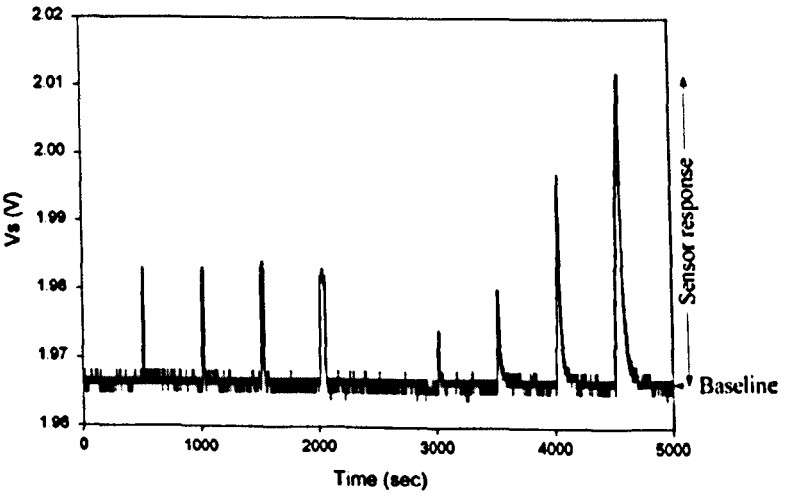

Figure 4.18: Example of a polymer sensor response to various pulses of ethanol and toluene vapour in air with baseline voltage.

When the sensor was exposed to a target analyte, the small response will override on top of the baseline voltage. It was not possible to amplify this signal significantly with a CMOS circuit as it only has a voltage range of 5 V. In order to enable higher amplification of the sensor response signal, the offset voltage has to be removed prior to amplification. Figure 4.18 shows an example of a sensor responding to 4 pulses of ethanol vapour followed by 4 pulses of toluene vapour of increasing durations (5, 10, 25, 50 s). The baseline voltage was about 1.965 V and any output voltage variation due to analyte exposure results in sensor response being added to the baseline. For example, the largest response to toluene vapour of 50 s duration results in the output voltage to change from the baseline of 1.965 V to 2.015 V. The signal variation is thus about 50 mV, however, due to the high baseline voltage of 1.965 V, it is not possible to amplify the signal beyond twice (2×) using CMOS circuitry.

Various options were studied, which including dynamic capacitive storage [4.13], digital storage [4.14] and floating gate [4.15]. However, due to the main constraint of having to hold the offset voltage for a long duration, a digital storage scheme was chosen. The block diagram of the circuit implementation of the DC-offset cancellation circuit is given in Figure 4.13. A 10-bit counter register, 10-bit DAC and comparator were used to implement the DC-offset cancellation circuit. An external clock was used to ramp up the counter which determines the output voltage of the DAC. This output voltage was compared to the sensor baseline voltage and the comparator's output will disable the counter when the DAC voltage exceeds the sensor baseline voltage. The Pspice simulation for the DC-offset cancellation circuit is shown in Figure 4.19.

Six signals of interest are shown here, three are digital and three are analogue signals. The sensor response (purple trace) has an offset (baseline) voltage of 1.5 V with a 100 mV first-order exponential response occurring between 200 μs and 320 μs. The three digital signals correspond to the comparator output (Comp), the externally driven clock (Clock) and the AND-gate output signal (AND_OP). For details about these tap points, refer to Figure 4.20. In this simulation, the external clock is pulsed at 1 MHz to slowly ramp up the DAC output voltage (DAC_OP, green trace) at 5 mV / μs (per step). While the DAC signal is being gradually increased, it is continuously compared to the sensor baseline voltage sitting at 1.5 V. The comparator output remains high, showing the sensor baseline is greater than the DAC voltage. When the DAC output exceeds the sensor baseline voltage (at 155 μs), the comparator output negates to low, thereby

disabling the clock signal connected to the counter via the AND-gate. As all counters are clocked simultaneously with each sensor sitting at a different offset voltage, the full 1024 cycles will be clocked. The signal conditioned output (red trace) was initially out of range due to the 10× amplification. However, as the difference signal falls within its operating range, it ramps up rapidly to stabilise at 2.5 V due to V_{ref} = 2.5 V. Upon completion of this initialisation phase, small sensor response signals can be amplified.

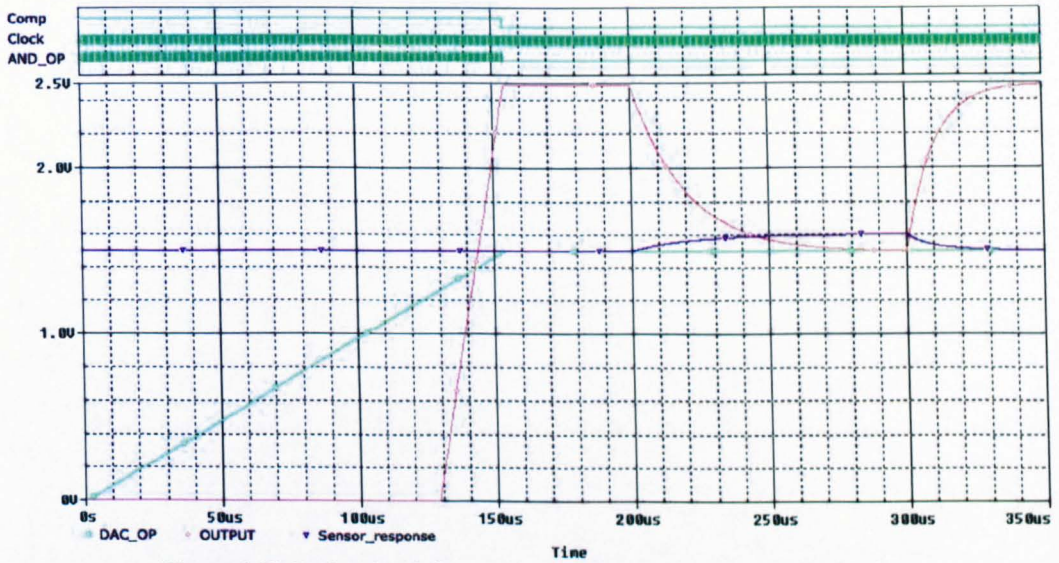

Figure 4.19: Pspice simulation result of the DC-offset cancellation circuit.

In the DC-offset cancellation mode, there was a need for an initialisation phase prior to the measurement phase. The initialisation phase is required to setup up the counter register such that it maintain the count of an equivalent DAC voltage that is slightly higher (± 1-bit error is only 5 mV) than the sensor baseline voltage. These voltages were higher than their corresponding sensor baseline voltages because as soon as the comparators detect that the DAC voltage exceed the baseline, they will be negated to disable the clock signal connected to increment the counter (counter halt). Since the counter is 10-bit, and as all sensor cells are clocked simultaneously, 1024 cycles are required to complete the offset calibration cycle. Using a 1 MHz clock, the offset calibration cycle only requires about 1 ms. Other operations required in the initialisation phase include setting up the current drive, sensor mode operation, sensor route and amplification selections.

4.4.3 Smart sensor cell and sensor array

For each sensor, there is a dedicated programmable current drive, DC-offset cancellation and amplification circuits. Detailed circuit implementation of each sensor cell is shown in Figure 4.20. The three programmable current drive selections are implemented using current mirror circuits. The values of these 3 selections are determined using external resistors and all 70 sensors are classified into 6 groups where their current selections are set to the same value. For simplicity, all the current selections are set to I = 1 μA, 10 μA and 100 μA as the sensor resistance can be controlled through the deposition process. A multiplexer (implemented using two switches) is used to select the sensor mode of operation either in resistive mode or FET mode. Depending upon the signal level, the sensor output can either be directly routed to the output pad or be amplified through the DC-offset cancellation circuits.

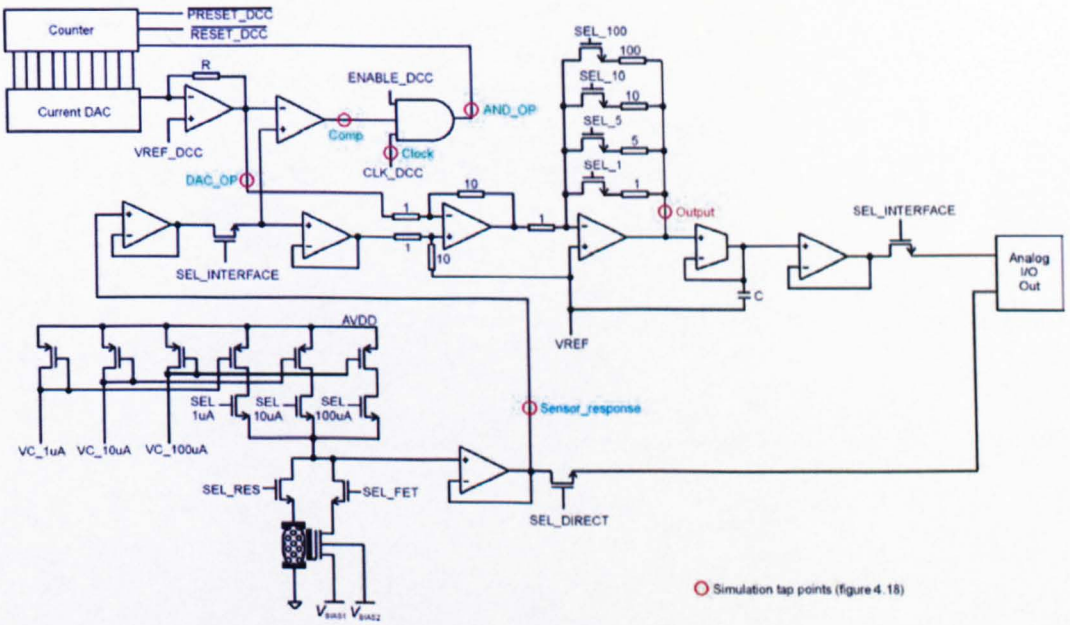

Figure 4.20: Detailed circuit implementation of a sensor cell.

On the DC-offset cancellation route (also referred as the select interface, SEL_INTERFACE), the nominal gain is ×10 on the differential amplifier. This signal can be further amplified by 5, 10 or 100 to obtain an effective gain of between 10 and 1000. A two-stage approach was necessary to avoid using large resistors necessary for producing high ratios needed to implement the gain amplifier. This reduced the need for large resistors, which is costly to implement in silicon design as it occupied a

considerable area. The signal was then filtered with a low pass filter set at a corner frequency of 1 kHz to remove high frequency noise. The sensor mode selection, current drive selection and gain selection are implemented using switches controlled with a D-latch. The D-latches hold the information for these selections and each sensor cell has 9 D-latches with their format shown in Figure 4.21.

SEL_RES	SEL_FET	SEL_1uA	SEL_10uA	SEL_100uA	SEL_GN_100	SEL_GN_10	SEL_GN_5	SEL_GN_1
D8 (MSB)	D7	D6	D5	D4	D3	D2	D1	D0 (LSB)

Figure 4.21: Data format for sensor cell operational parameters.

All D-latches within each cell, and across all cells are cascaded in series (row-by-row) to reduce the number of I/O's required to initialise the chip. In all, 630T (9 bits × 70 sensors) cycles are required to initialise the sensor mode, current drive and gain of all sensors. This requires only 630 μs with a 1 MHz clock. The complete initialisation phase requires only 1.63 ms (1 ms + 630 μs). However, in the unlikely event of having to modify a single selection, the complete cycle has to be re-programmed. The timing diagram for the complete initialisation phase is shown in Figure 4.22. Seven control signals are required to program the sensor array.

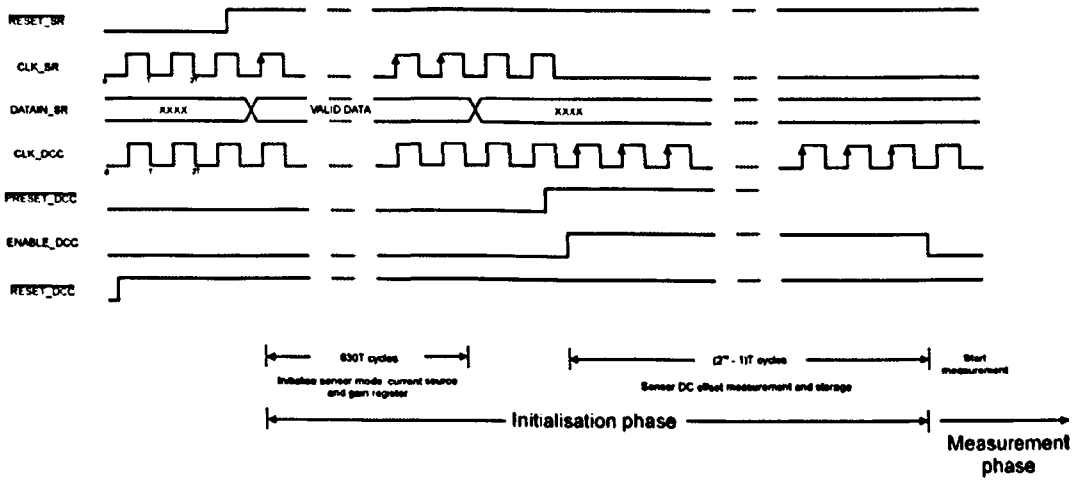

Figure 4.22: Timing diagram for initialisation phase of aVLSI sensor array.

The design of the sensor array was based on an incremental bottom-up approach where the basic components were designed and simulated before the upper level was built upon using these basic components. The final design for each sensor cell and the fabricated

footprint are shown in Figure 4.23(a) and (b) respectively. The size constraint limits each sensor cell to be less than 600 μm × 600 μm including the tracking (interconnects).

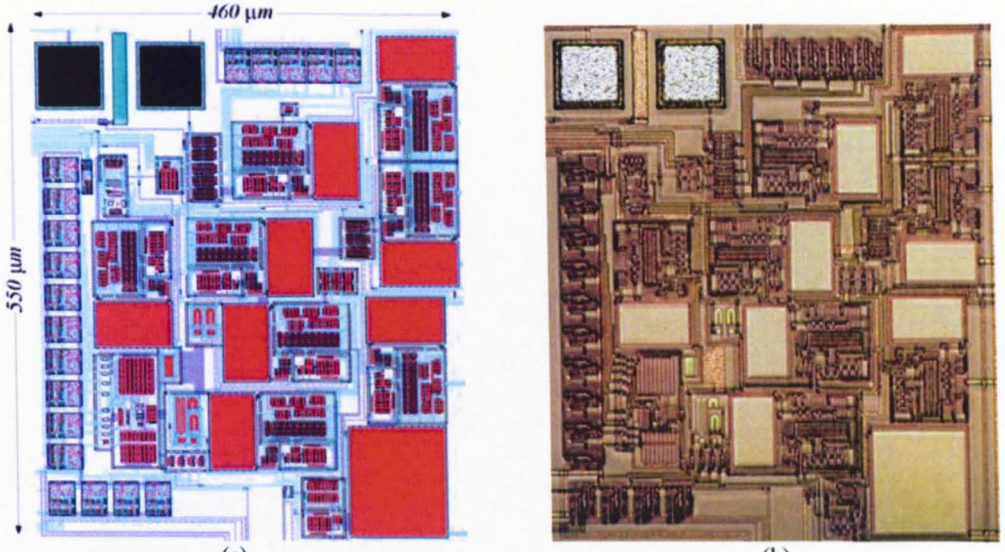

(a) (b)

Figure 4.23: Smart sensor cell. (a) Sensor cell design and dimension.
(b) Fabricated sensor cell footprint.

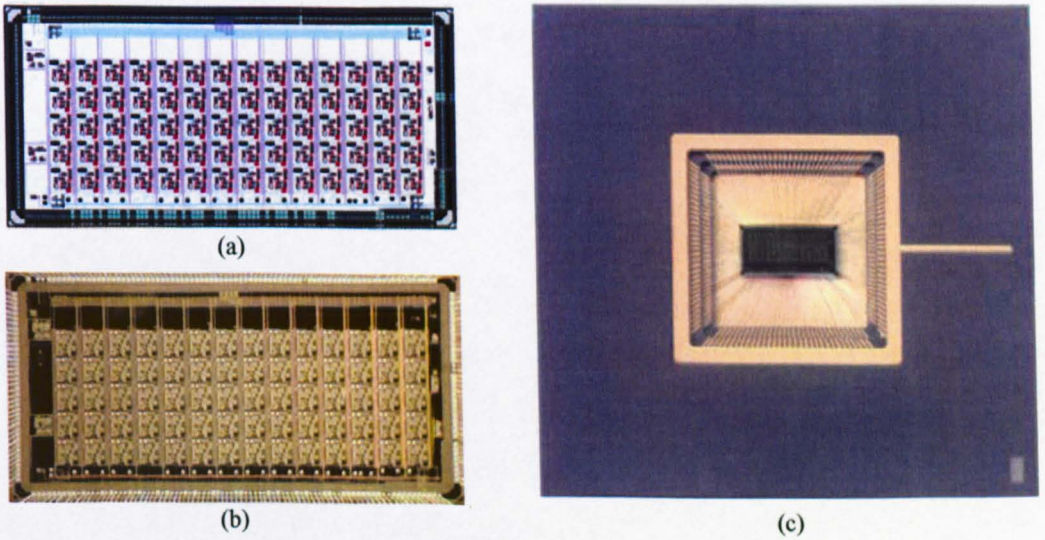

(a) (b) (c)

Figure 4.24: aVLSI sensor array. (a) Footprint of sensor array design. (b) Fabricated sensor array.
(c) Sensor array packaged onto PGA256 socket.

70 sensor cells were tiled into 5 rows of 14 elements. Together with the necessary I/Os pads, the circuit was routed to create the final footprint for the aVLSI chip (Figure

4.24(a)). Figure 4.24(b) shows the fabricated sensor array and Figure 4.24(c) shows the sensor array packaged onto the PGA256 socket.

4.4.4 aVLSI post-processing and polymers deposition

Although standard CMOS process provides numerous advantages for smart sensor array fabrication, there is an issue with the use of aluminium as the electrodes material. Due to the formation of aluminium oxide on the electrodes of the sensor, they have to be gold plated to ensure a stable contact between the sensing material and the aluminium.

The need for gold plating in the semiconductor industries is growing, especially in the area of flip chip bonding where aluminium is not desirable due to electromigration and brittle inter-metallic formation [4.16-4.17]. Although these processes are becoming standard, they are only available at wafer level. In-house gold plating process is an alternative to work at device level. A four steps electrode-less gold plating process described in [4.18] can be used. However, as these chemicals are only available in North America (Technic USA and Canada), other techniques have to be explored.

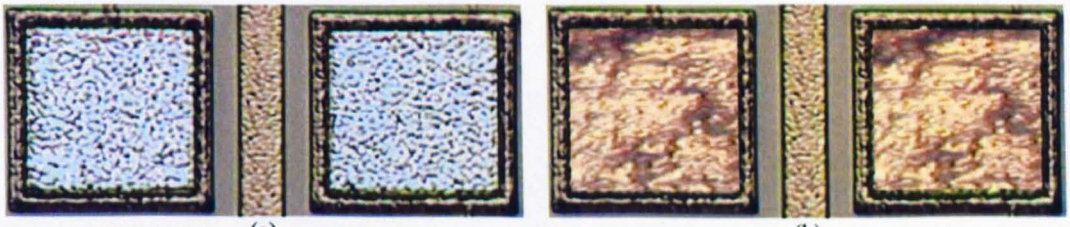

(a) (b)

Figure 4.25: Gold deposition of aluminium electrodes. (a) Aluminium electrodes before gold deposition. (b) Gold deposited electrodes.

Figure 4.25(a) shows the electrodes before the gold-plating process and Figure 4.25(b) shows the electrodes after the process. In this instance, a heat embossing technique using a wire bonder (Kulicke and Soffa Industries, USA) was employed. This technique required each electrode to be manually coated with several passes using a heated microtip. The result of this gold deposition is less precise with uneven surfaces. However, this does not affect the performance of the circuit.

The sensor array was then ready for polymer deposition. The same recipes given in Table 4.1 and 4.2 were used. The two deposition schemes produce two types of sensor arrays with two photographs of the deposited sensor array shown Figure 4.26. The

aVLSI-nose I sensor array was deposited with 5 different sensing materials, as shown in Figure 4.26(a). The aVLSI-nose II sensor array was deposited with 10 different sensing materials as shown in Figure 4.26(b).

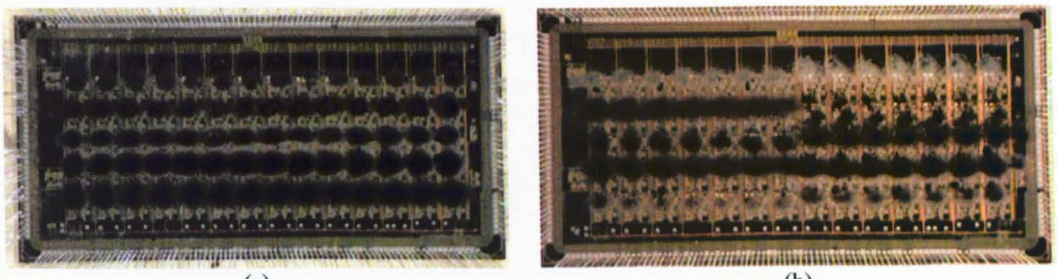

(a) (b)

Figure 4.26: Deposited aVLSI-nose sensor array. (a) aVLSI-nose I sensor array deposited with 5 different sensing materials. (b) aVLSI-nose II sensor array deposited with 10 different sensing materials.

A PCB similar to Figure 4.10 (not shown here) is used to monitor the resistance during the deposition process. The details about the deposition process are the same as described in Section 4.3.3.

4.5 Conclusions

In this chapter, the detailed fabrication processes for three different types of sensors have been discussed. They include discrete sensors, the hybrid-nose sensor array and the aVLSI-nose sensor array. In addition to the 5 types of sensing materials described in Chapter 2, five new recipes have been developed to increase the sensor diversity.

For the hybrid-nose sensor array, 80 resistive microsensors are built on a 10 mm × 10 mm silicon die to achieve miniaturisation. Two different hybrid-noses with 5 and 10 different types of sensing materials have also been fabricated.

In the aVLSI-nose chip, the integration of 70 sensors, drive and signal conditioning circuitries has been achieved. Both the resistive and FET mode of operating the sensor have been discussed. To improve small sensor response signal, a novel DC-offset cancellation circuit has been implemented for each sensor cell. The implementation and simulation of this circuit has been explained in detail, together with the appropriate timing protocols required to program it. Although circuit integration has been achieved, aluminium electrodes which are not compatible for sensing materials deposition requires additional post-processing. A heat-embossing technique is used here

to coat the electrodes with gold. Lastly, two different aVLSI-noses with 5 and 10 different types of sensing materials (as in hybrid-noses) were fabricated.

4.6 References

[4.1] B. Matthews, ***Effects of electrode configuration on polymer carbon-black composite chemical vapour sensor performance***, *MSc Thesis*, University of California, Los Angeles, 2002.

[4.2] B. Matthews, J. Li, S. Sunshine, L. Lerner, J.W. Judy, ***Effects of electrode configuration on polymer carbon-black composite chemical vapour sensor performance***, IEEE Sensor Journal, Vol. 2, pp. 160-168, 2002.

[4.3] SU-8 formulation 2-25 process guideline, http://www.microchem.com/products/pdf/SU8_2-25.pdf, MicroChem Corp., Rev. 2/02, 2002.

[4.4] J.A. Covington, ***CMOS and SOI CMOS FET-based gas sensors***, *PhD Thesis*, University of Warwick, Coventry, CV4 7AL, UK, 2001.

[4.5] B.J. Doleman, M. C. Lonergan, E.J. Severin, T.P. Vaid, N.S. Lewis, ***Quantitative study of the resolving power of arrays of carbon black-polymer composites in various vapour-sensing tasks***, Anal. Chem. 70, pp. 4177-4190, 1998.

[4.6] M.S. Freund, N.S. Lewis, ***A chemically diverse conducting polymer-based "electronic nose"***, Proc. Natl. Sci. USA, Vol. 92, pp. 2652-2656, 1995.

[4.7] Europractice IC service, http://www.europractice.imec.be/, 2001.

[4.8] Austria Mikro Systeme International AG, ***AMS 0.6 µm CMOS design rules***, Document 9931025, Revision 2.0, October 1998.

[4.9] E. Paris, S. Pawel, R. Herzer, T. Doll, P. Kornetzky, R.P. Gupta, G. Eranna, ***Low drift air-gap CMOS-FET gas sensor***, IEEE Sensor Conference, Toronto, 22-24 October, 2003.

[4.10] M. Burgmair, M. Zimmer, I. Eisele, ***Humidity and temperature compensation in work function gas sensor FETs***, Sensors and Actuators B 7054, pp. 1-5, 2003.

[4.11] J.A. Covington, J.W. Gardner, P.N. Bartlett, C.S. Toh, ***Conductive polymer gate FET devices for vapour sensing***, IEE Proc-Circuits Devices Syst., 151 (4), pp. 326-334 , 2004.

[4.12] Austria Mikro Systeme International AG, ***AMS 0.6 µm CMOS CUP process parameters***, Document 9933011, Revision B, October 1998.

[4.13] D.A. Johns, K. Martin, ***Analog integrated circuit design***, John Wiley and Sons, Inc, 1997.

[4.14] S. Franco, ***Design with operational amplifiers and analog integrated circuit***, 3rd edition, McGraw-Hill Book Company, USA, 1998.

[4.15] M. Ismail, T. Fiez, ***Analog VLSI signal and information processing***, McGraw-Hill International Editions, New York, 1994.

[4.16] A.J.G. Stradjord, S. Popelar, C. Jauernig, ***Interconnecting to aluminium and copper-based semiconductors (electroless-nickel.gold for solder bumping and wire bonding)***, Microelectronics Reliability 42, pp. 265-283, 2002.

[4.17] W.C. Yau, J.F. Gong, P. Chan, ***Al surface morphology effect on flip-chip solder bump shear strength***, Microelectronics Reliability 44, pp. 323-331, 2004.

[4.18] Electrodeless gold plating process, http://www2.ece.jhu.edu/faculty/andreou/495/2000/LabWork/Lab6.htm, Microfabrication Laboratory, School of Engineering, Johns Hopkins University, June 2004.

Chapter 5

Design and fabrication of microfluidic packages

5.1 Introduction

This chapter describes the design and fabrication of novel microfluidic packages using stereolithography. The basic design contains an embedded microchannel traversing through to the planar silicon microsensors upon assembly. Initial considerations included technologies such as silicon micromachining, deep Reactive Ion Etching (RIE), Lithography Galvonoforming Abforming (LIGA), as well as other high-aspect ratio microstructure and microchannel fabrication techniques using materials like SU-8 and benzocyclobutene (BCB). However, these techniques produce "2.5-D" planar structures which are not suitable to fabricated full 3-D structures. Moreover, these techniques are expensive for small to medium volume fabrication.

Introduced in the early 1980s by different teams in Europe, USA and Japan, microstereolithography (MSL) techniques have been established for the rapid prototyping of microcomponents. The main advantage of this technique over silicon micromachining, is that it is possible to fabricate full 3-D devices without the need for expensive sets of photo-masks or complex fabrication procedures.

In the scope of the project, three stereolithograhy (SL and MSL) systems have been used. Two systems were made available through our collaborators in USA and in UK, while the third system was installed at the Microsystems Laboratory at the University of Warwick. The Viper si2 SLA system (3D Systems, USA, installed at Georgia Institute of Technology, USA) was used to fabricate the first generation microfluidic packages. At the Rutherford Appleton Laboratory (Oxford, England), the Proform MSL machine (Proform AG, Switzerland) was used to fabricate variations on a simple microchannel package. At Warwick, as full access to the fabrication facilities is available, all remaining designs were fabricated using the Perfactory MSL system

(Envisiontec, Germany). The first two systems will be briefly described while the third system will be examined in detail.

5.2 Stereolithography and microstereolithograhy fabrication

Stereolithography and microstereolithography are 3-D fabrication processes based on photopolymerisation. Objects are fabricated by superimposing a large number of layers obtained by a light-induced and space-resolved polymerisation of a liquid resin into a solid polymer [5.1]. The process begins with the creation of the desired object in the form of a computer aided design (CAD) model. The 3-D model is sliced into a series of 2-D layers perpendicular to the direction of build. The basic building process is shown in Figure 5.1 [5.2].

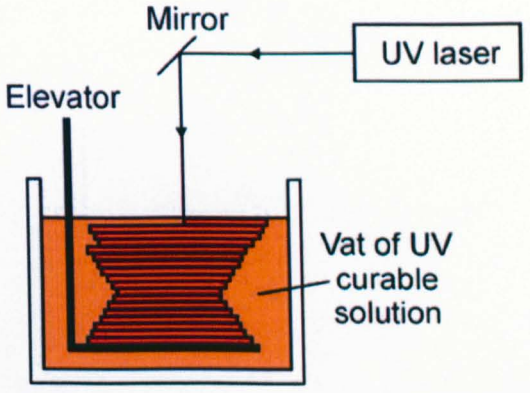

Figure 5.1: Basic principle of microstereolithography fabrication.

Most SL systems convert the layer information to trace out a path which is on the surface of each layer. The object is then lowered to allow resin to recoat over the previous layer. The next layer is then superimposed on top of the previous polymerised layer. This process continues until the whole object is built.

Photopolymerisation is a process that combines a number of monomers (small liquid molecules) to make them into polymers (larger solid molecules) with the aid of ultra-violet (UV) laser (or other form of light source). The curing depth and line-width of the photopolymerisation process are two most critical parameters that require careful control during the fabrication process. Figure 5.2 shows the theoretical intensity profiles of a UV beam (Gaussian) and the resultant spot cured within the resin [5.2]. The resin will only cure where the threshold (also known as the critical exposure) exceeds a desired

value. The Beer-Lambert law describes the fraction of light transmitted through an absorbing system. Other details pertaining to the photopolymerisation process is available in [5.2].

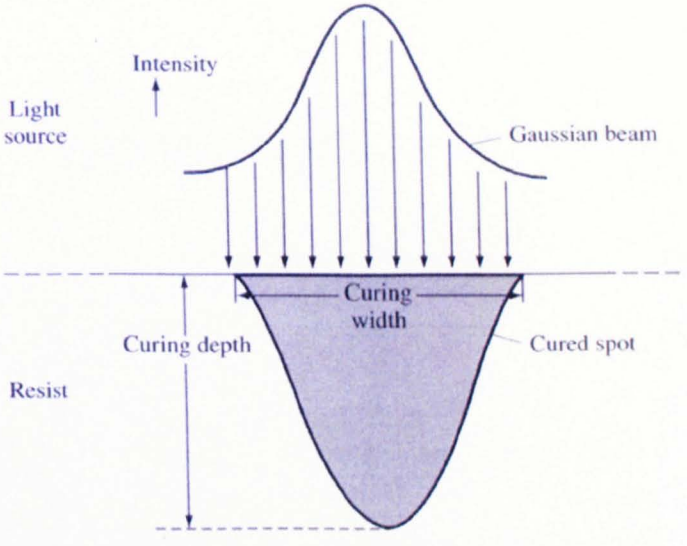

Figure 5.2: Theoretical intensity profile of the UV laser beam (approximately Gaussian) and the resultant spot cured within the resin.

Currently, two major classes of systems are available. They are classified as either the scanning (vector-by-vector) type or the projection (integral) type [5.3] depending on the photopolymerisation process. For scanning type MSL systems, a UV laser spot is scanned over the entire 2-D plane (similar to the scanning technique in analogue television (without interlacing)) using galvanometric mirrors. In such systems, curing is done in a spot-by-spot fashion on the 2-D plane (layer). Upon completion of a layer, the next adjacent layer is repeated. An example of such a system is shown in Figure 5.3.

Also known as the classical MSL system, these types of systems are the most common type of MSL systems developed today [5.3]. Significant improvements have been made on these systems of which some of the most notable include the integrated harden (IH) polymer SL process, the mass-IH system, the super-IH and the two-proton MSL system. The IH system was developed by Ikuta *et al.* [5.4] to overcome the beam-focusing problems found in classical MSL system. The mass-IH system was also proposed by Ikuta [5.5] in 1996. This system increases the throughput of the classical MSL system by utilising an array of fibre-optic multi-beam scanning.

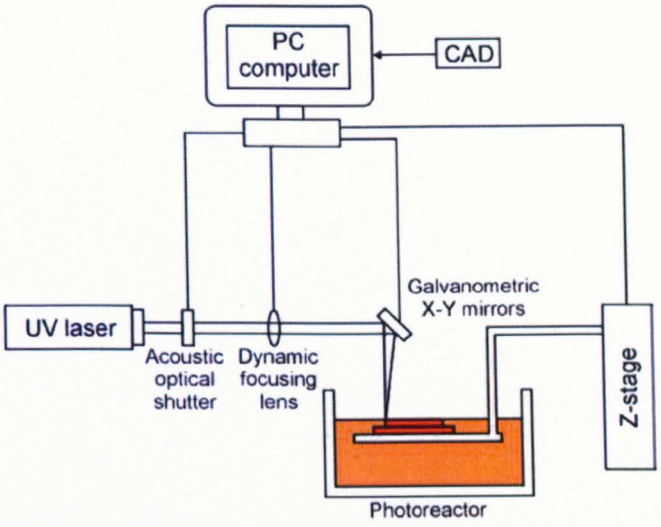

Figure 5.3: Classical MSL system using the vector-by-vector scanning process.

In 1998, Ikuta [5.6] proposed yet another improvement to his predecessor system known as the super-IH process. In all previous systems, a Z-stage is required to shift the partially built object downwards so that a new layer of uncured resin will coat the previous polymerised structure. Such a technique reduces the fabrication resolution due to the surface tension of the liquid monomer. To address this problem, the super-IH process was developed to cure the monomer at a specific point in 3-D space by focusing a laser beam into a liquid UV-curable monomer. An added advantage of such a system is that the build is freely movable without the need for support structure. Two examples of such objects are given in Figure 5.4 [5.7].

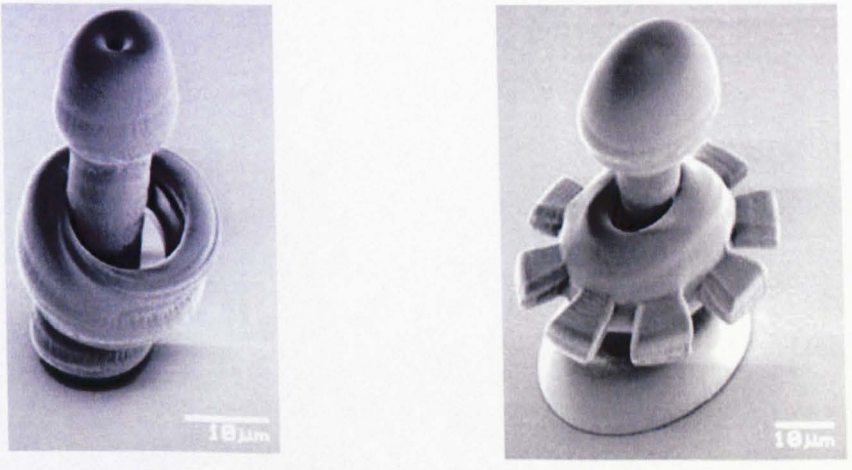

(a) (b)

Figure 5.4: Freely movable objects fabricated by super-IH process. (a) Micro ring rotator (Diameter: 24 μm, fabrication time: 3 min). (b) Micro ring rotator (Diameter: 47 μm, fabrication time: 20 min).

To further improve the resolution of the conventional MSL process, Maruo and Kawata [5.8] introduced the two-proton MSL process. The main feature in the two-photon MSL system is the requirement for two-photon absorption to occur before the polymerisation process can be initiated. The lateral resolution of such a MSL system is only 0.62 μm while the depth resolution is only 2.2 μm [5.3]. This is significantly better than any other type of MSL systems. A summary of the various MSL systems available is given in [5.1] and updated in Table 5.1.

Table 5.1: Major SL and MSL processes developed between 1993 and 2004.

Research team	Principle	Special feature	Build Envelope	Resolution	References
Ikuta *et al* 1993	Scanning	Constraint surface	10 × 10 × 10 mm	8-60 μm	[5.4]
Takagi *et al* 1993	Scanning	Constraint surface	20 × 20 × 20 mm	5 × 5 × 3 μm	[5.9]
Zissi *et al* 1994	Scanning	Free surface	Not reported	30 × 30 × 20 μm	[5.10]
Zhang *et al* 1998	Scanning	Free surface	Not reported	Spot is 1-2 μm	[5.11]
Bertsch *et al* 1993	Projection	LCD, laser 515 nm	1.3 × 1.3 × 10 mm	5 × 5 × 5 μm	[5.12]
Gőtzen *et al* 1996	Not reported	Used commercially	50 × 50 × 50 mm	10 × 10 × 1 μm	[5.13]
Chatwin *et al* 1998	Projection	LCD, laser 315.5 nm	Not reported	Not reported	[5.14]
Loubère *et al* 1998	Projection	LCD, lamp (visible)	3 × 2.4 mm (x-y)	5 × 5 × 10 μm	[5.15]
Bertsch *et al* 1998	Projection	DMD, lamp (visible)	6 × 8 × 15 mm	5 × 5 × 5 μm	[5.16]
Bertsch *et al* 2000	Projection	LCD, lamp (UV)	10 × 8 × 20 mm	10 × 10 × 10 μm	[5.17]
Maruo *et al* 1996	Under surface	2-photon process	A few 100 μm	Submicrometer	[5.8]
Ikuta *et al* 1998	Under surface	1-photon process	A few 100 μm	Submicrometer	[5.6]
Kawata *et al* 2001	Under surface	2-photon process	A few 10 μm	150 nm	[5.18]
Devaux *et al* 2001	Projection	Wavelength change	3 × 3 mm (x-y)	20 × 20 × 20 μm	[5.19]
Viper si2 2001	Scanning	Zephyr blade	125 × 125 × 250 mm	50 × 50 × 50 μm	[5.20]
Perfactory Mini 2002	Projection	Back projection	42 × 34 × 230 mm	32 × 32 × 25 μm	[5.21]

An important point to note is that although the resolution was gradually improved, the build envelope is reduced at the same rate because the building time increases as the resolution falls, making it costly. This implies that the higher resolutions can only be achieved for very small objects. However, in this case and many other potential applications, it is desirable to fabricate large parts with small feature size.

The other type of MSL system is known as the projection-based type MSL system. For this type of system, the entire 2-D plane is cured simultaneously using a dynamic mask projection system (such as the Digital Micromirror Device (DMD^{TM}) [5.22] or Liquid Crystal Display (LCD)). The most obvious advantage of this technique is the increase in throughput. However, there is a compromise between build resolution and build envelope. This limitation is inherited from the resolution of the DMD that will be discussed in detail in the next section.

5.3 Stereolithography and microstereolithography systems

Three systems used for micropackage fabrication as stated earlier will be described in this section. 3-D Systems (USA) produced the first commercial SL system in 1987 [5.3] with the Viper si2 system (Figure 5.5(a)) made available in 2001 [5.20]. The resolution for the Viper system in the high-resolution (HI-RES) mode of operation is 75 μm × 75 μm × 50 μm (X, Y, Z) with a 125 × 125 × 250 mm^3 build envelope. The transparent resin used is SL 5510 (Renshape, Switzerland) epoxy-based acrylate resin (details are available in Appendix C). The machine setup is similar to those of the classical SL system (shown in Figure 5.3). The main distinction of this system lies in the recoating mechanism.

(a) (b)

Figure 5.5: Stereolithography and microstereolithography systems. (a) Viper si2 SLA system from 3D Systems. (b) Proform MSL machine from Proform AG.

The Viper system employs a zephyr blade to level a freshly recoated resin on the top surface. This technique provides better layer thickness control compared to the "dipping" mechanism used in other SL systems. Two such parts fabricated by the Viper system in collaboration with Georgia Institute of Technology, USA are shown in Figure 5.6. The building time for these parts is about 1 hour. The layer building time worked out to be approximately 20-25 s / layer on average for these parts.

The Proform MSL system from Proform AG (Switzerland) is the result of research output from the Institute of Microsystems at the Swiss Federal Institute of Technology (EPFL, Switzerland) [5.17]. This system is based on the projection technique

that employs Digital Light Processing (DLP) technology [5.22]. The build envelope was $10.24 \times 7.68 \times 20$ mm^3, which is determined by the DMD with 1024×768 micromirrors.

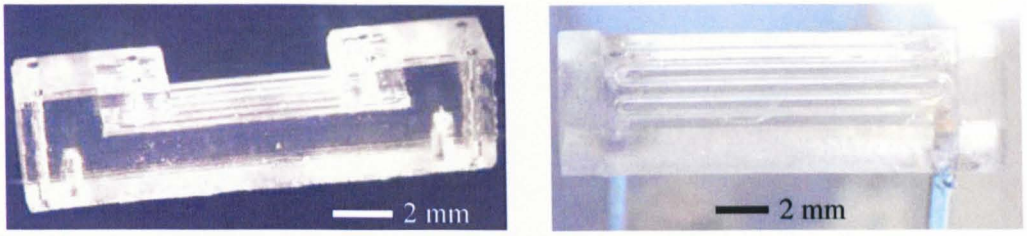

(a) (b)

Figure 5.6: Microchannel package fabricated using Viper si2 system. (a) Fabricated MSL101. (b) Fabricated MSL102.

It has a lateral resolution (X, Y) of 10 μm × 10 μm. The depth resolution (Z) is also 10 μm controlled via a Z-translation stage driven by a stepper motor. This system employs an epoxy-based acrylate resin (SL 5220, Renshape, Switzerland, details available in Appendix C) and uses the "dipping technique" to recoat the top layer with fresh resin prior to exposure.

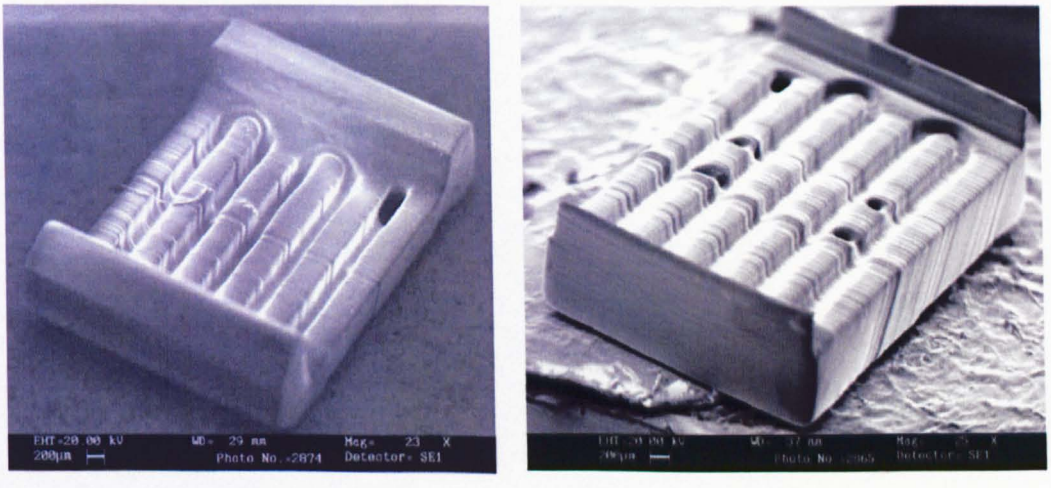

(a) (b)

Figure 5.7: Microchannel package fabricated using Proform MSL system. (a) Part 1 of MSL102. (b) Part 2 of MSL102.

A photograph of the Proform MSL system is shown in Figure 5.5(b). Due to the size of the build envelope of this MSL system, it was not possible to build the whole package in a single build cycle. Hence, the package was sliced into two parts, which had to be

assembled together prior to curing. Two of the fabricated parts are shown in Figure 5.7. The exposure time (7 s) in this system is consistent with other projection MSL systems, since each layer is cured simultaneously irrespective of the layer pattern. As the layer thickness is only 10 μm, it takes a long time (~ 3 hours) to fabricate the same package.

The fabricated packages showed considerable amount of geometrical errors, possibly due to the lack of support structures, and jitter between layers. It was also difficult to assemble them upon build without any post-processing. In addition, as only limited access to the machine is granted, it was decided to focus on the in-house systems.

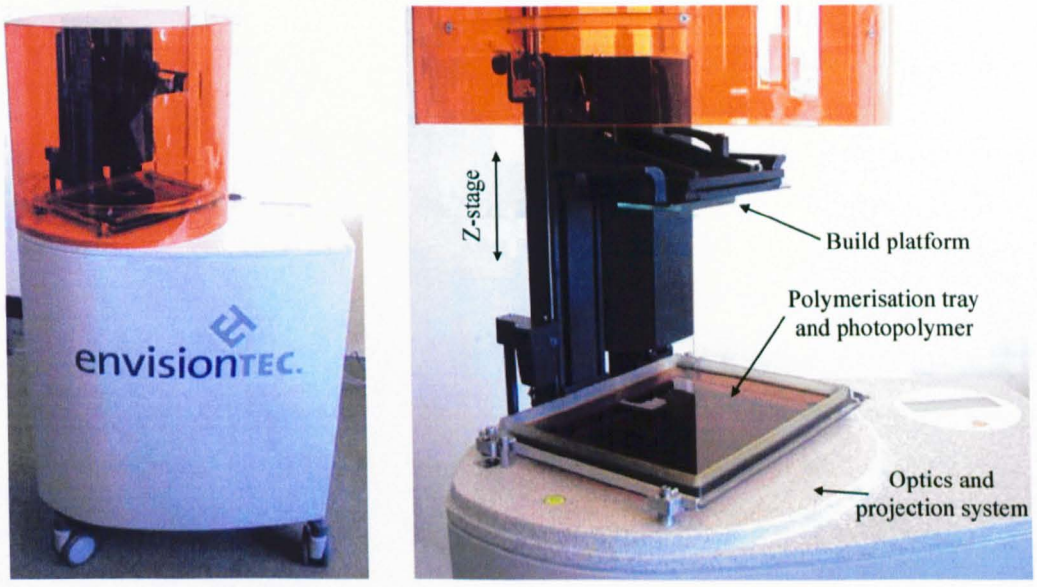

(a) (b)

Figure 5.8: Photographs of Perfactory MSL system. (a) Perfactory MSL system. (b) Exploded view of the MSL system.

The MSL systems available at Warwick were the Perfactory MSL systems from EnvisionTec (Germany) [5.21]. Two systems with different resolutions and configurations were available. The first system was a standard version with 93 × 93 × 50 μm^3 (X, Y, Z) resolution while the second system was a mini version with 32.8 × 32.8 × 25 μm^3 resolution. The build envelope was 120 × 96 × 230 mm^3 for the standard version and 41.98 × 33.59 × 230 mm^3 for the mini version. This directly corresponds to the DMD resolution of 1280 × 1024 micromirrors. Based on the back-projection technique, the system provides better layer recoating. As this technique 'sandwich' the fresh resin for new layer between the polymerised object and the base plate, the layer thickness is in theory consistent and flat (because it is being anchored to the base plate),

hence resulting in better build. Figure 5.8 shows various pictorial views of a Perfactory MSL system.

In addition to the uniqueness of the recoating mechanism, the Perfactory system also featured an integrated embedded system running Linux Operating System (OS). This removed the need for any dedicated PC (or in a form of PC plug-in card) required to run the system (as used in the previous two systems), thus further reducing the cost of the system. Any computer connected to the network (with Perfactory firmware installed) can be used to download the job file (via a Local Area Network (LAN) connection) to the Perfactory system.

5.3.1 System setup

The Perfactory MSL system setup is similar to any standard projection-based MSL system. The hardware consists of a visible light source, a dynamic mask modulator (implemented using DMD), a shutter with focusing optics, a photoreactor platform, a Z-stage for moving the base (build platform) and an embedded PC. For each layer, the DMD modulates the light such that the layer mask pattern appears under the resin. The DMD does this by flipping the mirrors toward or away from the light source. Each layer mask is stored as a mono picture file with each pixel corresponding to a micromirror state (ON/OFF), determined by whether it is black (OFF) or white (ON).

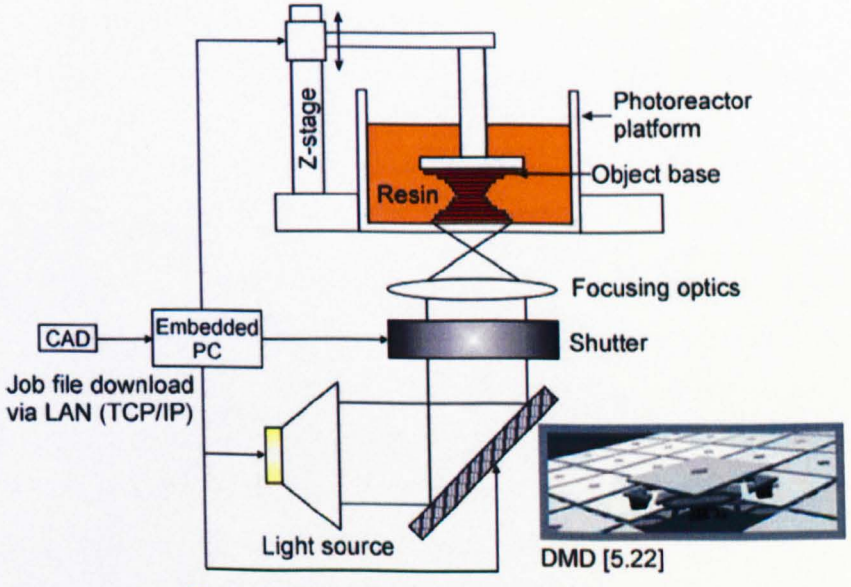

Figure 5.9: Setup of the Perfactory MSL system.

Upon exposure for a pre-determined amount of time (known as the exposure time), the pattern corresponding to the mask will be cured. Once a layer is cured, the Z-stage (driven by a lead screw coupled to a stepper motor) moves upwards by a layer thickness step. As the surface of the photoreactor is coated with a silicone-based material with lower coefficient of friction when compared to the object base, the cured layer will be attached to the object base instead. Figure 5.9 shows the setup of the Perfactory MSL system.

Similar to any other projection based MSL system, the building time is constant. For the standard setup, the building time is 15 mm per hour on 50 μm layer (12 s / layer). For the mini version, the building time is 9 mm per hour on 25 μm layer (10 s / layer).

Table 5.2: Resolution and build envelope of the two variant of Perfactory MSL systems.

System variant	Perfactory Standard SXGA (zoom)	Perfactory Mini SXGA (Multi Lens)	
Resolution	SXGA: 1280 × 1024 pixel	SXGA: 1280 × 1024 pixel	
Build envelope	190 × 152 × 230 mm to	Lensf = 60 mm	Lensf = 85 mm
XYZ	120 × 96 × 230 mm	77 × 61 × 230 mm	41 × 33 × 230 mm
Pixel size XY	148 μm pixel to 93 μm pixel	60 μm pixel	32 μm pixel
Layer thickness Z	50 μm to 150 μm	25 μm to 50 μm	

For each system setup, it is possible to vary the build envelope by compromising the pixel resolution. A larger build envelope allows larger objects to be built. However, as the DMD has a fixed number of micromirrors, this can only be achieved by extending the size of coverage for each pixel. Table 5.2 shows the resolution and build envelope of these two systems [5.21].

5.3.2 Support structures generation

For complex objects with protruding parts, support structures are required to hold these parts during the build. In other cases, it is desirable to preserve certain surface features or to build the object in a certain orientation. All of these techniques require some means of attaching the object to the base of the platform to support the weight of the partially built object. For example as shown in Figure 5.10(a), the inverted "T" structure requires support on its wings during the build. Consider the scenario without the support structure, as the object is progressively built, only the vertical portion is fabricated. Upon curing the first horizontal layer, the object base will move upwards, allowing fresh resin to flow

in. Due to the mechanical strength of this thin layer and the small anchorage connecting to the only support (vertical part of the "T"), the recoating process may deform or shift the position of the cured layers. In addition, bowing is likely to occur even if the build is successful.

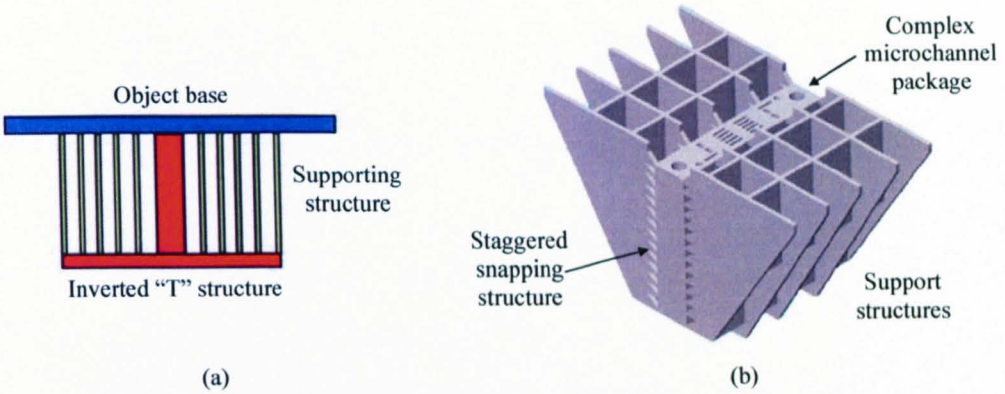

Figure 5.10: Support structure generation. (a) Support structure for inverted "T" object. (b) Support structure for complex microchannel package.

Figure 5.10(b) shows a complex microchannel package with the support structures. The base is at the top with the object slightly dipped below this level to retain its sharp top surface features. With this support structure, the object can be fabricated to preserve the feature on the top and bottom surfaces of the object. The build orientation of the package is such that the microchannels are vertical to allow draining of uncured resin inside the microchannel while it is being built progressively upwards. The support structure attached to the package has a staggered snapping structure so that they can be easily removed after the build.

Unlike some advanced MSL systems, which are capable of building freely movable microparts (discussed in Section 5.2), it is necessary to incorporate support structures into objects requiring freely movable parts. Figure 5.11 shows two one-way micro check valves with (a) a rectangular shaped flap, and (b) a cone shaped flap. In the normal mode of operation, the flow pressure from the inlet will lift the flap upwards, allowing the air or fluid to flow towards the outlet. However, if the flow is reversed due to the pressure applied on the flap, the inlet ("outlet" as the flow is reversed) will be blocked by the flap. As it is not possible to build an object with freely movable parts, support structures are required to hold the flap during the build. Upon completion, a

microneedle is inserted to remove the support structure, hence releasing the movable flap.

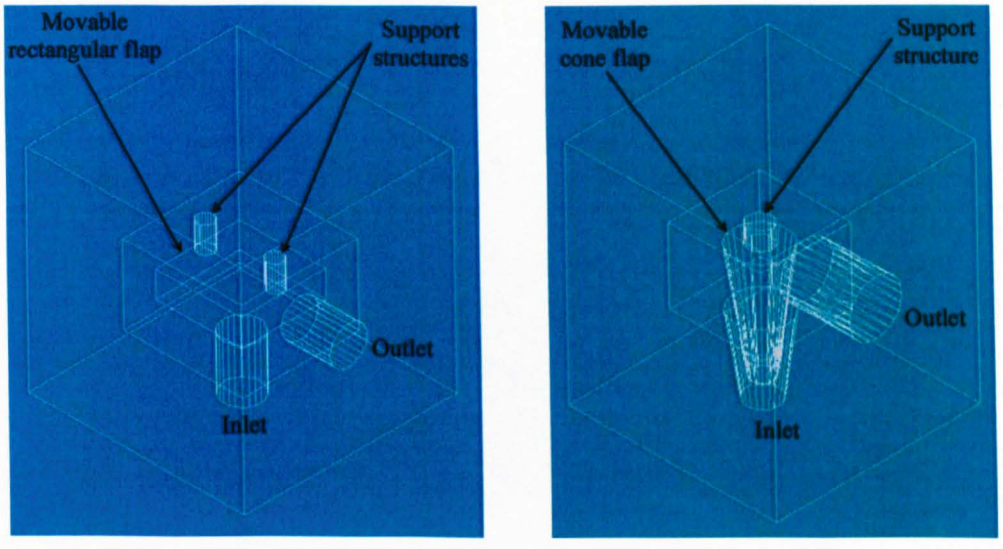

(a) (b)

Figure 5.11: Support structure for fabrication of objects with freely movable parts. (a) Micro check valve with freely movable rectangular flap. (b) Micro check valve with freely movable cone flap.

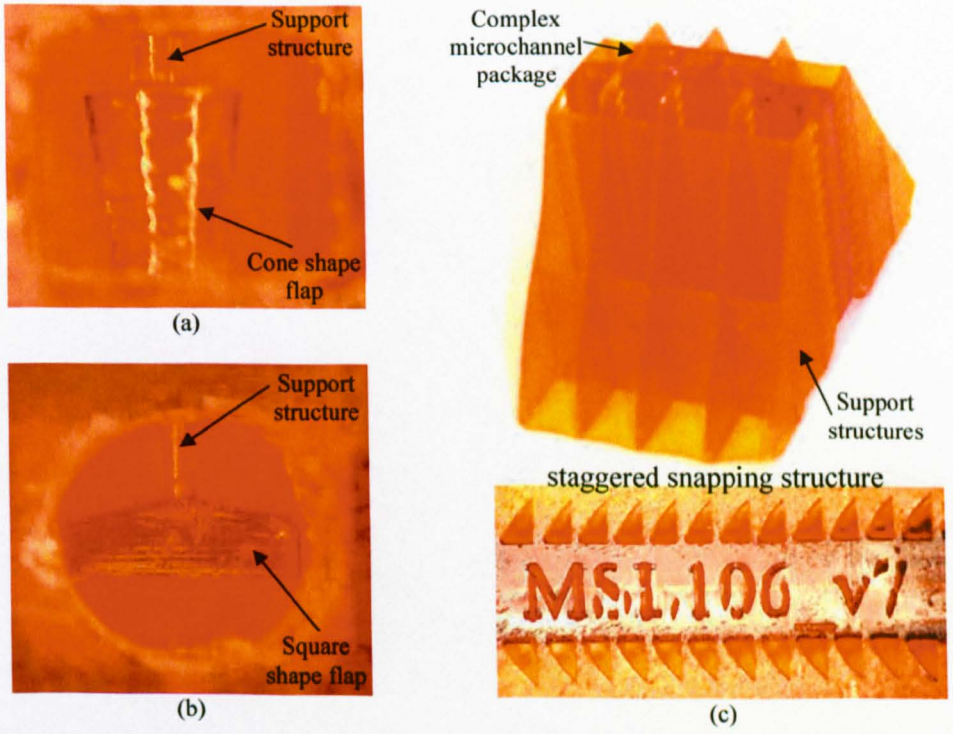

(a) (b) (c)

Figure 5.12: Fabricated objects with supporting structure. (a) Micro check valve with freely movable 'coned-shape' flap. (b) Micro check valve with freely movable 'square-shape' flap. (c) Complex microchannel package with support.

The Magic 9.01 (Materialise N.V., USA) [5.23] software is capable of generating support structures. However, it can only generate support structures vertically as shown in Figure 5.10(a). Custom-designed support structures are required to attach to the side-wall of the object as shown in Figure 5.10(b). Figure 5.12 shows the fabricated support structures discussed above. Figure 5.12(a) and (b) shows the support structure for the cone and rectangular flap respectively. Figure 5.12(c) shows the support structure for a complex microchannel package to enable the microchannels to run vertically; at the same time the top and bottom surfaces of the object are preserved. Figure 5.12(d) shows the sections of the support structures adjoining the package are designed with a staggered snapping structure to allow the support structure to be removed easily after the build.

5.3.3 Design and fabrication process

The design process begins with the simulation of the different geometrical designs that were conceptualised at the beginning of the project. Starting with a simple design, it was re-iterated to improve the system responses based on the simulation results, manufacturability and ease of integration. The simulation results have been covered in Chapter 3. The geometrical models from the simulation software (FEMLAB) can be exported as a CAD model file (*DXF*).

The Perfactory system accepts object data files in the form of "*STL*" (stereolithography) file. This file format is widely used in most rapid prototyping applications, especially among stereolithography systems. Most CAD softwares have an export feature to allow conversion from their native format into "*STL*". Here the AutoCAD 2002 is used to modify the simulated geometry model of the object before it is converted into *STL* format.

The object file in *STL* format is then analysed using Magic software for any triangulation error. The *STL* file stores the object information in the form of triangulated facets of all surfaces of the object. Depending upon the original software used to create the *STL* file, it may contain triangulation errors that requires repair. These geometrical flaws exist in *STL* file because many commercial tessellation algorithms used by CAD vendors are not robust [5.24]. In addition, the Magic software can also be used to calculate the volume of resin required and perform any mechanical analysis of the object mechanical properties using the parameters of the cured resin.

Upon object positioning and orientation adjustment, as well as support structure generation and triangulation error repair, the object in the form of a *STL* file is ready to build. The user selects the size of the building envelope (depending on the object size) and the layer thickness using the Perfactory host software. The object is then sliced into a number of layers depending on the object thickness. For example, a microchannel package with a thickness of 4 mm will be sliced into 160 layers if the selected layer thickness is 25 μm. Figure 5.13 shows 4 masks for a complex microchannel package. The size of each mask layer is 1280 × 1024 (XY build envelope) with the white pixels (shown in Figure 5.13(a)) defining the object shape. The remaining 3 masks show different cross-sections of the object with vertical microchannels. Obviously the orientation of object placement has an important impact on the building time. Consider the object where the bounding envelope for the object shown in Figure 5.13 is 40 mm (length) × 20 mm (width) × 4 mm (depth). When the object is built on its depth (4 mm), it will require 160 layers. However if the same object is built on its width, there will be 800 layers. This will takes 5 times longer to build when compared to the previous build orientation.

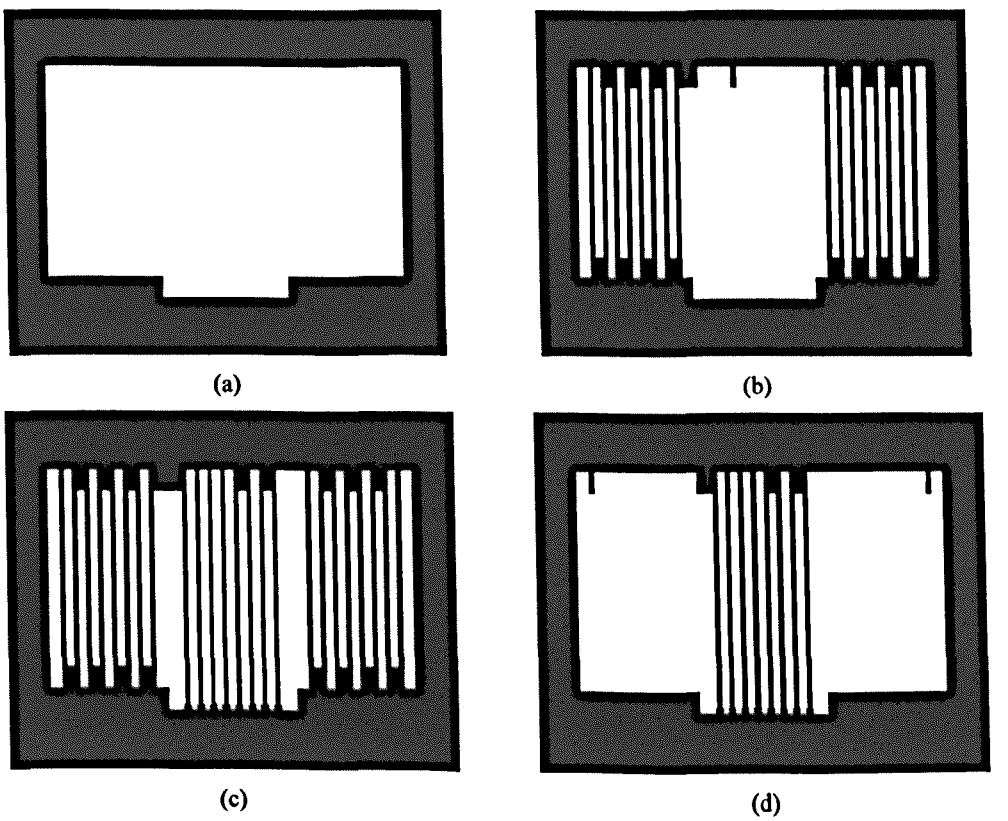

Figure 5.13: Four layer masks for complex microchannel package.
(a) Base layer. (b) Middle layer 1. (c) Middle layer 2. (d) Middle layer 3.

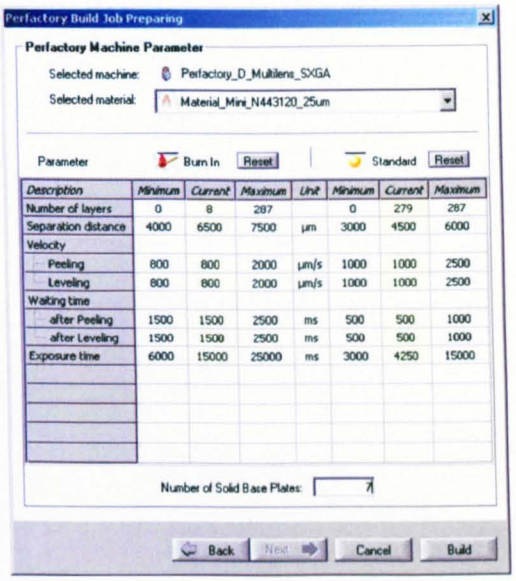

Figure 5.14: Perfactory machine parameter.

Once the object is sliced, the host software transfers the sliced layer masks together with a configuration file to the MSL machine for the build. The configuration file consists of the following information as shown in Figure 5.14. The important parameter is the exposure time of each layer; this is related to the resin property and will be discussed in Section 5.3.4.

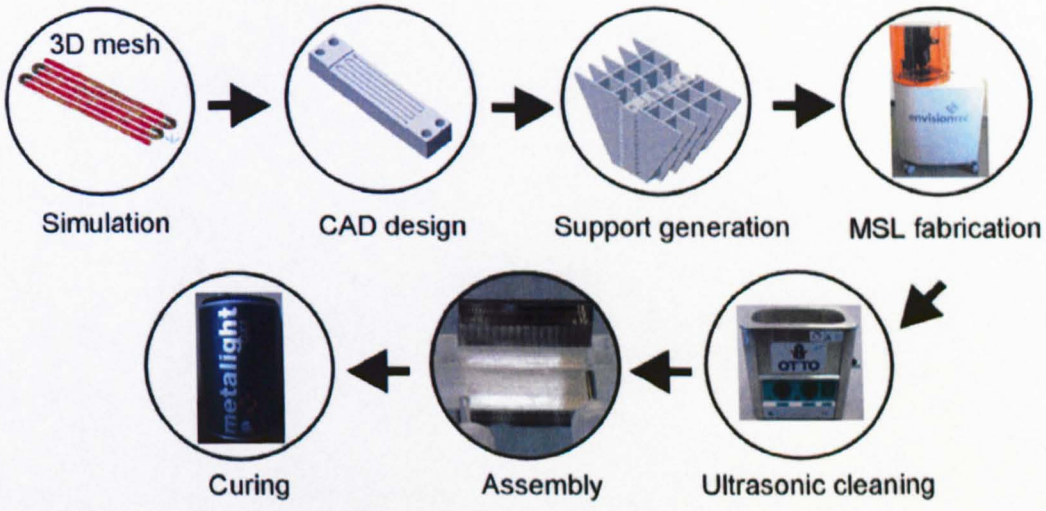

Figure 5.15: 7-step MSL fabrication process.

Upon completion, the object will be attached to the base platform. It has to be removed and cleaned to remove uncured resin on its surfaces and microchannels. For smaller

microchannels, a microneedle tool is used to remove any excess resin inside the microchannel. The object is placed in a breaker containing isopropanol before being immersed in an ultrasonic bath (Otto model 300, Italy). After ultrasonic cleaning, the object is dried with compressed air, assembled with the microsensor array and cured using a light box (Metalight QX1, Primotec, Germany) for 5 minutes. This 7-step MSL fabrication process is summarised in Figure 5.15.

5.3.4 Resin properties

The resin for the Perfactory MSL system is an orange methacrylate (Pentaerytgritoltri/tetraacrylate, details available in Appendix C). Unlike other MSL systems requiring expensive UV laser source, this type of resin only requires high-pressure mercury vapour lamp. The curing time is dependent on the layer thickness as shown in Figure 5.16.

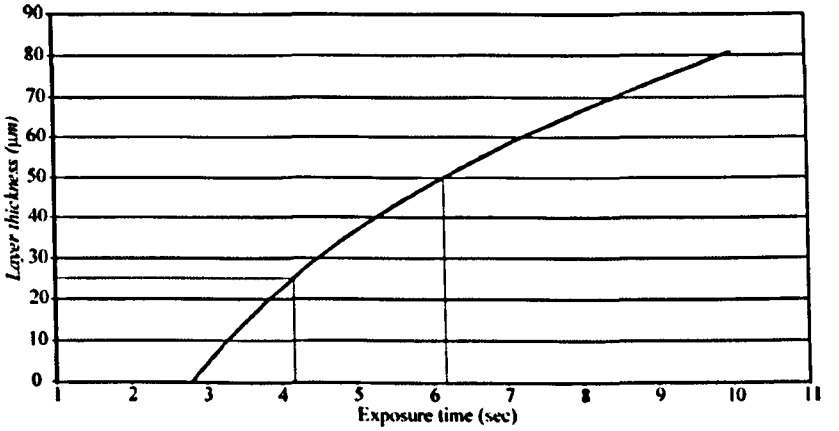

Figure 5.16: Exposure time versus layer thickness for Perfactory Mini material at 400 mW dm^{-2}.

As shown in Figure 5.16 [5.21], the exposure time for a 25 µm layer is about 4.25 s. For a 50 µm layer, the exposure time has to be increased to 6.25 s. Mechanical properties of the cured resin is discussed in Section 5.5.1.

5.4 Micropackages design and fabrication

The applications of STL and MSL systems for the fabrication of microcomponents have evolved at a rapid pace in recent years. Most researchers focused on creating miniature fluidic transport channels and the fabrication of microparts [5.1-5.19], but little attempt

has been made to investigate the possible union of this technology with silicon microfabrication [5.25-5.26]. Here several issues are investigated simultaneously through the use of this fabrication technique (although some new issues are generated). Firstly, it was identified that the prime advantage of using this technique to build a long microchannel is the possibility of creating multi-layers of microchannel within a small 3-D structure. As opposed to planar fabrication techniques, STL/MSL fabrication allows 'further compression' due to its ability to fabricate multiple-planar structures. This technique is even more favourable considering the fact that it does not require complex fabrication procedures and expensive masks. In addition, the object is simply created as a 3-D model file using suitable software.

The next challenge is the need to have access to various locations along the microchannel for generating spatio-temporal signals. This added dimension of complication arises due to the desire to integrate the microchannel package with a microsensor array (as opposed to discrete sensors that can be placed anywhere), fabricated using semiconductor technology that resulted in planar sensor array implementation (Chapter 4). Other issues (such as alignment and leakage) that arise when integrating the 3-D microchannel package with the silicon microsensor array have to be resolved. Details regarding these issues will be covered in Chapter 6.

The microchannel package is a 3-D solid structure with an embedded microchannel that is used to deliver test analyte to the microsensor array. The two microsensor arrays have different numbers of sensors but their sensor placements are the same, allowing the same microchannel package to be used for both arrays. Two main classes of packages were designed and fabricated; they are the simple type with single continuous microchannel and the complex type with multiple microchannel segments. These are discussed in Section 5.4.1 and 5.4.2, respectively.

5.4.1 Simple micropackages with single continuous microchannel

The simple microchannel package contains a 5 cm long microchannel with a cross-section of 200 μm × 200 μm. It has an inlet and outlet connected to the microchannel using micropipe connectors as shown in Figure 5.17(c). The microchannel sits on one side of the package while the inlet and outlet are on the opposite sides. The two designs for the simple micropackage are shown in Figure 5.17(a) and (b).

Figure 5.17(a) shows the version of the simple micropackage with the sensor array holder while Figure 5.17(b) shows the version without the microsensor array holder. The holder is a slot for the microsensor array to slide in with some holes at the bottom pushing the microsensor array towards the microchannel for a good seal. On the top-side, there is an inlet and outlet improvised with simple holes. These holes (as shown in Figure 5.17(c)) have the same size as the outer diameter of the micropipe connector. Micropipe connectors will be inserted into inlet/outlet holes for reconfigurable interface to the mass flow system. This is the simplest possible design since it uses a minimum channel length to connect all the sensors together.

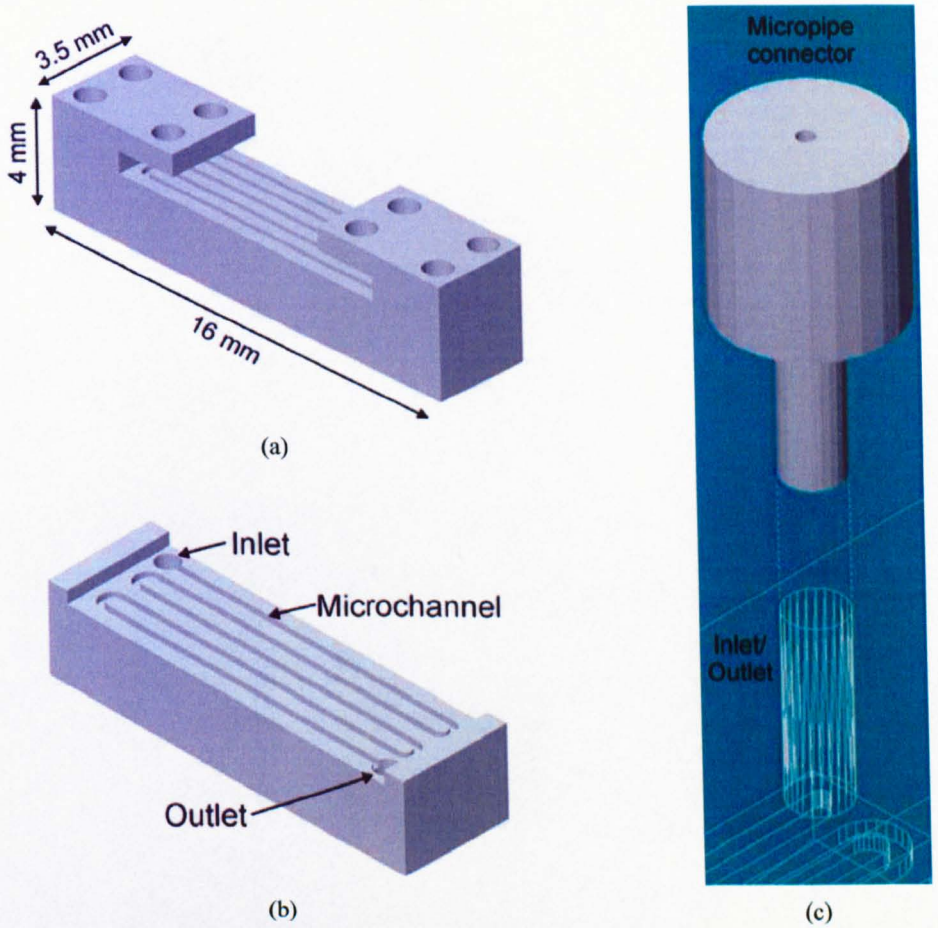

Figure 5.17: Simple microchannel package designs and assembly. (a) Simple microchannel package design 1, MSL101 (with sensor array holder). (b) Simple microchannel package design 2, MSL102 (without sensor array holder). (c) Microchannel package inlet/outlet assembly with micropipe connector.

Some examples of the fabricated micropackages using the Viper system are shown in Figure 5.6. Figure 5.18 shows some examples of the microchannel packages fabricated by the Perfactory MSL system. Figure 5.18(a) shows two MSL101 micropackages while Figure 5.18(b) (bottom) shows MSL102 and Figure 5.18(b) (top) shows MSL103. The basic microchannel footprint design for these packages is the same as they only differ in the housing or enclosure. Figure 5.18(c) shows the alignment of the package with a microsensor array and Figure 5.18(d) shows the assembly with a micropipe connector.

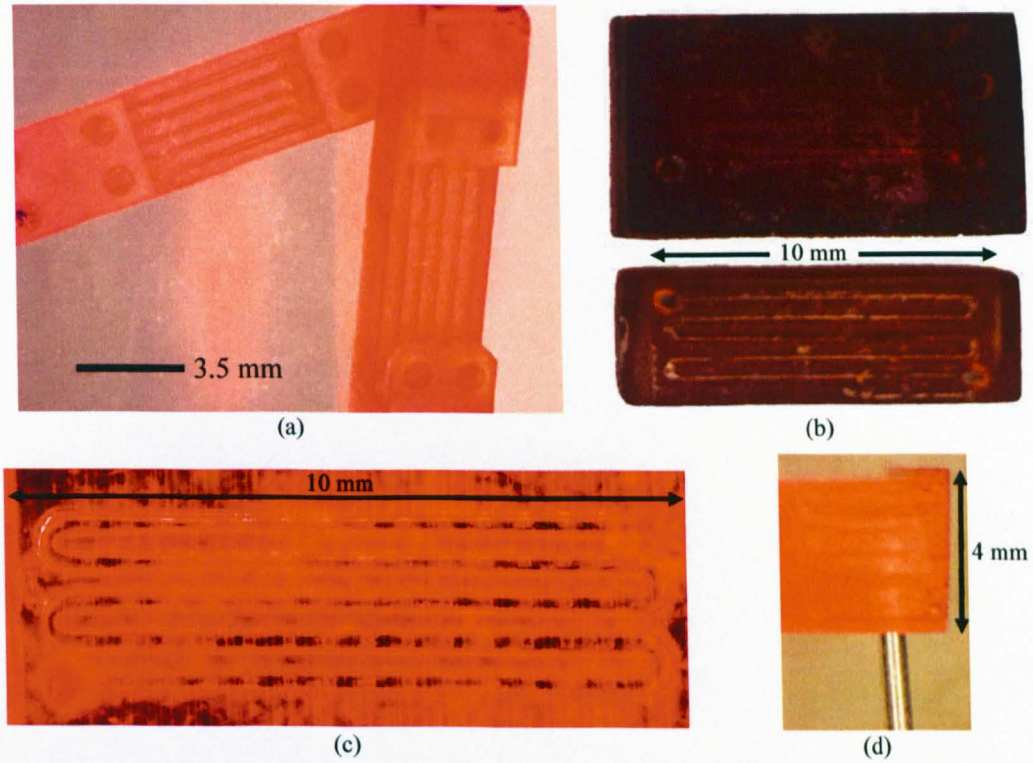

Figure 5.18: Simple microchannel packages fabricated by the Perfactory MSL system. (a) Simple microchannel packages MSL101 (with sensor array holder). (b) Simple microchannel packages, MSL102 (bottom) and MSL103 (top). (c) Simple microchannel package aligned with sensor array. (d) Simple microchannel package with inlet assembly.

5.4.2 Complex micropackages with multiple microchannel segments

The complex micropackage consists of multiple microchannel segments transversing across all sensors within the array. The microchannel runs vertically to achieve the desired length with horizontal segments connecting these vertical segments together to form a single continuous microchannel. Two different package designs were fabricated;

the first version consists of embedded U-shape microchannel. Although this type of design is favourable due to the completeness of the design, the post-processing complications render this design impractical (details available in the next section). To avoid such problems, alternative designs are implemented in Section 5.4.2.2.

During the conceptualisation of the designs for the complex microchannel packages, several proposals were studied. The three important considerations are the length of the microchannel, the overall size of the package and the access points along the microchannel for the microsensor array. To achieve the longest microchannel within a small size package, a 3-D rectangular spiral can be built. However this design will not have any control over the location of the sensors along the microchannel. To maximise the microchannel length while maintaining the flexibility to select the location of the sensors along the microchannel, a simple design technique is used. A mini-chamber was allocated for each group of sensors at the base of the micropackage. These mini-chambers were then connected to vertical microchannel segments (holes) which act as access points to these sensors. At all other empty locations (area without mini-chambers), more vertical microchannel segments will be created. Finally, horizontal segments were used to connect these vertical segments together to form a single continuous microchannel. Appropriate numbers of vertical segments are connected depending upon the desire length between mini-chambers. As such, this type of generic design can easily be reconfigured to accommodate a longer microchannel by extending either vertically or horizontally. In addition, maximised usage of 3-D space is guaranteed by having the vertical microchannel segments packed as closely to each other as possible.

5.4.2.1 Preliminary designs

There were many designs for the complex microchannel packages, however, the earlier versions failed. These earlier versions were designed with small microchannel cross-section ($\leq$ 200 μm × 200 μm) each about 2 cm long. This is desirable as smaller cross-section meant a longer microchannel within a smaller package (higher packing density). Some of these designs are shown in Figure 5.19. Figure 5.19(a) shows a 32 cm long microchannel 500 μm × 500 μm in cross-section. There is a single inlet and outlet for external interface and the microsensor array sits under the package. Figure 5.19(b) shows a complex microchannel package design featuring a 5 m long microchannel of 100 μm × 100 μm in cross-section. On its top surface, there are multiple inlets and outlets to enable

dynamic microchannels configuration (in parallel, series or mix connection) through external microvalves. There are 10 microchannel segments transversing through different sensors residing at the bottom of the package.

The main complication with these two designs is the embedded U-shape microchannel. Due to the high viscosity of the resin, uncured resin will reside in small microchannel after fabrication. It was extremely difficult to clean this resin away especially along the U-shape bend at the far-end of the microchannel. For MSL111, many microchannel segments are blocked and inaccessible due to the need to manoeuvre through numerous U-shape bends before the uncured resin can be removed.

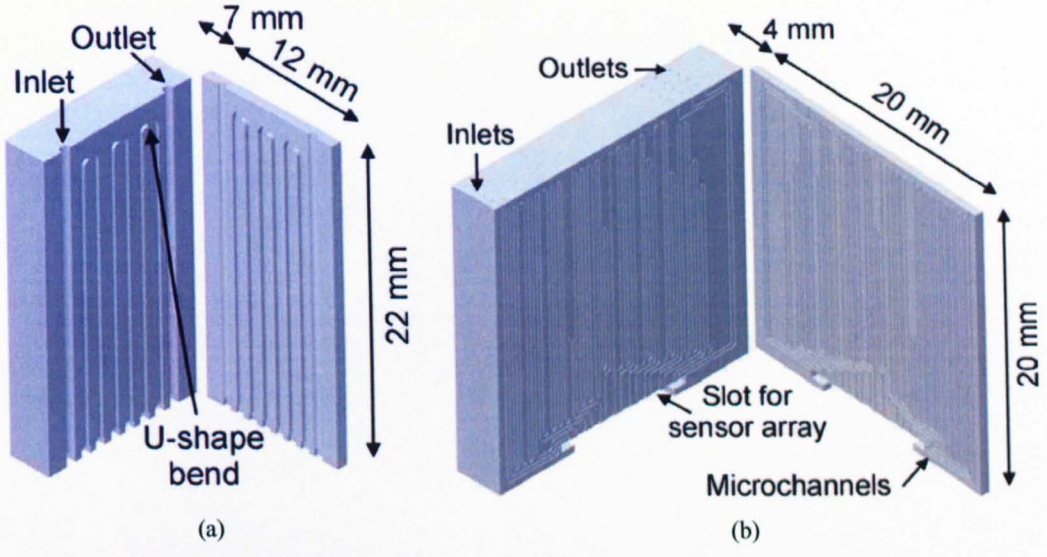

Figure 5.19: Complex microchannel packages earlier designs. (a) Complex microchannel package design 1, MSL110. (b) Complex microchannel package design 2, MSL111.

Other issues include the availability of microtools for cleaning the uncured resin in the microchannel. As the diameter of the microchannel falls below 200 μm, there are no efficient tools at this microscale to remove the uncured resin blocking the microchannels. Some examples of the fabricated first generation micropackages are shown in Figure 5.20. Figure 5.20(a) shows a sliced MSL110 with uncured resin in the U-shape bend. Figure 5.20(b) shows multiple straight microchannels being blocked with uncured resin. A microtool used to clean the uncured resin is also shown.

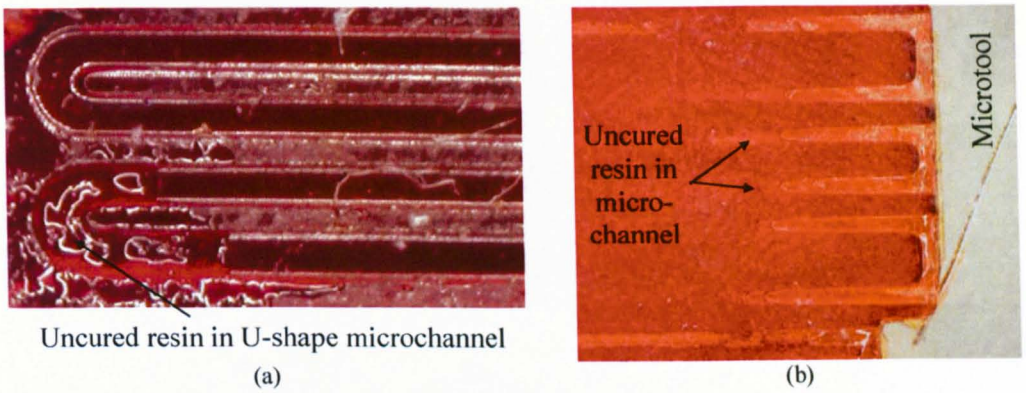

Figure 5.20: First generation complex microchannel packages. (a) Uncured resin in embedded U-shape bend in MSL110. (b) Microchannels blockage with uncured resin with microtool used for cleaning.

5.4.2.2 Updated designs for resolving post-processing complication

To resolve some of the issues highlighted in the previous section, all vertical microchannels were re-designed to run straight through the micropackage to allow easy cleaning. On both ends adjoining the microchannel, a gap is included between the microchannels to allow them to connect. This strategy is clearly demonstrated in Figure 5.21. Such technique allows both ends of the microchannel to be open and accessible by cleaning tool. The cleaning tool can be pushed in from one end to force any excess uncured resin to escape from the other end. However, this resulted in an open microchannel on both ends that needs to be sealed. An acrylate lid is used to form a leak-free microchannel.

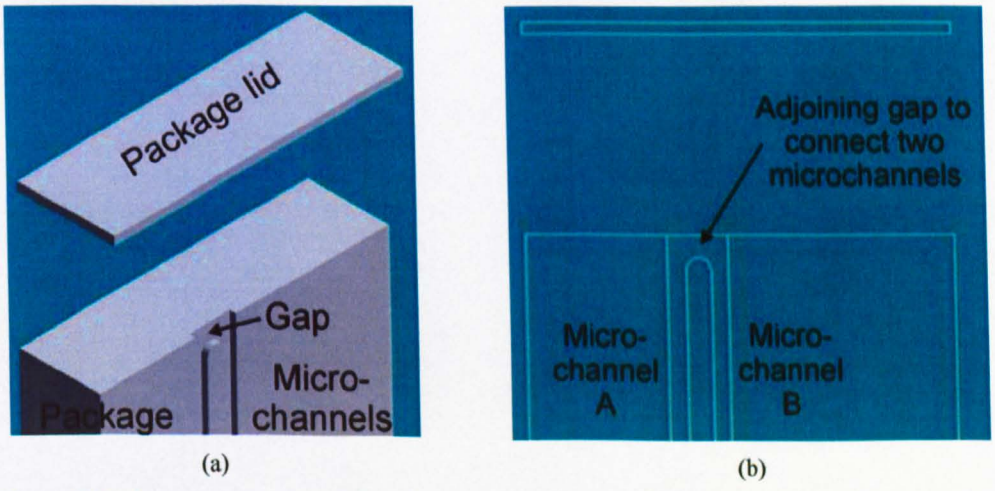

Figure 5.21: Strategy to resolve blockage by uncured resin for complex microchannel package. (a) Sliced 3-D view of the strategy. (b) Cross-section 2-D view of the strategy.

Based on this new technique, different variations of complex microchannel packages were designed as shown in Figure 5.22. These packages consist of two main classes of cross-section dimension (300 μm × 300 μm and 500 μm × 500 μm) of 4 different lengths (32 cm, 71 cm, 120 cm and 240 cm). The microsensor array holding slot at the bottom was removed for ease of interface by bonding the microsensor array onto standard PGA256 package and fitting the microchannel package from the top. The fabricated complex microchannel packages are shown in Figure 5.23. Figure 5.23(a) shows the fabricated MSL112. The top photograph shows 8 'mini-chambers' on the bottom side of the micropackage, each is designed to provide access to 10 sensors (two columns).

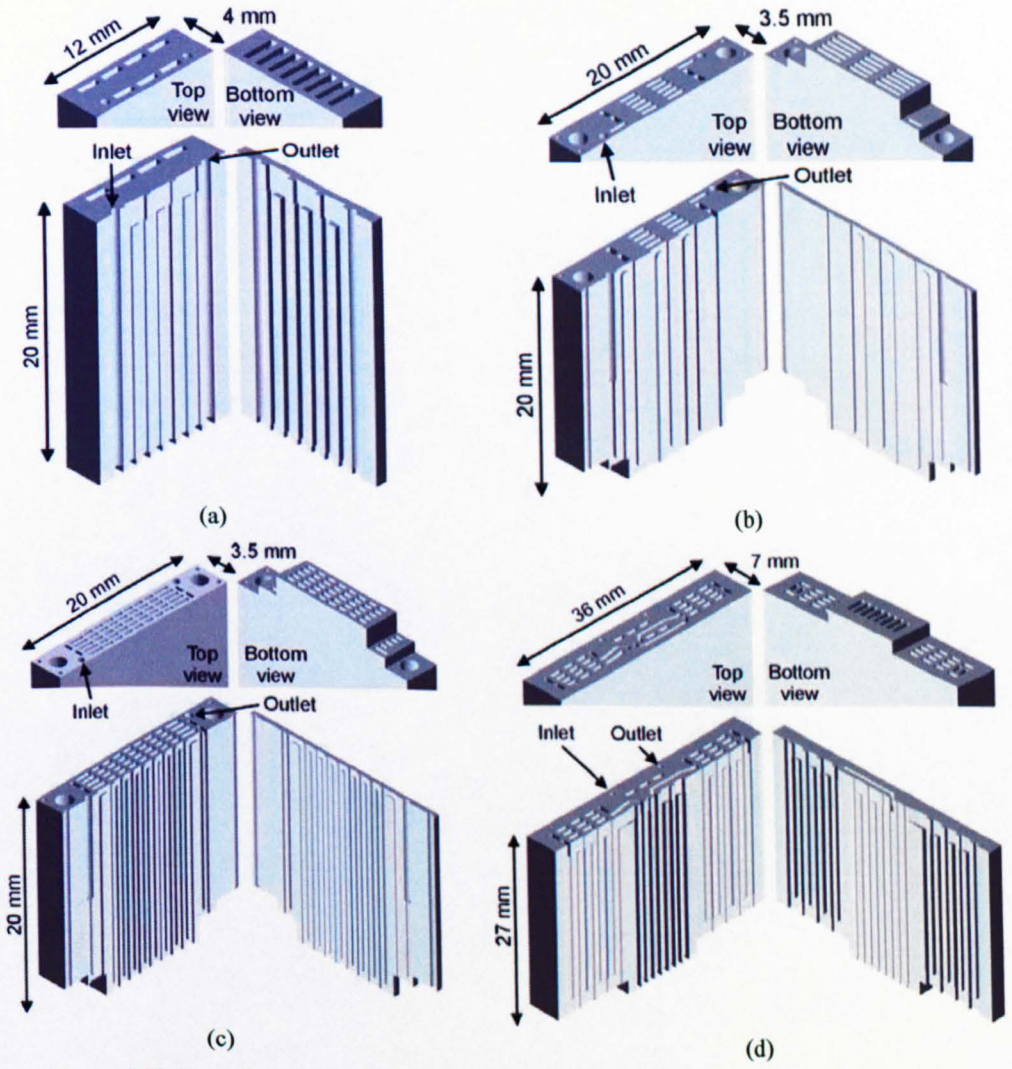

Figure 5.22: Complex microchannel package designs. (a) MSL112, 32 cm × 500 μm × 500 μm microchannel. (b) MSL113, 71 cm × 500 μm × 500 μm microchannel. (c) MSL114, 120 cm × 500 μm × 500 μm microchannel. (d) MSL115, 240 cm × 500 μm × 500 μm microchannel.

The microchannels for all complex micropackages have through channels to allow simple post-processing. Figure 5.23(a) and (b) shows some fabricated packages with the straight through microchannel designs while Figure 5.23(c) shows a fabricated MSL113 with an inlet and an outlet prior to assembly. This package has a different bottom design with 15 mini-chambers, each having access to 5 or 6 sensors. Figure 5.23(d) shows a collection of all fabricated complex microchannel packages.

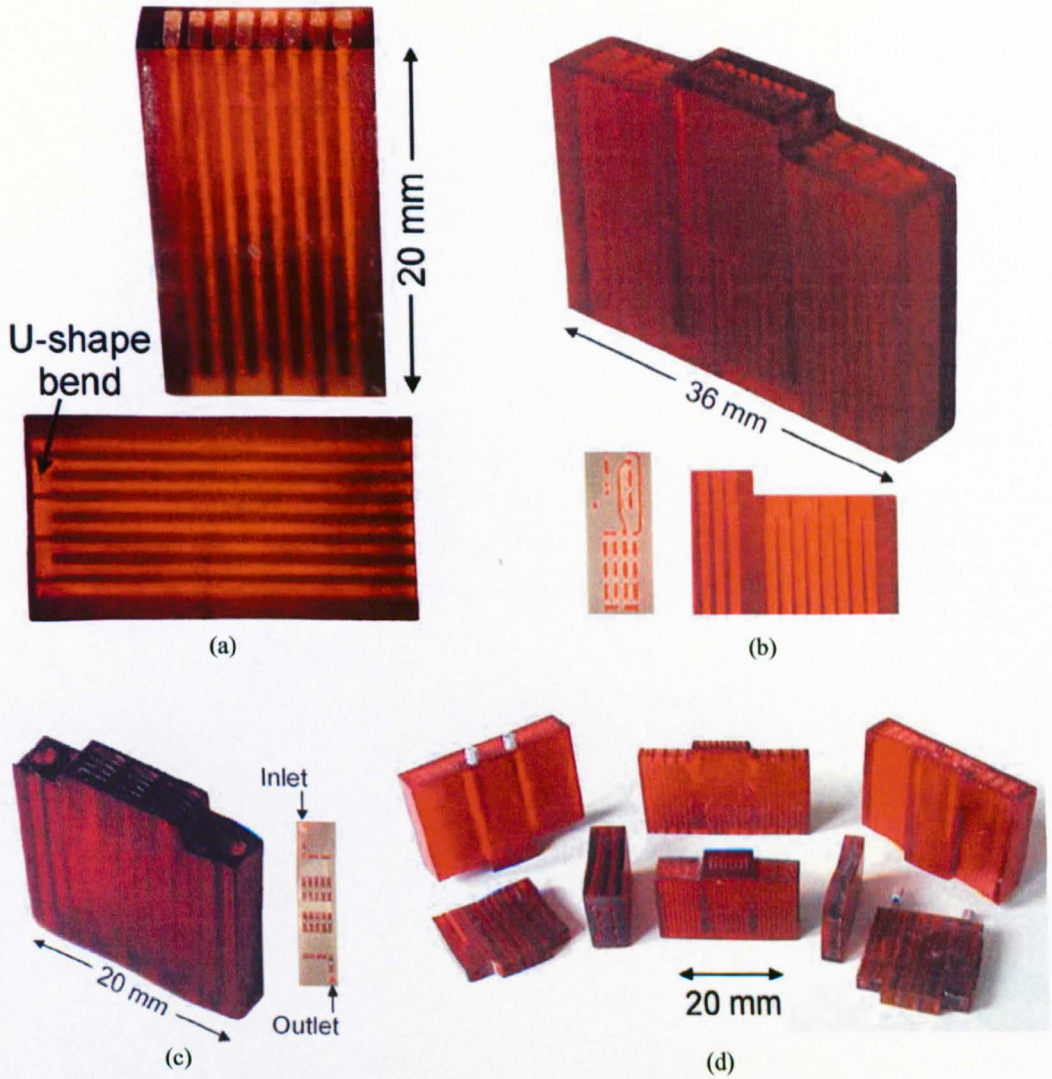

Figure 5.23: Fabricated complex microchannel packages. (a) MSL112 perspective and top view. (b) MSL115 isometric, partial front and partial top view. (c) MSL113 isomeric and partial top view. (d) Photographs of complex microchannel packages.

Fabricating through microchannels resolve the channel blockage issue, however, an additional step is required to passivate the open ends of the microchannel. Figure 5.24 shows two such assembled microchannel packages. Figure 5.24(a) shows MSL112 assembled with a transparent plastic with an inlet and outlet. Figure 5.24(b) shows a similar assembly for MSL113. Upon completion, the packages are ready for assembly with the microsensor array. Details regarding these assembling will be discussed in the next chapter.

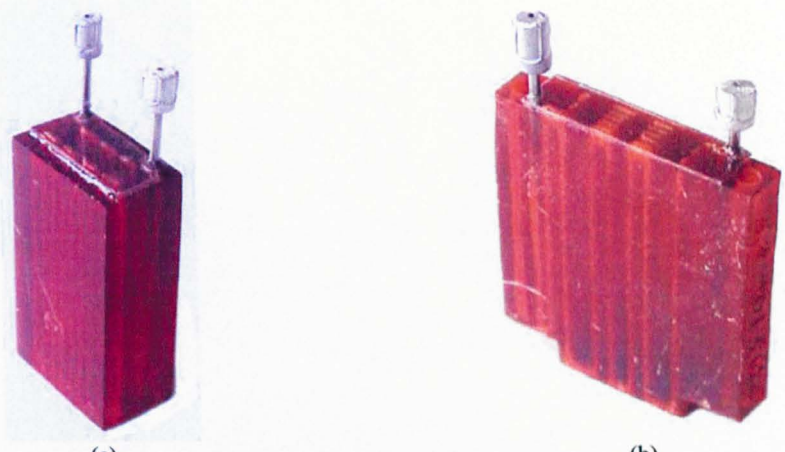

(a) (b)

Figure 5.24: Complex microchannel packages with lid assembly. (a) MSL112 with plastic lid. (b) MSL113 with plastic lid.

5.5 Micropackages and Perfactory system characterisation

The microchannel packages were characterised to determine their surface roughness and hardness. These tests are important to determine the operating range and limitation of the packages. The Perfactory MSL system is also characterised to determine the limitation of the machine and possibility of improving the build.

5.5.1 Mechanical properties: surface roughness and hardness

The surface roughness is measured over a 600 μm × 500 μm area on the package surface. The measurements were performed using the WYKO interferometer (NT-2000 optical interferometer, Veeco Instrument, UK) and the results are shown in Figure 5.25. Two main surfaces of interest are those parallel and perpendicular to the building base. Figure 5.25(a) shows a measurement with a surface parallel to the base and Figure 5.25(b) shows a measurement with a surface perpendicular to the base.

Comparing between these two measurements, the surface parallel has a lower surface roughness compared to the surface perpendicular to the base. This is because each layer is sandwich between the partially built object and the flat bottom of the photoreactor, ensuring the flatness of each layer (Figure 5.9). On the surface perpendicular to the fabrication plane, it is rougher due to the slight misalignment between each layer while the base (Z-stage) is moving upwards. The parallel surface measurements give an *Ra* (mean roughness) between 25 to 200 nm while the perpendicular surface measurements give an *Ra* between 500 nm to 5 μm.

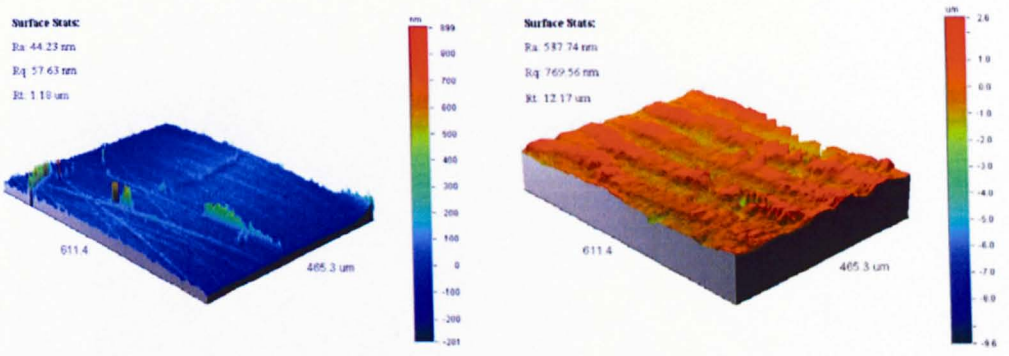

(a) (b)

Figure 5.25: Surface roughness of MSL115. (a) Surface parallel to the fabrication plane. (b) Surface perpendicular to the fabrication plane.

From Figure 5.25(b), uneven lines representing the misalignment between different layers can be clearly observed. A simple technique to optimise the desirable surface finish on certain surface is to re-orientate the object such that the surface is parallel to the build platform. Using the layer thickness, surface angle and layer profile, it is possible to estimate the surface roughness [5.27].

The polymerised resin has the following properties [5.21] as given in Table 5.3.

Table 5.3: Polymerised resin properties.

	Perfactory (5 min post exposure)	Light oven (20 min exposure)
Bending strength	90 – 100 MPa	70 – 80 MPa
Bending modulus	1800 – 2000 MPa	1500 – 1600 MPa
Elongation at break	6 – 9 %	10 – 13 %
Shore hardness DIN 53505	80 – 85	75 – 80

The results show that there is a slight decrease in the material strength and hardness for over curing. Separate hardness tests conducted at Warwick [5.26] show the effect of increasing the exposure time on the material hardness. The hardness increases by 60 % in the first 5 minutes. Thereafter, each subsequent 5 minutes interval the hardness increase only by 7 %. However, when the exposure time is extended beyond 20 minutes, the hardness is reduced (i.e. over-exposure). For these objects, cracks start to appear after some time. A detailed characterisation was not performed as this task is beyond the scope of this research.

5.5.2 Perfactory system resolution, repeatability and build accuracy

The XY (pixel) resolution of the Perfactory MSL system was determined by the size of the DMD device and the focusing optics. There is no issue on this lateral resolution except for the possibility of mis-alignment between layers discussed in the previous section. The Z-stage is however susceptible to larger error due to the mechanical nature for its movement. The vertical drive was implemented in the Perfactory system using a lead screw driven by a stepper motor. The resolution of this stage was 5 μm, which is derived from a 1.8 ° motor rotation step, and a 1 mm screw pitch. Using a Renishaw laser interferometer with environmental compensation unit to adjust for any temperature variation, the vertical movement is monitored. Measurement performed by the Warwick MSL team [5.26] shows a maximum error of ± 4 μm when operating at the minimum thickness resolution (25 μm). As the system employs a stepper motor in an open-loop control, there is no means of improving the Z-stage without major system modification.

The repeatability of the build has largely been time dependent. This time dependency can be attributed to the ageing of the brightness of the bulb and the monomer resin. Although the light bulb has a prescribed life time, it brightness varies throughout it lifespan. Such variation usually falls outside the acceptable limits after 50 hours of usage. Subsequently, the system required recalibration using a 48-point light meter test (inbuild in Perfactory system) to re-adjust the light intensity. The ageing of the resin was more difficult to determine as there is no simple measurements to assess it quality. It is also not possible to estimate the degradation process that is believed to be time dependent coupled with the effect of unnecessary exposure of the resin to ambient light. As the system was not placed is any special designed laboratory with shielded yellow light, when an object is built, it has to be removed from the base, the resin is exposed to ambient light for about

30 s or more. This degrades the quality of the resin by unwanted curing. The other possible source of resin degrading is time dependent due to the scattered light during the build, again altering the quality of the resin by partial curing. It is therefore recommended to replace the resin in the photoreactor completely after every 3 months instead of topping the depleted resin.

The build accuracy is a simple comparison between the designed dimension and the actual size of the fabricated object. All objects were cured prior to measurement and hence any errors due to shrinkage (if any) are included in the measurements. The measurements are performed with 5 packages with an outer dimension of 20 × 20 × 7 mm^3 fabricated at different time.

The X and Y errors for the objects have been found to be less than ± 25 μm in both directions. However, for down-facing systems where objects are built downwards, the fabricated objects exhibit a sloping effect on its side-walls (similarly for up-facing system, sloping effect still occurs but in the opposite direction) [5.27]. This slope was measured to be approximately 0.65 % for a 20 mm height. For the fabricated microchannels, the error was about ± 25 μm for both sizes of cross-sectional area. As for the depth accuracy, the error is slight larger and found to be ± 100 μm. This was probably caused by the Z-stage movement error as discussed previously. Similarly, the depth of the object was susceptible to the ± 1 step error.

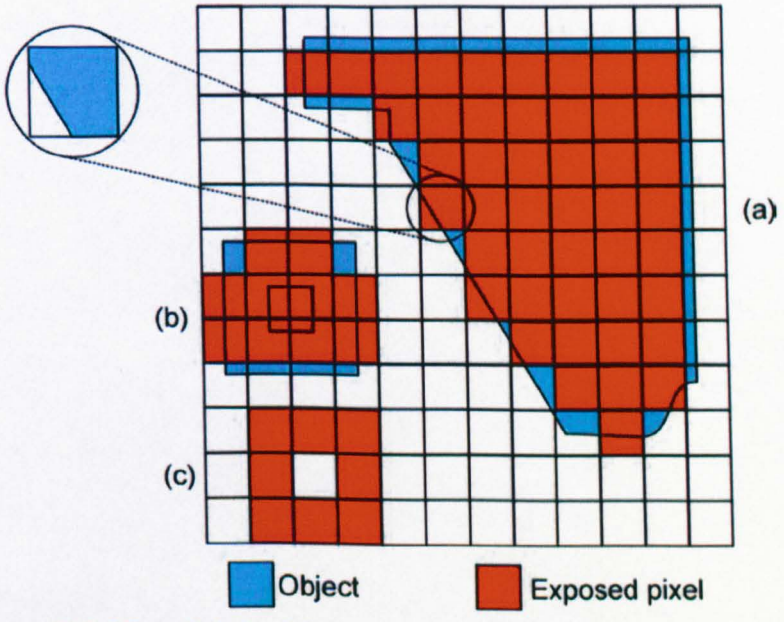

Figure 5.26: Effect of pixel and placement error. (a) Pixel error irregular shape object. (b) Effect of offset grid placement. (c) Effect of snap to grid placement.

It was also important to note that the ± 1 pixel error for the lateral resolution (the ± 1 step error for the depth). Figure 5.26 shows the effect of pixel error on the fabricated object. Shown with a reduced 12 × 12 pixel map, each pixel was controlled with a micromirror that cures a dot (spot) depending upon the design of the object. For pixels completely encapsulated within the object, they are obviously turned-on (exposed). However for pixels along the boundary, they become indeterminist as shown in Figure 5.26(a). A simple algorithm is to turn on those pixels that have more than 50 % area coverage.

Although such technique is simple to implement, it does not always produce the optimal results especially for diagonal and curve corners. More advance techniques employing anti-aliasing and many other algorithms (such as edge super-sampling and multi-sampling) [5.28] can produce better results. The other important issue relates to the placement of the object within the base grid. Figure 5.26(b) shows the placement of a square tube with a hole in the middle of the cross-section of the tube. In this extreme scenario, the object is not snapped to the grid but slightly offset. If a 50 % thresholding technique is employed to determine the pixel ON/OFF state, the resultant object will resemble a distorted solid rod instead of the square tube. However, if the object is snapped to the grid, as shown in Figure 5.26(c), the desired object will be fabricated instead. It is therefore very important for the designer to be aware of these issues and take them into account during the design and placement process to reduce unnecessary errors.

Another important issue is the layer thickness control. Looking from the side view of the same curved object, Figure 5.27 shows the effect of varying the layer thickness by a factor of 4. The horizontal pixel width (X or Y) is the lateral resolution while the vertical direction is the layer thickness. Figure 5.27(a) shows a large layer thickness (2X), Figure 5.27(b) shows a medium layer thickness (X) while Figure 5.27(c) shows a small layer thickness (0.5X). As layer thickness is decreased, the object produced can more faithfully approach the original design, and the surface quality is correspondingly improved [5.29]. The improvement in the final object profile is at the expense of fabrication time. A technique called dynamic slicing has been proposed by [5.27], this method improves the build quality while optimizing the building time by assigning different layer thickness depending upon the profile of the object. As shown in Figure 5.27(d), for parts with straight vertical profile, large layer thickness can be used to achieve a faster building time without compromising the object surface finish. For curve or diagonal lines, smaller layer thickness can be used to achieve better surface finishing.

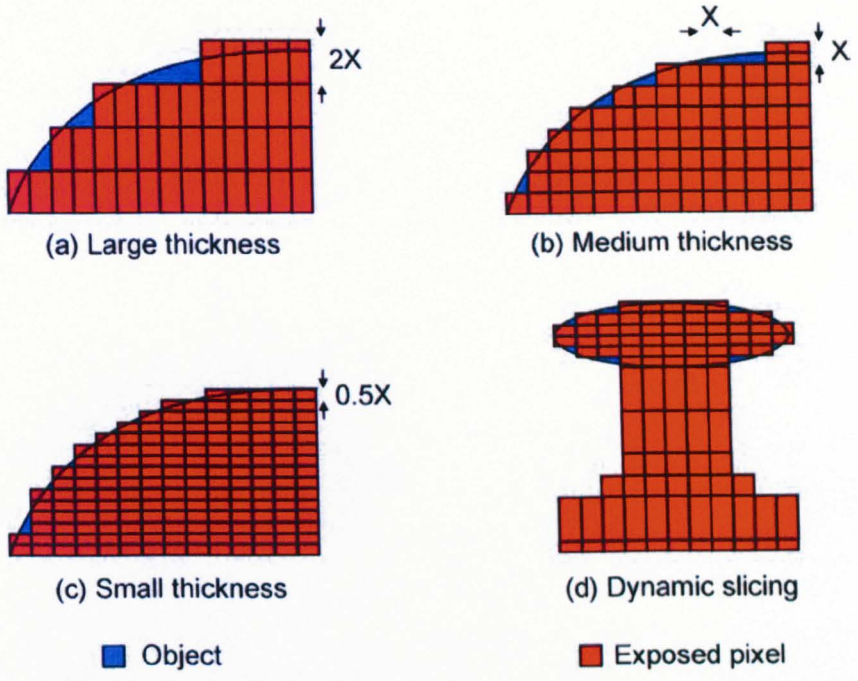

Figure 5.27: Effects of stairs-stepping as a function of layer thickness. (a) Large layer thickness. (b) Medium layer thickness. (c) Small layer thickness. (d) Dynamic layer slicing.

5.6 Conclusions

In this chapter, the general concepts of stereolithography and microstereolithography fabrication have been discussed. Two different systems have been briefly examined, namely the Proform system from RAL and the Viper si system from 3D System. A third system, the Perfactory MSL system available at Warwick has been discussed in detail. Using these systems, various microchannel packages ranging from simple to complex have been fabricated. The simple microchannel packages consist of MSL101, MSL102 and MSL103 that have the same microchannel size (5 cm × 200 μm × 200 μm) but different external form factors. The complex microchannel packages include MSL110 (32 cm × 500 μm × 500 μm), MSL112 (32 cm × 500 μm × 500 μm), MSL113 (71 cm × 500 μm × 500 μm), MSL114 (120 cm × 500 μm × 500 μm), MSL115 (240 cm × 500 μm × 500 μm) amongst others. Prior to fabrication, the microchannel has been designed, simulated and supporting structures added if necessary. Upon fabrication, the packages have to be cleaned, assembled and cured. These fabrication stages have been discussed in details.

During the fabrication of complex microchannel packages, one major problem was encountered. This is primary due to long microchannel segments with several bends

embedded within the solid package. Through the use of straight-through microchannel segments, the excess resin can easily be cleaned to remove any possible blockage. Finally, issues relating to the material and machine properties were briefly discussed to allow future users to be aware of the limitations so as to achieve better build quality. In the next chapter, the assembly of these microchannel packages with the sensor arrays to create nose-on-a-chip systems will be discussed.

5.7 References

[5.1] A. Bertsch, S. Jiguet, P. Renaud, ***Microfabrication of ceramic components by microstereolithograhpy***, J. Micromech. Microeng., 14, pp. 197-203, 2004.

[5.2] V.K. Varadan, X.N. Jiang, V.V. Varadan, ***Microstereolithography and other fabrication techniques for 3D MEMS***, John Wiley and Sons, 2001.

[5.3] J.W. Gardner, V.V. Varadan, O.O. Awadelkarim, ***Microsensors, MEMS and smart devices: technology, applications and devices***, John Wiley and Sons, 2001.

[5.4] K. Ikuta, K. Hirowatari, T. Ogata, ***Three dimensional micro integrated fluid systems (MIFS) fabricated by stereolithography***, Proc. IEEE MEMS, pp. 1-6, 1994.

[5.5] K. Ikuta, T. Ogata, M. Tsubio, S. Kojima, ***Development of mass productive microstereolithography (mass-IH process)***, Proc. IEEE MEMS, pp. 301-305, 1998.

[5.6] K. Ikuta, S. Maruo, S. Kojima, ***New microstereolithography for freely movable three-dimensional microstructure super-IH process with submicron resolution***, Proc. IEEE MEMS, pp. 290-295, 1998.

[5.7] S. Maruo, K. Ikuta, ***Submicron stereolithography for the production of freely movable mechanisms by using single-photon polymerization***, Sensors and Actuators A 100, pp. 70-76, 2002.

[5.8] S. Maruo, S. Kawata, ***Two-photon absorbed near-infrared photopolymerisation for three-dimensional microfabrication***, J. Micreoelectromech. Syst., 7, pp. 411-415, 1998.

[5.9] T. Takagi, N. Nakajima, ***Photoforming applied to fine machining***, 4th Int. Symp. On Micro Machine and Human Science, pp. 173-178, 1993.

[5.10] S. Zissi, A. Bertsch, J.Y. Jézéquel, S. Corbel, J.C. André, D.J. Lougnot, ***Stereolithography and microtechniques***, Microsyst. Technol., 2, pp. 97-102, 1996.

[5.11] X. Zhang, X. Jiang, C. Sun, ***Microstereolithography for MEMS***, MEMS ASME, 66, pp. 3-9, 1998.

[5.12] A. Bertsch, J.Y. Jézéquel, S. Corbel, J.C. André, ***Manufacture of multilayers microparts by microstereolithography***, 3rd France-Japan Congress and 1st Europe-Asia Congress on Mechatronics, Vol. 2, pp. 492-495, 1996.

[5.13] H. Bohlmann, R. Götzen, ***High aspect ratio components through RMPD***, 4th Int. Workshop on High Aspect Ratio Micro Structure Technology (HARMST'01), pp. 49, 2001.

[5.14] C.R. Chatwin, M. Farsari, S. Huang, M.I. Heywood, P.M. Birch, R.C.D Young, J.D. Richardson, ***UV microstereolithography system that uses spatial light modulator technology***, Appl. Opt. 37, pp. 75140-7522, 1998.

[5.15] S. Monneret, V. Loubère, S. Corbel, ***Microstereolithography using dynamic mask generator and a non-coherent visible light source***, SPIE Symp. on Design, Test and Microfabrication of MEMS/MOEMS, 3680, pp. 553-561, 1999.

[5.16] L. Beluze, A. Bertsch, P. Renaud, ***Microsterolithography: a new process to build complex 3D objects***, SPIE Symp. on Design, Test and Microfabrication of MEMS/MOEMS, 3680, pp. 808-817, 1999.

[5.17] A. Bertsch, P. Bernhard, C. Vogt, P. Renaud, ***Rapid prototyping of small size objects***, J. Rapid Prototyp., 6, pp. 259-266, 2000.

[5.18] S. Kawata, H-B, Sun, T. Tanaka, K. Takada, ***Finer features for functional microdevices***, Nature 412, pp. 697-698, 2001.

[5.19] F. Devaux, A. Mosset, E. Lantz, S. Monneret, G.H. Le, ***Image up-conversion from the visible to the UV domain: application to dynamic UV microstereolithography***, Appl. Opt. 40, pp. 4953-4957, 2001.

[5.20] 3D Systems, http://www.3dsystems.com/products/sla/viper/index.asp, Viper SLA system, Valencia, CA 91355 USA, July 2004.

[5.21] Evisiontec GmbH, http://www.envisiontec.com/02hperfa.htm, Perfactory Mini System, Elbestrasse 10 D-45768 Marl, Germany, July 2004.

[5.22] Texas Instruments, ***DLP (digital light processing) technology***, http://www.dlp.com/, 2005 Texas Instruments Incorporated.

[5.23] Materialise, http://www.materialise.com/magics-tooling/main1_ENG.html, Magic tooling software version 9.01, Glen Burnie, MD 21061 USA, July 2004.

[5.24] C-K. Chua, K-F. Leong, ***Rapid prototyping: principles and applications in manufacturing***, John Wiley and Sons, 1997.

[5.25] L.A. Tse, P.J. Hesketh, D.W. Rosen, J.L. Gole, ***Stereolithography on Silicon for Micro-fluidics and Microsensor Packaging***, Microsystem Technologies, Vol. 9, pp. 319-323, 2003.

[5.26] S. Hinrich, S. Jingree, P. Padhy, B. Pearce, A. Sanami, N. Smith, D. Walters, C. Weightman, ***Microstereolithography (Technical report)***, MEeng Thesis, School of Engineering, University of Warwick, 2004.

[5.27] P.E. Reeves, R.C. Cobb, ***Reducing the surface deviation of stereolithography using in-process techniques***, J. Rapid Prototyping, Vol. 3, pp. 20-31, 1997.

[5.28] S. Lin, R.W.H. Lau, X.L. Lin, P.Y.S. Cheung, ***An anti-aliasing method for parallel rendering***, Proc. Computer Graphics Int., pp. 228-235, 1998.

[5.29] P.F. Jacobs, ***Stereolithography and other RP&M technologies: from rapid prototyping to rapid tooling***, American Society of Mechanical Engineers (ASME press), 1996.

Chapter 6

Nose-on-a-chip: Integration

6.1 Introduction

In the two previous chapters, the design and fabrication of discrete sensors, microsensor arrays and microchannel packages were discussed. These components are the essential building blocks for the proto-nose and the nose-on-a-chip (NOC) microsystems. For the proto-nose microsystems, only the design and fabrication of discrete sensors had been described in Chapter 4. The remaining details to assemble the complete proto-nose system will be discussed here. In addition, "fast-nose" microsystem, which is built to characterise the discrete sensors prior to their usage on the proto-nose II system will be discussed. Using this system, numerous other characteristics of the polymer-composite sensors were investigated, such as velocity dependence of the response time. Upon calibration, the discrete sensors were assembled in a custom machined PCB base with the parylene C coated lid to produce the proto-nose II system.

Building the NOC microsystems required careful assembly of the microsensor arrays with the microchannel packages. Two microsensor arrays with identical sensor placements have been designed and fabricated to enable the same microchannel packages to be used. Lastly, the deposition of a thin layer of parylene C material on the microchannels to act as a retentive material (alike the stationary phase coating in a gas chromatography column) will be discussed.

6.2 Proto-nose microsystems

The proto-nose microsystems consist of two main configurations, proto-nose I and proto-nose II. The two major distinctions between these two systems lie in their lengths and the existence of intra-channel slots to eliminate intra-channel leakage. For each proto-nose

system, two types of lids were fabricated. The first type was made of Perspex for use as an uncoated microchannel while the second type was made of an inert plastic material (Acetal copolymer) for use as a coated microchannel after deposition with parylene C. An intermediate system, the fast-nose microsystem used to characterise discrete sensors will also be discussed.

6.2.1 Proto-nose I microsystem

Proto-nose I consists of a PCB base assembly with polymer-composite discrete sensors and a machined plastic lid with microchannel for analyte delivery. The PCB base has 40 rectangular trenches machined within it to allow the sensors to sit flush with the surface of the PCB. Figure 6.1 shows details of the PCB base assembled with the sensors. 40 sensors are installed onto the PCB base. The sensors are classified into 5 groups of 8 sensors with 5 different types of sensor tunings. The sensors are glued to their designated location and thereafter wire-bonded to the electrical track on the PCB as shown in Figure 6.1(b). An empty machined rectangular trench prior to sensor assembly is also shown.

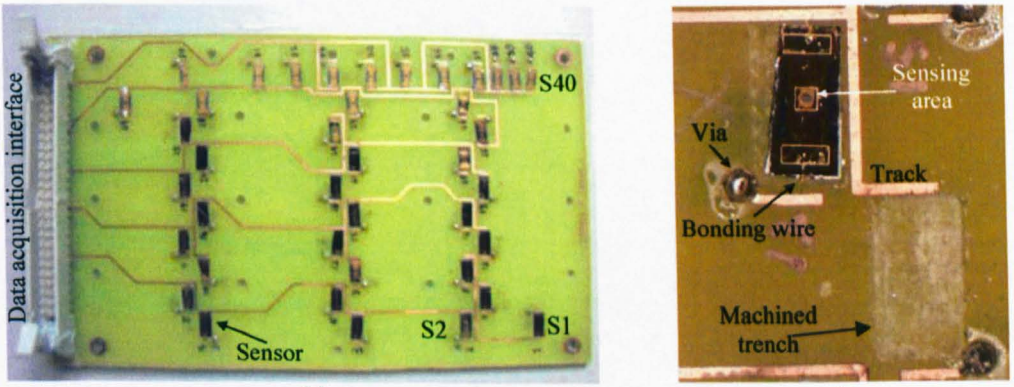

Figure 6.1: PCB base of proto-nose I. (a) PCB base assembled with 40 discrete sensors. (b) Details of the machined trench and sensor assembly.

The uncoated Perspex plastic lid was machined to contain a 1.2 m long microchannel (500 μm × 500 μm in cross-section), 40 sets of bonding wire housings, assembly holes on one side and an inlet/outlet on the opposite side. Figure 6.2(a) shows the machined Perspex lid and (b) shows a detail photograph of the microchannel and the bonding wire housing.

The fully assembled proto-nose I system is however susceptible to leakage on all the four sides with small gaps sandwich between the base and lid. To fully seal the system, an inert RTC (room temperature curable) adhesive (3145 MIL-A-46146, Dow Corning, UK) was applied on all gaps along the edges to eliminate the leak. Although any external leakage was successfully contained, the possibility of intra-channel leakage remains. By referring to Figure 6.2(a) and (b), the term "intra-channel leakage" is used to describe the flow of analyte across 'short-circuited' path instead of along the microchannel. This is due to unwanted gaps between the base and lid possibly because of uneven surfaces and assembly misalignment. The deduction was made based on the responses of sensors that were placed sequentially, but they do not response according to their placement order.

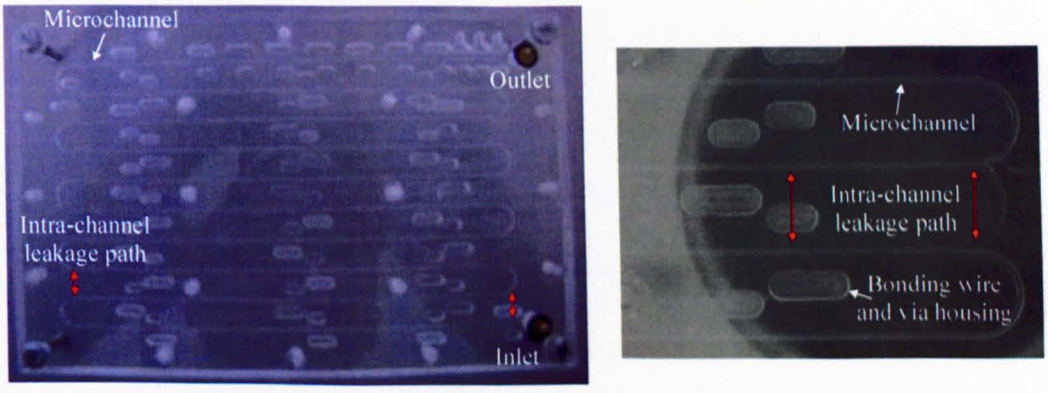

(a) (b)

Figure 6.2: Perspex lid of proto-nose I. (a) Machined Perspex lid. (b) Photograph of microchannel and bonding wire housing.

A fully assembled uncoated proto-nose I system is shown in Figure 6.3(a). Figure 6.3(b) shows the coated proto-nose I system while (c) shows the cross-sectional assembly details. An in-house fabricated double-sided PCB consists of tracks on both surfaces required for the electrical interconnection. On the top-side, 40 rectangular trenches slightly larger than the sensors were machined. Once the sensors were assembled, they were wire-bonded to the PCB track. As the bonding wires form protruding arc shape, bonding wire housings were machined on the lids to prevent damaging these electrical interconnections. A microchannel machined on the lid runs directly across the sensing area of the sensor. On the top side of the lid, an inlet and outlet for interfacing to the vapour test station were created.

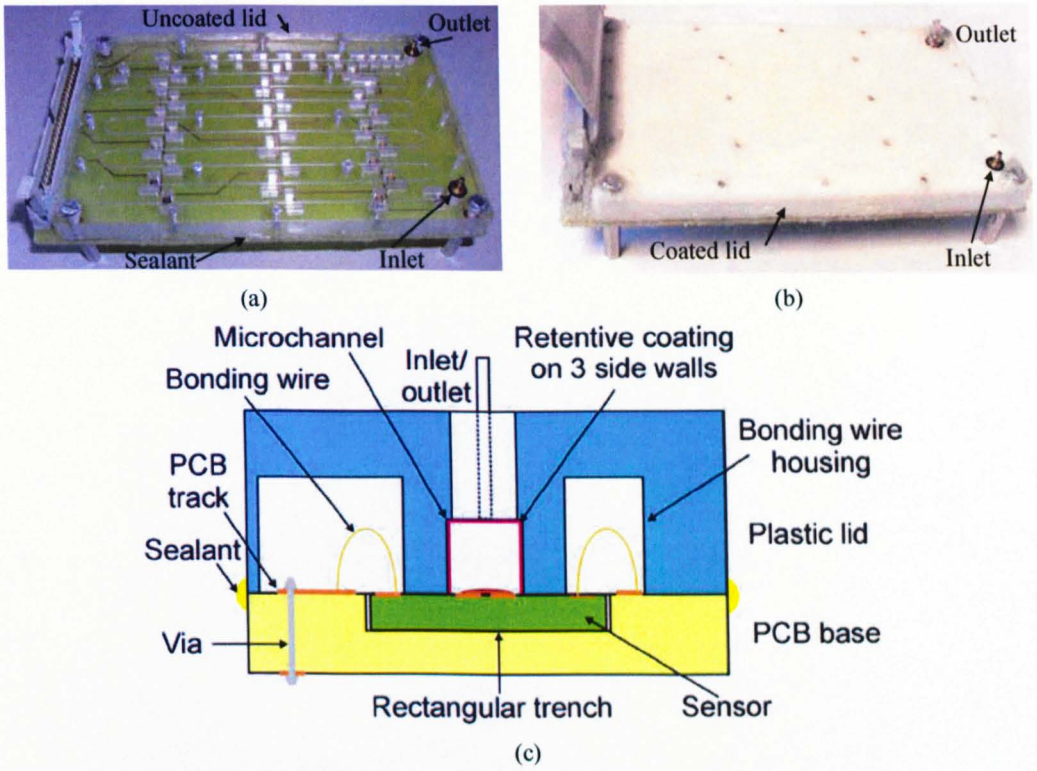

Figure 6.3: Fully assembled proto-nose I system. (a) Photograph of an uncoated proto-nose I system. (b) Photograph of a coated proto-nose I system. (c) Cross-sectional assembly details.

Table 6.1: Sensor placements on the proto-nose I.

No.	Distance (mm)	Type
S1	5	PSB
S2	25	PEVA
S3	55	PEG
S4	95	PCL
S5	137	PVPH
S6	177	PSB
S7	217	PEVA
S8	259	PEG
S9	289	PCL
S10	329	PVPH
S11	370	PSB
S12	410	PEVA
S13	450	PEG
S14	492	PCL
S15	522	PVPH
S16	562	PSB
S17	604	PEVA
S18	644	PEG
S19	684	PCL
S20	726	PVPH

No.	Distance (mm)	Type
S21	756	PSB
S22	796	PEVA
S23	838	PEG
S24	878	PCL
S25	918	PVPH
S26	959	PSB
S27	989	PEVA
S28	1029	PEG
S29	1050	PCL
S30	1081	PVPH
S31	1101	PSB
S32	1111	PEVA
S33	1121	PEG
S34	1131	PCL
S35	1141	PVPH
S36	1151	PSB
S37	1161	PEVA
S38	1166	PEG
S39	1171	PCL
S40	1176	PVPH

From Figure 6.4, it can be seen that towards the front of the microchannel (closer to the inlet), the sensors are placed sparsely while at the end of the microchannel, the sensors are placed closer together. The idea behind this placement strategy is to focus on the information towards the end of the microchannel where more separation is expected to occur. The detailed sensor placements are given in Table 6.1.

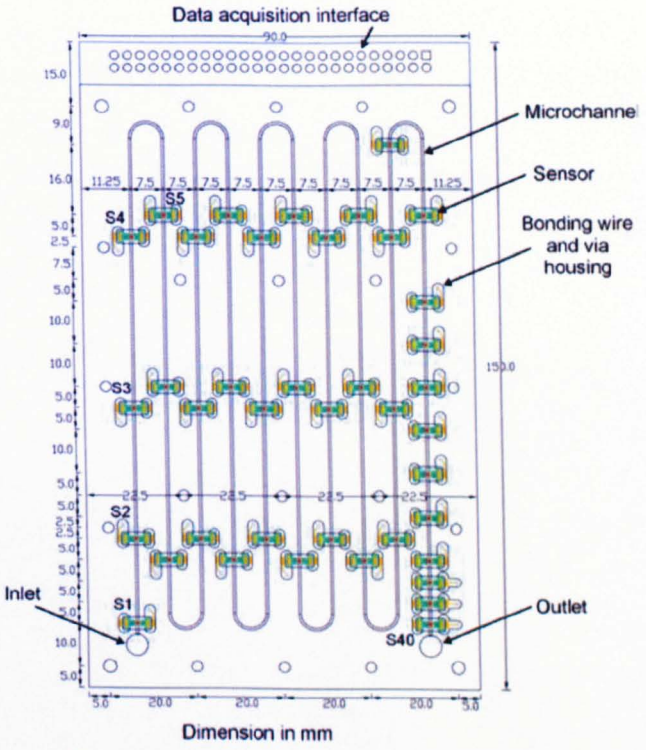

Figure 6.4: Detailed schematic of proto-nose I design.

Figure 6.4 shows the detailed schematic of proto-nose I design with the corresponding sensor placements. Proto-nose I was initially designed and fabricated early in the project development. However, testing yielded two unexpected results which will be fully described in Chapter 8 (Figure 8.5). Firstly, sensors placed sequentially along the microchannel did not respond according to their placement order. Secondly, sensors that were further away from the inlet experienced a significant magnitude reduction compared to sensors closer to the inlet. Repeated measurements with various analytes revealed similar results suggesting two plausible causes. Although the vapour test station had suggested there was a minimal leakage from system, intra-channel leakage could still occur (Figure 6.2). Also, as the discrete sensors were not characterised for their response variations, real natural differences could have caused the large magnitude disparity.

6.2.2 Fast-nose microsystem

Due to the uncertainty surrounding the results produced by proto-nose I, an intermediate system with a reduced microchannel length was designed and fabricated. This system is intended to use for measuring the variation in response magnitudes and profiles of 10 discrete sensors (of the same type) so that numerical compensation can be applied to offset any differences when they are assembled in the new proto-nose II system. The cross-sectional size of the microchannel was 500 μm × 500 μm while the length has been reduced to 10 cm. Ten sensors are assembled in the system each time and the system is sealed using the same technique discussed in Section 6.2.1. The design of the fast-nose system is shown in Figure 6.5(a) and a photograph of the fully assembled system is shown in (b).

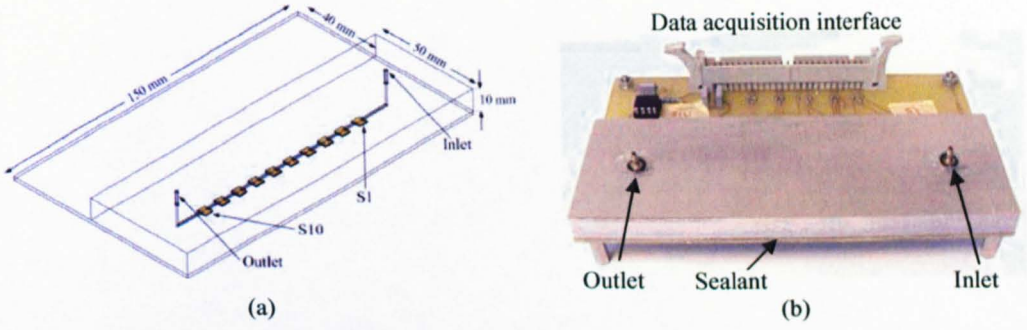

Figure 6.5: Fast-nose microsystem. (a) Fast-nose microsystem design. (b) Fully assembled fast-nose microsystem.

6.2.3 Proto-nose II microsystem

Although the discrete sensors can be pre-measured to compare their responses prior to assembly, the issue of intra-channel leakage could not be resolved without a new proto-nose hardware system. As such, proto-nose II was produced to overcome this deficiency. The microchannel length was doubled to improve the efficiency of the system.

The issue of intra-channel leakage has been the most daunting due to the need to accommodate a long microchannel into a small enough area so that it will fit inside the stationary phase deposition chamber (Section 6.4). The technique used here was to create slots between the straight segments of the microchannel for filling sealant, hence preventing intra-channel leakage. The second modification was to extend the length of the microchannel from 1.2 m to 2.4 m. The rationale was to improve column efficiency

(Chapter 3), as this is directly proportional to the length of the column. Although the length of proto-nose II is doubled, it is still relatively short compared to traditional GC systems (usually > 10 m) [6.1-6.2]. Lastly, the number of sensor diversities was increased from 5 to 10 and their placements re-arranged. The increase in sensor tunings has provided more diversity which previously had been proven to improve discrimination [6.3-6.4]. The strategy for proto-nose I sensor placements had produced considerable results (Chapter 8). However, as the sensors toward the end of the microchannel were placed too closely together, little additional information can be extracted. Hence they differ only in spatial information, but yield no temporal information. In proto-nose II, the 40 sensors are grouped into eight groups of fives based on their tunings. Within each group, their distances are fixed at 20 mm apart. The placement sequence is specifically designed such that each group of sensors at both ends are the same (group 1 with 8, 2 and 7, etc).

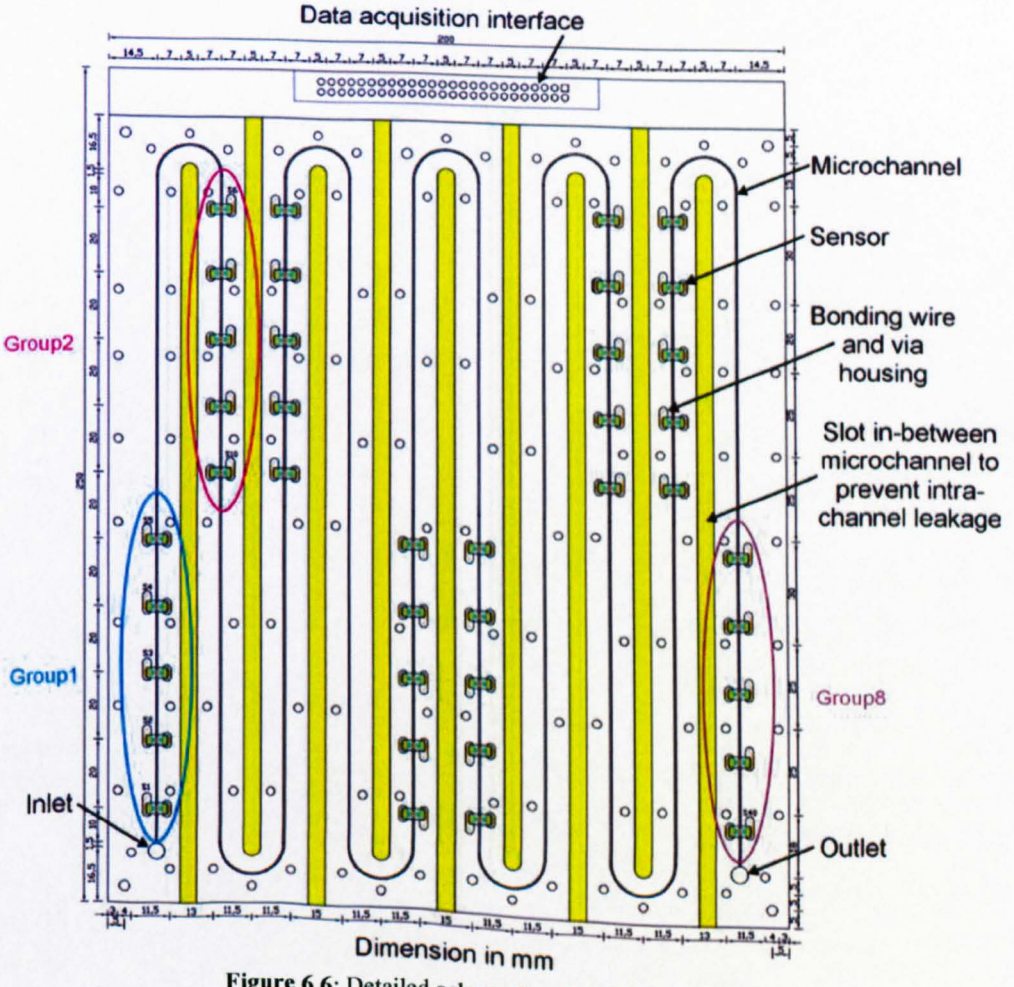

Figure 6.6: Detailed schematic of proto-nose II design.

The details of the sensor types and their placement distances are given in Table 6.2. Figure 6.6 shows the detailed schematic design of proto-nose II. Sensor S1 and S36 are both of type PEVA, S2 and S37 are of type PSB and so on. The distances between S1 to S36 and S2 to S37 are the same; hence some correlations can be made to aid discrimination for these two groups (and others) of sensors. Also shown in Figure 6.6 is the area marked in yellow; these are the slots where sealant can be filled to eliminate intra-channel leakage.

Table 6.2: Sensor placements on the proto-nose II.

No.	Distance (mm)	Type	No.	Distance (mm)	Type
S1	10	PEVA	S21	1260	PVC
S2	30	PSB	S22	1280	PVPD
S3	50	PEG	S23	1300	PBA
S4	70	PCL	S24	1320	PSF
S5	90	PVPH	S25	1340	PCX
S6	240	PVC	S26	1620	PEVA
S7	260	PVPD	S27	1640	PSB
S8	280	PBA	S28	1660	PEG
S9	300	PSF	S29	1680	PCL
S10	320	PCX	S30	1700	PVPH
S11	570	PEVA	S31	1950	PVC
S12	590	PSB	S32	1970	PVPD
S13	610	PEG	S33	1990	PBA
S14	630	PCL	S34	2010	PSF
S15	650	PVPH	S35	2030	PCX
S16	930	PVC	S36	2180	PEVA
S17	950	PVPD	S37	2200	PSB
S18	970	PBA	S38	2220	PEG
S19	990	PSF	S39	2240	PCL
S20	1010	PCX	S40	2260	PVPH

The 3D design of the modified lid is shown in Figure 6.7(a) and the fabricated PCB base (prior to machining) with the Perspex lid is shown in Figure 6.7(b). The assembly technique of the sensor with the base and lid had remained the same as that of proto-nose I shown in Figure 6.3(c). The sensors are glued to their designated locations and wire bonded for electrical connectivity. The lid is then aligned with the base and held in place by numerous screws. Finally, the edges and slots are filled with sealant (3145 MIL-A-46146, Dow Corning, UK) to obtain a leak-free system. The top and bottom view of the fully assembled system are shown in Figure 6.7(c) and (d), respectively.

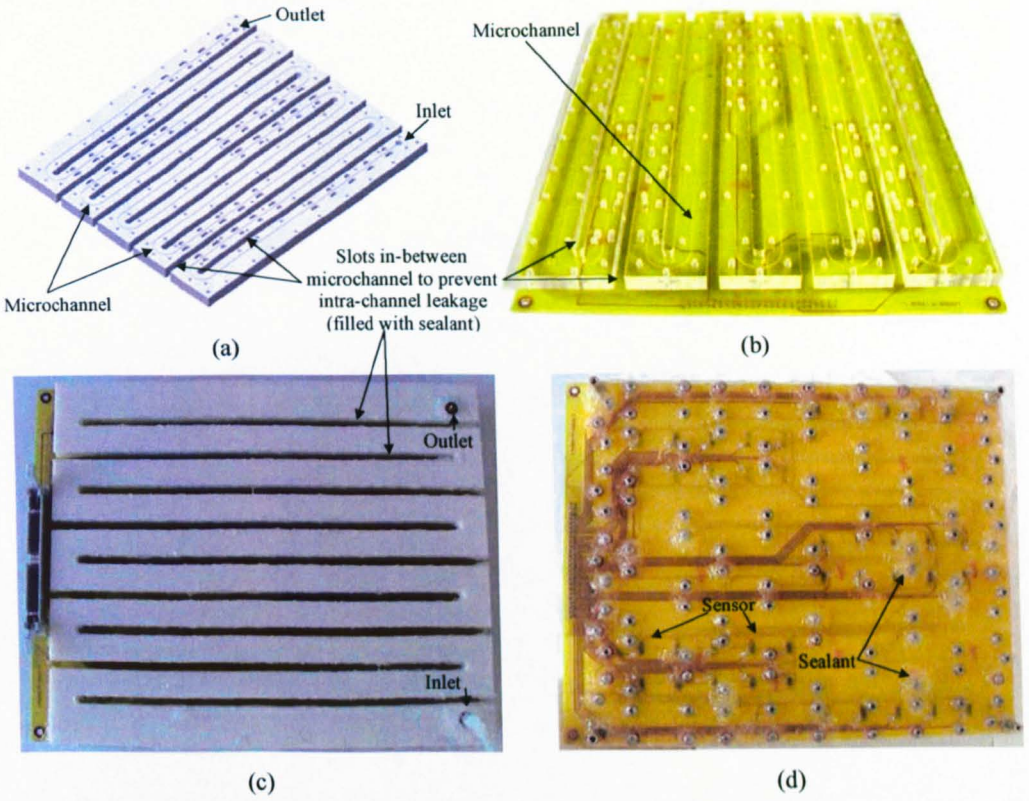

Figure 6.7: Proto-nose II system. (a) STL design of the proto-nose II lid. (b) Fabricated PCB base assembled with Perspex (uncoated) lid. (c) Top-view of the parylene coated proto-nose II system. (d) Bottom-view of the proto-nose II system.

6.3 Nose-on-a-chip microsystems

The design and fabrication of the various components for the NOC have been discussed in previous chapters. In this section, several issues relating to the assembly of these components to realise the NOC microsystem will be discussed. These issues include the alignment of the microchannel package onto the sensor array and sealing it to ensure leak-free integration. To facilitate the characterisation (measuring magnitude variations across the sensor array) of the hybrid-nose and aVLSI-nose sensor arrays prior to assembly, a microchamber was designed and fabricated.

6.3.1 Microchamber design and fabrication

It is essential to characterise the two types of microsensor arrays to study the variation in response magnitudes and profiles prior to assembly with the microchannel packages. Furthermore, the studies of sensor array responses have received widespread interest due

to their improved discriminatory capabilities [6.3-6.4]. Investigation for a suitable microchamber package design has been demonstrated with extensive simulations, as discussed in Chapter 3. The final design consists of a rectangular microchamber with a 40 µl (10 mm × 4 mm × 1 mm) volume. Figure 6.8(a) shows the design for the microchamber with mounting holes that is used to attach the microchamber on top of the microsensor array. A photograph of the fabricated microchamber is shown in Figure 6.8(b).

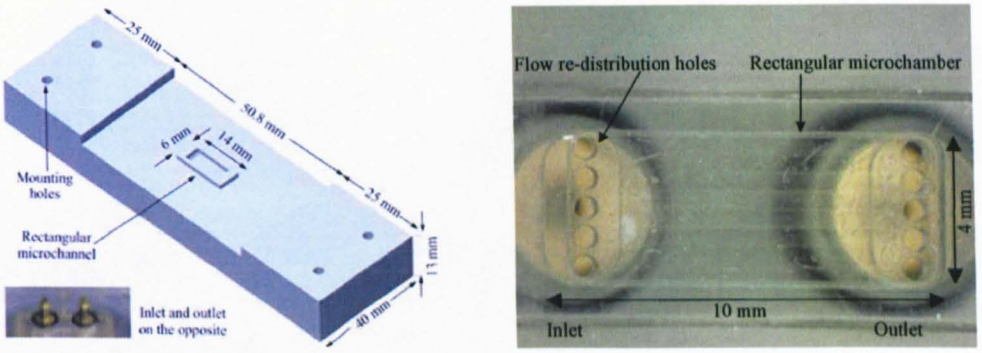

(a) (b)

Figure 6.8: Microchamber design. (a) Bottom design of the microchamber. (b) Photograph of a fabricated microchamber (only the microchamber is shown).

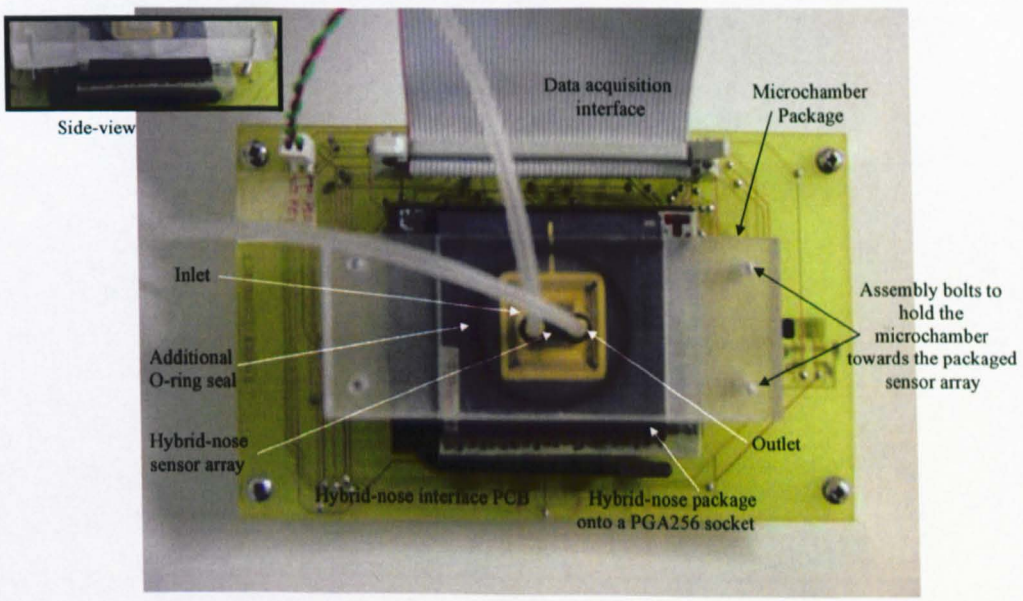

Figure 6.9: Microchamber assembled with hybrid-nose microsensor array.

A fully assembled system with the microchamber package attached to a hybrid-nose sensor array is shown in Figure 6.9. The PCB base has a holder to house the hybrid-nose packaged onto a PGA256 socket. The bolts are attached from the bottom of the PCB to pull the microchamber towards the sensor array and hold them in place (shown in the side-view photograph in Figure 6.9). An O-ring provides a secondary protection against possible leak. Interconnecting tubings are then used to connect this system with the vapour test station. The aVLSI-nose PCB uses the same layout to house the aVLSI-nose; hence the same microchamber can be used for both systems.

6.3.2 Microchannel package with microsensor array alignment

The microchannel package has to be carefully aligned to the microsensor array to ensure each groups of sensors are housed in their designated mini-chamber. To simplify the assembly procedure for ensuring that the microchannel package is placed in the right position, numerous alignment markers are created on the silicon substrate of the arrays.

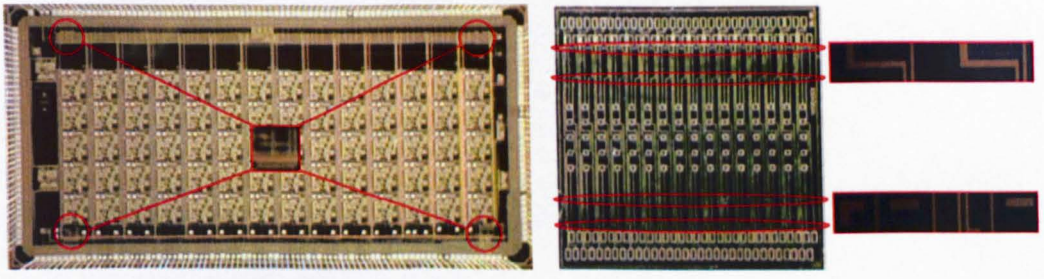

(a) (b)

Figure 6.10: Microchannel package vertical alignment markers. (a) Alignment markers for aVLSI-nose sensor array. (b) Alignment markers for hybrid-nose sensor array.

Figure 6.10(a) shows the alignment markers for the aVLSI-nose and (b) shows the alignment markers for the hybrid-nose. These markers are placed at a fixed distance away from the outer row of sensors to guide the positioning of microchannel package. The above alignment markers are only capable of ensuring that the microchannel package is in the correct vertical position. The horizontal placement is more difficult as most microchannel packages are longer than the horizontal size of the sensor array; hence it is not possible to use the same alignment technique.

Figure 6.11 shows two different types of base designs for the microchannel package, as discussed in Chapter 5. Figure 6.11(a) shows the slot type design where the

sensor array can be slotted into place. The horizontal alignment was guided by the edge of the slot while the vertical alignment is adjusted against the vertical markers. The step type of base design is similar except that it can be pushed down from the top. This design has numerous advantages over the former design. Firstly, this type of base design allows a packaged sensor array to be assembled, while in the former case, the sensor array has to be removed from the packaging as it can only be slotted in. Secondly, the slot type base design requires the sensor array to slot-in, thereby creating potential of damaging the deposited sensing materials on the surface of the array.

(a) (b)

Figure 6.11: Microchannel package base designs for horizontal alignment. (a) Base design 1 (slot type). (b) Base design 2 (step type).

6.3.3 Sealing

Besides ensuring the packaging is in the right location, sealing was also important. Each group of sensors have to be housed in the right 'mini-chamber' and there should be no inter-mini-chamber leakage. The base of the package was applied with a thin layer of resin (the same resin used to build the package, see Section 5.3.4 for details) before they are aligned and press together with an in-house designed jig. The nose-on-a-chip system is then cured with UV light to produce a leak-free system.

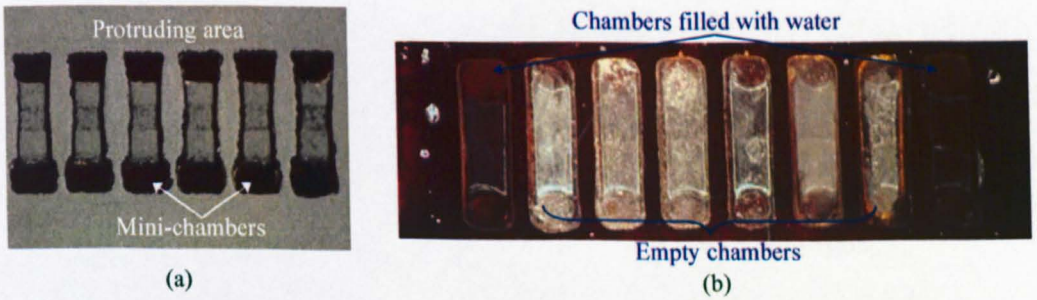

(a) (b)

Figure 6.12: Microchannel package sealing. (a) Microchannel package base. (b) Microchannel package leakage characterisation showing no leakage across different mini-chambers.

Figure 6.12(a) shows the base of a microchannel package prior to assembly. The protruding area was coated with a thin layer of liquid resin. In Figure 6.12(b), it is

assembled with a glass plate to study the leakage characteristics. The mini-chambers at each end were filled with water while the rest were empty. No inter-chamber leakage was observed as water was injected to fill the remaining chambers. Figure 6.13 shows the photographs of 4 fully assembled systems. A photograph of MSL101 package (slot type) assembled with the hybrid-nose is shown in Figure 6.13(a) while another hybrid-nose assembled with MSL102 (step type) is shown in (b). In Figure 6.13(c), a MSL115 package was assembled with a hybrid-nose sensor array while in (d), a MSL113 was assembled with the aVLSI-nose sensor array. An in-house jig (not shown here) was used to guide the microchannel package to the general location. The precise location was then adjusted against the alignment markers under a microscope before they were pressed together. Once assembled and cured, the nose-on-a-chip system was ready for use. As a precautionary measure, an additional sealant was applied along the outer edges of the interface. For taller packages, external supporting structures were used to reinforce the assembly.

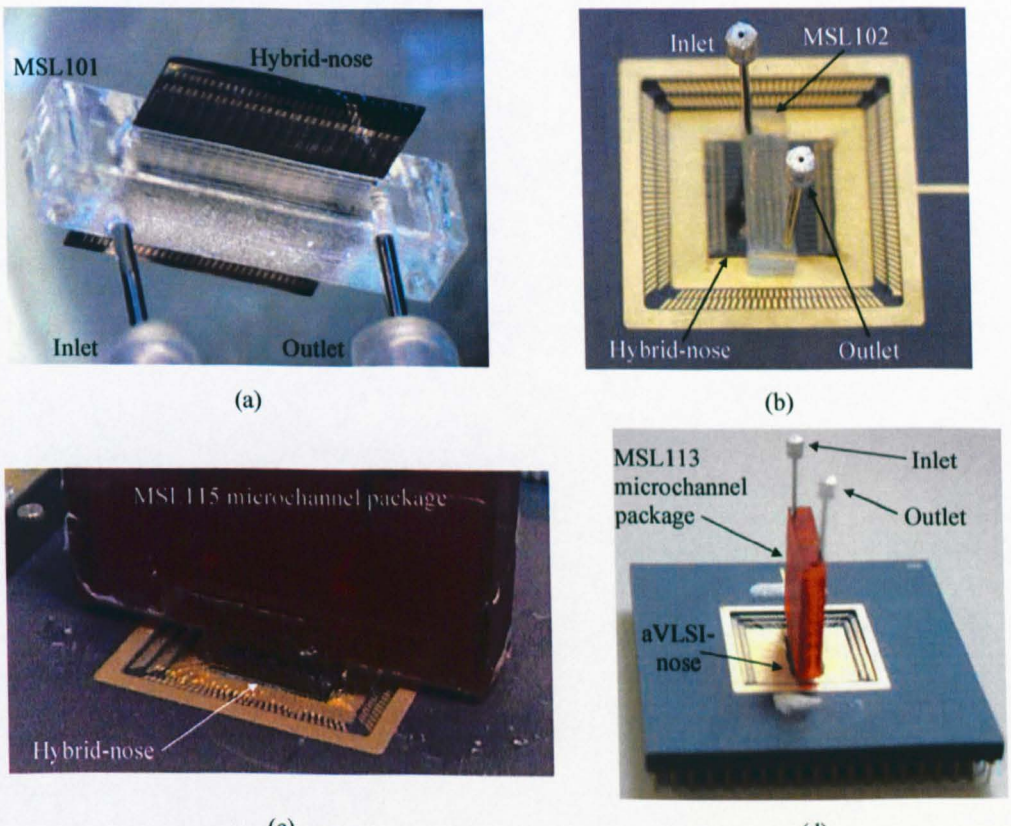

Figure 6.13: Fully assembly nose-on-a-chip microsystems. (a) Hybrid-nose assembled with MSL101 (slot type). (b) Hybrid-nose assembled with MSL102 (step type). (c) Hybrid-nose assembled with MSL115. (d) aVLSI-nose assembled with MSL113.

6.4 Stationary phase deposition

Both the proto-noses and microchannel packages require a thin layer of uniform stationary phase coating. A study was conducted to determine the techniques used to coat commercial GC columns. It was found that the coating techniques could be largely divided into two groups, namely the dynamic and static techniques [6.5-6.6]. Besides the actual coating process, some pre and post processing of the column were required. In addition, a survey of the coating techniques used in the recently emerging micro-GC columns was done as they offered many similarities with the coating of microchannel packages.

Contemporary GC coating technology for the preparation of a column is both time consuming and requires three major, individually executed steps. These are surface deactivation, coating and stationary phase immobilization [6.7]. Column deactivation is an important step as the fused silica capillary inner wall (a commonly used GC column material) is prone to undergo adsorptive interactions with the stationary phase coating material. It is also used to reduce these active surface sites. This has the effect of chemical and/or physical modification to enhance surface wettability [6.7]. The static coating is usually used to coat the capillary inner wall of the stationary phase. Immobilization is necessary to avoid undesirable effects through free cross-linking that leads to the formation of chemical bridges between coated polymer molecules of the stationary phase. It greatly controls the tendency to lose viscosity with increasing temperature during temperature programming and it produces a stationary phase film that is resistant to wash out by organic solvents [6.7]. This is especially important for the moderate polar to polar stationary phases.

In the dynamic coating technique, a solution containing about 10 % liquid phase dissolved in a suitable low-boiling solvent is forced through a column under closely controlled flow conditions [6.5-6.6, 6.8]. Helium or other inert gases is usually used to force this volume of solution through the column at a velocity of approximately 1-2 cm s^{-1}. Continual flushing with helium after coating evaporates the remaining solvent and leaves a thin coating of stationary phase. Due to this continuous flushing, the liquid stationary phase can move towards the end of the column, causing an uneven thickness. As the coating solution discharges from the end of the column, the coating velocity increases sharply; which also results in a thicker film at the end of the column. A buffer column is often attached to the end of the column to avoid this problem.

In the static coating technique, the column is completely filled with a dilute solution of the liquid phase, dissolved in a suitable low-boiling point solvent. The completely filled column is sealed at one-end, while the other end is either connected to a vacuum pump or it is left at an elevated temperature (250 °C to 400 °C) to allow the solvent to evaporate under quiescent condition. The static coating technique is reported to yield a highly uniform column that results in higher separation efficiency and resolution although it is time consuming compared to the dynamic technique. Two important conditions are necessary to produce a highly uniform coating [6.8]. Firstly, the solution of stationary phase must be absolutely free of dissolved gas in order to prevent dispersion of the solution inside the column. Secondly, the column must be completely free from bubbles within the sealed column.

For micro-GC columns, similar techniques have been used. Wiranto *et al.* [6.9] coated their micro-GC column using the dynamic coating scheme by forcing the stationary phase dissolved in a volatile solvent through the column at a constant velocity. Alternative coating techniques were investigated by Hudson *et al.* [6.10] from Sandia National Laboratory, although details are not available. Terry *et al.* [6.11], who created the first micro-GC column, employed a dynamic coating technique by blowing the dissolved stationary phase through the column. Kolesar *et al.* [6.12] employed a radically different approach to coat their column. An etched silicon wafer was evaporated with the stationary phase using a sublimation technique. Then, the wafer was polished prior to anodically bonding it to a Pyrex lid to form the coated micro-GC column. Although static coating technique is more popular with commercial GC columns, it was noted that dynamic coating technique is more commonly used with micro-GC columns.

Polyethylene glycol (PEG, polar compound), a widely used stationary phase material (also known as CW20M or more commonly called carbowax [6.13]) was initially used for experimental coating on the proto-nose microchannel using the static technique. The PEG static coating procedure is as follows. Firstly, the column was cleaned with an organic solvent diethylether for 30 s and dry with clean air. Next, the column was filled with a solution (PEG 5 g, dichloromethane 20 ml) and held for 30 minutes at room temperature. Lastly, the column was heated to 100 °C in an oven and held for 24 hours.

The above coating processes were based on common practice used to coat commercial glass and fused silica capillary columns [6.13]. The process has been modified as the material used was not able to accommodate high temperature. To enable the immobilization of the column at this lower temperature, the drying duration was doubled. Figure 6.14 shows 3 photographs of the coating process. In Figure 6.14(a), a photograph of the microchannel prior to cleaning is shown. Once cleaned and dried, the microchannel was filled with the mixture solution (PEG in dichloromethane) using a syringe. As it is left to stabilise at room temperature, it resembles the photograph in (b). Once it is dried in the oven for over 24 hours, it becomes (c).

Although the process can be easily replicated in-house, it did not result in a thin film coating (< 25 μm). The thickness achieved was in excess of 100 μm, hence other techniques were explored.

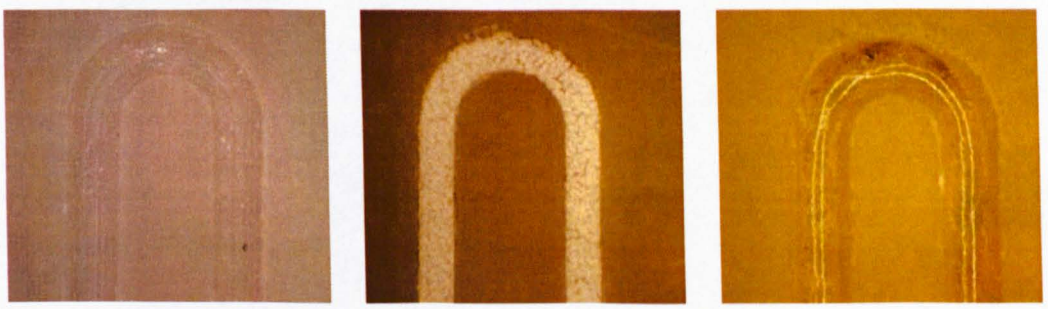

(a) (b) (c)

Figure 6.14: Deposition of stationary phase using static coating. (a) Microchannel prior to cleaning. (b) Microchannel filled with PEG solution. (c) Microchannel after immobilization.

The coating techniques for traditional GC columns have remained the same for many years. An exception to this is the introduction of simpler techniques that attempt to combine various stages together, and one such technique is the sol-gel based method [6.14]. For micro-GC system, the stationary phase coating process is still evolving due to the reduction in column dimensions, overall size and assembly (usually a micromachined channel is bonded to a glass plane to form a long microchannel instead of a standard tube). Recently, an evaporation technique using a commercial machine (PDS 2010 Labcoater™ 2, Specialy Coating Systems, Indianapolis, USA, as shown in Figure 6.15(a)) was introduced by Hesketh *et al.* [6.15]. The material used is parylene C (Poly mono-chloro-para-xylylene) which is similar to other stationary phase materials. However, as this material is new as a stationary phase, its retention characteristics have

not been fully studied (hence the diffusion and partition coefficients of various analytes are not available) although initial investigation showed that it had a similar retention characteristics to PEG [6.15].

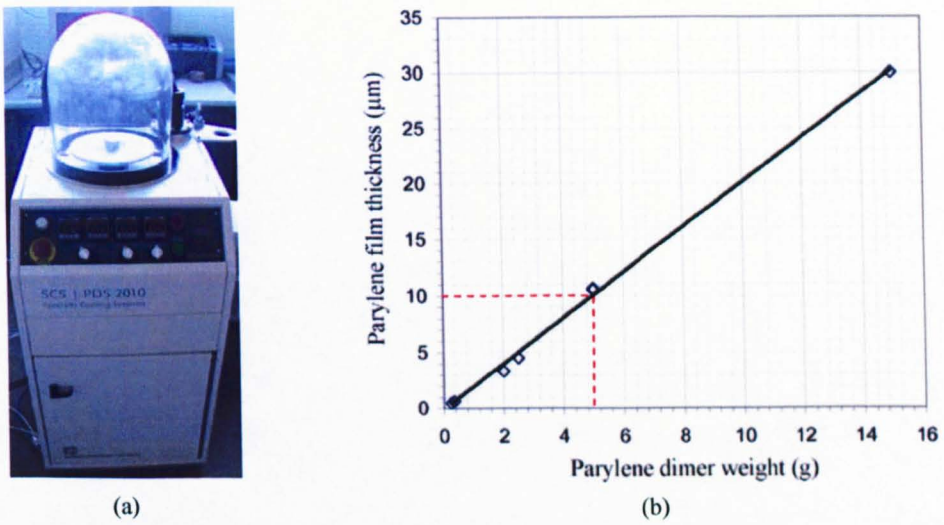

(a) (b)

Figure 6.15: Parylene deposition. (a) Photograph of PDS 2010 Labcoater™ 2, Specialty Coating Systems, Indianapolis, USA. (b) Parylene film thickness versus dimer weight.

The parylene deposition machine performs deposition under vacuum at room temperature, and hence, is well suited for both the proto-noses and microchannel packages. The parylene deposition process is as follows [6.16]:

- A fixed amount of parylene dimer (parylene C) is loaded according to the desired final coating thickness (~ 2 µm per 1 g as shown in Figure 6.15(b)).
- Solid phase parylene dimer becomes gas phase parylene dimer at 175 °C.
- Parylene dimer is then pyrolized into reactive monomers at 690 °C.
- The reactive monomers are introduced into the chamber where samples become polymerized as soon as they contact any surfaces inside the chamber that is kept at room temperature.
- The excess amount of dimer is collected in a chiller thimble to protect the vacuum pump.
- The inner pressure of the system is kept at 25 mBar (2.5 kPa).
- The total deposition time depends on the final thickness. It usually takes 3.5 hours for a film thickness of 10 µm including the heating time.

Figure 6.15(a) shows a photograph of the parylene deposition system. The bell jar has been improvised to accommodate proto-nose II. A specially designed holder was fabricated to allow the proto-nose to be attached to the central shaft, which rotates during the deposition process, so as to ensure uniform deposition. Figure 6.15(b) shows a plot of the parylene dimer weight against the deposited film thickness [6.17]. For a 10 μm thick film, 5 g of dimer was required.

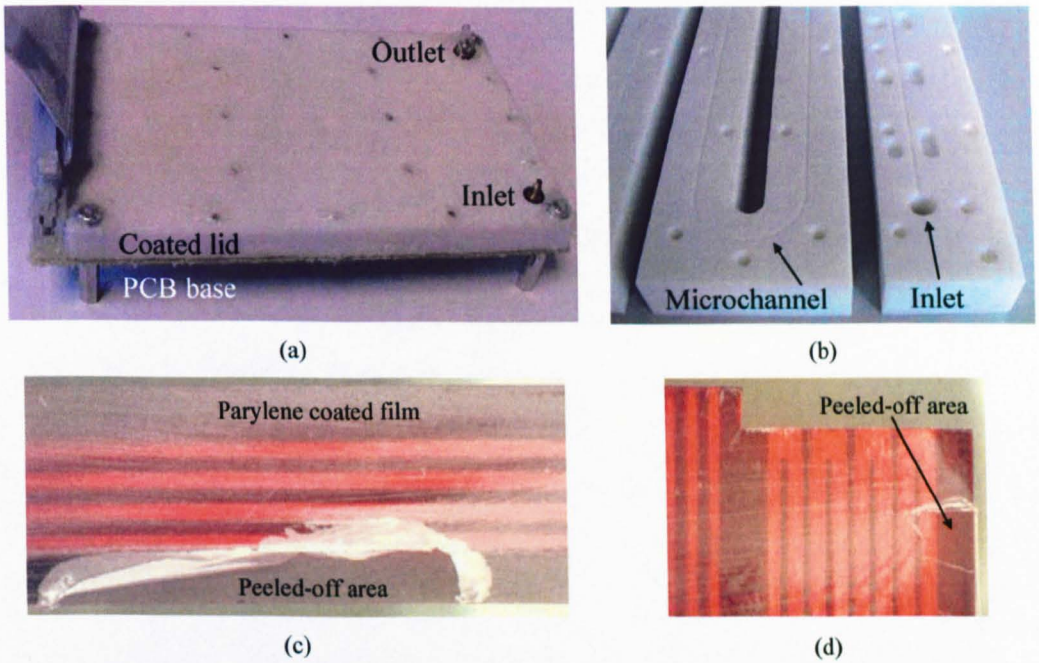

Figure 6.16: Parylene C coated proto-noses and microchannel packages. (a) Parylene coated proto-nose I. (b) Parylene coated proto-nose II. (c) Parylene coated MSL113. (d) Parylene coated MSL115.

Figure 6.16(a) shows a photograph of the coated proto-nose I while (b) shows a photograph of the coated proto-nose II. It is difficult to observe the difference between coated and uncoated surfaces. The main difference between them is that the coated lid appears to be glossier. For the microchannel packages, as the outer surfaces are not used, the coatings on these surfaces were not critical. To simplify the process, masking tape is used to hold the microchannel packages onto the rotating base platform. This was necessary to ensure these small packages will not be sucked into the vacuum pump during the de-pressurisation of the vacuum chamber. A disadvantage of this technique is that those surfaces covered by the tape were not coated. Also, when the tape is removed, the films along the edges tend to peel off. The results are shown in Figure 6.16(c) and (d)

for MSL113 and MSL115 respectively. However, this does not affect the coating within the microchannel. These parylene coated parts were then ready to be assembled with their respective counterparts as explained earlier.

6.5 Conclusions

In this chapter, the integration of the nose-on-a-chip microsystem has been discussed. The assembly processes for the two proto-noses were presented and the removal of intra-channel leakage by proto-nose II was explained. The design and fabrication of the fast-nose microsystem which was used to characterise the discrete sensors was also discussed.

In the previous two chapters, the fabrication of the two microsensor arrays (hybrid-nose and aVLSI-nose) and microchannel packages were discussed. Here, the procedures used to assemble these components to create the nose-on-a-chip microsystem were reported. Finally, the process used to coat the proto-noses and microchannel packages was described. This process deposits a thin layer of uniform retentive material onto the inner surface of the microchannel to act as the stationary phase of the column. Upon assembling the nose-on-a-chip microsystem, it is necessary to interface the system to the data acquisition and vapour test systems; this will be described in the next chapter.

6.6 References

[6.1] M. Frank, H. Ulmer, J. Ruiz, P, Visani, U. Weimar, ***Complementary analytical measurements based upon gas chromatography-mass spectrometry, sensor system and human sensory panel: a case study dealing with packaging materials***, Analytica Chimica Acta 431, pp. 11–29, 2001.

[6.2] T. Aishima, ***Correlating sensory attributes to gas chromatography–mass spectrometry profiles and e-nose responses using partial least squares regression analysis***, Journal of Chromatography A, 1054, pp.39–46, 2004.

[6.3] K.J. Albert, N.S. Lewis, C.L. Schauer, G.A. Sotzing, S.E. Stitzel, T.P. Vaid, D.R. Walt, ***Cross-reactive chemical sensor arrays***, American Chemical Society, Chemical Review, Vol. 100, No. 7, pp. 2595-2625, 2000.

[6.4] H.V. Shurmer, P. Corcoran, J.W. Gardner, ***Integrated arrays of gas sensors using conducting polymers with molecular sieves***, Sensors and Actuators B 4, pp. 29-33, 1991.

[6.5] W. Jennings, ***Gas chromatography with glass capillary columns***, 2nd edition, Academic press, New York, 1980.

[6.6] M.L. Lee, F.J. Yang, K.D. Bartle, ***Open tubular column gas chromatography: theory and practice***, John Wiley and Sons, New York, 1984.

[6.7] D.X. Wang, S.L. Chong, A. Malik, ***Sol-gel column technology for single-step deactivation, coating, and stationary-phase immobilization in high-resolution capillary gas chromatography***, Analytical chemistry, 69, 1997, pp. 4566-4576.

[6.8] S.M. Volkov, V.M. Goryayev, V.I. Anikeyev, ***Coating of glass capillary chromatographic columns: a new variant of the static method***, Journal of chromatography 190, 1980, pp. 445-447.

[6.9] G. Wiranto, M.R. Haskard, D.E. Mulcahy, D.E. Davey, E.F. Dawes, ***Microengineered open tubular columns for GC analysis***, Proc. of SPIE-Electronics and Structures for MEMS, Royal Pines Resort, Queensland, Australia, Oct 1999, pp. 168-177.

[6.10] M.L. Hudson, R. Kottenstette, C.M. Matzke, G.C. Frye-Mason, K.A. Shollenberger, D.R. Adkins, C.C. Wong, ***Design, testing and simulation of microscale gas chromatography columns***, DSC-Vol. 66, MEMS, ASME Int. Mechanical Engineering Congress and Exposition, 1998, pp. 207-214.

[6.11] S.C. Terry, J.H. Jerman, J.B. Angeli, ***A gas chromatographic air analyzer fabricated on a silicon wafer***, IEEE Transaction on Electron Devices, 1979.

[6.12] R.P. Reston, E.S. Kolesar, ***Silicon-micromachined gas chromatography system used to separate and detect ammonia and nitrogen dioxide, Part I: Design, Fabrication and Integration of gas chromatography system***, Journal of the Microelectromechanical System, Vol. 3, No. 4, Dec 1994.

[6.13] C.F. Poole, Q.L. Li, W. Kiridena, W.W. Koziol, ***Selectivity equivalence of poly (ethylene glycol) stationary phases for gas chromatography***, Journal of Chromatography A, vol. 898, pp. 211-226, 2000.

[6.14] J.D. Hayes, A. Malik, ***Sol-gel chemistry-based ucon-coated columns for capillary electrophoresis***, Journal of Chromatography B, 695, pp. 3-13, 1997.

[6.15] H.S. Noh, P.J. Hesketh, G.C. Frye-Mason, ***Parylene gas chromatographic column for rapid thermal cycling***, J. Microelectromechanical Systems, vol. 11, no. 6, pp. 718-725, 2002.

[6.16] Cookson Electronics, Specialty Coating Systems, ***Labcoater PDS2010 parylene deposition machine user reference manual***, Indianapolis, USA, June 2004.

[6.17] T. Stanzchk, E. Kasman, ***Labcoater 1 parylene deposition unit***, http://www.mal.uic.edu/manuals/PARYLENE.PDF#search='parylene%20thickness', Microfabrication Applications Laboratory, University of Illinois at Chicago July 2004.

Chapter 7

Micro gas test station for device characterisation

7.1 Introduction

In this chapter, the data acquisition electronics and vapour test station necessary for the characterisation of different nose microsystems is fully described. The designs of these components are complicated by the fact that significant flexibility is required to accommodate three different olfactory system interfaces. In this chapter, various aspects of the test systems, including the electromechanical interfaces and the vapour test station, will be discussed. The software required to control the vapour test station and data acquisition hardware is also important due to the flexibility required to automate different systems. Many communication protocols are implemented using software to reduce hardware cost and to simplify the interfacing. In addition, the testing has been automated by the same software to free the operator when performing experiments over a long period of time.

7.2 Vapour test station

The vapour test station (VTS) provides a repeatable process for generating consistent amount of test analytes to the microsystem under test. It was decided at the start of the project that this miniature system will not have any form of environmental (temperature and humidity) control unlike some commercial systems [7.1-7.2] so that it relates better to real world operating conditions. As a result, the final system will be smaller and consume less power (because it does not need to maintain constant temperature or humidity), making it more suitable for low-cost, portable implementation.

7.2.1 System setup

The schematic of the VTS setup is shown in Figure 7.1. The micropump, located at the input, pumps environmental air through the test liquids and across the microsensors. The system operates in a binary mode in which the test analyte is switched in and out of the carrier gas flow. Prior to the injection of test analyte, carrier gas is selected (green route, V_C ON, V_1 & V_2 OFF) to flow through the system for a user defined period of time. The test analyte is then injected by switching V_C OFF and V_1 or/and V_2 (single or mixture) ON for a designated duration. The valves are then switched back to allow the carrier gas to flow. On the test analytes route, depending upon the desired analytes, V_1 or V_2 (single analyte test) or V_1 & V_2 (mixture test) will be switched ON.

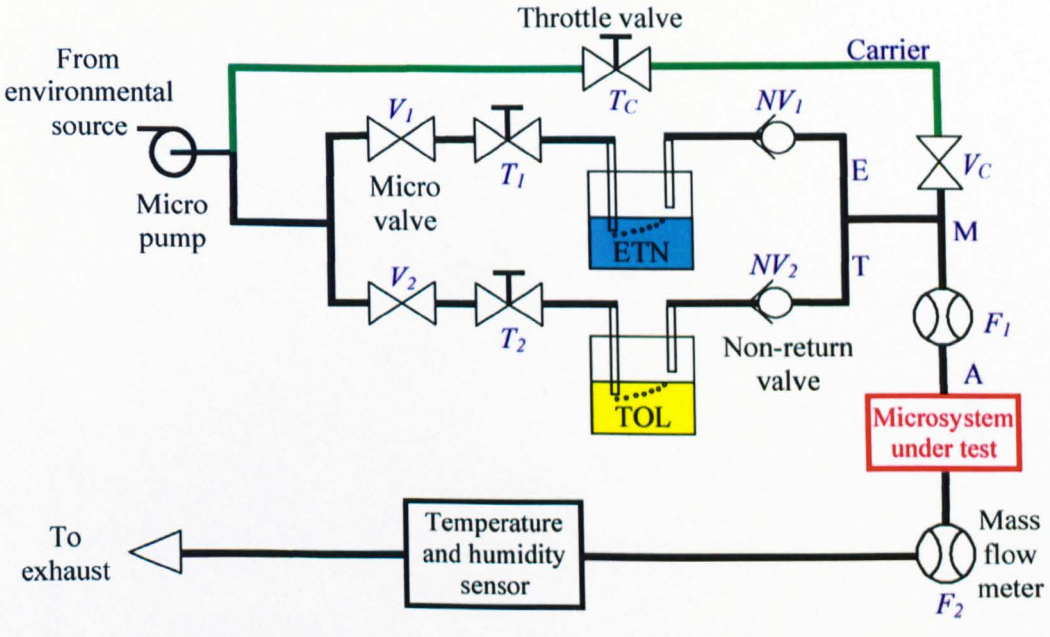

Figure 7.1: Schematic of vapour test station setup (refer to the legend in Table 7.1)

The throttle valve (T_C) in the carrier gas route provides an additional means to control the flow rate (beside the micropump) of the carrier gas while the two throttle valves (T_1 & T_2) in the analyte routes are meant to ensure an even blend (50 % to 50 % mix ratio) when a compound analyte test is selected. The two analytes are combined (at the junction T/E) to produce the mixture, which is joined with the carrier gas at point M. At each end of the system-under-test are two mass flow meters (F_1 & F_2) which are used to measure

the flow rate and leakage of the system. The piping (at point A) between the mixture outlets and the inlet of the system-under-test is critical as slight broadening can occur if it is too long. The test analyte finally passes through a temperature and humidity sensor (two-in-one integrated sensor) before it is routed to an exhaust. In order to vary the concentration of the test analytes, they are placed in a cooling bath (Colora, Messtechnik GmBH Germany). A key to the VTS system is given in Table 7.1.

Table 7.1: Hardware components of the VTS system.

Symbol	Part	Photograph	Supplier	Usage
	Micropump		KNF Neuberger, UK NMP-05	To transport carrier gas and test analytes
	Microvalve		Lee Co., UK LFAA1206110H	Select between carrier gas and test analytes
Temperature and humidity sensor	Temperature and humidity sensor		Sensirion AG, Switzerland AH31	Temperature and humidity measurement
	Mass flow meter		Sensirion AG, Switzerland ASF1430	Flow rate and leakage rate measurement
	Throttle valve		Cole-Parmer, UK	Regulate carrier gas and test analytes flow rate
	Non-return valve	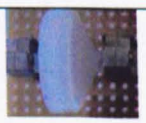	Cole-Parmer, UK	Ensure unidirectional flow
	CFLEX tubing		Cole-Parmer, UK	For inert carrier gas
	PTFE tubing		Cole-Parmer, UK	For corrosive test analytes

Figure 7.2(a) shows a photograph of the cooling bath and (b) a photograph of the VTS. The system has been inter-connected using flexible CFLEX (Tygon 3350 silicone, platinum-cured, EW-06424-60, Cole-Parmer UK) tubing on the carrier gas route and with inert Poly (tetrafluoroethylene) (PTFE, EW-06407-41, Cole-Parmer UK) tubing on the remaining interconnections.

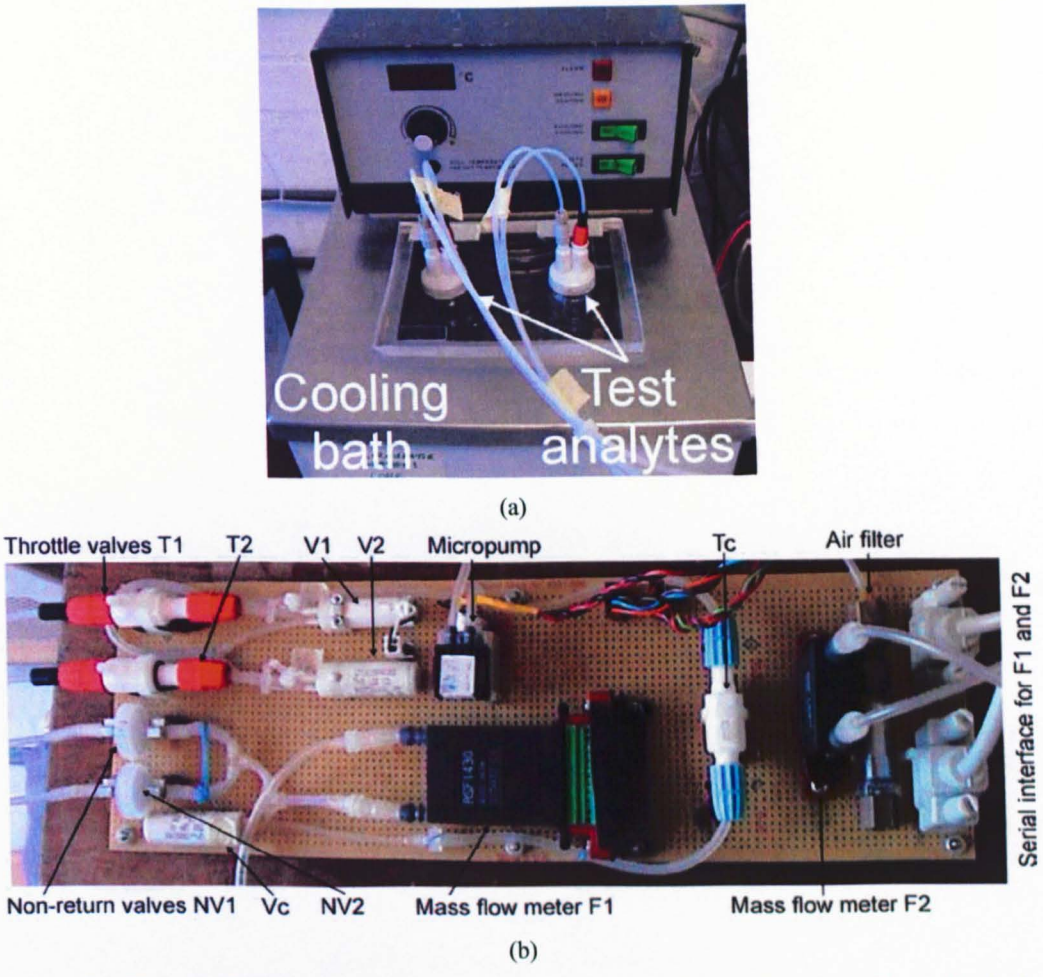

Figure 7.2: Photographs of the vapour test station. (a) Photograph of test analytes placed in cooling bath. (b) Photograph showing various components of VTS.

7.2.2 Electronic interfaces and controls

It is essential to be able to control the VTS electronically so that the measurements can be automated over long duration without human intervention. A general purpose PC installed with a National Instruments (NI) PCI-DIO-96 [7.3] digital I/O (input/output) card is used to interface to the VTS and data acquisition system. LabView™ (version 6.1) from NI is the host software used to automate the system. Complex electronic interfaces for the VTS components were required as digital I/O only provide two states (ON/OFF) that is only suitable for controlling devices, like the microvalve.

Figure 7.3 shows the interface electronics for the mass flow meter (ASF1430 [7.4], Sensirion) and microvalve (LFAA1206110H, Lee Co., UK). Figure 7.3(a) shows the microvalve control interface via port C pin 4 for valve V_1. A Transistor-Transistor-

Logic (TTL) signal from the I/O card was used to turn ON the power transistor (for switching the high power microvalve at + 12 V). A diode was used to protect against back emf (electro-motive force) voltage spikes generated by the microvalve inductive coil during switching. The two other microvalves have the same circuit configuration except they are controlled by different I/O port pins. Figure 7.3(b) shows the interface of a mass flow meter connected to the serial port of the PC. Although the flow sensor has an integrated temperature sensor (required for internal temperature compensation for flow rate adjustment), it is not used as it reduces the data acquisition rate for the flow rate data.

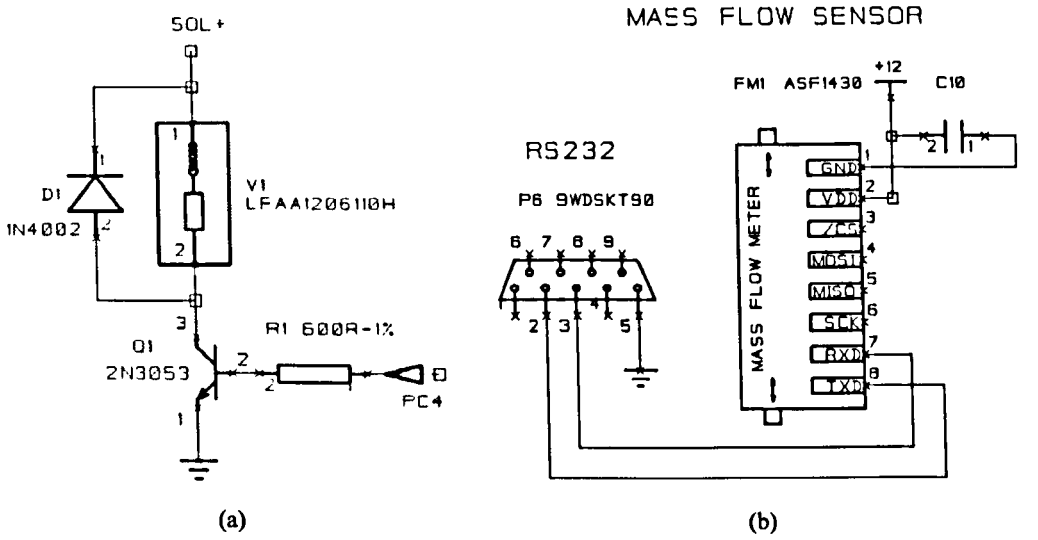

Figure 7.3: Schematics of interface electronics to microvalve and mass flow meter. (a) Microvalve interface control electronics. (a) Mass flow meter interface control electronics.

Figure 7.4(a) shows the electronic interface for the programmable voltage source using the LTC1446 [7.5] (12-bit serially programmable digital to analogue converter (DAC)) to control the micropump. The timing protocol (Figure 7.4(b)) [7.5] used to program the desired output voltage has been implemented in software (LabView) by generating the appropriate protocol on the digital output pins connected to the DAC. As the DAC produces a range of between 0 to 4.096 V (12-bit), an external differential amplifier is used to increase the voltage range to 5 V.

Although the DAC is capable of providing a differential output, it is not required because the micropump only operates between 0 - 5 V. A differential amplifier connected to the output of the DAC amplifies the signal to between 0 - 5 V by providing a marginal gain of + 1.22.

$$V_{OUT}(AN1) = OUTB\left(\frac{R25+R27}{R12+R13}\right)\frac{R23}{R25} - OUTA\left(\frac{R27}{R25}\right) \quad (7\text{-}1)$$

$$V_{OUT}(AN1) = 1.22\times OUTB - 0.84\times OUTA \quad (7\text{-}2)$$

Equation (7-1) gives the output voltage for the differential amplifier implementation shown in Figure 7.4(a). The equation can be computed to give the effective values in Equation (7-2). This translates to a resolution of 1.22 mV per bit.

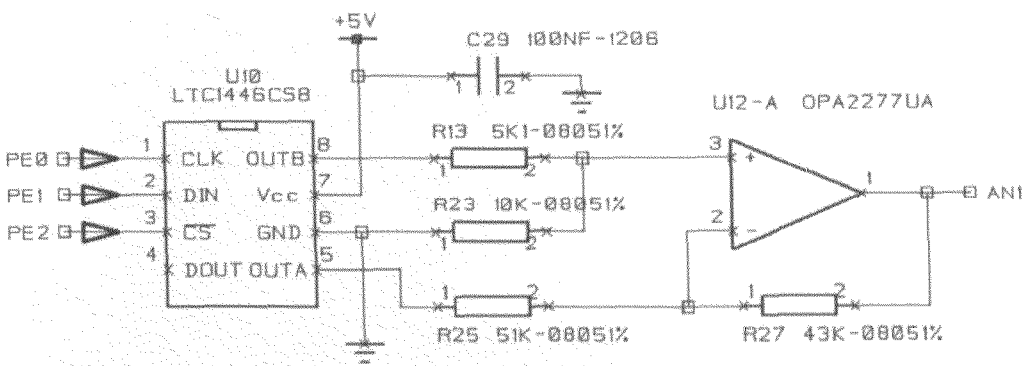

(a)

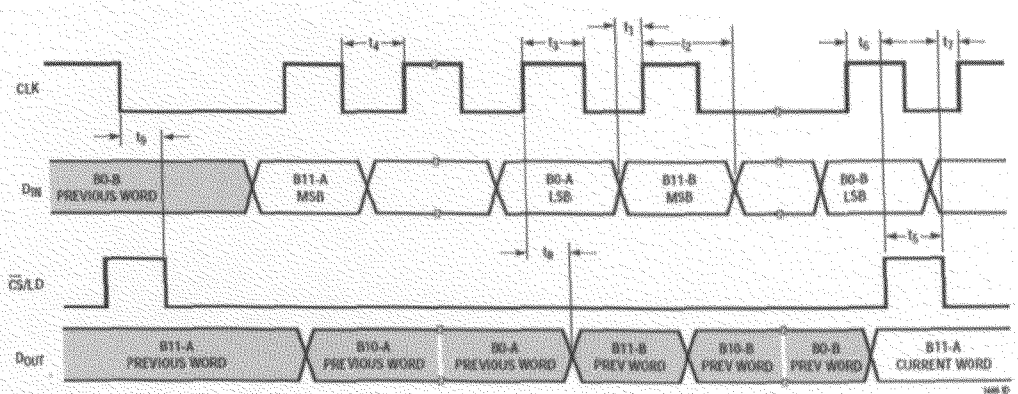

(b)

Figure 7.4: Micropump programmable operating voltage. (a) Interface for serially programmable DAC with amplifier circuit. (b) Timing protocol of LTC1446 [7.5].

The voltage from the amplifier (Figure 7.4(a)) does not provide enough power to drive the micropump (KNF Neuberger, UK) as it required large peak currents. Thus, an

external driving circuit was used to control the micropump from the power source directly. To facilitate the monitoring of the operating current of the micropump, a current sensing circuit, shown in Figure 7.5, was built. This circuit was designed to convert the current drawn by the micropump into a voltage signal that can be measured by an 8-bit analogue to digital converter (ADC, AD7819 [7.6]). To reduce the number of digital I/O required, the parallel ADC was interfaced to a parallel to serial converter (MC14014 static shift register [7.7]) before connecting to the data acquisition card.

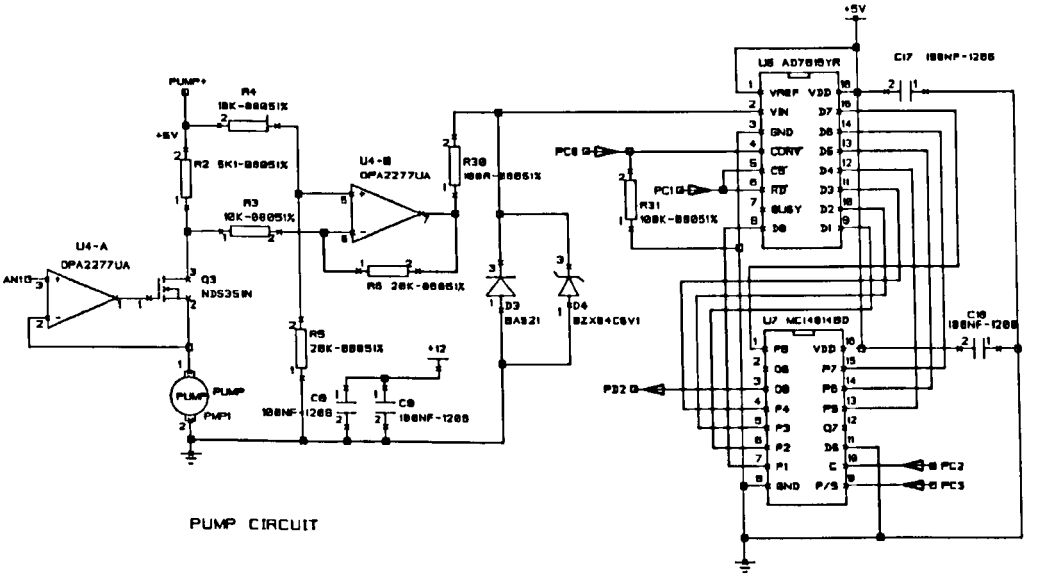

Figure 7.5: Micropump interface electronics with current sensing ADC.

Temperature and humidity measurement is important as they can be used to compensate for fluctuations in sensor responses due to environmental variations [7.8-7.9]. An integrated temperature and humidity sensor (AH31, Sensirion [7.10]) was used for this purpose. The AH31 has a unidirectional serial peripheral interface (SPI) that provides an updated 8-bit relative humidity and an 8-bit temperature output every 512 cycles of the clock (CLK). The CLK is generated by a comparator (LM311) oscillatory circuit with an output frequency of 38.46 kHz. Figure 7.6(a) shows the electronic interface while Figure 7.6(b) shows the timing protocol used to read out the data. Similarly, the SPI protocol was implemented in software using LabView.

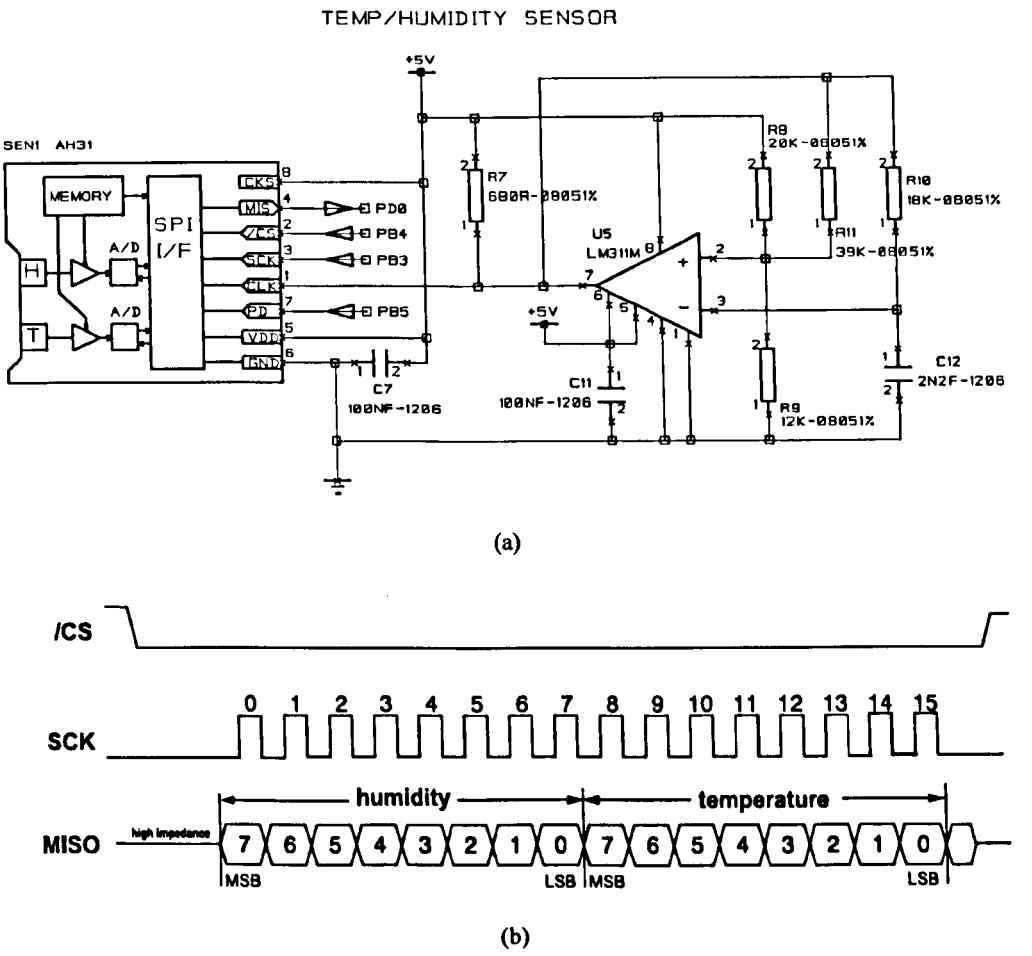

(a)

(b)

Figure 7.6: Temperature and humidity sensmitter (AH31, Sensirion) interface and timing protocol. (a) Electronic interface for AH31. (b) Timing protocol for reading the humidity and temperature data.

7.3 Data acquisition system

The custom data acquisition system was interfaced through the NI data acquisition card (PCI-DIO-96), which is also used to control the VTS (18 digital I/Os were used for VTS). The fast-nose system, the proto-nose system and the hybrid-nose system use the same data acquisition hardware. As the design and interface of aVLSI-nose was not compatible with other nose systems, an additional AT-MIO-16XE50 (NI) [7.11] data acquisition card was installed. This was necessary as the aVLSI-nose already has an integrated current source, therefore the resistive sensing circuit used to translate resistance variation into voltage variation could not be used. As the digital I/Os on this new card were insufficient, 4 extra I/Os from the previous card (PCI-DIO-96) were used to control the multiplexing of sensors for the aVLSI-nose.

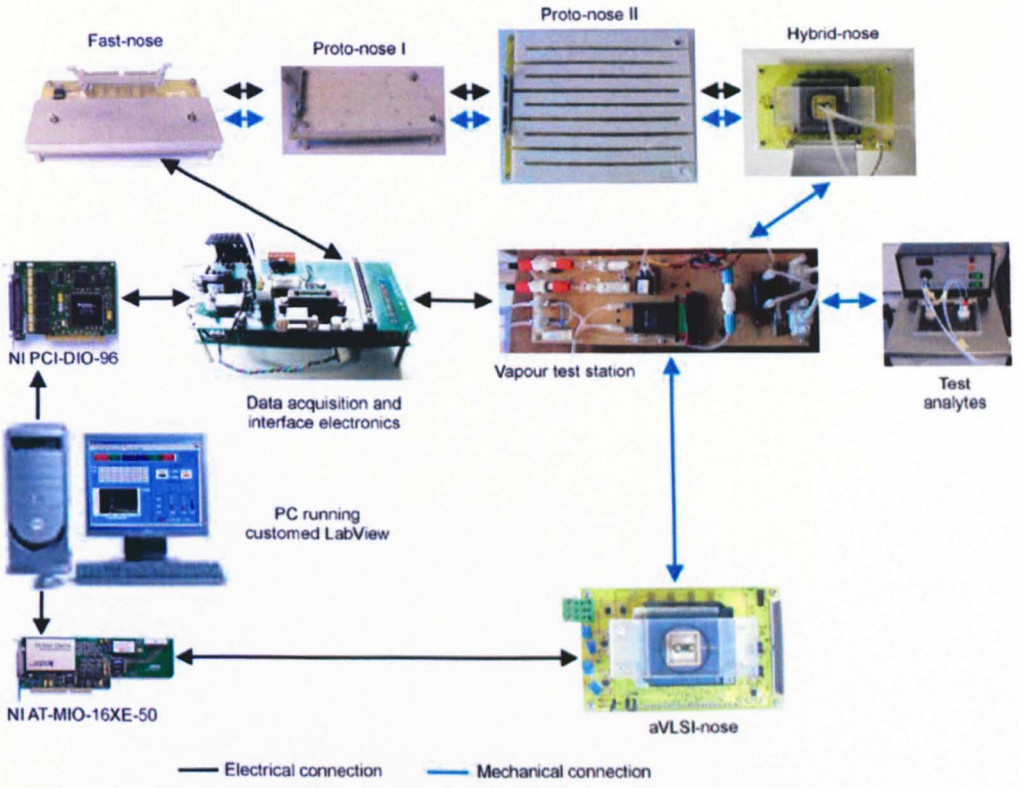

(a)

(b)

Figure 7.7: Overview of system setup. (a) Overall system setup for various noses. (b) Photograph of the complete system.

Figure 7.7(a) shows a pictorial overview of the complete system setup and (b) shows a photograph of the complete system. A PC installed with two NI cards running custom-designed LabView software was used to automate the control and data logging.

7.3.1 Data acquisition electronics

The data acquisition electronics are the circuitries required to support the interfacing for fast-nose, proto-nose and hybrid-nose microsystems to the National Instruments data acquisition card residing in the PC. Here, a general overview of the two basic components is given before a more detailed discussion on each system is presented.

Figure 7.8 shows the setup for a sensor bank (of 8 sensors) resistance measurement multiplexing circuit. A simple op-amp configured in the inverting mode is used for each sensor bank together with an 8-to-1 multiplexer (*U12, DG408*). Using digital select signals (*A0, A1, A2*), one of the eight sensors was selected and connected to the feedback path (R_{Sensor}, *CR33* to *CR40*) while a fixed reference resistor was placed at the input (R_i, *RPLUG6*). The drive signal was derived from a stable negative reference source (V_{REF}, *DRIVE*) of - 2.5 V (circuit not shown here, but the complete schematic of all circuitries are available in Appendix D).

$$V_{OUT} = -\frac{R_{Sensor}}{R_i} \times V_{REF} \tag{7-3}$$

This simple inverting amplifier configuration produces a positive output voltage (V_{OUT}) according to Equation (7-3). However, as the analogue multiplexer has a finite R_{ON} (on resistance, 100 Ω max), the output voltage will be slightly modified to become Equation (7-4)

$$V_{OUT} = -\frac{R_{Sensor} + R_{ON}}{R_i} \times V_{REF} \tag{7-4}$$

This does not affect the sensitivity of the circuit except for shifting of the output voltage, which can be easily compensated by increasing R_i. There are 5 sets of sensor banks (to accommodate a maximum of 40 sensors for the proto-nose) and together with an optional on-board temperature sensor, these 6 channels are multiplexed into 2 channels using a dual 4-1 multiplexer (*U13, DG409*) to connect to the programmable amplifiers and ADCs.

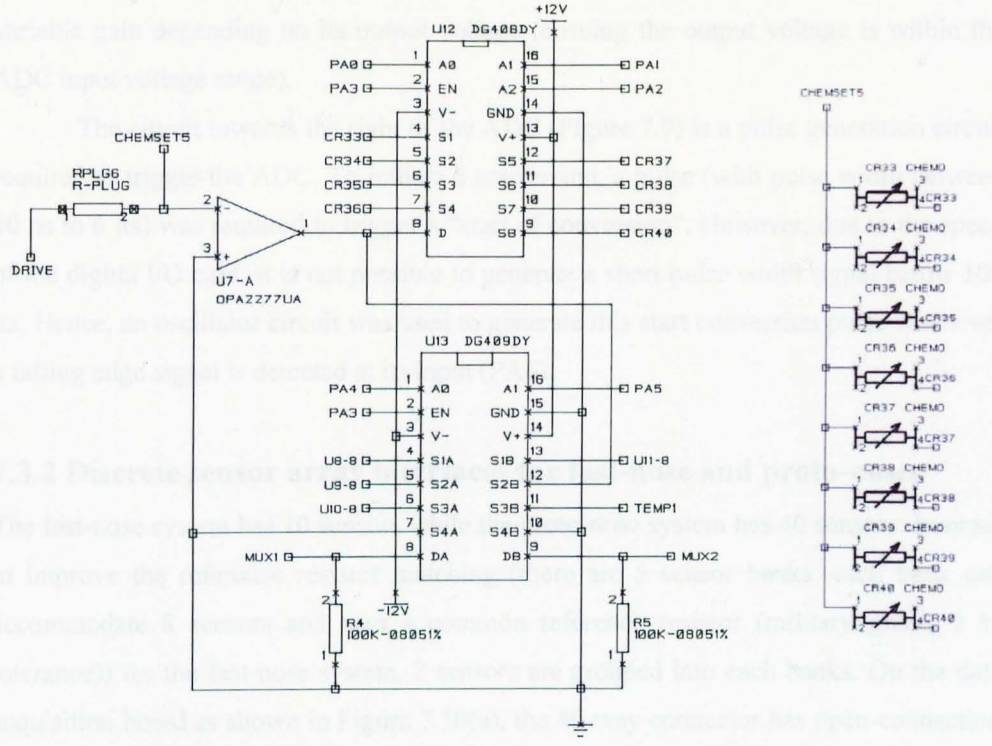

Figure 7.8: Multiple resistive sensors multiplexing and sensing circuit.

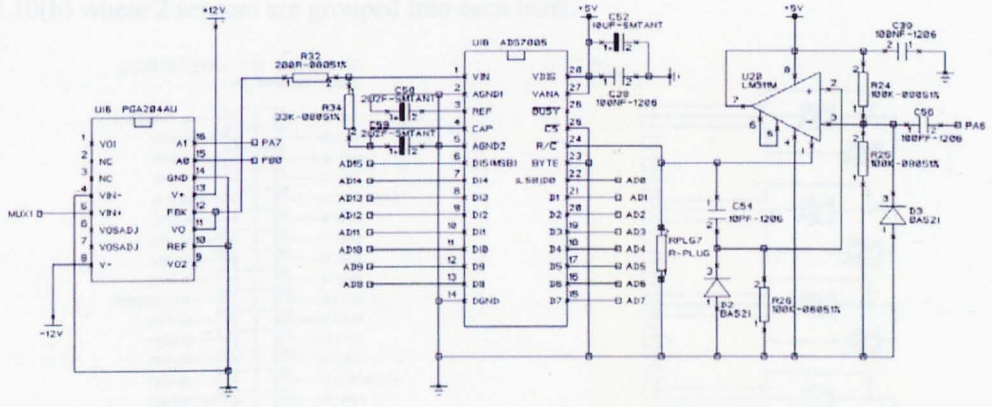

Figure 7.9: Programmable amplifier and 16-bit ADC circuit.

The output signal from the sensor measurement circuit is then fed into a programmable amplifier (*U16, PGA204*) before being converted into its digital equivalent using a 16-bit ADC (*AD7805* [7.12]) as shown in Figure 7.9. The programmable instrumentation amplifier (*PGA204* [7.13]) is capable of amplifying the signal by 1×, 10×, 100× or

1000×. Upon software control, a desirable sensor can be selected and amplified with a variable gain depending on its output voltage (ensuing the output voltage is within the ADC input voltage range).

The circuit towards the right of the ADC (Figure 7.9) is a pulse generation circuit required to trigger the ADC. To initiate a conversion, a pulse (with pulse width between 40 ns to 6 µs) was required to trigger a "start of conversion". However, due to the speed of the digital I/O card, it is not possible to generate a short pulse width signal below 100 µs. Hence, an oscillator circuit was used to generate this start conversion pulse whenever a falling edge signal is detected at its input (PA6).

7.3.2 Discrete sensor array interfaces for fast-nose and proto-noses

The fast-nose system has 10 sensors while the proto-nose system has 40 sensors. In order to improve the reference resistor matching (there are 5 sensor banks, each bank can accommodate 8 sensors and uses a common reference resistor (military grade, 1 % tolerance)) for the fast-nose system, 2 sensors are grouped into each banks. On the data acquisition board as shown in Figure 7.10(a), the 40-way connector has open-connection for 5 common sensor bank selected signal (*CHEMSET1-5*) and 40 open-ends connectors (*CR1-40*). The connection setup on the fast-nose interface board is shown in Figure 7.10(b) where 2 sensors are grouped into each bank.

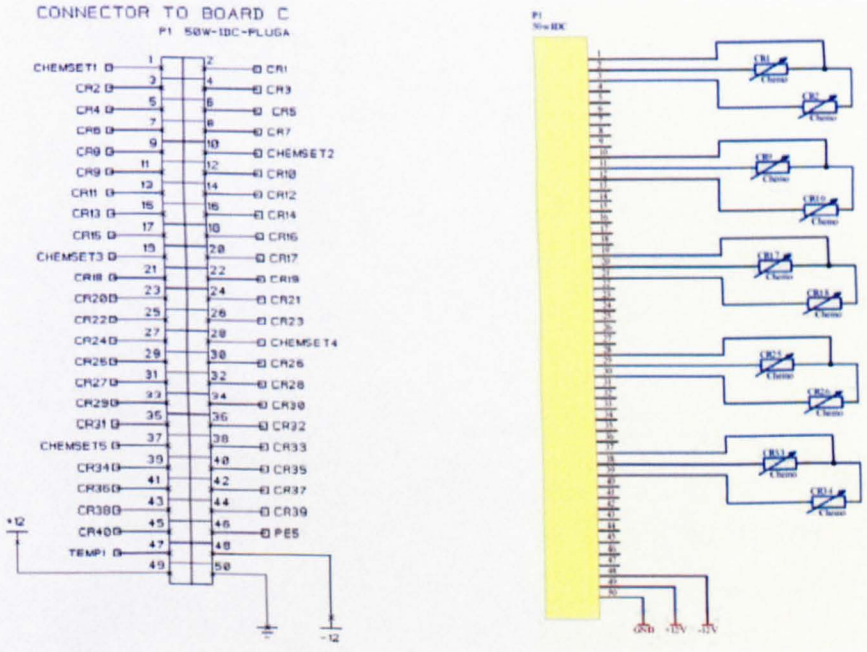

(a) (b)

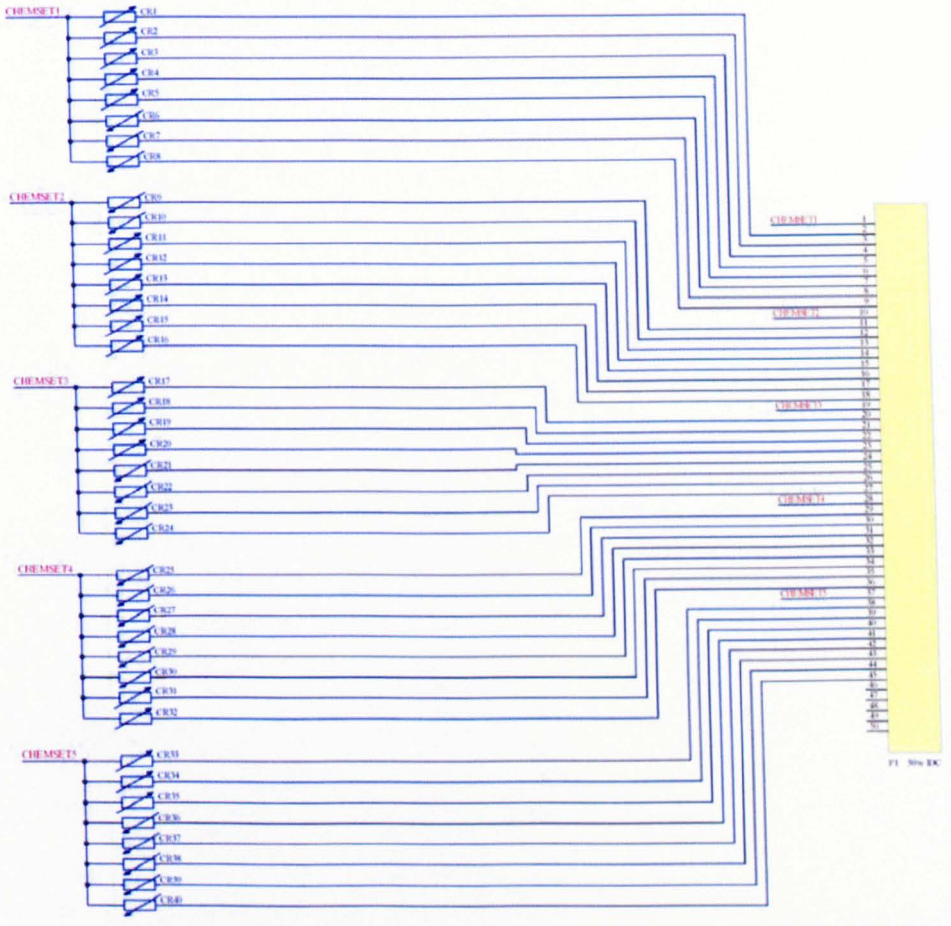

(c)

Figure 7.10: Data acquisition interface for fast-nose and proto-nose systems. (a) 40-way interface connector on data acquisition board. (b) 40-way interface connector on fast-nose board. (c) 40-way interface connector on proto-nose board.

For the proto-nose system, 8 sensors are grouped into each bank to give 40 sensors as shown in Figure 7.10(c). Beside this slight difference in terms of the number of sensors for each system, the remaining electronic interfaces are the same.

7.3.3 Microsensor array interface for hybrid-nose

The number of sensors on the hybrid-nose sensor array was increased to 80 from 40 in the proto-nose systems. In addition, some of the sensor pins are shorted together (Section 4.3.1) to reduce the number of I/Os required. Hence certain sensors are grouped together to form a bank. Since the interface electronic is designed for only 40 sensors, an additional level of multiplexing was required to double the number of sensors supported

to 80. On the hybrid-nose interface board, 10 additional multiplexers were used to provide this second level of selection. To support the selection, 3 extra digital I/Os select logics are required.

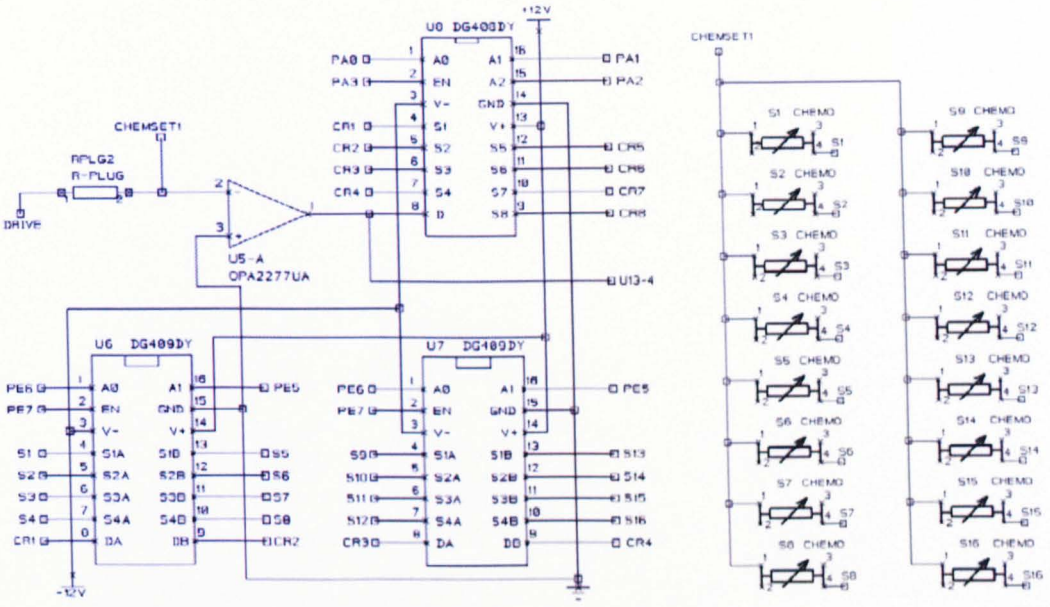

Figure 7.11: Hybrid-nose second level multiplexing circuits to support 80 sensors.

A partial implementation of this design is shown in Figure 7.11 with the full details available in Appendix D. The sensing amplifier (*U5-A*) with an 8-1 multiplexer (*U8*) was the original circuit design, implemented on the data acquisition board, while the rest are the new circuitries added to the hybrid-nose interface board. Two dual 4-1 multiplexers (*U6* & *U7* in Figure 7.11, *DG409* [7.14]) are used to map 16 sensors to each sensor bank. Equation (7-4) used to derive the output voltage was modified to Equation (7-5) to include the second level on resistance (R_{ON2}) introduced by the second multiplexer.

$$V_{OUT} = -\frac{R_{Sensor} + R_{ON1} + R_{ON2}}{R_i} \times V_{REF} \qquad (7\text{-}5)$$

The 16 inputs are multiplexed into four signals (*CR1* to *CR4*) to connect to the four original inputs. As mentioned previously (Chapter 4), due to the shorting of one electrode of each sensor (on all columns) on row 1 to row 4 and row 2 to row 5, sensors on these two commoned rows have to be connected to the same bank.

7.3.4 Microsensor array interface for aVLSI-nose

While the fast-nose, proto-nose and hybrid-nose can all be interfaced directly to the data acquisition system, the aVLSI-nose does not have a compatible interface. The main reason for the incompatibility is due to the aVLSI-nose simply output a voltage representing the sensor signal and does not require separate perturbation. As such, an additional data acquisition card (NI AT-MIO-16XE-50) was required to monitor the output voltage. This card has 8 digital I/Os, 16 analogue input channels (16-bit resolution) and 2 analogue output channels (12-bit precision). Due to the need for programmability, the 8 digital I/Os available on the new card were insufficient. Hence 4 additional digital I/Os from the other interface card (PCI DIO-96) were used. The aVLSI-nose 70 sensor outputs were multiplexed using nine 8-1 multiplexers to fit them into the 16 analogue input channels available. 7 digital I/Os are used to generate the timing signals corresponding to DATA_IN, RESET_SR, PRESET_DCC, RESET_DCC, ENABLE_DCC, CLK_SR and CLK_DCC as discussed in Section 4.4.3. These signals select the current source, sensor mode, sensor interface, gain and digital offset cancellation for all 70 sensors. The four additional digital I/Os were used to select the desired sensor output to sample by switching the multiplexers.

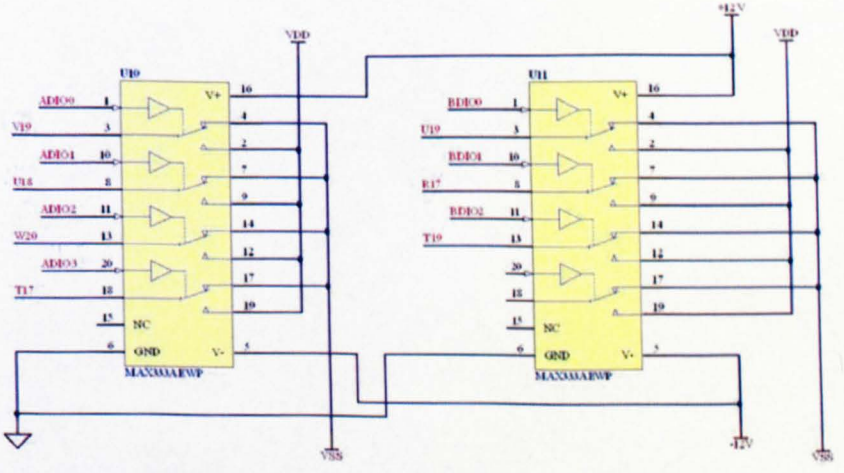

Figure 7.12: aVLSI-nose control signal level shifting.

The design of the aVLSI-nose interface board was predominately the same as the hybrid-nose system except for some additional biasing. However, the potential need to bias the aVLSI-nose with different negative operating voltages complicated the design. The use of different operation voltages was resolved by employing a variable power regulator

circuit design (Appendix D). As a result programmable control signals were required to shift by the same amount. However, they are not compatible because the digital outputs are at TTL levels. An elegant way to resolve this issue is to employ two bipolar quad 2-1 multiplexers (max 333 [7.15]). Each of the 7 control signals are connected to the control input of the multiplexer with its two selection inputs tied to the variable supply sources of the system. The control input signal is TTL compatible while the output voltage changes according to the two selectable inputs, which varied with the operating voltages. This simple technique allows the control signal level to vary with the operating voltages. The implementation of this circuit is shown in Figure 7.12.

7.4 Software control system

The software was primary used to control, arbitrate and automate the VTS and data acquisition system. It was also used to drive the numerous interfaces of the hardware timing protocols (for example, SPI, serially programmable DAC, etc). The choice of using LabView (version 6.1 [7.16], National Instrument) as the host software was natural as it provide graphical programmability and simple communication with data acquisition hardware (through a huge library of communication modules). LabView enables the user to treat an entire complex system as a simple instrument (virtual instrument or VI) without exposing the complicated underlying details which may not be of interest to some end-users. However, the programmer is able to decompose the entire system into smaller modules (called sub-VI) for implementation, using either a top-down or bottom-up (or a combination of both) approaches.

7.4.1 Modular hierarchical design

The LabView software is a data-driven graphical-based programming language which is well-suited for seamless integration with the data acquisition system. Each sub-VI performs a specific task or deals with the communication with a hardware device. These modules or sub-VIs are fully tested before they are integrated to form the next level VI.

Figure 7.13 shows the hierarchy of the proto-nose data acquisition software in LabView. The proto-nose VI at the top level is the main program where all other sub-VIs are invoked. Each sub-VI has been designed to deal with a specific task (such as acquiring the flow rate), hence they can be re-used for the fast-nose, proto-nose, hybrid-nose and aVLSI-nose system.

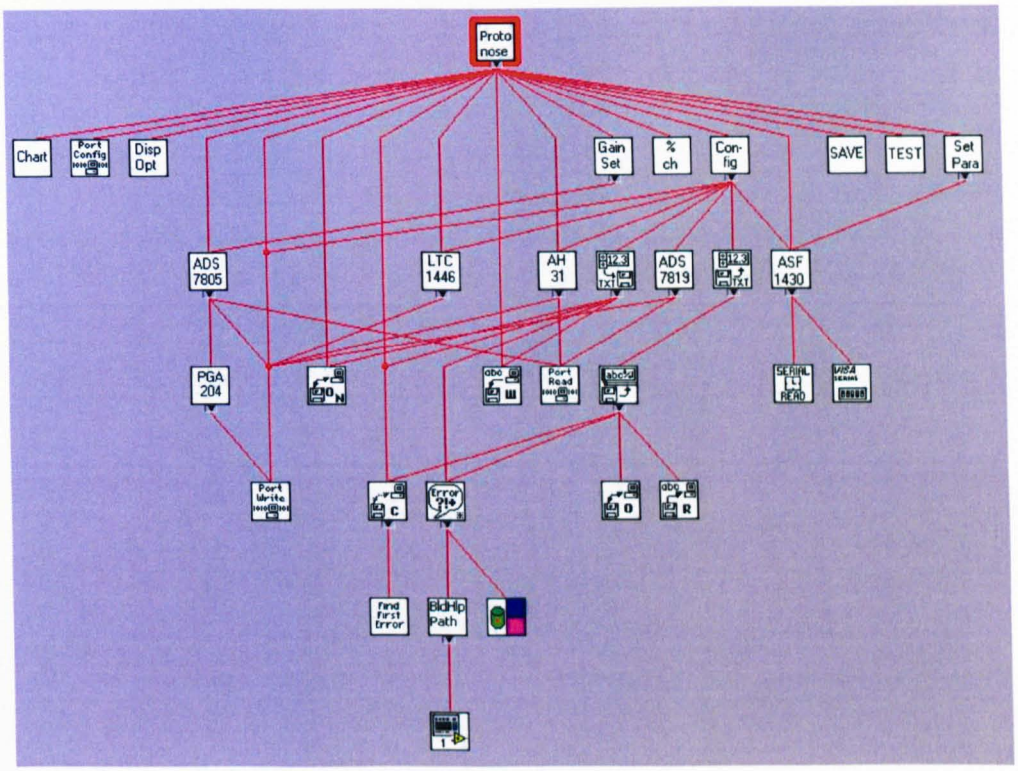

Figure 7.13: Proto-nose software hierarchy.

To better illustrate the underlying approach, an example will be described here to demonstrate how the temperature and humidity sensor (AH31) can be programmed and interfaced in LabView (refer to Figure 7.6 (hardware interface and timing diagram) and Figure 7.14). Each sub-VI consists of two components; one is called the panel (Figure 7.14(b)) which represent the virtual instrument graphical user interface (GUI) while the other is known as the diagram (Figure 7.14(a)) used to program the VI. Each VI can run on its own or can be invoked by other VIs as a sub-VI. Here, the AH31 sub-VI consists of 3 I/Os. It has an input on the left (task ID) and two outputs on the right (temperature and humidity data) as shown in Figure 7.14(a). Upon invoking this sub-VI, the task ID is supplied by the calling VI. This task ID is an array of I/O addresses used to access the individual port on the hardware. Once the temperature and humidity data are collected and processed by the sub-VI, they will be returned to the calling VI.

Using the I/O address provided by task ID, the programmer has to design the software algorithm to communicate with the hardware to acquire the necessary data. The SPI interface of AH31 was connected to 3 I/O ports where the timing protocols will be emulated in software. The detailed implementation is shown in Figures 7.14(a), (c) and

(d). The task ID or the addresses for the I/O port connected to the sensor was decoded before it is being fed to an outer *sequence*. A *sequence* is basically a series of operations executed in sequential order. The outer sequence has 3 set of operations (the '0..2' represent 3 sequences) to be executed in series, only sequence 1 is shown in Figure 7.14(a). The first operation is the assertion of the chip select (*CS**) while the last operation is the negation of chip select (refer to Figure 7.6(b) for details). Once the sensor is selected (or turned ON), a *FOR* loop is encountered. The *FOR* loop repeats a set of operations for a predetermine number of cycle, which in this case is 16 because the temperature and humidity data are both in 8-bit format (16-bit in total).

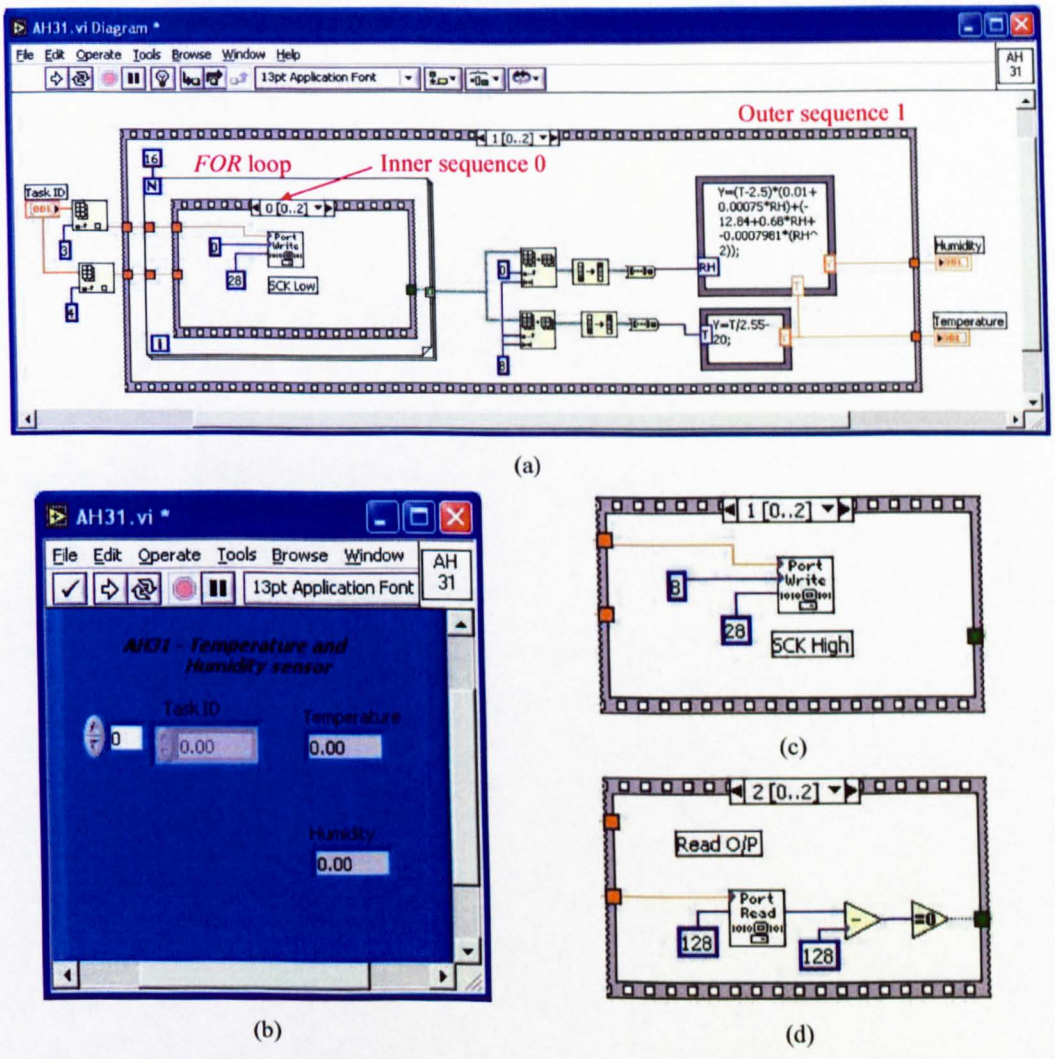

Figure 7.14: Sub-VI example, temperature and humidity sensor interface (AH31). (a) AH31 diagram (program). (b) AH31 panel (user interface). (c) AH31 programming sequence 1 of 2. (d) AH31 programming sequence 2 of 2.

To read each bit of data from the sensor, a clock (SCK) has to be supplied, hence an inner *sequence* is required for this purpose. This inner *sequence* performs 3 operations, it set the clock to LOW in Figure 7.14(a), set the clock to HIGH in Figure 7.14 (c) and then read in data from the sensor MISO output in Figure 7.14(d). A single bit of data was read after the clock was set high because the rising edge of the clock (shown in Figure 7.6(b)) shifts the 16-bit data into the output buffer connected to the MISO pin. When these 3 operations were repeated in sequence for 16 times, it will resemble the timing protocols required by the sensor as shown in Figure 7.6(b). Upon reading the 16-bit of temperature and humidity data, they have to be processed by splitting it into two 8-bit words. Each word then undergo a binary to decimal conversion and subsequently multiplied by a conversion factor as specified in the data manual of the sensor [7.10] to generate the equivalent temperature (in °C) and humidity (in R.H.). Other sub-VIs were implemented using similar design strategies and hence not elaborated.

7.4.2 Fast-nose, proto-nose and hybrid-nose software interfaces

The software interfaces for the 3 noses are similar in terms of design though each system contains different number of sensors. Therefore, only the proto-nose software will be illustrated here. For the remaining systems, their unique differences will be highlighted.

Figure 7.15 shows the various control menus of the proto-nose data acquisition and logging software. The main-VI will be invoked when the program is executed. The instantaneous voltages across the sensors will be displayed along with the status of the VTS, such as the microvalves, temperature, humidity, flow rate and leakage information. The user is then required to setup the test procedures by invoking the 'test parameter' sub-menu by clicking on the test parameter button on the main-VI. The test parameter sub-VI will be invoked for the user to input the number of test cycles, test duration, analyte selection, analyte injection duration and flow rate. The 'save' sub-VI will next be called upon to specify the additional parameters and location to save the results file. These additional parameters include the temperature and flow rate for each sampled point as they may vary over a long measurement period.

The display menu selects the update option for the main-VI while the testing is in progress. This has a side-effect of reducing the sampling rate because the CPU has to spent time acquiring the data to update the display. The gain menu allows a user to manually select the gain for each sensor. When the main-VI is first invoked, an

automated gain selection algorithm is used to scan all the sensors to configure their gain. In any case if the user decides to select a different gain, each sensor can be manually re-configured to take on a different gain by modifying the gain selector of the programmable gain amplifier. The configuration menu shows the current status of the VTS and allows the user to perform a manual test (such as turning on valves and changing the flow rate) of the system to ensure functionality prior to commencing a test.

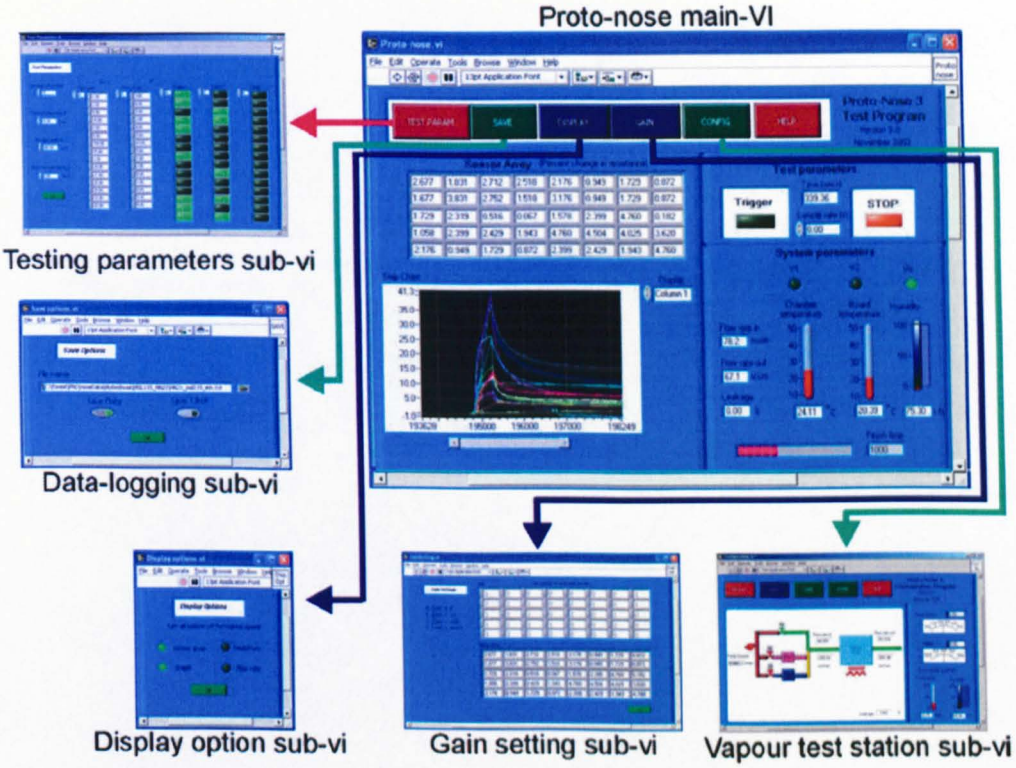

Figure 7.15: Proto-nose control software and data-logging hierarchy menus.

Once the user is satisfied with the setup, gain and testing procedure, the test may commence by pressing the 'trigger' button on the main-VI menu. Next to the trigger button is the sampling rate control where the user can specify the desirable sampling rate prior to the start of the test. As all the data acquisition and VTS control are performed within the software, the maximum sampling rate is determined by the minimum time required to complete one execution cycle (limited by the PC performance). This cycle is variable as it depends on the user selection of the desirable display to update (display sub-VI) and the parameters to measure (such as temperature and flow rate that can be specify in the save sub-VI). If the user enters a sampling rate that is above the maximum

sampling rate, the maximum sampling rate will be used. However if a lower sampling rate is specified, the software will delay (wait) until the next sample period before it commences the next set of sensor responses acquisition. For the proto-nose, the maximum sampling rate is approximately 6 ms/cycle or 150 μs/sensor. The sensor sampling rate per sensor was similar for three other systems, however, as each system has different number of sensors, the effective sampling will be inversely proportional to the number of sensors. The plots on the bottom left of the main-VI show the responses of the selected sensor bank against time. Their offset (baseline) voltages have been removed to show their relative response magnitudes.

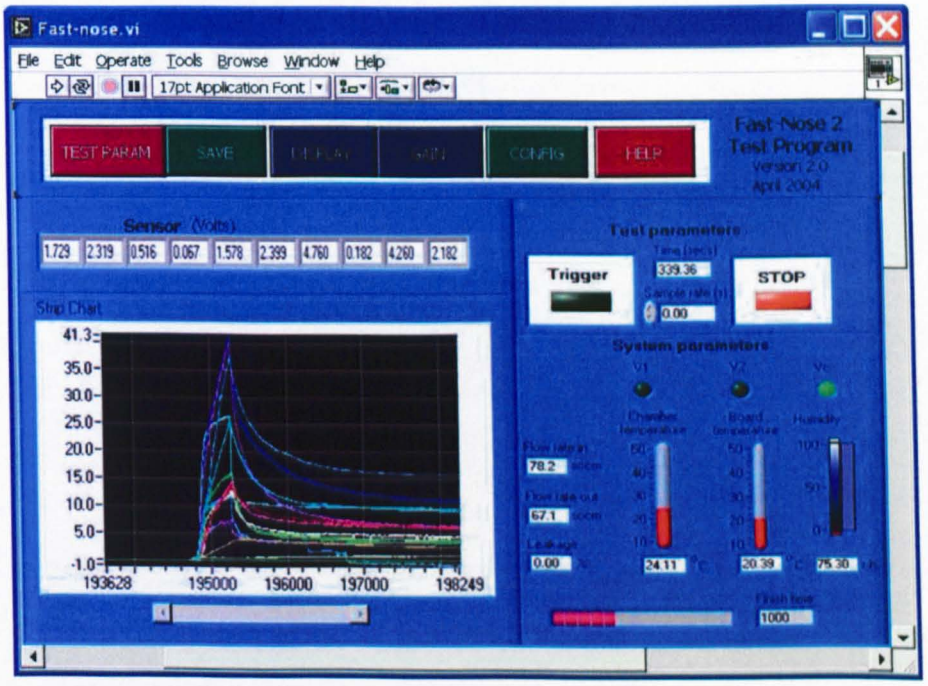

(a)

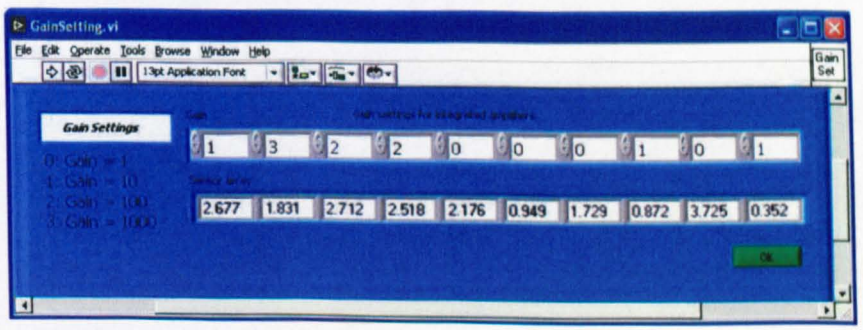

(b)

Figure 7.16: Fast-nose data acquisition software. (a) Modification to the main-VI. (b) Modification to the gain selection sub-VI.

The fast-nose microsystem has a similar software implementation. As discussed in Section 7.3.2, only 2-out-of-8 possible selections are required for each sensor bank. The data acquisition software simply has to reduce the scanning selection from 8 to 2. On the display panel, only 10 sensor readings are displayed as shown in Figure 7.16. The changes made on the hybrid-nose software is also minimal as the same circuit was used, except for the addition of a 2^{nd} level multiplexing required to support 80 sensors. Similar modifications are made for the main-VI and gain sub-VI to extend the display for the sensor voltages and the gain selections to accommodate 80 sensors.

7.4.3 aVLSI-nose software interface

For the aVLSI-nose, various sub-VIs have to be added to support its programmability. As the sensor responses had to be acquired using the other data acquisition card (AT-MIO-16XE-50), the entire software have to be overhauled. Two new sub-VIs were added; they were the "sensor mode, driving current and gain selection" sub-VI (Figure 7.17) and the "DC-offset cancellation" sub-VI. Details pertaining to the data formats and timing protocols have been explained in Section 4.4.3. Each sensor has an associated data byte (9-bits) used to define the sensor operation mode, current and gain settings. The data bytes of the 70 sensors are cascaded in series to reduce the number of I/Os required to configure the aVLSI-nose chip. Two control signals, a clock and a data signal are used to coordinate the configuration by serially latching the right data signal (refer to Figure 4.22) on each rising edge of the clock signal.

The DC-offset cancellation circuit has been designed to simplify the programming, as only a clock signal is required to increment the counter once it is reset (cleared). 1024 (10-bit) clock pulses are generated to drive the counter until the DAC (which is driven by the counter) output is slightly (one-count) above the sensor offset voltage. At this point, a disable signal from the comparator will automatically halt the counter. Although the remaining pulses are still supplied externally, the AND gate (refer to Figure 4.20) will mask them away. As all DC-offset cancellation circuits are being clocked simultaneously, this operation is performed once only. Each counter associated with their corresponding sensor holds a different count because each sensor has a different offset (baseline) voltage.

For the data acquisition circuitries, all 70 sensor outputs are multiplexed using nine 8-1 multiplexers to connect to 9 (out of the 16 possible) analogue inputs of the data

acquisition card. Using a similar strategy as the hybrid-nose and proto-nose, the sensors outputs are sequentially scanned and converted into their digital equivalent voltages.

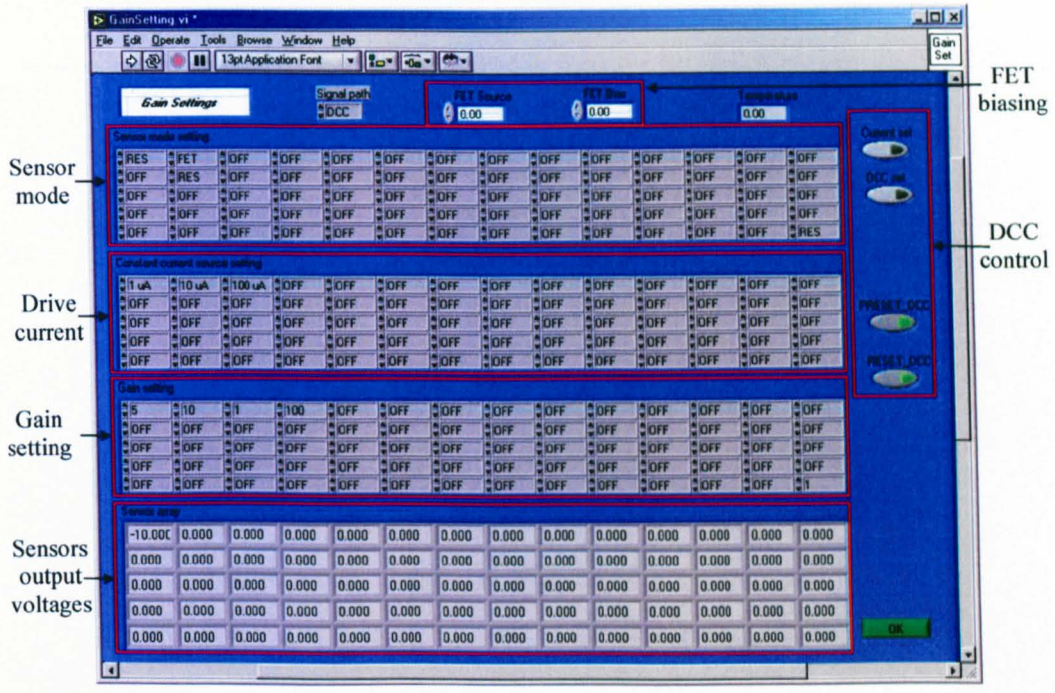

Figure 7.17 : aVLSI-nose configuration menu sub-VI.

7.4.4 Automated test cycles and data logging

The main-VI is the most complex as it was required to coordinate between the data acquisition and VTS control. Figure 7.18 shows two sequences of the main-VI diagram used to automate the test cycles and data logging.

By this point of execution, the user has already setup all the test cycles and parameters required for data logging. The first sequence on Figure 7.18(a) was used to control the VTS and communicate with any other devices pre-selected by the user. On the left of the diagram are various combination of commands used to monitor the timing of the system to the nearest millisecond. On the right is sequence 0 where the VTS are activated when the test cycle selected by the user is required to fire. This will encompass a sequential switching of certain microvalves in combination, to fulfil the desirable pulse width, analyte mixtures and test duration.

Figure 7.18(b) shows sequence 1 of the data acquisition and logging block. The ADC sub-VI is invoked to measure all the sensor output voltages in sequence before they

are reorganised and sent for storage. If the user decides to update the display while performing the data acquisition, the graphical plots will be updated accordingly. These sequences are then repeated until the entire test cycle is completed.

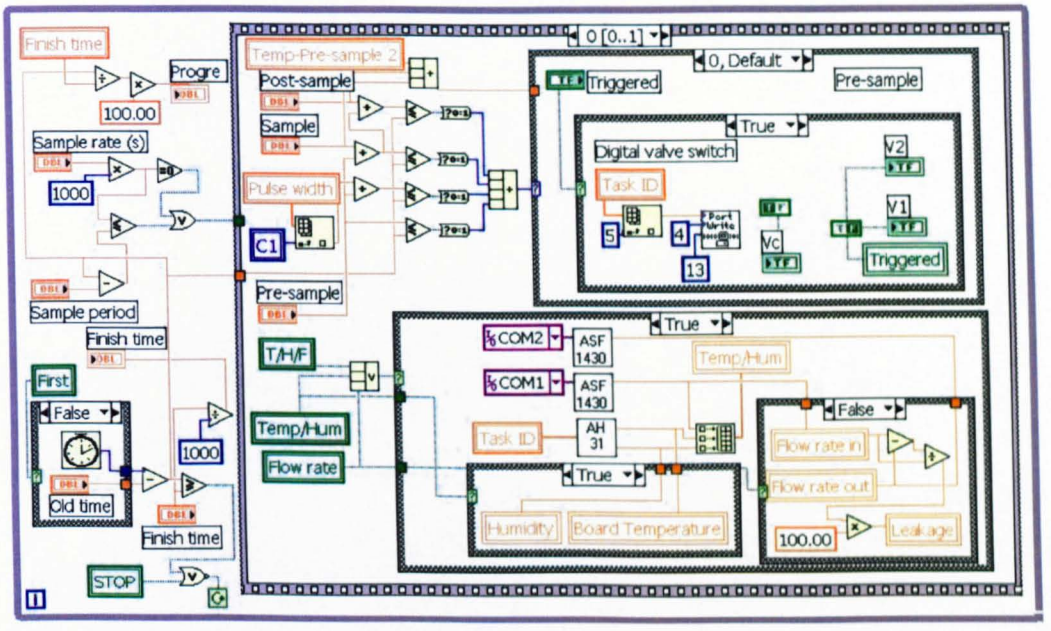

(a)

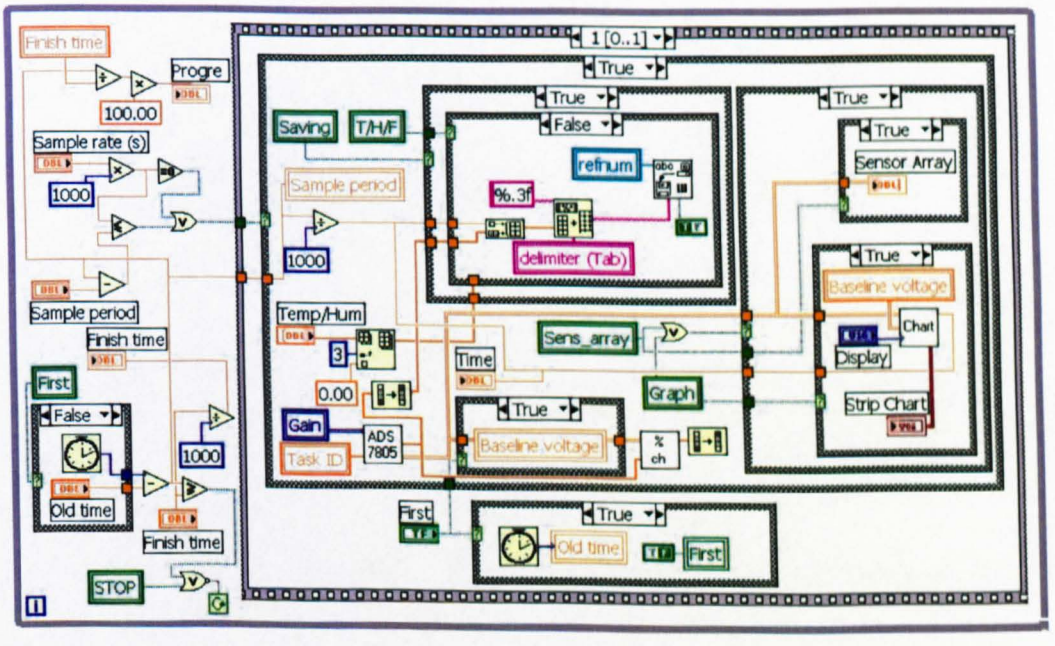

(b)

Figure 7.18: Data logging main-VI. (a) Data logging diagram sequence 0. (b) Data logging diagram sequence 1.

7.5 Conclusions

The design and fabrication of vapour test station and data acquisition electronics have been discussed in this chapter. For the vapour test station, the design and construction of the system was depicted along with the details of the component used. As an automated system is required to facilitate continuous unattended testing, each component will be required to be controlled electronically. The design of these electronic interfacings and the controls via software were also discussed.

While the VTS can be interfaced seamlessly to all four systems (fast-nose, proto-nose, hybrid-nose and aVLSI-nose), the data acquisition system has to be made extensible to accommodate the different number of sensors and interfaces on each system. For the fast-nose, proto-nose and hybrid-nose system, the extension is simpler because they employ the same type of chemoresistive sensors, differing only in the number of sensors. However, for the aVLSI-nose system, a complete different approach is required as each sensor has integrated driving and conditioning circuitry. Lastly, the design and implementation of the software control algorithms and timing protocols generation (to simplify hardware interfacing) were discussed.

7.6 References

[7.1] Alpha MOS, http://www.alpha-mos.com/en/products/profox.php, Electronic Nose Fox Aroma and Odour Sensing System, July 2004.

[7.2] Smart Nose, http://www.smartnose.com/, Electronic nose system, July 2004.

[7.3] Sensirion, ***ASF1430 bidirectional mass flow meter user manual***, Sensirion AG, Zürich, Switzerland, Version 2.0, April 2003.

[7.4] Linear Technology, ***LTC1446 dual DACs with 12-bit resolution user manual***, Linear Technology Corporation, Milpitas, CA 95035-7417, 1996.

[7.5] National Instruments, ***PCI-DIO-96/PXI™ 6508/PCI-6503 user manual***, National Instruments Corporation, Part Number 320938C-01, March 1998 Edition.

[7.6] Analog Devices, ***AD7819 8-bit analogue to digital converter (ADC) data manual***, Analog Devices Inc, Norwood, MA 02062-9106, C01318–0–10/00 (rev. B), 2000.

[7.7] Motorola, ***MC14014 8-bit static shift register semiconductor technical data***, Motorola Inc, Phoenix, Arizona 85036, 1995.

[7.8] M. Burgmair, M. Zimmer and I. Eisele, ***Humidity and temperature compensation in work function gas sensor FETs***, *Sensors and Actuators B: Chemical, Vol. 93, pp. 271-275, 2003.*

[7.9] J. García-Guzmán, N. Ulivieri, M. Cole, J.W. Gardner, ***Design and simulation of a smart ratiometric ASIC chip for VOC monitoring***, *Sensors and Actuators B: Chemical, Vol. 95,pp.232-243, 2003.*

[7.10] Sensirion, ***AH31 humidity and temperature sensmitter user manual***, Sensirion AG, Zürich, Switzerland, September 2001.

[7.11] National Instruments, ***DAQPadTM-MIO-16XE-50 user manual***, National Instruments Corporation, Part Number 370511A-01, June 2002 Edition.

[7.12] Burr-Brown products from Texas Instruments, ***AD7806 16-bit analogue to digital converter (ADC) data manual***, Texas Instruments Inc, SBAS020A, Dallas, Texas 75265, January 1996 – Revised May 2003.

[7.13] Burr-Brown products from Texas Instruments, ***PGA204 programmable gain instrumentation amplifier user manual***, Texas Instruments Inc, Dallas, Texas 75265, 1993.

[7.14] Maxim, ***DG408/DG409 8-channel/dual 4-channel CMOS analog multiplexers user manual***, Maxim Integrated Products, Sunnyvale, CA 94086, 2002.

[7.15] Maxim, MAX333 ***quad SPDT (single-pole-double-throw) CMOS analog switch user manual***, Maxim Integrated Products, Sunnyvale, CA 94086, 1995.

[7.16] National Instruments, ***LabView 6.1 user manual***, National Instruments Corporation, Part Number 320999D-01, November 2001 Edition.

Chapter 8

Microsystems characterisation and experimental results

8.1 Introduction

In the past chapters, the design and fabrication of two separate but complementary groups of systems had been discussed. These systems include the fast-nose, the proto-nose, the hybrid-nose, and the aVLSI-nose. Two proto-nose systems were developed to investigate some of the unsatisfactory results from the first system, details of which are given here. The primary aim of the proto-nose systems was to generate spatio-temporal signals; this will be examined in detail for both simple analytes and complex odours.

With the hybrid-nose microsystem, its high density and diversity already provides added discriminatory information. These arrays have been characterised independently to investigate any superiority over discrete sensors. Finally, micropackages ranging from simple to complex microchannel packages have been assembled with the hybrid-noses to form "nose-on-a-chip" microsystems. These systems are capable of generating spatio-temporal signals (similar to those generated by the proto-nose) but with significant reduction in size.

The aVLSI-nose has similar sensor placements to the hybrid-nose except that it also has all the required integrated circuitries to transform it into a smart sensor array. The experiments for this system have been focused on characterising the performance of these circuitries as the packaging and spatio-temporal signal generation issues have been dealt within the hybrid-nose microsystem.

8.2 Proto-nose microsystems characterisation

The two proto-nose microsystems have been characterised to determine their responses to simple analytes and complex odours. Proto-nose I was tested to determine its capability to generate spatio-temporal data. Initial results had shown that spatio-temporal signals

can be generated; however, the sensor responses (of the same type) gave two major concerns. When comparing the response magnitudes of the same type of sensors along the microchannel, the sensor signal towards the outlet was attenuated by more than 20 times compared to the sensor signal near the inlet (Figure 8.5). This had neither been predicted by the simulation nor the experimental results obtained from the hybrid-nose sensor array where all sensors are exposed simultaneously. Two possible causes were identified. Firstly, this could be due to variations in sensitivities of different sensors, caused by a deviation in coating thickness. The second ambiguity is that the sensors do not respond according to their placements order (plausibly due to intra-channel leakage). To alleviate these possible causes, two solutions were applied. A fast-nose microsystem was developed to calibrate the deviation in response magnitudes of the sensors before packing them in the proto-nose. Hence, compensation could be applied. Next, the proto-nose II was developed, where the intra-microchannel segments are carefully sealed to remove intra-channel leakage.

8.2.1 Discrete sensor characterisation using fast-nose microsystem

The fast-nose microsystem has been designed primary for calibrating the deviation of discrete sensor response magnitudes prior to assembly onto the proto-nose II. The fast-nose has a 10 cm × 0.5 mm × 0.5 mm microchannel. It can accommodate 10 sensors, which are placed equi-distance to each other (1 cm apart),. Ten groups of different sensor types were characterised on the fast-nose microsystem with simple analytes (toluene and ethanol vapour).

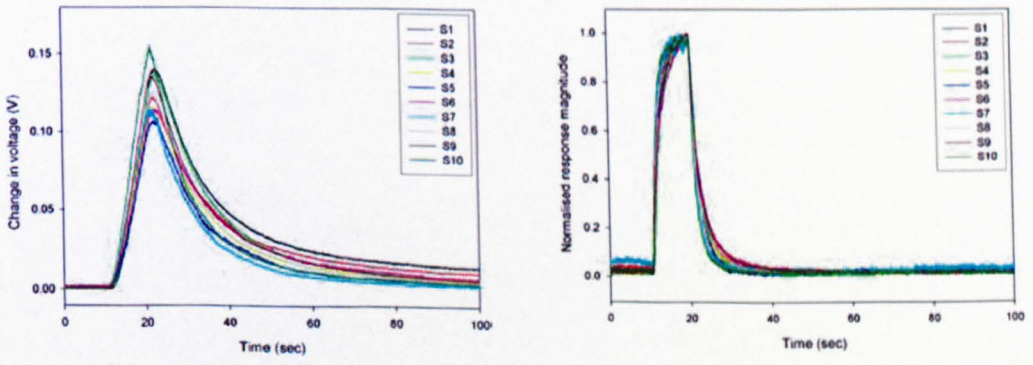

(a) (b)

Figure 8.1: Discrete sensor response magnitudes characterisation at room temperature. (a) PEVA sensor response to toluene vapour in air. (b) Normalised PEVA sensor responses to ethanol vapour in air.

Figure 8.1 shows two plots of the response magnitude characterisation for 10 PEVA sensors to toluene and ethanol vapour in air. Figure 8.1(a) shows that the variation in response magnitudes of 10 PEVA sensors to toluene vapour in air is less than 5 %. In Figure 8.1(b), the PEVA sensor responses to ethanol vapour are normalised to determine the variation in response profiles. Upon normalisation, it shows that there is little variation in the profiles between different sensors. Other types of sensors give a 10 % or less variation in response magnitudes with similar minute variation in response profiles.

In addition to the sensor response magnitudes and profiles characterisation, the fast-nose microsystem was also used to study other sensor characteristics. These include the stability of the sensor resistance over time and more importantly, the effect of carrier gas flow velocity on the sensor response.

The baseline resistance is the resistance of the sensor prior to any exposure to an analyte using environmental air as the carrier gas. Shift in sensor baseline resistance due to ageing, poisoning and other effects are common with these types of polymer-based composite sensors [8.1-8.3]. Therefore, it is necessary to monitor the sensor resistance over a period of time in order to determine its stability.

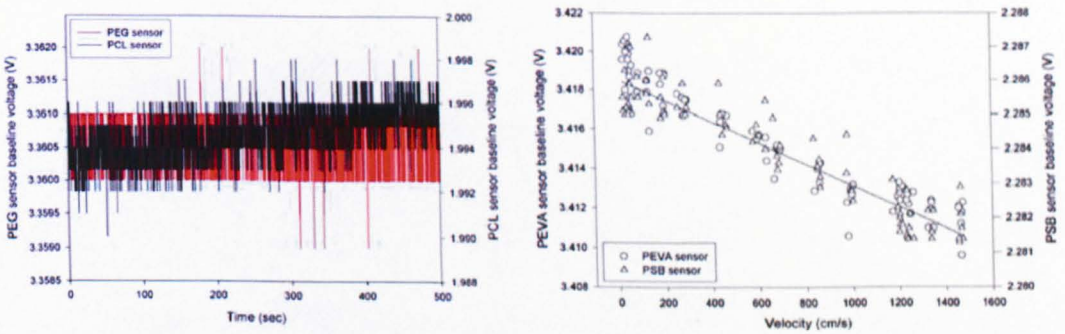

(a) (b)

Figure 8.2: Sensor resistance variations. (a) Sensor baseline voltage (proportional to resistance) variation over time. (b) Effect of flow velocity on baseline voltage for two different polymer sensors.

Figure 8.2(a) shows the baseline voltage (equivalent resistance) across a PEG and a PCL sensor over a period of 500 s. The maximum variation is 5 mV with a standard deviation of approximately 1 mV. In order to determine the impact of carrier gas flow velocity on the sensor response, the baseline voltage has to be measured at different flow velocities to ensure that any shift in response is not a result of the shift in the baseline voltage. The baseline voltage was monitored while the flow velocity was increased. Figure 8.2(b)

shows the baseline voltage versus flow velocity plot for a PEVA and a PSB sensor. It was found that the sensor resistances varied less than 0.2 % ($\Delta V/V$) in a linear decreasing trend with an average variation of ± 1.5 mV. This may be due to the cooling effect when the flow velocity is increased. In spite of this, it is still insignificant compared to the response magnitude that could vary as much as 40 %.

Next, the effect of flow velocity on the sensor response was investigated. All the experiments were performed at the same nominal concentrations of ethanol and toluene vapour in air. The reason for not having environmental control on the temperature and humidity of the air was to simplify the system and work under real-world conditions. In practice, the measurements were conducted within a time frame of 1 hour; therefore the measurement conditions were similar. The temperature throughout all experiments was around 30 °C (± 2 °C) and the relative humidity was around 40 % (± 5 %). The carrier gas flows through the system one minute prior to each experiment to stabilise the sensor resistance. The vapour pulse is then turned on at time, t = 1 s and is turned off at time, t = 6 s to give a 5 s pulse duration. Similar measurements were conducted at increasing velocities. Figures 8.3(a) and (b) show the typical normalised responses of a PSB sensor to 5 s pulses of ethanol and toluene vapour in air at different flow velocities, respectively.

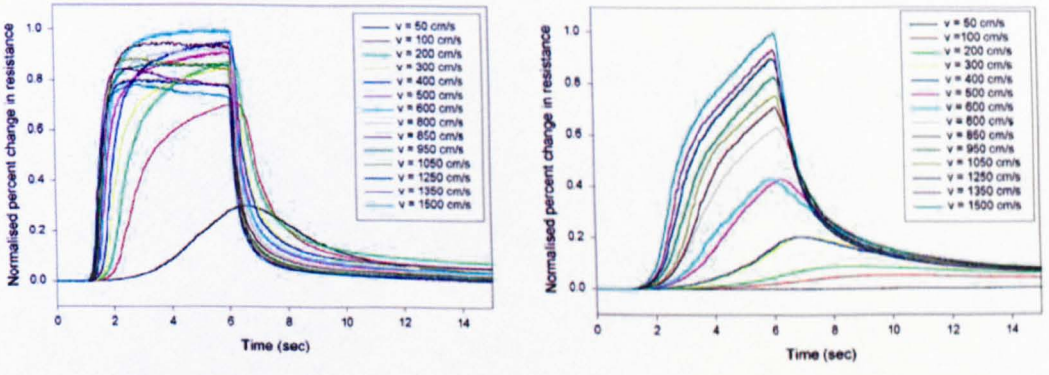

(a) (b)

Figure 8.3: Effect of flow velocity on sensor response. (a) Normalised PSB sensor response to a pulse of ethanol vapour in air at different flow velocities. (b) Normalised PSB sensor response to a pulse of toluene vapour in air at different flow velocities.

Figures 8.4(a) shows the normalised maximum response magnitudes of the sensors to toluene vapour in air at the different velocities. The ΔV_{max} / ΔV of the responses are used in all plots. For toluene vapour, the response magnitude increased linearly with velocity.

It is important to note that the increase in response magnitude is not due to any increase in delivered toluene vapour concentration, but as a result of an increase in response time. This will approach the saturation limit if the exposure duration is increased, even at lower flow velocity.

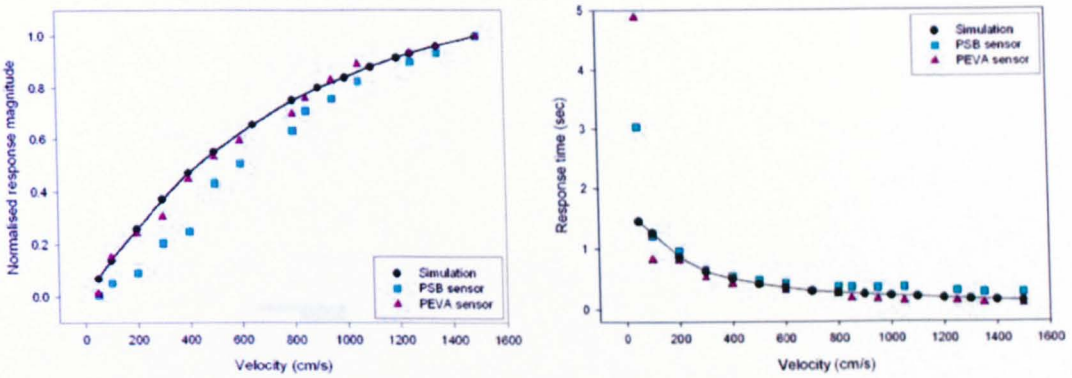

(a) (b)

Figure 8.4: Effect of flow velocity on sensor response magnitude and response time. (a) Normalised experimental and theoretical magnitude of response to a pulse of toluene vapour in air at different flow velocities. (b) Observed and theoretical response time of two polymer sensors to a pulse of ethanol vapour in air at different flow velocities.

The effect of temperature on the sensor response magnitude was studied from 30 °C to 50 °C. Table 8.1 shows that as the temperature is increased, the response magnitude decreases for PEVA sensor responding to ethanol vapour in air. Within the tested temperature range, the rate of decrease is approximately 0.5 % / °C (though not linear throughout the entire operating range [8.4]). This is expected considering the processes being governed by the partition coefficient, which is inversely proportional to the absolute temperature.

Table 8.1: Effect of temperature on the response magnitude of PEVA sensor to ethanol vapour in air.

Flow velocity	Temp=30 °C	Temp=35 °C	Temp=40 °C	Temp=45 °C	Temp=50 °C
100 cm s^{-1}	17.2 %	16.1 %	15.7 %	12.7 %	9.9 %
200 cm s^{-1}	20.2 %	18.1 %	15.8 %	13.7 %	10.3 %
300 cm s^{-1}	21.4 %	18.8 %	15.8 %	14.0 %	10.8 %

Figures 8.4(b) shows the effect of flow velocity on the response times of the sensors. It is well known that polymer sensors employed for chemical detection can be

approximated to a first-order exponential response model [8.5-8.6], as given in Equation (8-1).

$$R = R_{ON}\left(1 - e^{-\tau_{ON}t}\right) \qquad (8\text{-}1)$$

where R_{ON} is the base resistance and τ_{ON} is the response time coefficient.

This has been used to generally compare the response time of different polymer sensors [8.5-8.6]. Clearly, the response (rise) time for both types of sensors decreases as the flow velocity is increased, showing that the sensors have responded faster to ethanol and toluene (not shown here) vapour in air when the flow velocity is increased. The extent of the impact of velocity on the diffusion coefficient differs for ethanol and toluene vapour in air. For ethanol vapour, the velocity coefficient (v_o in Equation (3-18)) is 1, while for toluene vapour it is approximately 15. This is possibly related to the size of the analyte molecule and the porosity of the polymer sensing layer. The fastest responding sensor has a rise time of only 95 ms, hence considered ultra-fast as compared to typical response time of similar polymer-based sensors typically in the range of seconds to minutes [8.1-8.6]. Similar work by Briglin *et al.* had shown that it is possible to achieve even faster response (< 5 ms) with their polymer-composite sensors by depositing ultra-thin sensing film (< 200 nm) and operating at high flow velocity (5.9 L min^{-1}) [8.7].

Temperature affects the rise time positively as opposed to response magnitude. As the temperature is increased, the rise time decreases, giving a faster responding sensor. The average improvement is approximately 10 ms $^{o}C^{-1}$. This can be understood from the basic Arrenhenius diffusion equation as follows

$$D = D_0 e^{-\frac{Q}{RT}} \qquad (8\text{-}2)$$

where Q is the activation energy, T is the absolute temperature and R is the gas constant.

As the diffusion coefficient of analyte in the polymer sensing material (D_s) is a strong function of temperature, any increase in temperature will result in a large increase in the diffusion coefficient, hence a reduction in rise time. Although this will also increase the pulse-broadening effect (resulted from an increase in the diffusion coefficient of the analyte in mobile phase, D_m), it is nevertheless insignificant to impact the response time at high velocity.

8.2.2 Proto-nose I and II characterisation

The characterisation results for the two proto-nose systems will be discussed in this section. The primary aim is to show how spatio-temporal data can be extracted from these systems and used to aid the classification of simple analytes and complex odours. Within each system, two types of lids were employed. One of the lids was left uncoated while the other was coated with a 10 μm thick of parylene C so as to enable a direct comparison between the two different microchannels.

For the proto-nose I system, experimental results, shown in Figure 8.5(a), revealed that the response magnitudes of the sensors, towards the end of the microchannel, are highly attenuated. The ratio between the response magnitude of S1 over S36 for various pulses of toluene and ethanol vapour in air varied between 20 and 100 comparing between the sensors toward the front (S1) and end (S36) of the microchannel. The response magnitude ratio of the sensors, for toluene to ethanol vapour, was found to be similar. In Figure 8.5(b), the normalised responses show that there is no response for S36 as the signal has completely disappeared.

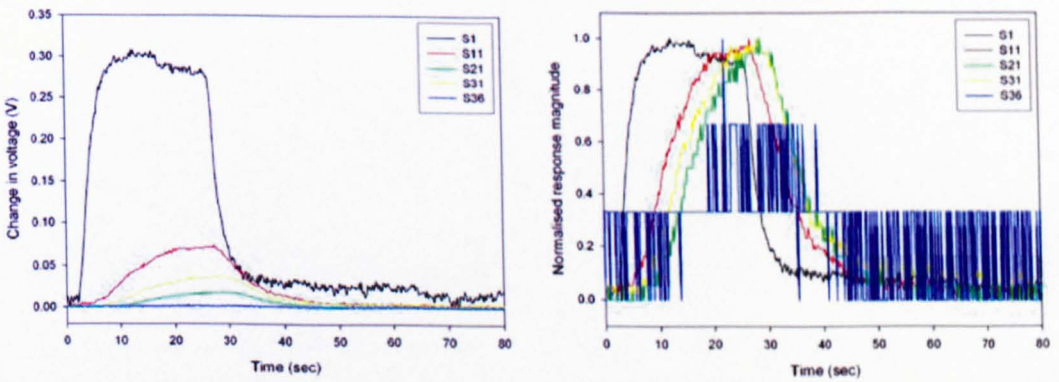

Figure 8.5: Analyte absorption along microchannel. (a) 5 PCL sensor responses to ethanol vapour in air. (b) Normalised PCL sensor responses of (a).

In addition, the sensors along the microchannel of proto-nose I did not respond in sequence (not shown here), indicating intra-channel leakage could possibly exist. However, the primary aim of generating spatio-temporal data was achieved with this system.

In an attempt to eliminate these two ambiguities, proto-nose II was designed and fabricated. Detailed characterisation was performed on this system with both simple

analytes and complex odours of different pulse widths and flow rates. Analysis of the results show that it is capable of generating spatio-temporal signals that are superior and more consistent compared to proto-nose I.

8.2.2.1 Comparison between uncoated and coated microchannel

The proto-nose II system was initially assembled with an uncoated lid to study the effects of sensor responses along a long microchannel with simple analytes. The lid was subsequently swapped with a coated one to compare the sensor responses between the uncoated and coated lids. Simple analytes (toluene and ethanol vapour in air) used in the simulations are employed here for direct comparison. Figures 8.6(a), (b) and (c) show the sensor responses of S1, S26 and S39 to these analytes with the uncoated lid while (d), (e) and (f) show the same sensor responses with the coated lid. Comparing the two sensor responses as shown in Figure 8.6(a) and (d) for S1, it was observed that both the ethanol and toluene vapour reaches the sensor at the same time when either lid is used. As the pulse travel along the microchannel, it became obvious that with the coated microchannel, the toluene pulse starts to be delayed, while with the uncoated microchannel, both analyte pulses arrived at the sensor at approximately the same time. Towards the end of the microchannel at sensor S39 as shown in Figure 8.6(c) and (f), the delay between ethanol and toluene vapour pulse is further enhanced in the coated system while in the uncoated system, the two analyte pulses reach the sensor simultaneously.

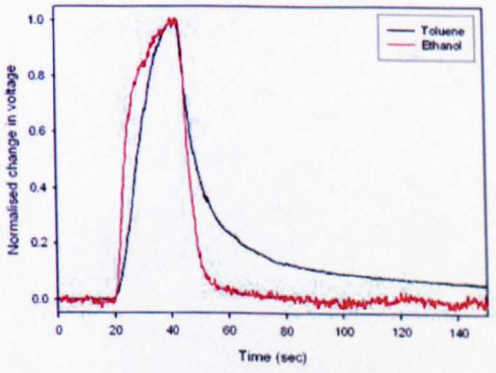

(a)

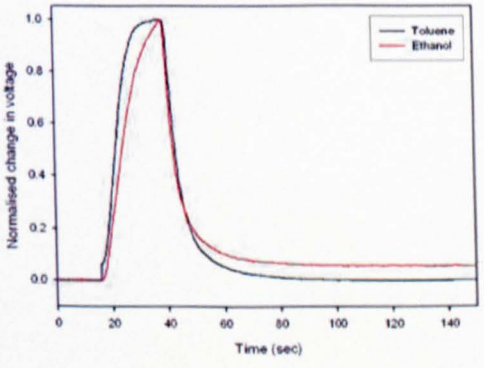

(d)

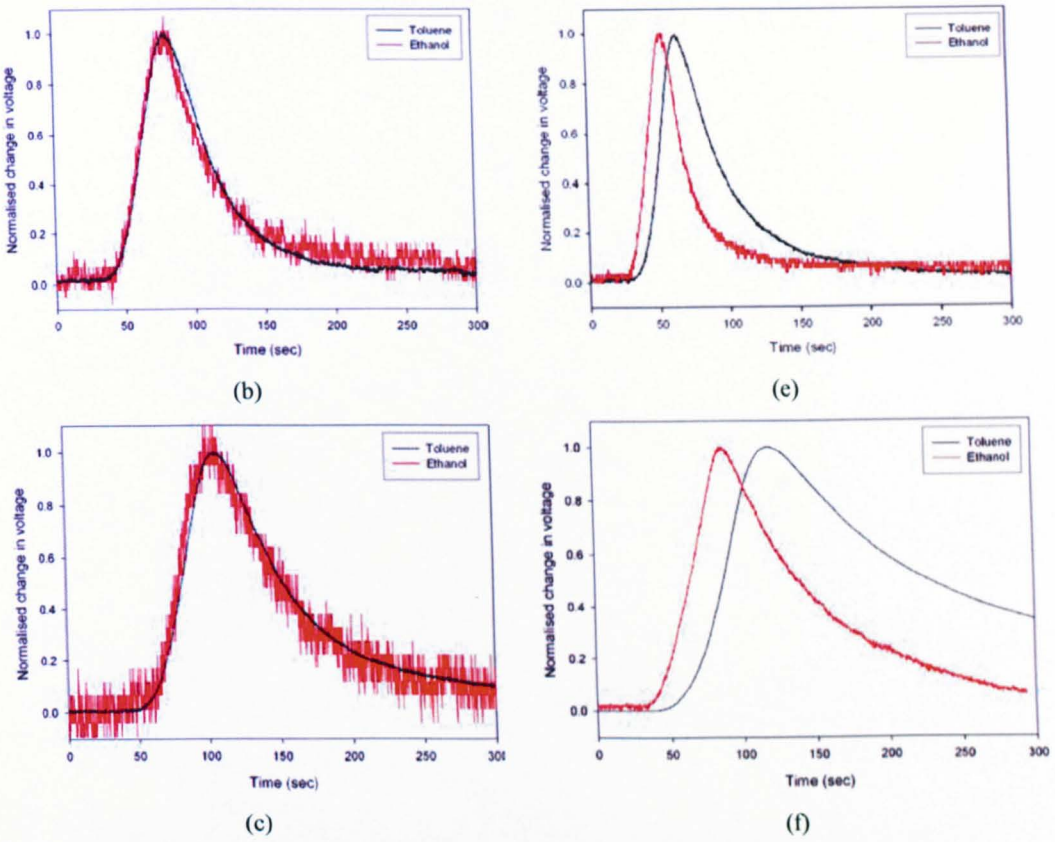

Figure 8.6: Sensor responses along a coated and uncoated microchannel. (a) S1. (b) S26. (c) Normalised S39 response to toluene and ethanol vapour in air in an uncoated microchannel. (d) S1. (e) S26. (f) Normalised S39 response to toluene and ethanol vapour in air in a parylene C coated microchannel.

These results clearly resemble the finite element simulation results discussed in Section 3.2.5. Figure 8.6 have been normalised to emphasize on the temporal time delay, hence their spatial information diminishs.

8.2.2.2 Spatio-temporal signals

In proto-nose II, 10 different types of sensor coatings were used to achieve a wider diversity. These different sensor types have distinct responses to different analytes, depending upon their partition coefficient. Figure 8.7(a) shows their responses to a 10 s pulse of ethanol vapour in air while Figure 8.7(b) shows their responses to a 10 s pulse of toluene vapour in air. The response profiles and magnitudes information correspond to the spatial signals. Comparing the responses of PCL and PEVA sensor to ethanol vapour

in air (shown in Figure 8.7(a)), both sensors have the same response magnitude to ethanol vapour. However, their response profiles are different. Although the response profiles (transient information) provide added discriminatory information, it has been rarely used until recently [8.8-8.10].

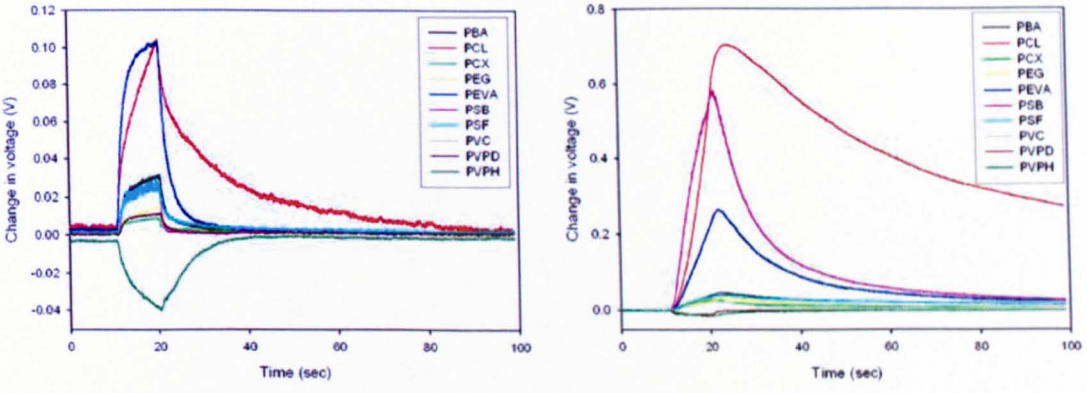

(a) (b)

Figure 8.7: Spatial signal of different types of sensors responding to simple analytes. (a) Sensor responses to ethanol vapour in air. (b) Sensor responses to toluene vapour in air.

Figure 8.8 shows the spatial signals of the same set of sensors responding to complex analytes (a) peppermint essence vapour and (b) vanilla essence vapour. Clearly, each type of sensor has a different spatial signal to a particular analyte although it is still possible to obtain similar spatial signal.

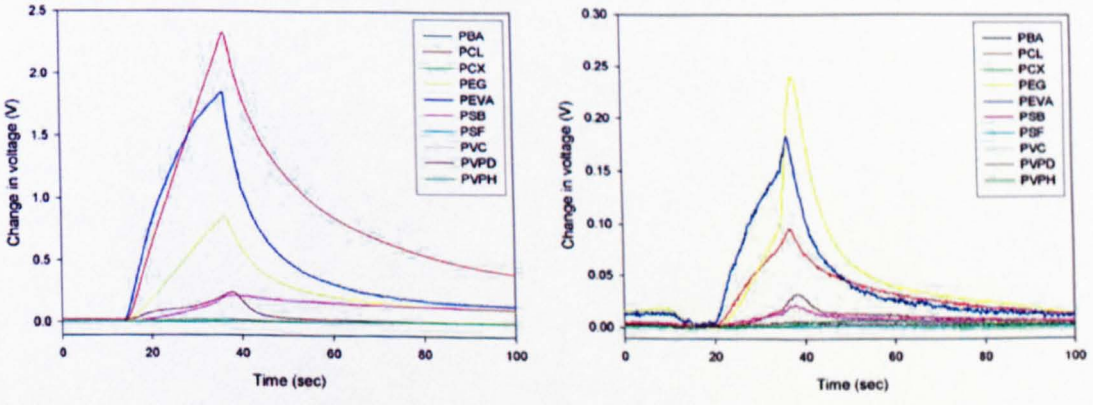

(a) (b)

Figure 8.8: Spatial signal of different types of sensors responding to complex analytes. (a) Sensor responses to peppermint essence vapour in air. (b) Sensor responses to vanilla essence vapour in air.

Beside the spatial signals, the proto-nose system is also capable of generating temporal signals. As discussed in Section 3.3.6, an analyte pulse travelling along a coated microchannel (i.e. GC column) experiences a different retention delay (time) depending on the partition coefficient of the analyte with the stationary phase material (in this case parylene C). Figure 8.9 shows 3 sets of sensor responses to (a) toluene vapour, (c) ethanol vapour and (e) peppermint essence vapour. Eight different sensor responses along the microchannel are depicted to illustrate different spatial signals (except S1 and S39 which are used for comparison). Figure 8.9 shows their normalised responses for (b) toluene vapour, (d) ethanol vapour and (f) peppermint essence vapour. Clearly, the sensors have responded in sequence according to their placements. The time at which the sensor response magnitude reaches 50 % will be used for comparing the retention time delay (temporal delay) as shown in Figure 8.9.

The relative retention time between S1 and S39 is approximately 92 s for toluene vapour, 58 s for ethanol vapour and 45 s for peppermint essence vapour. Using this temporal information, different analytes can be easily identified. Comparing these results to those obtained by the finite element simulation, the general trend shows much resemblance. For toluene vapour, it has a greater retention time when compared to ethanol vapour. However, a detailed comparison cannot be performed due to the lack of partition coefficients for various analytes with parylene C (the stationary phase material).

Using the responses of 5 sensors (S2, S12, S19, S28 and S39) placed along the microchannel, the spatio-temporal signals for various analytes were extracted for PCA (Principal Components Analysis) in order to determine the possibility of basic pattern classification. PCA is a technique that can be used to simplify a dataset; more formally it is a linear transformation that chooses a new coordinate system for the data set such that the greatest variance by any projection of the data set comes to lie on the first axis (then called the first principal component (PC1)), the second greatest variance on the second axis (PC2), and so on.

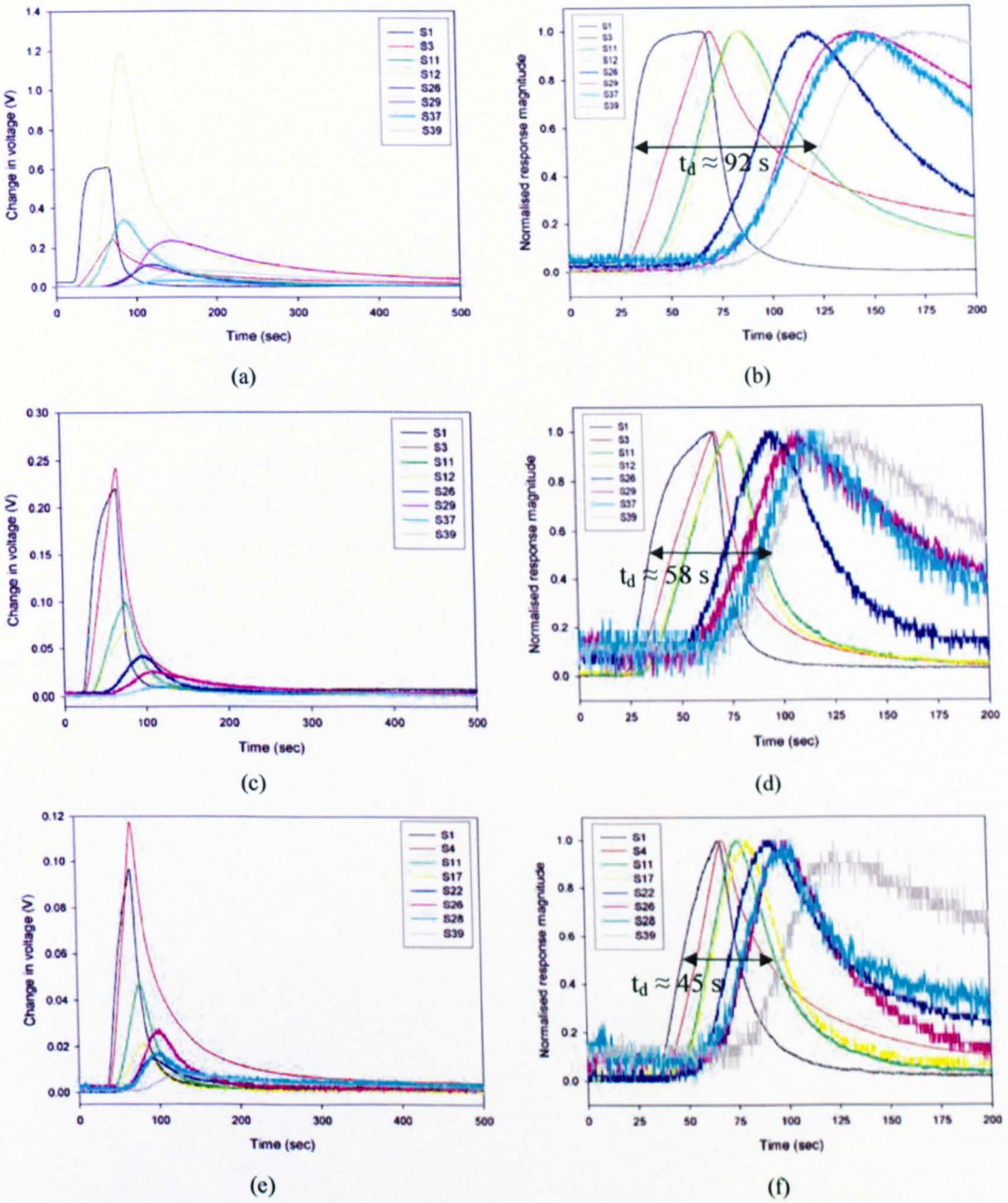

Figure 8.9: Temporal signals of sensors responding to simple and complex analytes. (a) Sensor responses to toluene vapour in air. (b) Normalised sensor responses of (a). (c) Sensor responses to ethanol vapour in air. (d) Normalised sensor responses of (c). (e) Sensor response to peppermint essence vapour in air. (f) Normalised sensor responses of (e).

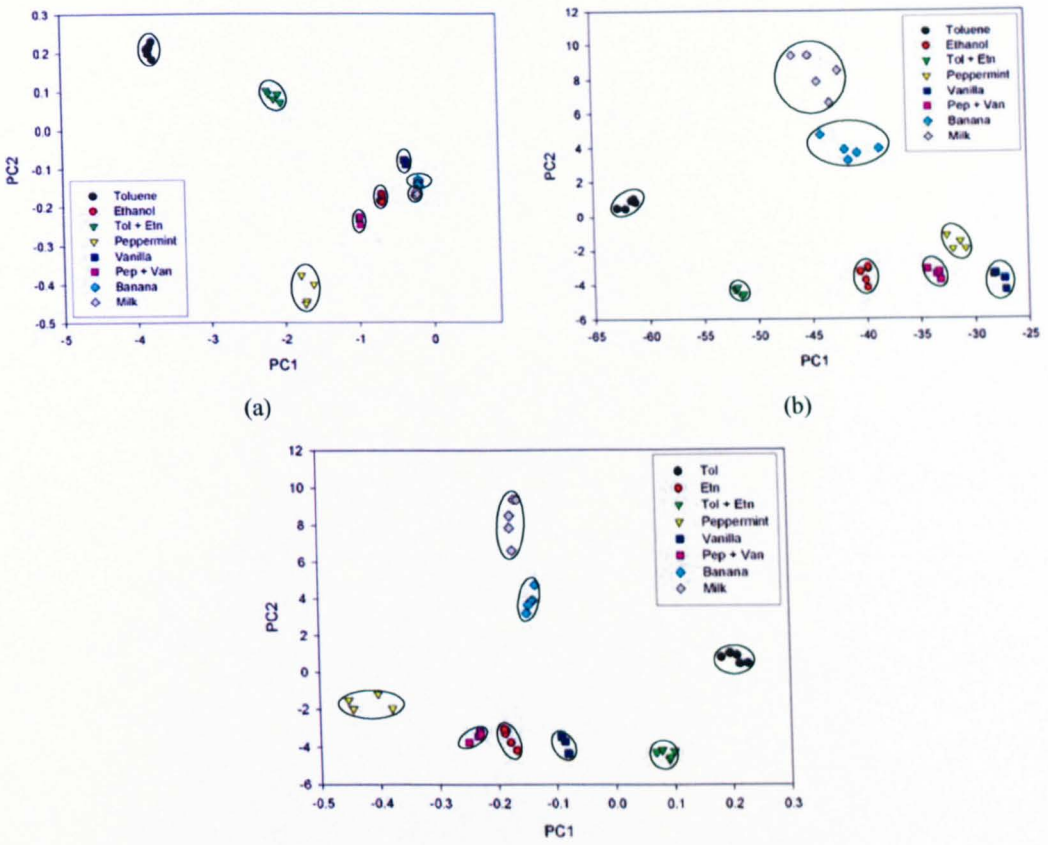

Figure 8.10: PCA plots with spatio-temporal data of 5 sensors (S2, S12, S19, S28, and S39) on proto-nose II. (a) Spatial (response magnitude, ΔV) data of 5 sensors. (b) Temporal (time at 50% of ΔV) data of 5 sensors. (c) Spatiotemporal data of 5 sensors.

For simplicity, the spatial signal utilised only the response magnitude (ΔV, change in voltage) and the temporal signal used the time at 50 % of ΔV. 8 different analytes consisting of simple analytes, complex odours and their mixtures were used for this experiment. It was conducted at the same flow rate of 25 ml min^{-1} and pulse width of 25 s with 5 repetitions at room temperature (25 °C ± 2 °C, 40 % ± 5 % R.H.). 3 PCAs were performed; one operates on the spatial data only, one uses the temporal data, while the last one utilises the combined data (spatio-temporal data).

Figure 8.10(a) shows the result of the PCA analysis using the spatial data. In this case, classification can be achieved for most analytes except milk and banana. However, when the temporal data are used for the analysis, distinct classes can be observed as shown in Figure 8.10(b). For banana and milk, the variation within each cluster is much larger compared to other test analytes. This is believed to be a result of the degradation of

fresh banana and milk over a long test duration (20 hours). In this instant, a better classification is achieved when the temporal data is used as compared to the spatial data. When both the spatial and temporal data of these sensors are included, a slight improvement is observed as shown in Figure 8.10(c).

8.3 Hybrid-nose characterisation

The hybrid-nose sensor array consists of 80 microsensors within a 10 mm × 10 mm silicon substrate. The hybrid-nose I has 5 different sensing materials while hybrid-nose II has of 10 different materials. The primary aim was to generate spatio-temporal signals with a minaturised system to achieve a nose-on-a-chip integration. To ensure the hybrid-nose microsensor arrays were functioning prior to assembly with the micropackages, they were calibrated using a microchamber. Within this microchamber the array was characterised with simple analytes, complex odours and their mixtures to determine their capability to perform discrimination without micropackages (simply relying on the spatial information based on the diversity of a large sensor array). Other more advance processing techniques such as those employing biological sniffing characteristics were also experimented with. Finally, these hybrid-noses were characterised when assembled with various microchannel packages.

8.3.1 Hybrid-nose characterisation with microchamber

The hybrid-nose sensor arrays were first characterised with simple analytes to determine their disparity in responses as a result of array based deposition. Similar to those discussed in Section 8.2.1 for discrete sensors, sensors with the same sensing material exhibit variation in response magnitudes.

Figure 8.11(a) shows the variation of 8 PSB sensors responding to ethanol vapour in air and (b) shows 8 PCL sensors responding to toluene vapour in air. The maximum variation in response magnitudes for PSB sensors to ethanol vapour is 7 % and 6 % for PCL sensors to toluene vapour. However, the remaining types of sensors show a much higher variation of 20 % (max) as compared to 10 % for discrete sensors. This has been largely expected as the variation in resistance for the hybrid-nose array is 3 times higher than the discrete sensors. Upon normalisation, their response profiles show great resemblance.

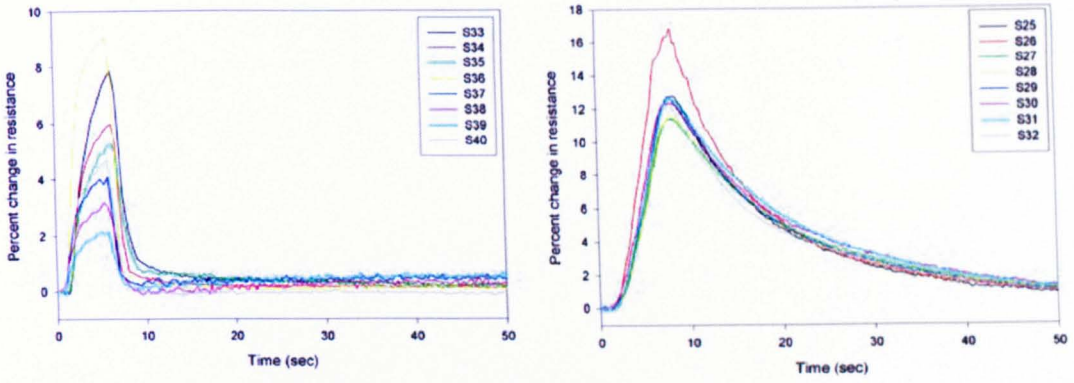

(a) (b)

Figure 8.11: Hybrid-nose sensor array response to simple analytes. (a) 8 PSB sensors responding to ethanol vapour in air. (b) 8 PCL sensors responding to toluene vapour in air.

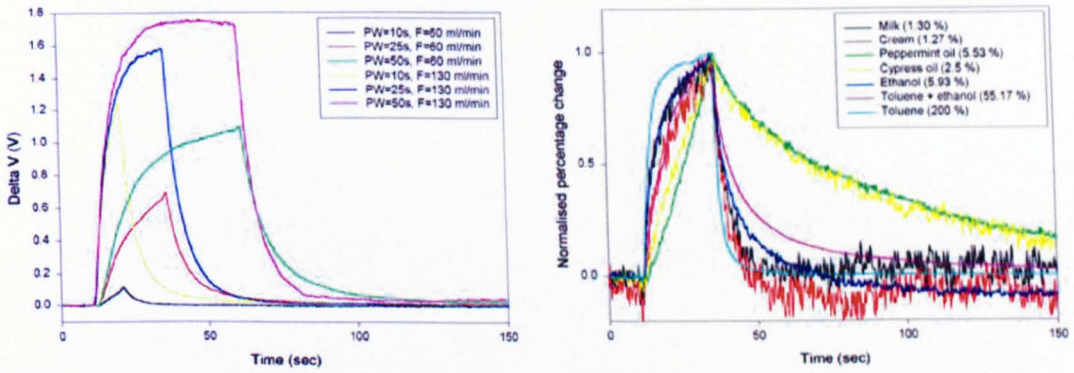

(a) (b)

Figure 8.12: Typical sensor responses to different analytes with varying pulse widths and flow rates. (a) PEVA sensor responses to peppermint oil vapour at two flow rates and 3 pulse widths. (b) Normalised PSB sensor responses to 7 test analytes.

The hybrid-nose sensor array not only has distinct responses to a particular analyte, it also responds differently when the pulse widths and flow rates are varied. Figure 8.12(a) shows a typical sensor responses to peppermint oil vapour where the pulse widths (PW) and flow rates (F) are varied. The results show that with the same sensor, the response magnitude and response time increase when either the flow rate or the pulse width is increased while the concentration are kept constant. This increase is expected to peak at some point due to the saturation limit of the sensor. Figure 8.12(b) shows the normalised (to unity) sensor (PSB) responses to 7 analytes. All analytes were tested at the same flow rate (60 ml min^{-1}) and pulse width (25 s). As the pulse width and flow rate are kept constant, the variation in response magnitude and response time, with different analytes,

is a result of different partition coefficient and diffusivity of the analyte within the sensing material. Some sensor responses (e.g. cream, milk) are nosier as the sensors have lower sensitivity to these analytes.

8.3.2 Discrimination analysis using olfactory imaging

The rapid expansion in sensor array components has resulted in an enormous increase in the amount of data one can obtain for each odour measurement. One of the most natural ways is to represent these data as an image [8.11]. Olfactory images are not new and are believed to be one the features enhancing the capability of mammalian olfactory systems [8.11-8.15]. Chemical imaging is an established principle of analysis which has been used for many years in biological tasting and smelling [8.15].

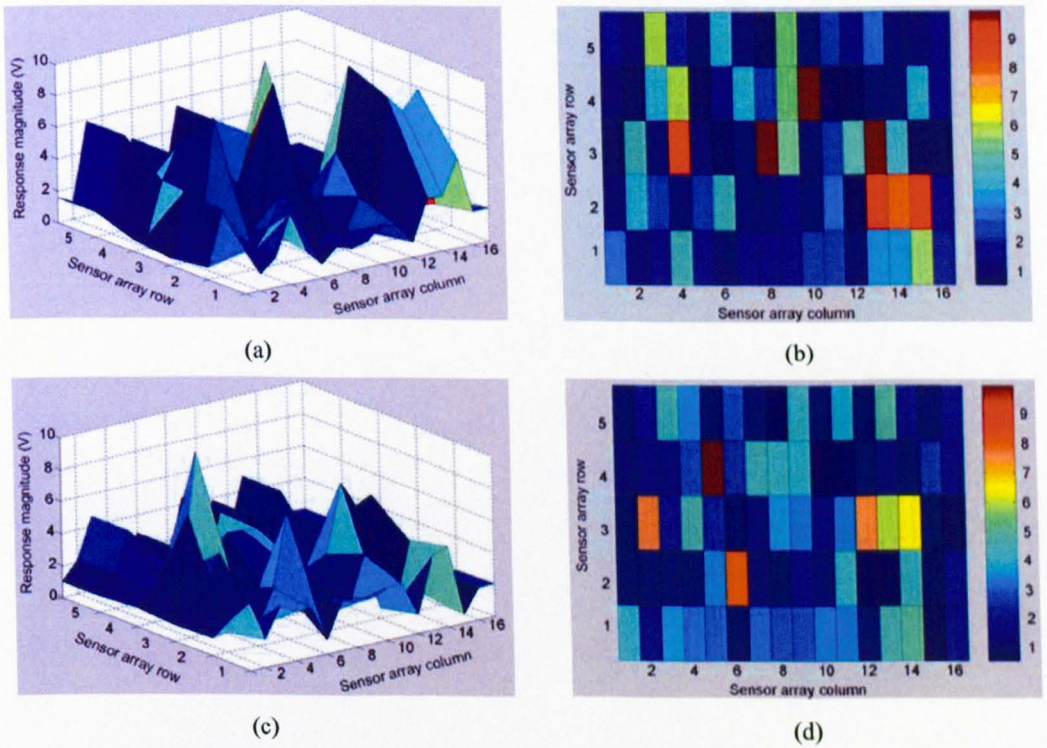

Figure 8.13: 3D and 2D fingerprint of cream vapour and peppermint oil vapour. (a, b) Sensor array fingerprints to cream vapour (maximum response), PW = 25 s, F = 130 ml min^{-1}. (c, d) Sensor array fingerprints to peppermint oil vapour (maximum response), PW = 25 s, F = 130 ml min^{-1}.

Figure 8.13(a) and (b) show the hybrid-nose sensor array responses to cream vapour as a 3D and 2D fingerprint. If each temporal fingerprint is arranged in sequence, an animated evolution video will represent the complete response. These 3D fingerprints can also be converted into 2D by representing the magnitude of the response as depth information

related to a colour bar. The fingerprints to peppermint oil vapour are shown in figures 8.13(c) and (d). These fingerprints could be used as templates for future comparison to identify the target analyte (using template matching).

To improve our ability to identify different odorants, the sniffing duration and speed will normally be varied [8.16]. This relates to varying the pulse width and flow rate of odorant delivery. Varying these parameters alters our ability to discriminate and identify different odorants. In this experiment, an attempt was made to replicate the scenario by studying the effect of varying pulse width and flow rate. Each analyte was tested at two different flow rates and three different pulse widths, with 5 repeated measurements at room temperature (25 °C ± 2 °C, 40 % ± 5 % R.H.).

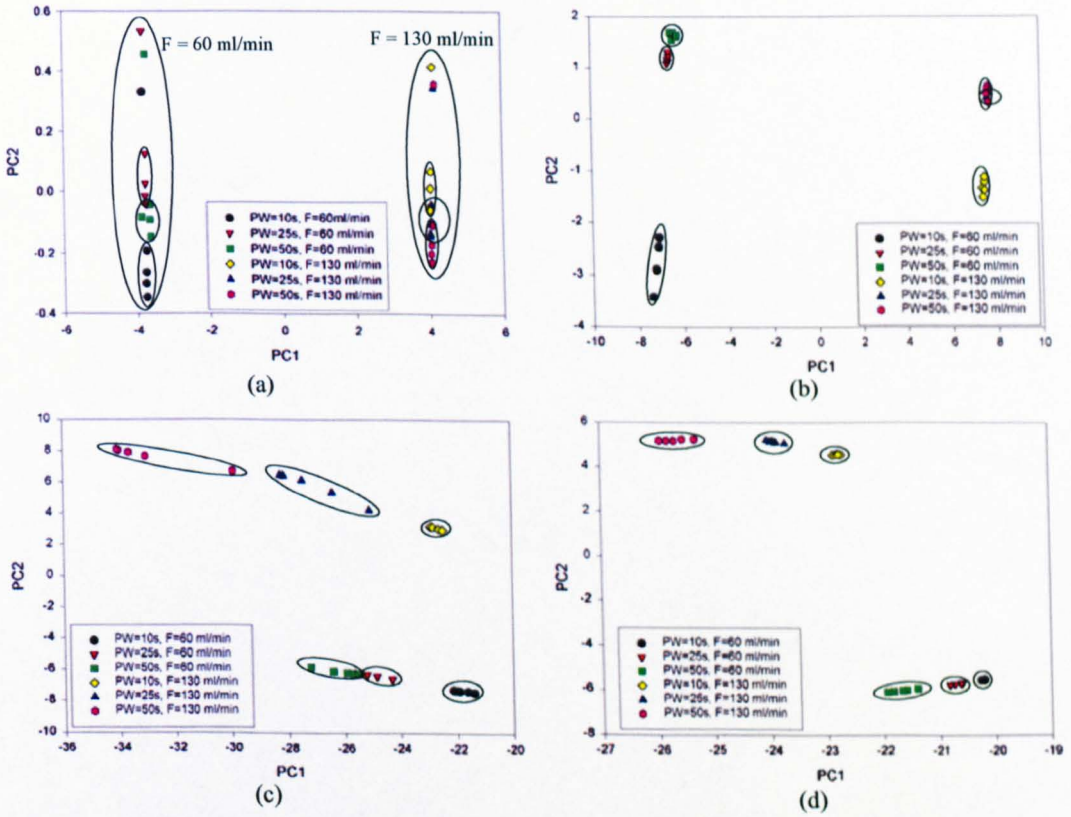

Figure 8.14: Effect of varying pulse widths and flow rates. (a) PCA plot of ethanol vapour in air. (b) PCA plot of toluene vapour in air. (c) PCA plot of milk vapour in air. (d) PCA plot of cypress oil vapour in air.

For each measurement, a 2D fingerprint was created using the maximum response magnitude. A simple PCA was used to determine the similarities in multi-dimensional space between these images. Figure 8.14 shows the plot for (a) PCA plot of ethanol vapour in air, (b) PCA plot of toluene vapour in air, (c) PCA plot of milk vapour in air

and, (d) PCA plot of cypress oil vapour in air. Ethanol vapour gave the poorest discrimination among the 7 (3 analytes are not shown here) tested analytes. For ethanol vapour, approximate classification can be achieved although there are a number of outliers. At different flow rates, the results clustered within a zone, enabling identification for different flow rates to be easier. In addition, increasing the pulse widths while maintaining the flow rate, makes it more difficult to exclusively cluster the samples. This is due to the fact that the sensors have responded much faster to ethanol vapour, and resulted in sensor saturation. When the pulse width is extended, the response magnitude is similar and hence less discrimination was achieved. For other analytes, distinct clusters can be identified at different flow rates and pulse widths. One interesting observation for all analytes is that the results fall distinctively into two clusters, based on the flow rate. For complex odours, higher flow rates result in easier discrimination. Although this cannot provide conclusive evidence, a higher flow rates have resulted in better discrimination for complex odours, compared to a longer exposure duration in this experiment.

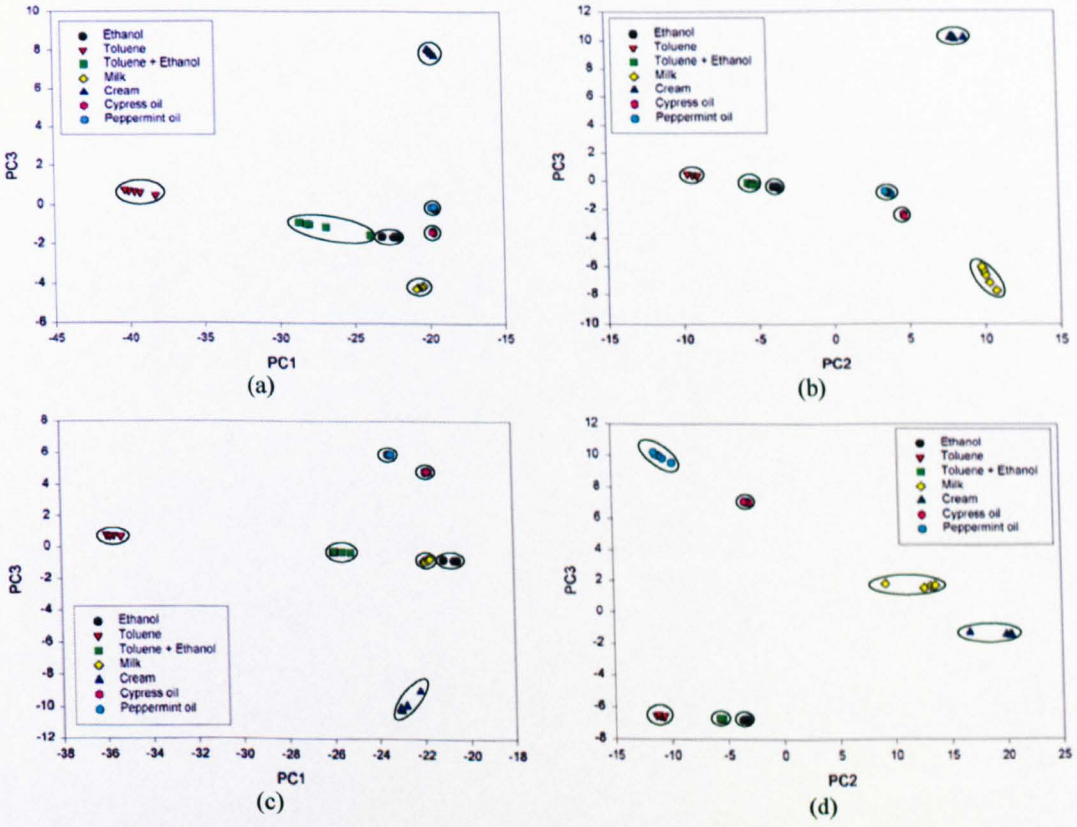

Figure 8.15: PCA plots of seven analytes at various pulse widths and flow rates. (a) PW=10 s, F=60 ml min^{-1}. (b) PW=50 s, F=60 ml min^{-1}. (c) PW=10 s, F=130 ml min^{-1}. (d) PW=50 s, F=130 ml min^{-1}.

The image matching technique can also be used to identify an analyte, even in the case of highly similar analytes. Figure 8.15 shows the PCA plots of seven analytes at various pulse widths and flow rates. At all tested pulse widths and flow rates, all 7 analytes can be distinctively segregated into exclusive clusters. In order to determine the effectiveness of varying the pulse widths and flow rates, the Euclidean (linear) distance between each cluster centre was calculated using the first 3 principal components (PC). As the pulse widths and flow rates are increased, the Euclidean distance between any two clusters increases, showing better discrimination as depicted in Table 8.2. There are some similarities between this system and the human olfactory system as the discrimination ability is improved as we sniff harder and longer [8.16]. One other technique that was normally used is to perform multiple sniffs. This successive odour sampling technique is believed to produce better discrimination through a process usually known as receptor adaptation [8.17] – not to be confused with odour adaptation that reduced our ability to smell an odour with time.

Table 8.2: Average Euclidean distance between any two odorant clusters.

	F = 60 ml min^{-1}	F = 130 ml min^{-1}
PW = 10 s	13.05	13.47
PW = 25 s	15.06	16.09
PW = 50 s	14.74	19.87

To further improve the discrimination capabilities of the microsensor array, 'stereo' olfactory images have been used [8.16, 8.18-8.21]. In these experiments, stereolfactory images were generated from test replicates operating at two different flow rates. Here, three olfactory images were used; one stereo and two mono (one at F=60 ml min^{-1} and the other at F=130 ml min^{-1}) images by varying the operating voltage of the micropump. Three sets of images were also available for comparison as three different pulse widths were experimented. Figure 8.16 shows a comparison between two monolfactory images and a stereolfactory image for 7 test analytes. Discrimination can be achieved in all cases.

To make a more appropriate comparison, two matrices commonly used for discrimination analysis are used. The Mahalanobis (non-linear) distance function determines the similarity of an unknown sample set while the Euclidean distance (linear) measures the ordinary distance between any two points using the Pythagorean theorem. Within each olfactory image, the intra-cluster and inter-cluster distance were extracted

using the first 3 principal components. The intra-cluster distance measures the distance between samples of repeated measurements while inter-cluster measures the distance between the centres of each cluster. The analysis with monolfactory images show that for all pulse widths, at a lower flow rate, results in smaller intra-cluster distance when compared to higher flow rate. However, the opposite is observed for inter-cluster distance. This is reflected in both the Mahalanobis and Euclidean matrices. The stereolfactory image gives a compromise between intra-cluster and inter-cluster distance. As both distances are important in determining the success of discrimination, this compromise in both intra and inter-cluster distances shown in stereolfactory images is believed to provide the additional discriminatory feature.

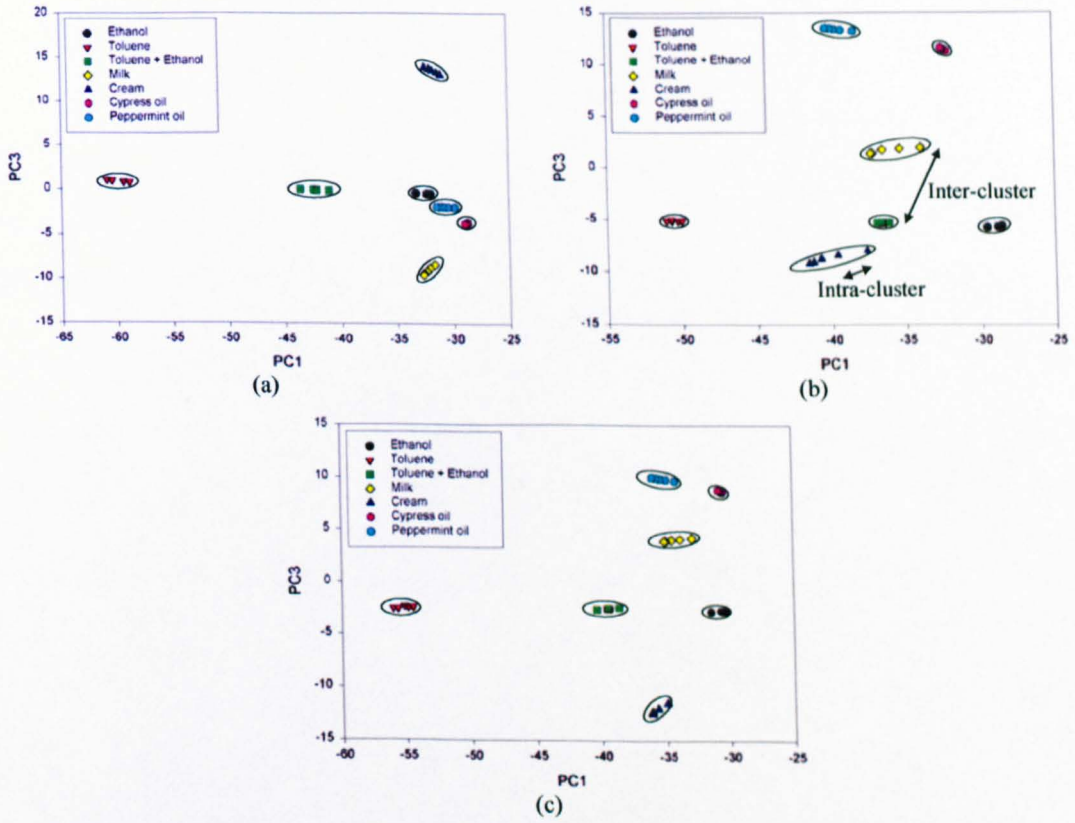

Figure 8.16: Comparison between mono and stereolfactory images. (a) Monolfactory image (F=60 ml min^{-1}, PW=25 s). (b) Monolfactory image (F=130 ml min^{-1}, PW=25 s). (c) Stereolfactory image.

Although the hybrid-nose sensor array is capable of performing discrimination (due to the large array and sensor diversity), it is not possible to generate any temporal signal (spatial signal is provided by the sensor diversity). However, due to the spatial placement of the 80 sensors in an array fashion (5 rows of 16 elements), occupying a surface area of

10 mm × 2.5 mm, it is still possible to differentiate the flow direction by comparing the response of the sensor at each end of a row. Figure 8.17 shows the responses of 3 sensors along a row (front, middle and end of the row). Figure 8.17(a) shows the sensor responses when the flow direction is forward while (b) shows the sensor responses when the flow direction is reversed. The sequence of responses when the flow direction is reversed indicates that there is a slight difference in temporal signals. However this is too small to provide any significant contribution to aid discrimination.

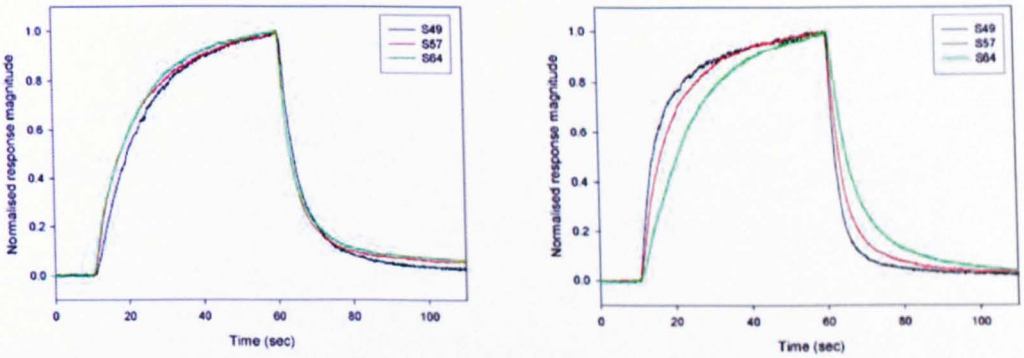

Figure 8.17: Bidirectional hybrid-nose responses to ethanol vapour in air. (a) Normalised PCL sensor responses in forward flow direction. (b) Normalised PCL sensor responses in reverse flow direction.

8.3.3 Nose-on-a-chip characterisation

Preliminary characterisation of the hybrid-nose reveals its superiority in generating spatial signals and thus, provides a good classification for both simple analytes and complex odours. However, little or no temporal signal can be extracted. Three micropackages, fabricated using microstereolithography were assembled with the hybrid-nose to realise nose-on-a-chip microsystems. These systems have the same sensing characteristics as the proto-nose, but with a huge reduction in size (proto-nose II is 250 × 200 × 15 mm^3 while hybrid-nose with MSL115 is only 36 × 27 × 10 mm^3).

8.3.3.1 Microchannel package MSL101 (5 cm long microchannel)

The MSL101 micropackage has a single continuous microchannel that traverses through the 80 microsensors in a row by row fashion. To ensure the sensors are not affected by the assembly process, the sensors are re-calibrated as shown in Figure 8.18. These experiments are also used to study other effects such as the speed at which these sensors

respond. The low dead volume (2 µl) of the microchannel package requires less analyte and produces rapidly responding sensors.

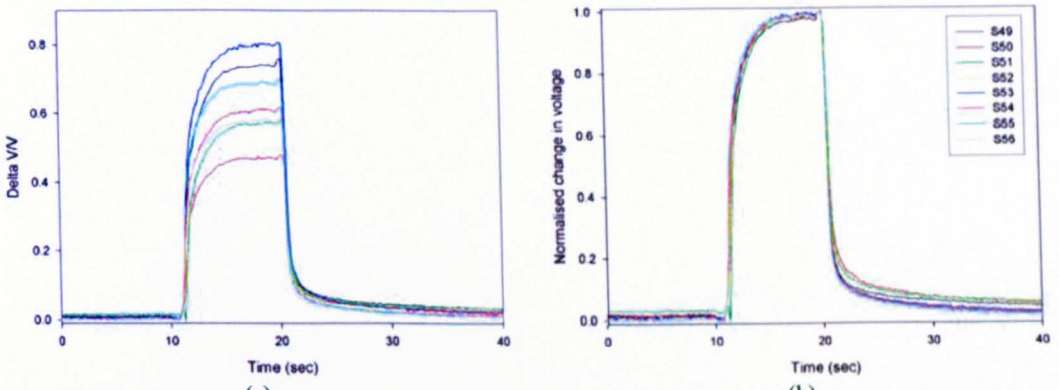

(a) (b)

Figure 8.18: PVPD sensor responses to vanilla. (a) 8 PVPD sensors responding to a 10 s pulse of vanilla essence vapour in air. (b) Normalised responses of (a) to unity.

Figure 8.19 shows two fast responding sensors, (a) a PCL sensor responding to toluene vapour in air and (b) a PEG sensor responding to vanilla essence vapour in air. Their respective response time is found to be only 480 ms and 92 ms, with many other sensors showing sub-second response times. These response times are a huge improvement over similar types of sensors exhibiting response times from seconds to minutes [8.4, 8.8-8.9].

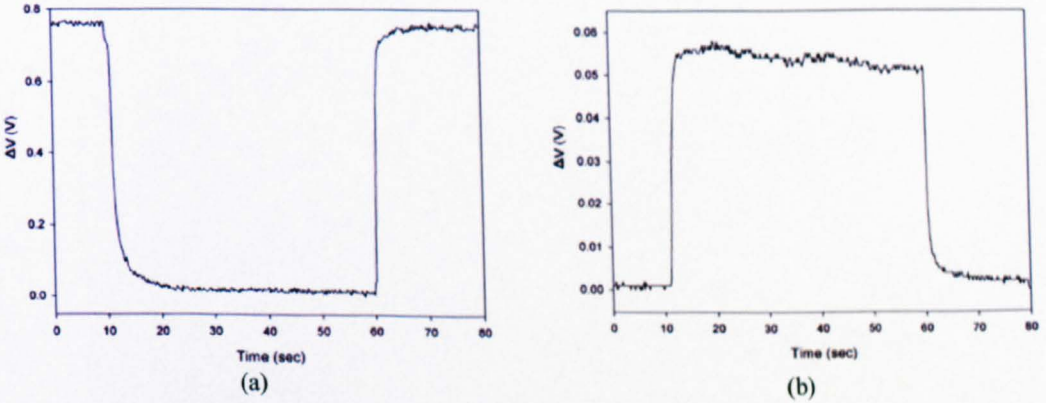

(a) (b)

Figure 8.19: Ultra-fast sensor responses. (a) Fast PCL sensor responding to toluene vapour in air with response time of 480 ms. (b) Fast PEG sensor responding to vanilla essence vapour in air with response time of 92 ms.

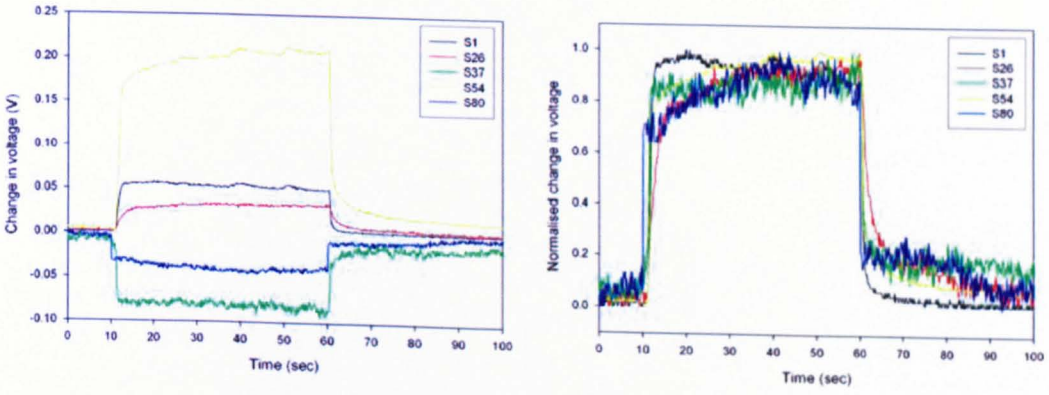

(a) (b)

Figure 8.20: Temporal signals of sensors along MSL101 microchannel. (a) 5 sensor responses to vanilla essence vapour. (b) Normalised responses of (a).

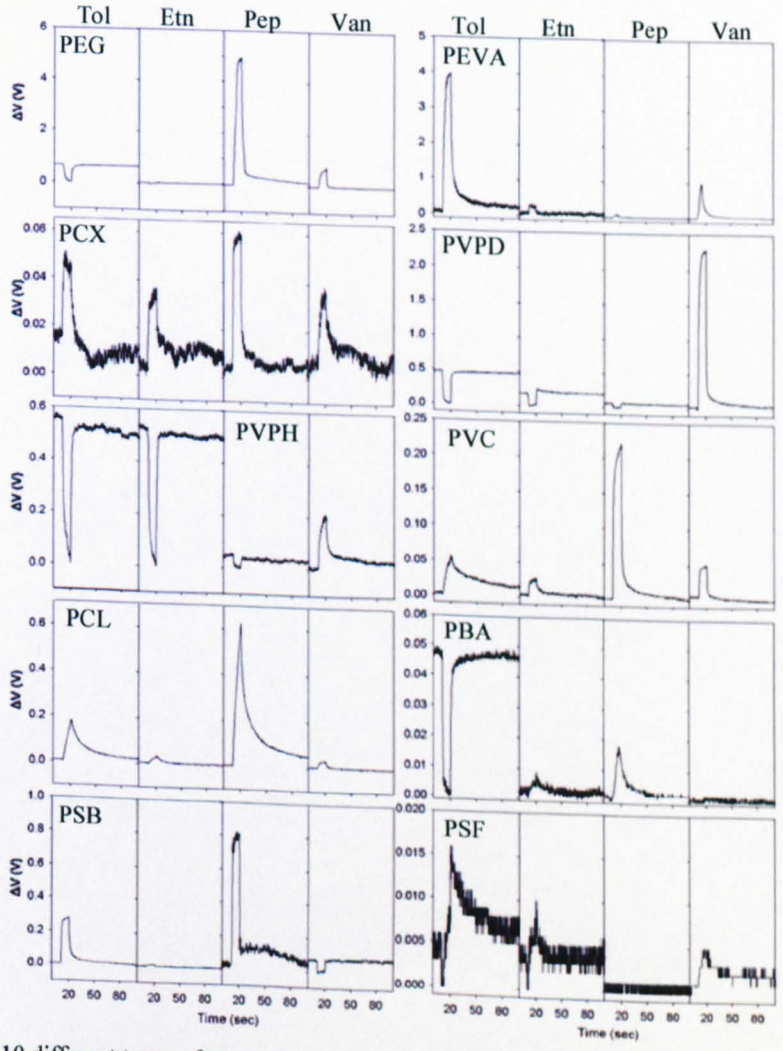

Figure 8.21: 10 different types of sensors responding to 10 s pulses of simple (toluene and ethanol vapour in air) and complex (peppermint and vanilla essence vapour in air) analytes in air at 30 ml min^{-1}.

Although MSL101 has a low dead volume and produces fast responding sensors, its short microchannel length does not provide enough time delay to generate distinct temporal signals for different analytes, as predicted by the simulations. Figure 8.20 shows the temporal signals for 5 sensors responding to vanilla essence vapour. Figure 8.20(a) shows their relative responses and (b) shows their normalised responses. The responses of these sensors are in sequence according to their placements; however there is no evidence to suggest that there are any significant differences in temporal signals when compared to other test analytes.

A comparison between 10 different types of sensors depicted in Figure 8.21 has shown that the system is capable of generating spatial signals for both simple analytes as well as complex odours.

8.3.3.2 Microchannel package MSL112 (32 cm long microchannel)

With MSL112, a 32 cm long microchannel package was assembled with the hybrid-nose. In the last section, the MSL101 system was shown to be capable of generating spatial signals. However, due to its short microchannel length, no temporal signal was obtained. In this section and the following one, the focus will be directed on the generation of temporal signals. For MSL112, the base of the microchannel package is divided into 8 'mini-chambers' (Section 5.4.2.1). Each mini-chamber contains 10 sensors (in 2 columns) and adjoining each mini-chamber is a 40 mm segment of microchannel.

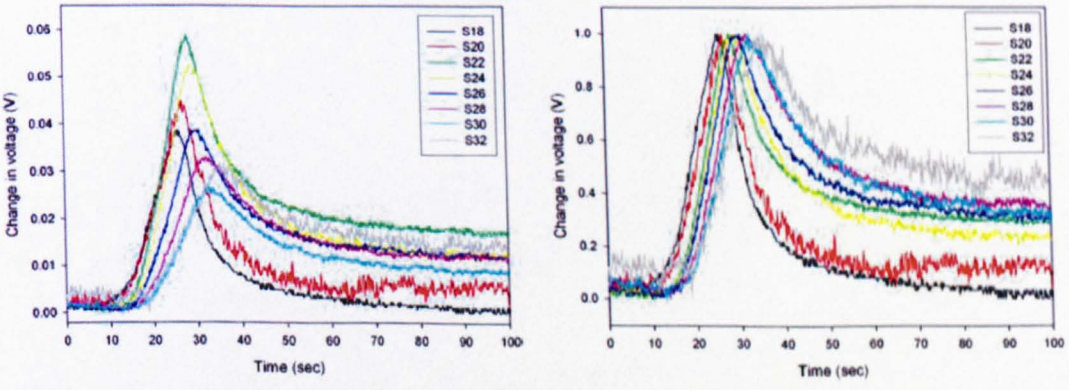

(a) (b)

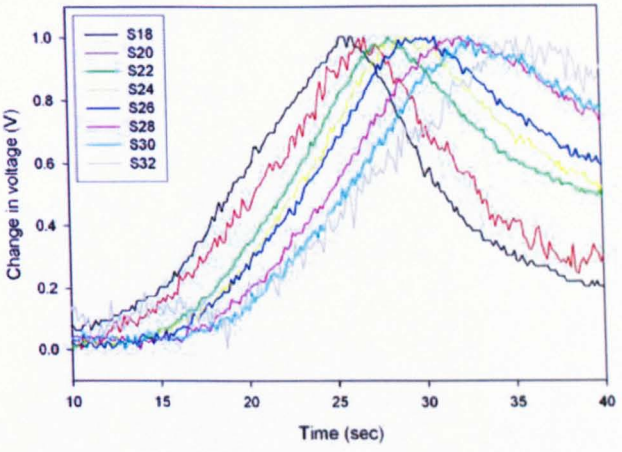

(c)

Figure 8.22: Temporal signals of sensors along MSL112 microchannel. (a) 8 sensor responses to ethanol vapour in air at each respective mini-chamber zones. (b) Normalised responses of (a). (c) Expanded view of (b) showing the temporal signal as each sensor responded in sequence.

Figure 8.22 shows the responses of 8 sensors across a row with each sensor residing in a different mini-chamber. Figure 8.22(a) gives the spatial signals while (b) shows the normalised responses and (c) shows an expanded view of the temporal signals to ethanol vapour in air. The results show that the temporal signals have been greatly enhanced, as compared to MSL101 due to the longer length of the microchannel. The time delay between each pulse is consistent as their physical distances apart are identical.

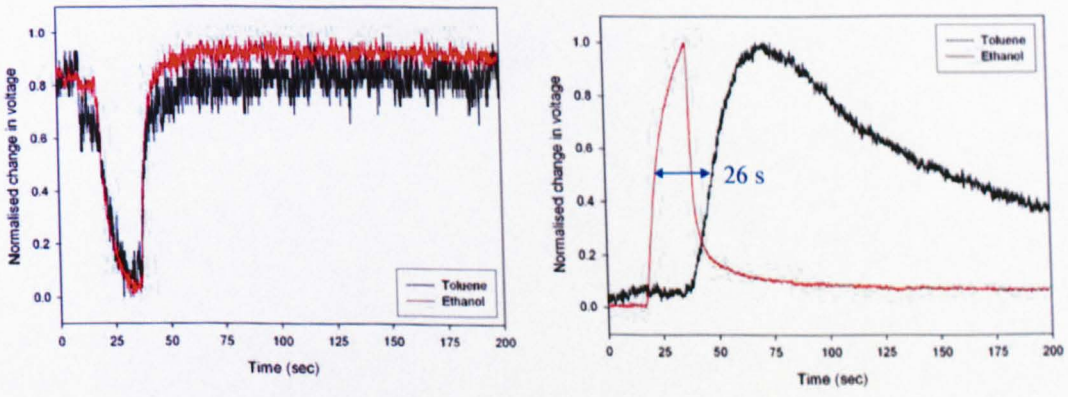

(a) (b)

Figure 8.23: Difference in temporal signal between toluene and ethanol vapour in air on MSL112 microchannel. (a) S65 (inlet) sensor response to toluene and ethanol vapour in air. (b) S32 (outlet) sensor to toluene and ethanol vapour in air.

Here simple analytes (toluene and ethanol vapour) have been used for these tests. Figure 8.23 shows the varying temporal signal for two simple analytes. Figure 8.23(a) shows that the sensor closer to the inlet of the microchannel receives both analytes at approximately the same time; whilst in (b) towards the outlet of the microchannel, a significant amount of time delay can be observed on the toluene vapour pulse in relation to the ethanol vapour pulse. This clearly demonstrates the capability of MSL112 microchannel package to generate distinct temporal signals for different analytes, hence fulfilling the aim of spatio-temporal signal generation with a nose-on-chip system.

8.3.3.3 Microchannel package MSL115 (240 cm long microchannel)

To further improve the performance of the micronose system, an even longer microchannel package, similar to proto-nose II, was designed and fabricated (Section 5.4.2.1). This package was designed to obtain the same length (240 cm) and dimensions as proto-nose II in order to achieve equivalent performance.

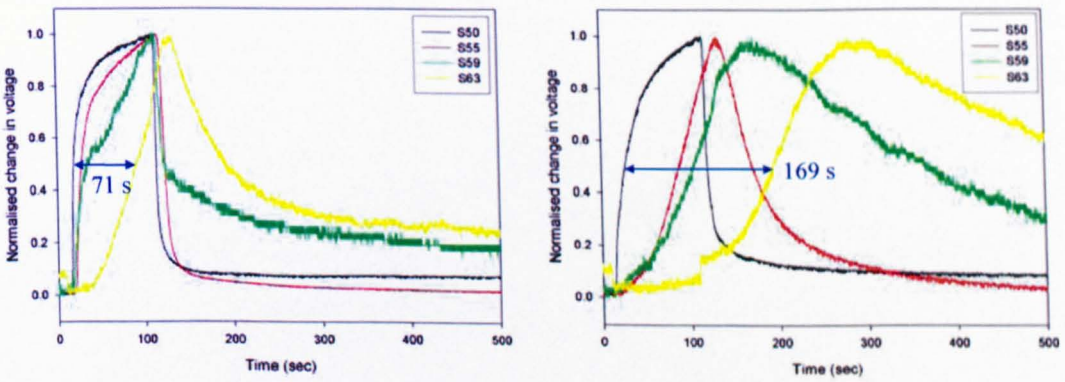

Figure 8.24: Hybrid-nose temporal signals when assembled with MSL115 microchannel package. (a) Normalised sensor responses to ethanol vapour in air. (b) Normalised sensor responses to toluene vapour in air.

Figure 8.24 shows the responses of 4 sensors of the hybrid-nose responding to ethanol and toluene vapour in air when assembled with MSL115 microchannel package. Figure 8.24(a) shows the responses to ethanol vapour while (b) shows the responses to toluene vapour. The temporal signals for ethanol vapour are significantly less when compared to toluene vapour; this is similar to the results obtained in proto-nose II.

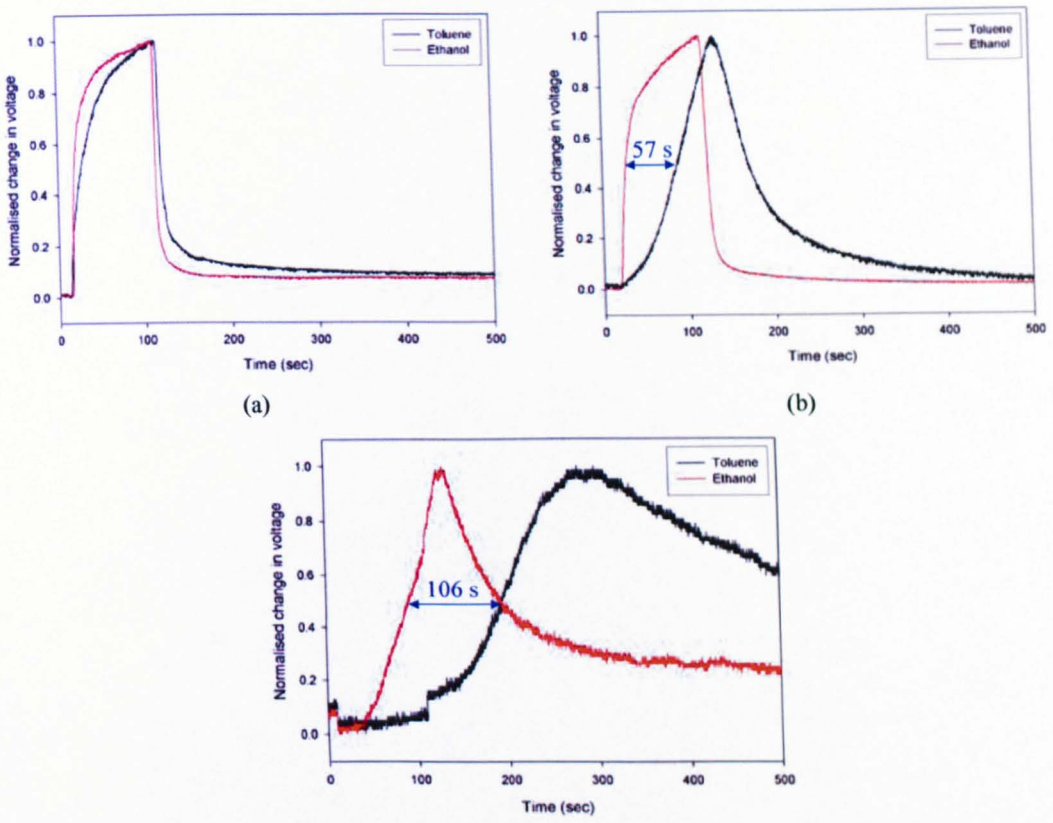

Figure 8.25: Varying temporal signals for simple analytes on hybrid-nose when assembled with MSL115 microchannel package. (a) Sensor S50 (30 mm from inlet) response. (b) Sensor S54 (1060 mm from inlet) response. (c) Sensor S63 (2280 mm from inlet) response.

Figure 8.25 shows the comparison results between the sensor responses along the microchannel to simple analytes. Closer to the inlet of the microchannel at (a), both ethanol and toluene vapour pulse reaches the sensor at the same time. As the pulses travel along the microchannel to (b), the retention effects of the two analytes become significant. Towards the outlet at (c), the two analyte pulses are nearly separated. For complex odours, it has a similar effect of providing different retention delays. In order to determine the performance of this microsystem, PCA was conducted on the spatio-temporal signals (similar to those for proto-nose as given in Figure 8.10) of 5 sensor responses.

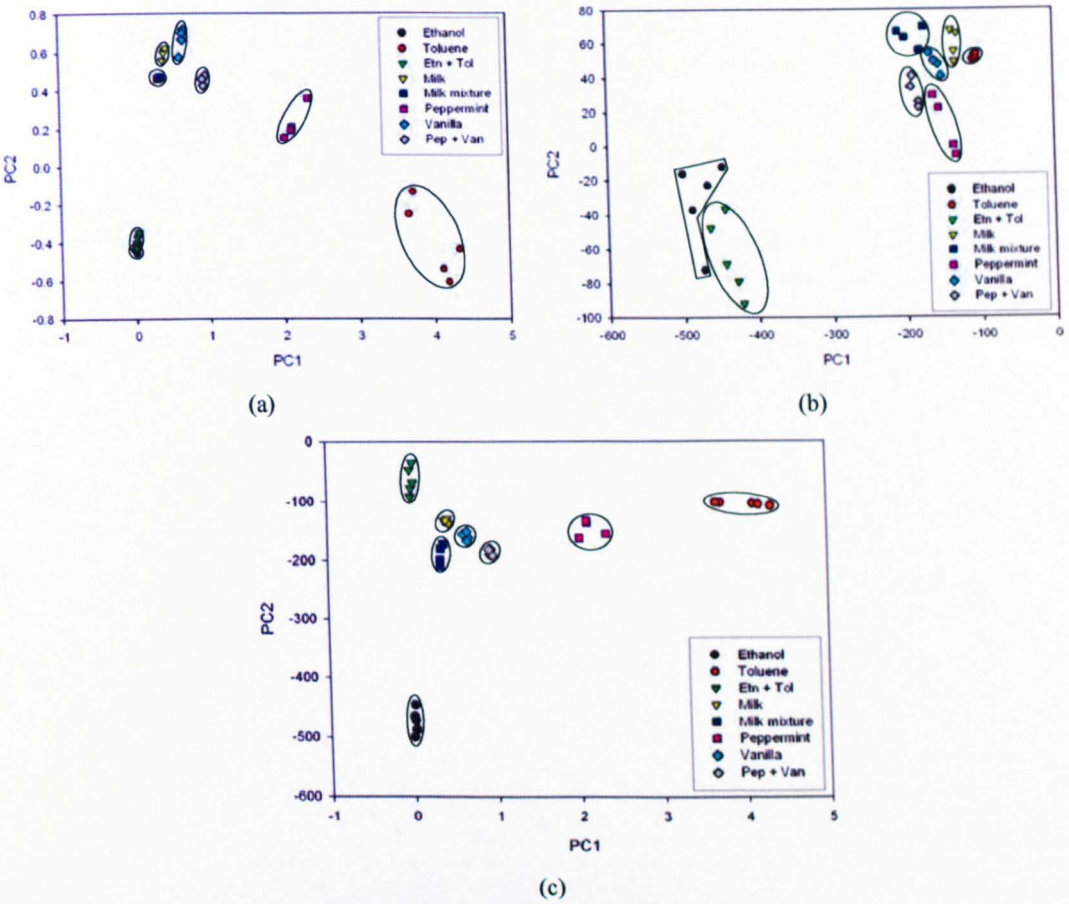

Figure 8.26: PCA plots with spatio-temporal data of 5 sensors (S34 (30 mm from inlet), S38 (1060 mm from inlet), S57 (2100 mm from inlet), S27 (2160 mm from inlet), and S30 (2200 mm from inlet)) for hybrid-nose with MSL115 microchannel package. (a) Spatial (response magnitude, ΔV) data of 5 sensors. (b) Temporal (time at 50% point) data of 5 sensors. (c) Spatiotemporal data of 5 sensors.

Figure 8.26 shows the results of the PCA performed on the (a) spatial data, (b) temporal data, and (c) spatio-temporal data. The results have shown that it is possible to perform classification based on either parameter or both. However, when compared to the results obtained from the proto-nose II system, the nose-on-a-chip system is less favourable. There are three plausibly causes for the poorer results obtained from this nose-on-a-chip microsystem. Firstly, the set of experiments conducted here were done continuously with minimum recovery time allocated between each test. This might cause the sensors to be exposed to the next test analyte before they had recovered from the previous test and returned to their original baseline. Secondly, there could be 'intra-channel leakage' which was not fully characterised. Last and most importantly, these experiments were conducted in a laboratory where the environmental temperature was similar to the

outdoor temperature (variation ≈ 10 °C or more); whereas the previous experiments on the proto-nose systems were conducted in another laboratory with temperature variation of less than 5 °C. Nevertheless, this provides a good indication that the spatio-temporal feature extraction and classification technique is robust and is capable of subjecting to drastic environmental variation.

8.4 aVLSI-nose characterisation

The aVLSI-nose consists of 70 microsensors arranged in 5 rows of 14 elements. The sensor placements and packaging were identical to the hybrid-nose so as to allow the same microchamber and micropackages to be used on both designs. Each sensor contains a dedicated programmable driving, offset cancellation, amplification and filtering circuit to remove the need for any external drive and conditioning circuitries, unlike the case of hybrid-nose. The details pertaining to the programmability and interfaces for the aVLSI-nose were discussed in Chapter 7. Within each smart sensor cell, the sensor can be operated either in resistive or FET mode of operation. There are also two possible routes for the sensor signal to be either in direct mode or interface mode. The FET test sensor has been included by other members within the group and has been characterised separately. Hence, all subsequent measurements depicted are made in resistive configuration. The direct mode of operation will be discussed in Section 8.4.1 and the interface mode of operation in Section 8.4.2. In addition, as the responses with microchannel packages would be expected to be similar to those captured by the nose-on-a-chip systems given in Section 8.3.3, all measurements have been performed with the microchamber to simplify the setup.

8.4.1 Smart sensor cell

In the direct mode of operation (Section 4.4.3), each sensor is connected to a programmable current drive circuit that is cascaded to a buffer op-amp. This mode of operation is the minimal building block for an integrated sensor. It is used when the sensor response magnitude is sufficiently large and does not require amplification. Three select logics per cell are required to be programmed; they are the sensor mode select (2 bits), the current drive select (3 bits to select the desirable driving current) and the route select (2 bits). After these modes are setup, the sensor array is ready for testing.

The smart sensor cell was initially characterised for the stability of its constant current drive circuit. Figure 8.27(a) shows the change in output voltage across a fixed resistor (a fixed resistor is used for characterising the programmable current drive to ensure that the noise fluctuation is due to the current drive and not that of the sensor) when the current setting was programmed. Upon settling, the noise is within 2 mV. Next, the sensor cell is being characterised for its basic functionalities. Six pulses of toluene, ethanol vapour and their mixture are used and the results are shown in Figure 8.27(b). The repeatability of the sensor response was excellent, except for the case of ethanol vapour where the slight deviation was attributed to the testing protocol (this test was commenced before the sensor resistance stabilised). In addition, the sensor baseline remains relatively constant even after prolonged testing.

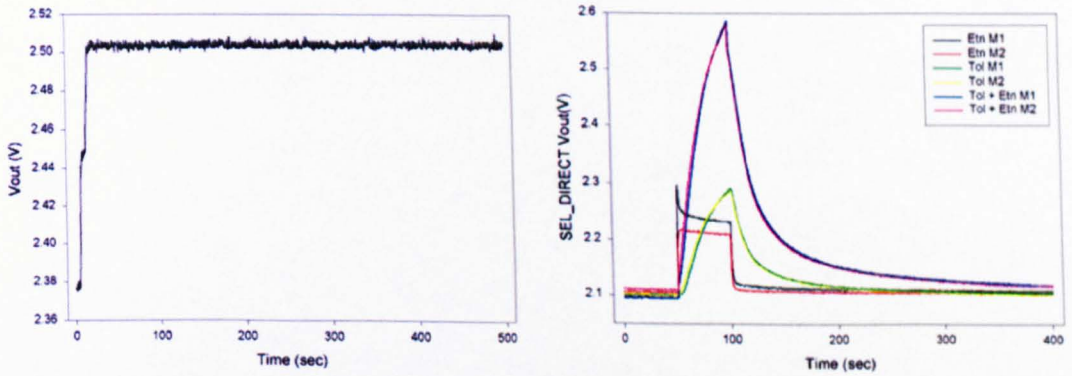

(a) (b)

Figure 8.27: Driving current and sensor response stability. (a) Constant driving current stability across a fix resistor. (b) Repeated sensor exposure to simple analytes.

There are two rationales for providing programmable driving currents over a wide range. Firstly, this is to accommodate for considerable variation in sensor baseline resistance as a result of spraying deposition. Secondly, the variation in sensor response due to the selectivity of different sensing materials with target analytes can be adjusted to limit its voltage swing. In the former case, for a sensor resistance of 200 kΩ, the three driving current selections (1 μA, 10 μA or 100 μA) will ideally produce an output voltage of 200 mV, 2 V or 20 V. Due to the reduced operating range (0 V to +5 V for CMOS process) of the buffer op-amp, the best operating current selection should be I = 10 μA to allow the baseline to be in the middle of the operating range (+2.5 V, so as to allow maximum positive and negative voltage variations) of the op-amp.

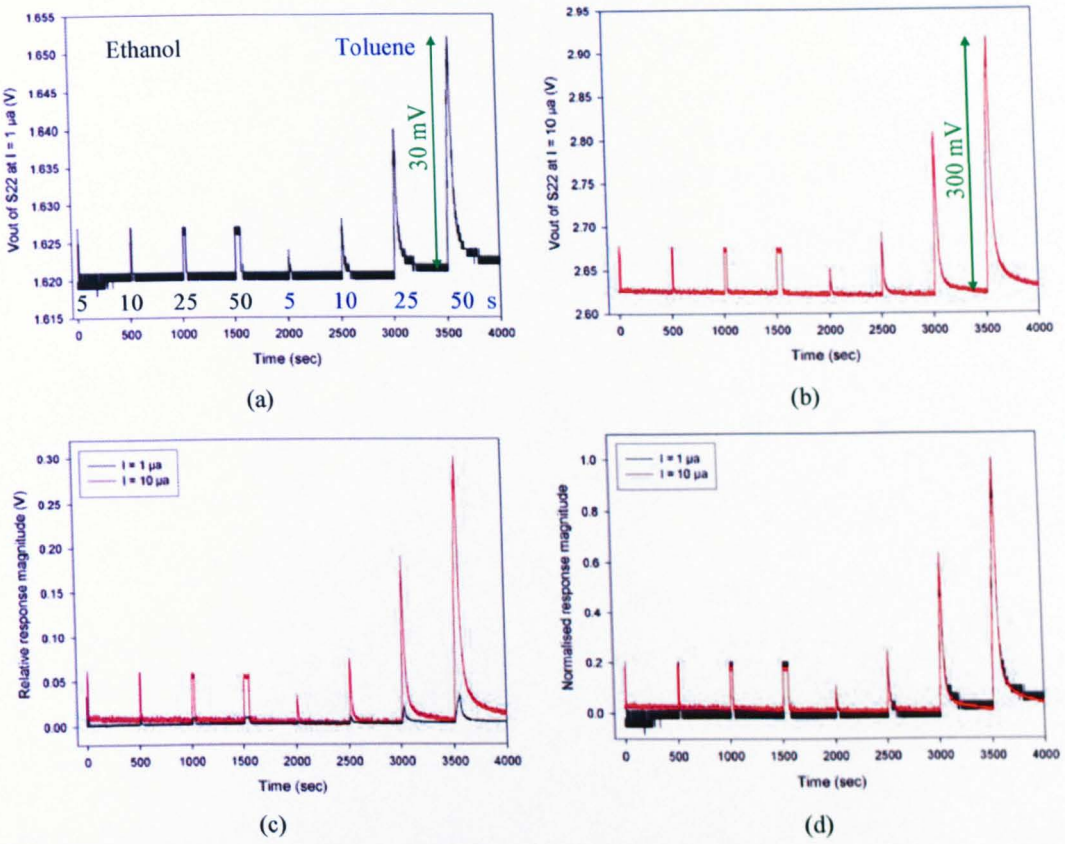

Figure 8.28: Effect of varying drive current on sensor response to simple analytes. (a) Sensor S22 response to ethanol and toluene vapour at I = 1 µA (offset = 1.35 V). (b) Sensor S22 response to ethanol and toluene vapour at I = 10 µA (offset = 0 V). (c) Comparison between (a) and (b). (d) Normalised response of (c).

In the latter scenario, the current drive selection was altered to boost the signal level of the response magnitude. Figure 8.28(a) shows the response of sensor S22 responding to various pulses of ethanol and toluene vapour in air at I = 1 µA (offset voltage = 1.35 V) and (b) at I = 10 µA (offset voltage = 0 V). The response magnitude in (a) is only 30 mV while in (b) the response magnitude is 300 mV, an increase of 10 times. These two responses are compared in (c) with their baseline voltages removed and in (d) their responses are normalised. Clearly in this scenario, operating the sensor at 10 µA driving current is more favourable (in terms of resolution) as it produced a larger response magnitude. Upon normalisation to unity, they give similar responses.

In the following test, the effect of concentration variation was studied. Here, a sensor (PSB) has been exposed to five different concentrations of ethanol (180, 260, 370, 520 and 1150 ppm (parts per million)) vapour and toluene (100, 160, 220, 310 and 700 ppm) vapour in air at a constant temperature of 30 °C and humidity (20 % R.H.) as

shown in Figure 8.29(a). The response refers to the percentage change (ΔR/R) in resistance. From these results, the static effect of toluene and ethanol vapour in air to a PSB sensor are plotted as shown in Figure 8.29(b). The sensitivity to ethanol vapour is about 0.00012 % ppm^{-1} and 0.00644 % ppm^{-1} to toluene vapour. Other types of sensors show similar linear model across the same range of ethanol and toluene vapour concentration.

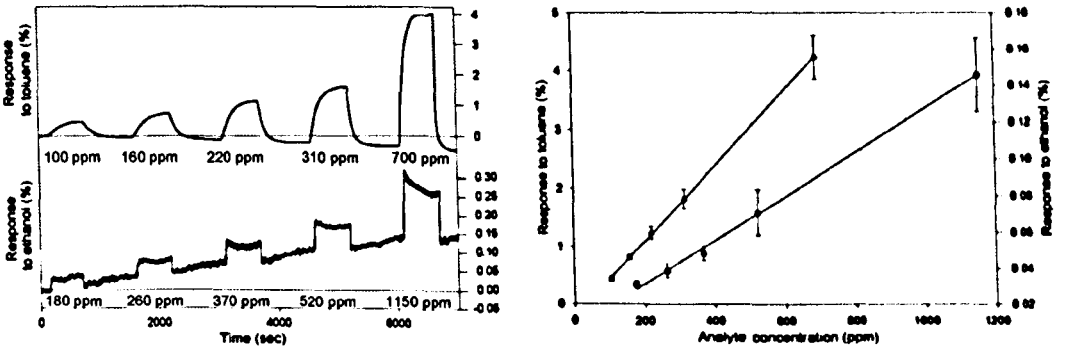

(a) (b)

Figure 8.29: Sensor response magnitudes characterisation. (a) Responses of PCB sensor to five different concentrations of ethanol and toluene vapour in air. (b) Static sensor output, fitted with a linear model.

Although the smart sensor is capable of varying the driving current, depending on the sensor resistance and affinity to different analytes, the response magnitude is still relatively low considering the voltage swing of the CMOS circuit is only 5 V. It is not possible to amplify the sensor's output signal significantly without any processing as the baseline voltage (ideally at 2.5 V) will saturates the output voltage of 5 V (with a gain of 2×). To improve the dynamic response range of the sensor, a novel DC offset cancellation circuit was implemented for each sensor [8.22-8.24].

8.4.2 DC-offset cancellation circuit for offset removal

The primary limitation for the integrated design is the need to hold the offset (or baseline) voltage for a long duration of time throughout the entire measurement cycle. It soon becomes evident that digital techniques provide the simplest means of implementing such storage. The setup for each smart sensor cell has been discussed in Section 4.4.2 and 4.4.3 and it can be summarised as follows. Prior to the measurement phase, a setup phase calibrates all sensor baseline voltages simultaneously with counters,

DACs and comparators by comparing the baseline voltage with the DAC output (which is driven by the counter). As each counter gradually counts upward, the DAC output voltage increases up to the point where it just exceeds the baseline voltage. At this point, the comparator output negates to stop the counter from increasing any further. The whole process takes only 1 ms where all 70 sensors are calibrated simultaneously.

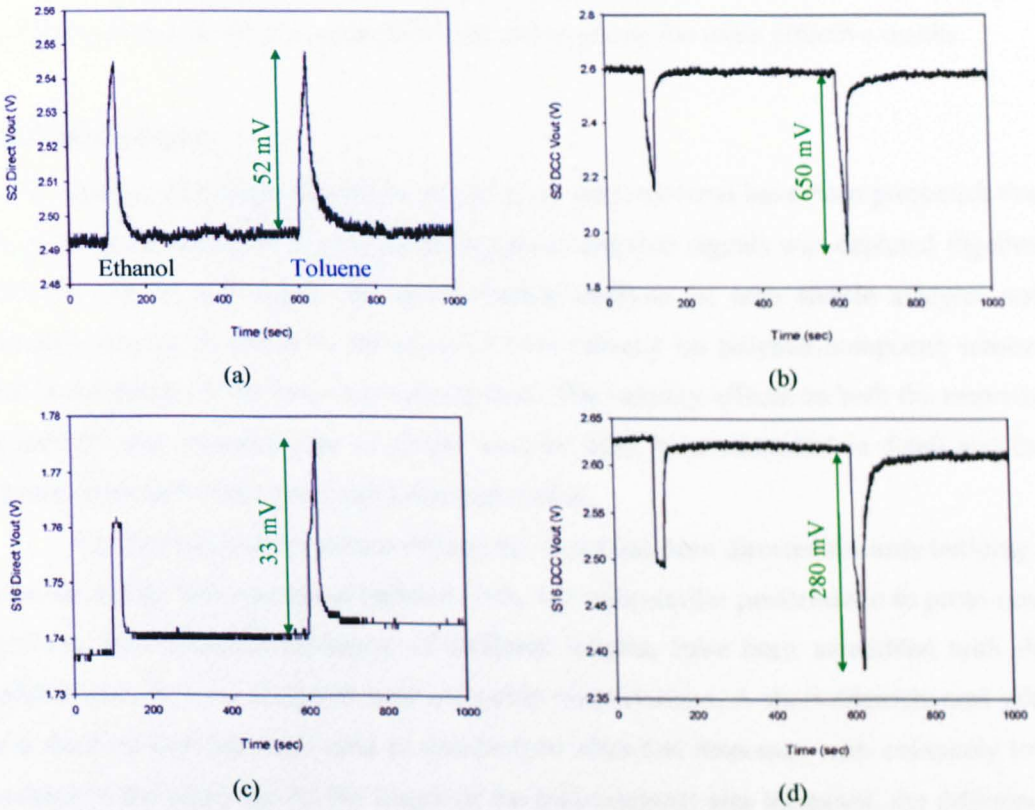

Figure 8.30: Sensor responses to simple analytes for direct and interface mode of operation. (a) S2 response in direct measurement mode. (b) S2 response in interface mode. (c) S16 response in direct measurement mode. (d) S16 response in interface mode.

The sensors are then ready to perform any measurements with the baseline voltages stored digitally in counters. With the baseline signal removed, the sensor response can be amplified; this is critical when the response magnitude is small. Figure 8.30 shows two sensors responding to low concentration of ethanol and toluene vapour pulses in air. In Figure 8.30(a), sensor S2 (PEG) response is measured in direct mode of operation while in (b), it is measured with the DC offset cancellation circuit (interface mode). Figure 8.30(c) shows the response for sensor S16 (PVPH) in direct mode and (d) the same sensor responding in interface mode. Comparing the responses of both sensors in the

direct and interface mode, it can be clearly observed that there is a 10 times amplification on the responses measured in interface mode. The slight variation in responses of both sensors is attributed to the lower resolution when the direct sensor responses are measured. The responses in the interface mode are inverted due to the differential amplifier configuration (Figure 4.20). However, this should not pose any problem as it is possible to have both positive and negative sensor responses. In the interface mode of operation, all sensor responses are inverted, hence giving the same effective results.

8.5 Conclusions

In this chapter, the characterisations of 3 primary microsystems have been presented. For the proto-nose systems, the generation of spatio-temporal signals was depicted together with the use of each signal for discrimination analysis on both simple analytes and complex odours. In addition, the effect of flow velocity on polymer-composite sensors was investigated on the fast-nose microsystem. The velocity effects on both the response magnitude and response time to simple analytes have been examined in detail and the results fitted well to the proposed analytical model.

For the hybrid-nose microsystems, the focus has been directed towards building a nose-on-a-chip microsystem at reduced scale, but with similar performance to proto-nose systems. Microchannel packages, of different lengths, have been assembled with the hybrid-noses to form complete nose-on-a-chip microsystems. A short microchannel with low dead volume has been used to demonstrate ultra-fast responses with extremely low volume of test analytes. As the length of the microchannel was increased, the difference in retention behaviour (time delay) between various analytes becomes evident. This provides clear indication that this system was approaching the performance of the proto-nose system.

Finally, the characterisation results of the aVLSI-nose were presented. The aim here is to replace the hybrid-nose sensor array with the aVLSI-nose as each sensor includes its own smart circuitries (which includes driving and signal conditioning). All functionalities incorporated in the design have been tested and work in accordance to those predicted by the simulations.

8.6 References

[8.1] M. Holmberg, F. Winquist, I. Lundström, F. Davide, C. DiNatale, A. d'Amico, ***Drift counteraction for an electronic nose***, Sensors and Actuators B, Vol. 36, pp. 528-535, 1996.

[8.2] B. Lazzerini, F. Marcelloni, ***Counteracting drift of olfactory sensors by appropriately selecting features***, Electronics Letters , Vol. 36, pp. 509-510, 2000.

[8.3] J.E. Haugen, O. Tomic, K. Kvaal, ***A calibration method for handling the temporal drift of solid state gas-sensors***, Analytica Chimica Acta, Vol. 407, pp. 23-39, 2000.

[8.4] J.A. Covington, J.W. Gardner, D. Briand, N.F de Rooij, ***A polymer gate FET sensor array for detecting organic vapours***, Sensors and Actuators B 77, 2001.

[8.5] N. Matsunaga, G. Sakai, K. Shimanoe, N. Yanazoe, ***Formulation of gas dynamics for thin film semiconductor gas sensor based on simple reaction-diffusion equation***, Sensors and Actuators B, Vol. 96, pp. 226-233, 2003.

[8.6] J.W. Gardner, P.N. Bartlett, K.F.E. Pratt, ***Modelling of gas-sensitive conducting polymer device***, IEEE Proc.-Circuits Devices Syst., Vol. 142, pp. 321-333, October 1995.

[8.7] S.M. Briglin, N.S. Lewis, ***Characterization of the temporal response profile detectors to volatile organic vapours***, *J. Phys. Chem. B 107*, pp. 11031-11042, 2003.

[8.8] J.W. Gardner, E.L. Hines, F. Molinier, P.N. Bartlett, T.T. Mottram, ***Prediction of health of dairy cattle from breath samples using neural network with parametric model of dynamic response of array of semiconducting gas sensors***, IEE Science, Measurement and Technology, Proceedings, Vol. 146 , pp. 102-106, 1999.

[8.9] D. M. Wilson, S. P. DeWeerth, ***Odour discrimination using steady-state and transient characteristics of tin-oxide sensors***, Sensors and Actuators, B 28, pp. 123-128, 1995.

[8.10] P. Accettola, M. Balsi, A. d'Amico, C. Di Natale, A. Macagnano, F. Sortino, ***Time-constant extracting filters for fast gas identification in electronic noses***, Electronics Letters , Vol. 38 , pp. 510–511, 2002.

[8.11] I. Lundström, ***Artificial noses: Picture the smell***, Nature 406, pp. 682-683, 2000.

[8.12] I. Lundström, R. Erlandsson, U. Frykman, E. Hedborg, A. Spetz, H. Sundgren, S. Welin, F. Winquist, ***Artificial 'olfactory' images from a chemical sensor using a light-pulse technique***, Nature 352, pp. 47-50, 1991.

[8.13] J. Mizsei, ***Olfactory images by scanning Kelvin method***, Sensors and Actuators B 48, pp. 300-304, 1998.

[8.14] H. Ishida, T. Tokuhiro, T. Nakamoto, T. Moriizumi, ***Improvement of olfactory video camera: gas/odour visualization system***, Sensors and Actuators B 83, pp. 256-261, 2002.

[8.15] J. Mizsei, S. Ress, ***Chemical images by artificial epithelia***, Sensors and Actuators B 83, pp. 164-168, 2002.

[8.16] S. Sobel, R.M. Khan, C.A. Hartley, E.V. Sullivan, J.D.E. Gabrieli, ***Sniffing longer rather than stronger to maintain olfactory detection threshold***, Chem. Senses 25, pp. 1-8, 2000.

[8.17] M. Stopfer, G. Laurent, ***Short-term memory in olfactory network dynamics***, Nature 402, pp. 664-668, 1999.

[8.18] O. Rochel, D. Martinez, E. Hugues, F. Sarry, ***Stereo-olfaction with a sniffing neuromorphic robot using spiking neurons***, 16th European Conference on Solid-State Transducers - EUROSENSORS, Prague, Czech Republic, September 2002.

[8.19] B. Hirshon, N. Sobel, ***Stereo smell***, Science Net Link, http://www.sciencenetlinks.com/, December 2003.

[8.20] J.J. Principato, J.M. Ozenberger, ***Cyclical changes in nasal resistance***, Arch. Otolaryngol., 91, pp. 71-77. 1970.

[8.21] M. Hasegawa, E.B. Kern, ***The human nasal cycle***, Mayo Clin. Proc., pp. 28-34, 1977.

[8.22] S. McKennoch, D.M. Wilson, ***Autoranging compensation for variable baseline chemical sensors***, SPIE Proceedings Photonics East, Boston, MA, 2001.

[8.23] D.M. Wilson, T.A. Roppel, ***Hardware architectures for chemical sensing electronics***, SPIE Proceedings Photonics East, Boston, MA, 1999.

[8.24] P.I. Neaves, J.V. Hatfield, ***Current-mode multiplexer for interrogating resistive sensor arrays***, Electronics Letters, Vol. 30, pp. 942-943, 1994.

Chapter 9

Conclusions and further work

9.1 Overiew

The increasing demand for electronic nose systems in a broad spectrum of applications such as the food industries, environmental monitoring, medical diagnostics and security applications, have produced an emerging industry. The first commerical e-nose system became available in 1993 (Fox 2000 by Alpha-MOS, France) with an estimated total market value for such systems of only €300,000. In 2000 this market had increased to an estimated almost €150 million [9.1] and it is estimated to be about €950 millions in 2004 [9.2].

E-nose systems provide an alternative to the use of organoleptic panels because the human olfactory system fatigues easily and is unsuitable for applications involving toxic odorants. Most existing commercial electronic nose systems are bench-top units, which are expensive and bulky. In addition, these systems usually require a trained operator to collect and analyse the data. Futhermore, these systems are only a rudimentary implementation of the biological olfactory system, providing basic discrimination in controlled environment compared to the mammalian olfactory systems that are mobile and capable of adapting to environmental changes.

The research undertaken in this project was motivated by the disparity in performance, size and cost of electronic nose systems compared to the biological olfactory systems. As many of the mysteries regarding the biological olfactory system and smell continue to be solved, it is inevitable some of these findings will be significant in revealing the features underpinning the superiority of the biological olfactory system. One key factor, providing this superiority, could be the discovery of the nasal chromatography effect, which produces spatio-temporal signals. In addition, the unique

operating features of the biological olfactory systems could also supplement this ascendancy; they include stereolfaction (two nostrils sniffing at different flow rates) and sniffing rate (flow velocity) and duration (pulse width) variations. Based on these phenomena, various artificial systems have been designed, fabricated and tested. This study has been divided into two sections: the development of prototype systems to model nasal chromatography effects for generating spatio-temporal signals; and the development of nose-on-a-chip systems employing microfabrication technologies to address cost and miniaturisation issues.

9.2 Project objectives

Many of the objectives in this study have been realised, these are summarised as follows:

- Finite element models have been constructed for microchannels, GC microchannels, polymer-composite sensors and used to investigate the effects of flow velocity on sensor responses.
- Microsensors, microsensor arrays and CMOS compatible smart sensor arrays with novel processing circuitry have been designed, fabricated and tested.
- Full 3-D microchannel packages of various lengths (5 cm, 32 cm, 71 cm, 120 cm, 240 cm) have been designed, fabricated using stereolithography (SL) and microstereolithography (MSL) systems, and characterised.
- Biological olfactory operations such as sniffing rate (flow velocity) and duration (pulse width) variation, and stereolfaction have been experimented to investigate their effects on e-nose system.
- Proto-nose systems mimicking the nasal chromatography effect which was observed in the biological olfactory systems have been designed and evaluated to demonstrate the generation of spatio-temporal signals to aid discrimination analysis.
- Lastly, nose-on-a-chip systems have been developed by integrating the sensor arrays with microchannel packages and characterised to demonstrate the commercialisation potential using modern microfabrication technologies while sustaining the generation of spatio-temporal signals.

9.3 The development of artificial biological olfactory systems

A number of artificial olfactory systems have been developed to investigate some of the key biological discoveries. The main focus was directed towards the development of systems that mimick the nasal chromatography effect. The first group of systems consist of fast-nose, proto-nose I and proto-nose II systems. The basic design principles for these systems are similar. Each system comprises a PCB base with trenches machined on one side for discrete sensors to be embedded within. The other component is the lid with a microchannel machined onto its surface such that when it is assembled with the PCB base, the microchannel transverses across the sensors. The challenge here was to achieve the maximum microchannel length while maintaining the sensors positions with respect to their physical distances from the microchannel inlet. In addition, the microchannel traversing path cannot interfere with the sensors (and vice-versa) and circuitries on the PCB base. The length of the microchannel was 10 cm for the fast-nose, 120 cm for the proto-nose I and 240 cm for the proto-nose II. The cross-sectional areas of the microchannel on all three systems were 500 μm × 500 μm. The fast-nose can accommodate up to 10 sensors while proto-nose I has 40 sensors of 5 different tunings and proto-nose II has 40 sensors of 10 different tunings. The fast-nose system was designed to characterise the discrete sensors prior to their usage on the proto-nose II system. For the proto-nose systems, two different types of lids (microchannels) were fabricated: one is the normal microchannel (without coating) while the other is coated with a thin layer (10 μm) of retentive materials (in this case parylene C). Such a design essentially implements the basic 'nasal chromatography' concept by placing a series of sensors (of different tunings) along a coated GC microchannel to generate spatio-temporal signals. This is the first time such a design has been implemented for a gas sensing system. The increase in microchannel length (from 120 cm in proto-nose I to 240 cm in proto-nose II) by extending the distances between adjacent sensors enhances the temporal signals, which translate into an equivalent improvement in the discrimination capability of the system.

The second group of systems are the nose-on-a-chip systems that combine microsensor arrays fabricated using silicon microfabrication processes with microchannel packages fabricated using microstereolithography. The components include hybrid-nose sensor arrays, aVLSI-nose smart sensor arrays, and the microchannel packages of different lengths. The development of the nose-on-a-chip systems focused on optimising

the proto-nose systems through employing modern microfabrication technologies. The hybrid-nose sensor array was fabricated in-house on a 3" silicon wafer, using standard photolithography processes, with the primary aim of achieving miniaturisation. The fabricated sensor array consisted of 80 microsensors arranged in 5 rows of 16 elements on a 10 mm × 10 mm silicon substrate. This sensor array is considered low density compared to other higher density sensor arrays (> 1000 sensors) reported earlier due to the need to allow individual sensor or group of sensors to be accessible through the microchannel package separately. Furthermore, the sparse sensor placements technique improves the yield of sensing material deposition and allows individual sensor to be deposited with a different material by ensuring a minimum distance of 400 μm between any two sensors.

A survey was conducted to investigate feasible techniques and technologies for building the microchannel packages. The traversing path of the microchannel is an important design issue due to the need to place the sensors at different locations along the microchannel. On the fast-nose and proto-nose systems, the delivery microchannel resides on the surface of the lid. Recently, there has been a considerable interest in the fabrication of microchannel for various applications. However, most techniques utilise micromachining processes that are only capable of producing 2.5-D structures. Long microchannel (1 m) was fabricated on small area (10 mm × 10 mm) by etching a spiral shape pattern on silicon prior to bonding it with a flat base (similar to the proto-nose system). These techniques have been deployed to build microchannel GC columns. However they are not suitable to build full 3-D microchannel packages. Microstereolithography and stereolithography systems were used to fabricate these microchannel packages. Unlike conventional micromachining techniques, complex full 3-D microchannel packages can be built without complicated fabrication procedures. The length of the microchannel is extensible through simple modification of the CAD model file (in software). Microchannels of various lengths (5 cm, 32 cm, 71 cm, 120 cm, 240 cm) were designed and built. Using external microvalve arrays, it is possible to construct a microchannel of dynamic length. These packages also allow drastic reduction (75 times in external dimension) in the overall system size.

The aVLSI-nose is a smart microsensor array compatible (in terms of sensor placements) to the hybrid-nose sensor array. This microsensor array was fabricated using standard CMOS process (AMS 0.6 μm CUP) via Europractice. The aim is to incorporate

programmable driving and conditioning circuitries into each sensor to alleviate the need for external supporting circuits. The primary constraint for most resistive gas sensors lies with the existence of a drifting baseline or offset voltage superimposed on the small differential sensor response. This makes it difficult to amplify the sensor response directly due to the saturation limit of CMOS circuit. Through numerous studies, it was identified that a digital means of maintaining (sample and hold) the baseline voltage is more appropriate due to the long measurement duration required. A novel DC-offset cancellation circuit was designed and implemented for each sensor cell to remove the baseline voltage at the input to a differential amplifier. This allows the small sensor response to be amplified within the dynamic range of CMOS amplifier. The fabricated microsensor array consisted of 70 sensors arranged in 5 rows of 14 elements on a 10 mm × 5 mm silicon substrate. As each sensor has a set of dedicated circuitries to support its operation, the sensors can be programmed to operate at different conditions (driving current, sensing mode, baseline and gain). The sensor placements and layout are identical to the hybrid-nose sensor array so that the same microchannel packages can be used.

To assist the design and development of these systems, finite element models were created to simulate and predict the performance of various proposed designs prior to fabrication. These systems, unlike the existing electronic nose systems, offer some resemblance to the biological olfactory system. Although the existing e-noses and the proposed NOC systems utilise the same basic components (gas sensors, headspace sampler, mass flow system, etc), the unique implementation of the NOC systems using the nasal chromatography phenomena produces additional signals (spatio-temporal) to aid discrimination. These additional features bestow performance improvements that will otherwise be lost.

Custom-designed vapour test station and data acquisition systems have been built to facilitate the characterisation of these e-noses. The data acquisition boards consist of multiplexing circuitries to support the measurement of individual sensor response on the fast-nose, proto-nose, hybrid-nose and aVLSI-nose. Each sensor will be driven and its response signal conditioned and sampled at regular intervals for recording on a PC. The interface hardware was designed to be extensible to accommodate different number of sensors on each system. The vapour test station (VTS) facilitates automated flow injection control to vary the test conditions by changing the flow rate, pulse duration and test analyte(s) selection. The VTS accomplished these operations through the switching

of various microvalves sequences (analytes mixing and pulse duration control) and adjusting the operating voltage of the micropump (flow rate control) at appropriate timings. In addition, the operating conditions (temperature, humidity, flow rate and leakage) are monitored to allow possible correlation and compensation across different experiments when the system operates under different conditions. Both the data acquisition board and VTS were controlled by a custom software control program, written in LabView, to automate the entire process.

Table 9.1 shows the major components of various systems fabricated in this project and the technologies involved to produce them.

Table 9.1: Major components of various systems and the technologies used for their fabrication.

System	Components	Fabrication technology
Fast-nose	Fast-nose base	Standard PCB, CNC machining
	Fast-nose lid	CNC machining
Proto-noses (I & II)	Proto-nose I base	Standard PCB, CNC machining
	Proto-nose I lid (1.2 m long microchannel)	CNC machining
	Proto-nose II base	Standard PCB, CNC machining
	Proto-nose II lid (2.4 m long microchannel)	CNC machining
	Discrete sensors	Photolithography, microfabrication
Hybrid-noses (I & II)	Microchamber	CNC machining
	Hybrid-nose interface board	Standard PCB
	Microchannel packages (MSL101, MSL112, MSL115)	Microstereolithography, stereolithography
	Hybrid-nose sensor array	Photolithography, microfabrication
	Hybrid-nose polymer deposition monitoring board	Standard PCB
aVLSI-noses (I & II)	aVLSI-nose interface board	Standard PCB
	aVLSI-nose sensor array	Standard CMOS (foundry)
	aVLSI-nose polymer deposition monitoring board	Standard PCB
Vapour test station	Vapour test station board	Wire-wrapping
Data acquisition system	Data acquisition boards	Standard PCB

9.4 Characterisation and performance of the nose-on-a-chip systems

The various components described earlier were assembled to realise different systems, Table 9.2 list these systems along with their main features and test vapours used to evaluate their performance.

The fast-nose system was primarily used to measure the response magnitudes and profiles of discrete sensors to simple analytes (ethanol and toluene vapour in air). All the 10 different types of sensors exhibit a 10 % or less variation in response magnitudes with negligible variation in response profiles to both vapours (across the same type of

sensors). These discrete sensors were designed to be used in the proto-nose II system. For each experiment, 10 sensors of the same type were used. As it is possible to select individual sensor prior to assembly (because they are discrete sensors) on the proto-nose II system, the selection criteria for these sensors can be made on a similar bases of their properties (i.e. baseline resistance, thickness of sensing material coating, uniformity, physical appearance), therefore providing an array of sensors with similar response characteristics.

Table 9.2: Nose-on-a-chip systems description and analyte tested.

System	Packaging	Microchannel Size (L × W × H)	Sensor Number	Sensor Diversity	Test Vapours
Fast-nose	PCB base with Aluminium lid	10 cm × 500 μm × 500 μm	10	10	Simple
Proto-nose I	Uncoated microchannel	120 cm × 500 μm × 500 μm	40	5	Simple, complex
	Parylene C coated microchannel	120 cm × 500 μm × 500 μm			Simple, complex
Proto-nose II	Uncoated microchannel	240 cm × 500 μm × 500 μm	40	10	Simple, complex
	Parylene C coated microchannel	240 cm × 500 μm × 500 μm			Simple, complex
Hybrid-nose I	Microchamber	10 mm × 4 mm × 1 mm	5 rows × 16 columns	5	Simple, complex
	Uncoated MSL101	5 cm × 200 μm × 200 μm			Simple, complex
	Parylene C coated MSL101				Simple, complex
	Parylene C coated MSL112	32 cm × 500 μm × 500 μm			Simple, complex
	Parylene C coated MSL115	240 cm × 500 μm × 500 μm			Simple, complex
Hybrid-nose II	Microchamber	10 mm × 4 mm × 1 mm	5 rows × 16 columns	10	Simple
	Parylene C coated MSL101	5 cm × 200 μm × 200 μm			Simple, complex
	Parylene C coated MSL112	32 cm × 500 μm × 500 μm			Simple, complex
	Parylene C coated MSL115	240 cm × 500 μm × 500 μm			Simple, complex
aVLSI-nose I	Microchamber	10 mm × 4 mm × 1 mm	5 rows × 14 columns	5	Simple, complex
aVLSI-nose II	Microchamber	10 mm × 4 mm × 1 mm	5 rows × 14 columns	10	Simple

During the course of characterising these discrete sensors, it was observed that the response magnitude and response time exhibited significant variations to flow velocity. For the two tested types of sensors (PSB and PEVA), the response magnitude and response time improved as the flow velocity increased. Fast responding sensors with

response times of less than 100 ms were obtained by operating the fast-nose system at a flow rate of 1500 cm s^{-1}. This response time is fast compared to similar types of sensors exhibiting response time ranging from seconds to minutes. Finite element models, developed to study these effects, matched well to the experimental results. These studies are important when designing a gas sensing system with a long delivery channel or those resembling GC systems as the performance of the system will not be optimal if they are operating at an incorrect flow velocity. The broadening effect of a test vapour pulse is affected by the flow velocity, which is directly related to the performance of the system. Low flow velocity increases the amount of time the analyte spends in the GC microchannel, resulting in the analyte pulse to broaden further. However, injecting these test pulses at high velocity is inappropriate as it undermines the retention effect (the analyte pulse is flush out of the microchannel very quickly without interacting with the stationary phase coating) of the analytes in the GC column, which will result in less temporal signals.

The response times of the polymer-composite sensors were also investigated. This was necessary to ensure the behaviour of the system is not misinterpreted. For example, a system operating at a slow flow velocity (< 10 cm s^{-1}) will cause the analyte pulse to broaden significantly when it reaches the far end of a long microchannel. The slower responding sensors may mask-off the response completely, erroneously indicating the absence of any analyte. Therefore it is important to understand the effect of flow velocity on the sensor responses. In addition, the temperature characterisation on the sensors shows that the response magnitude decreases when the temperature is increased. Furthermore, the response time increases (i.e. the sensors response faster) with increasing temperature. A good understanding of the impact of varying the temperature on the sensor response was necessary to compensate for any differences in sensor responses caused by a change in temperature.

The two proto-nose systems each employs 40 discrete sensors placed along the length of a long microchannel. However, due to variations of sensor response magnitudes in the proto-nose I system (as these sensors were not characterised prior to use) and the possibility of 'short-circuited' flow path, it was superseded by the proto-nose II system. The primary aim here was to investigate the feasibility of generating spatio-temporal signals using the nasal chromatography phenomena. Both the uncoated and coated proto-noses were found to exhibit responses that resemble those predicted by the finite element

models. Comparing the sensor responses between the uncoated and coated proto-noses, when experimented with simple analytes (ethanol and toluene vapours), showed that there was no notable difference in terms of retention delay of both analytes on the uncoated proto-nose. However, on the coated proto-nose, the toluene vapour pulse was significantly delayed by approximately 25 s when compared to the ethanol vapour pulse. Subsequently, the coated proto-nose II was studied in detail by expanding the test vapours to include complex odours. Peppermint essence, vanilla essence, fresh banana, milk vapours and their mixtures were included in the tests. Here, the investigation focused on producing different spatio-temporal signals to aid discrimination. In total, 8 vapours were tested at various flow rates (10, 25, 50, 100, 250, 500 cm s^{-1}) and pulse widths (1, 5, 10, 25, 50, 100 s) with 5 repetitive experiments each. The proto-nose was found to be capable of generating both spatial and temporal signals for simple analytes and complex odours. To demonstrate the use of these data for discrimination, they were fed separately (spatial, temporal and spatio-temporal) for Principal Component Analysis (PCA). The PCA employing spatial signals can easily cluster the different vapours. This was largely expected since all existing sensor-based e-nose make use of the spatial signal for discrimination analysis. Next, the temporal data were analysed using the same PCA algorithm. The results show that distinct clusters for different vapours and their mixtures can be obtained. These temporal signals should be exploited for analysis to provide additional information (which will otherwise be lost) to improve discrimination. This is also the first documented account for using such information to perform discrimination analysis in an electronic nose system. These experimental results have provided adequate evidence that spatio-temporal signals will improve discrimination since temporal signals provide an additional dimension of information regarding the test analytes.

While the proto-nose systems were adequate in establishing that biological emulation of the nasal chromatography principle can indeed enhance discrimination, the development of hybrid-nose systems were essential to investigate the feasibility for commercial realisation. Utilising the hybrid-nose sensor array, as a cost-effective vehicle for various trials, the nose-on-a-chip systems were created by assembling the hybrid-nose sensor arrays with various microchannel packages. These microchannel packages include MSL101 (5 cm column), MSL112 (32 cm column) and MSL115 (240 cm column) amongst others, which were fabricated using a commercial Envisiontec Perfactory MSL system. The hybrid-nose I sensor array was deposited with 5 different materials (16

sensors for each type of material) and the hybrid-nose II sensor array was deposited with 10 different materials (8 sensors for each type of material). Prior to the assembly, these hybrid-nose sensor arrays were characterised with simple analytes using a microchamber where all 80 sensors were exposed simultaneously to simple analytes. The results show a variation of less than 20 % in response magnitude (across the same type of sensors). This variation was higher compared to the 10 % variation for discrete sensors attributed to the higher disparity in sensor properties as a result of array deposition. Using the same setup, stereolfaction was emulated (two nostrils sniffing at different rates) by measuring the sensor array responses to simple analytes and complex odours at two different flow rates. While it was possible to discriminate all odours at each flow rate, the Mahalanobis and Euclidean matrices show that stereolfactory images provide a better classification compared to monolfactory images. Separate experiments were also performed at different flow rates (10, 25, 50, 100, 250, 500 cm s^{-1}) and pulse durations (1, 5, 10, 25, 50, 100 s) in an attempt to mimic the biological sniffing behaviour, where mammals vary their sniffing rate and duration. The results converge with the biological observations that sniffing harder for longer duration improves discrimination.

The nose-on-a-chip systems were based on the assembly of the hybrid-nose sensor arrays and the three microchannel packages of increasing lengths. Here, the three systems were characterised with simple analytes and complex odours to determine their ability to generate spatio-temporal signals. Upon characterisation, they were all found to be capable of producing spatial signals. However, negligible temporal signals were observed in the sensor responses of the system with MSL101 (5 cm column), significant temporal delays were observed on MSL112 (32 cm column) and clear distinct pulses with different retention delays can be observed on MSL115 (240 cm column). The MSL115 system was further evaluated and it was found to be capable of discriminating between various analytes based on either the spatial or temporal signals (as in the proto-nose). However, the performance was slightly inferior when compared to the proto-nose II due to two factors. Firstly, the sensor array has a higher response variation due to the array deposition technique described earlier. This was unlike the proto-nose system where each discrete sensor was characterised and selected prior to use. Secondly, the integration technique for assembling the sensor array with the microchannel package has to be improved to alleviate possible intra-channel leakage and sensor yield. Nevertheless,

the huge reduction in size (factor of 75) while maintaining similar performance still provides strong justification to investigate this option further.

To achieve complete nose-on-a-chip integration, the hybrid-nose sensor array was replicated to incorporate smart processing circuitries. The aVLSI-nose sensor array has the same sensor placements (but 10 sensors less than hybrid-nose sensor array) and each sensor has a dedicated driving and conditioning circuitries to ameliorate the need for external discrete circuitries. The operation of individual sensor is programmable in four functional blocks. The first block deals with the selection of a suitable driving current (out of the three options that can take on different current values using an external potentiometer) depending upon the resistance of the sensor. With this flexibility, it becomes possible to accommodate a larger range of sensor resistances, making the aVLSI-nose sensor array less reliance on the polymer deposition process. The second programmable block allows the sensor to operate either in resistive or FET mode. The third and most important module is the novel DC-offset cancellation circuit designed to remove the baseline voltage of the sensor. This enables the small sensor response to be amplified internally within the CMOS chip by the last functional block of programmable amplifier. All the circuitries incorporated in the aVLSI-nose sensor array were characterised and found to match well to the results predicted by simulation. In addition, the linearity of PSB sensor responding to simple analytes was investigated in detail. Within the tested range of 100 ppm to 1200 ppm, the response magnitude was found to be linearly proportional to the analyte concentration (ppm). The sensitivity to ethanol vapour in air was 0.00012 % ppm^{-1} and 0.00644 % ppm^{-1} to toluene vapour in air.

For the DC-offset cancellation circuit, although there was a need for the sensor array to determine the baseline voltage of each sensor, all the counters (connected to the DAC) were clocked simultaneously to reduce the initialisation time (which takes less than 1 ms with a 2 MHz clock). This was accomplished through the use of a ramping DAC-comparator pair by incrementing their respective counter from 0 to 1023. Furthermore, it is only performed once prior to the start of measurement. The other possible issue is the response inversion when operating the sensor with the baseline removal and dynamic amplification circuit. Due to the differential amplifier configuration, used to remove the baseline signal, the sensor response will be inverted with respect to the actual response obtained directly from the output of the sensor. While this is acceptable when all sensors are operating in the same mode, it will create opposite

polarity responses for those sensors operating in a different mode. To avoid such problem, a flag can be implemented in software to denote which mode each sensor is operating at, so that the polarity of the sensor response can be maintained for subsequent compensation through software response inversion.

Table 9.3 summarised the characterisation results of the main experiments conducted on these systems.

Table 9.3: Summary of the characterisation results.

System	Experiments	Results
Fast-nose system	• Simple analytes	▶ Response magnitude and time characterisation.
	• Flow rate effect	▶ Improved response magnitude and time. ▶ Ultra-fast sensor response of less than 100 ms.
	• Temperature effect	▶ Lower response magnitude, improved response time.
Proto-nose systems	• Uncoated and coated microchannel	▶ No retention delay difference for different analytes in the uncoated system. ▶ Varying retention delay was observed in the coated system.
	• Simple analytes & complex odours	▶ Spatio-temporal signal generation. ▶ Discrimination with spatial signals. ▶ Discrimination with temporal signals.
Hybrid-nose systems	• Simple analytes	▶ Response magnitude and time characterisation.
	• Mono and stereolfaction	▶ Improved discrimination with stereolfactory images.
	• Sniffing rate (flow rate) and sniffing duration (pulse duration) variation	▶ Higher flow rate with long duration improved discrimination.
	• Nose-on-a-chip systems	▶ Spatio-temporal signal generation. ▶ Discrimination with spatial signals. ▶ Discrimination with temporal signals.
aVLSI-nose systems	• Constant driving current module	▶ 3 selectable settings at 1 μA, 10 μA & 100 μA.
	• Sensor mode selection module	▶ Resistive or FET mode of operation.
	• DC-offset cancellation module	▶ Able to operate at different baseline voltage.
	• Programmable gain amplifier module	▶ Able to select the desirable gain.
	• Simple analytes	▶ Linear of response magnitude versus analyte concentration. ▶ Operation of the sensor array in various modes.

9.5 Further work

There are two main strands to this research project that should be pursued further. The first strand is related to improving the yield of fabricating the nose-on-a-chip system to a level acceptable for commericalisation and mass production. Secondly, the complete biological olfactory system can be emulated by incorporating various models for the neuron, glomeruli cell and olfactory bulb all implemented onto a single silicon chip.

Although it has been shown that it is possible to build a miniaturised nose-on-a-chip system that mimics its biological counterpart closely, the techniques and procedures used were not optimised to a yield level (> 90 %) attractive enough for mass production. The two underlying factors that require further investigation are the polymer-composite sensing material deposition technique and the integration of the sensor array with the microchannel package. The current deposition technique utilises mechanical masking with air-brush spraying. Such a method suffers from poor resolution, cross-contamination (for sensor array with multiple materials), sensor to sensor variation and batch to batch variation. Other techniques such as ink-jet printing [9.3] and electrochemical deposition [9.4] in their respective stages of development are possible alternatives, but both have a number of issues in regard to CMOS compatibility, response magnitude and sensor to sensor variation. The other issue arises from the need to integrate the microchannel package with the sensor array. Due to poor resolution of the deposited sensor array, excess material is deposited outside the designated sensor outline. This creates uneven surfaces for integration, resulting in intra-channel leakage. In addition, a manual procedure has been used to apply resin along the gaps between the mini-chambers on the base of the microchannel packages to ensure leakage-free system. Such a procedure is time-consuming and suffers from significant system to system variation, which is not suitable for mass production. Soft lithography techniques could be plausible alternative [9.5]. Direct write-on MSL technique that allows the microchannel to be build directly on the silicon is another possible emerging substitute [9.6-9.7].

The other potential development area is the complete amalgamation of sensor, integrated firing neuron (IFN), glomeruli cell and higher level olfaction processing into a single silicon chip. As highlighted earlier (Chapter 1), this project was part of a bigger project towards creating an adaptive neuromorphic analogue VLSI chip for integrated odour sensing [9.8] in collaboration with Universities of Leicester and Edinburgh. The group is currently working on a few key areas which include integrating neuromorphic

operations within the sensor array on a single silicon chip [9.9]. Many other researchers are working on related areas targeting different aspects of the olfactory system [9.10-9.12]. The ultimate goal is to achieve a complete single chip implementation of a biologically olfactory system. Part of these efforts has resulted in partial integration, as shown in Figure 9.1. Figure 9.1(a) shows a aVLSI-neuromorphic chip with 3 Receptor Neurons (RN), 27 synapses and 1 Principal Neuron (PN) implemented on a 7 mm × 4.5 mm silicon using analogue circuits designed to mimic the biological processing. It was targeted to interface to the aVLSI-nose sensor array. Figure 9.1(b) shows an integrated version aVLSI-plenary e-nose chip with 3 sensors and their corresponding neuron circuitries implemented on a 7 mm × 7 mm silicon. These systems are currently being evaluated by other members and the results will certainly be useful to aid the design of future electronic nose system incorporating biological principles.

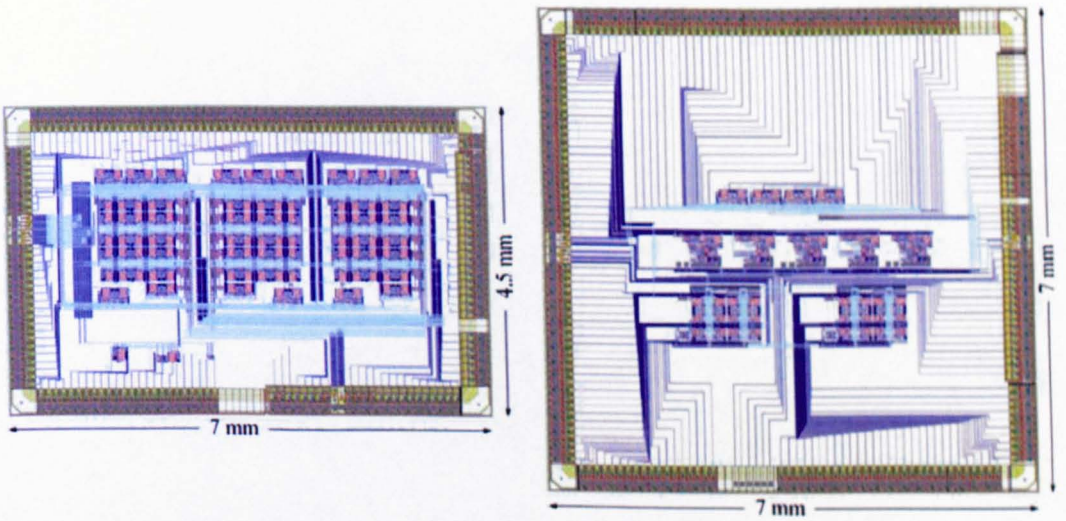

(a) (b)

Figure 9.1: Advanced version of electronic nose components with neuromorphic features. (a) Footprint of aVLSI-neuromorphic chip circuit implementation. (b) Footprint of aVLSI-plenary chip with neuromorphic circuit and integrated sensors implementation.

9.6 References

[9.1] J.W. Gardner, P.N. Bartlett, ***Electronic noses: principles and applications***, Oxford University Press, Inc, New York, 1999.

[9.2] Intotech Consulting Group (Germany), ***Electronic nose market forecast 2004***, http://www.odotech.qc.ca/resources/aboutodors.html, May 2003.

[9.3] W-F. Shen, Y. Zhao, C-B. Zhang, ***The preparation of ZnO based gas-sensing thin films by ink-jet printing method***, Thin Solid Films, Vol. 483, pp. 382-387, July 2005.

[9.4] Q. Fang, D.G. Chetwynd, J.A. Covington, C-S. Toh, J.W. Gardner, ***Micro-gas-sensor with conducting polymers***, Sensors and Actuators B: Chemical, Vol. 84, pp. 66-71, 2002.

[9.5] M. Heule, L.J. Gauckler, ***Miniaturised arrays of tin oxide gas sensors on single microhotplate substrates fabricated by micromolding in capillaries***, Sensors and Actuators, B 93, pp. 100-106, 2003.

[9.6] L.A. Tse, P.J. Hesketh, D.W. Rosen, J.L. Gole, ***Stereolithography on silicon for micro-fluidics and microsensor packaging***, Microsystem Technologies, Vol. 9, pp. 319-323, 2003.

[9.7] S. Hinrich, S. Jingree, P. Padhy, B. Pearce, A. Sanami, N. Smith, D. Walters, C. Weightman, ***Microstereolithography (Technical report)***, MEeng Thesis, School of Engineering, University of Warwick, Coventry, UK 2004.

[9.8] T.C. Pearce, J.W. Gardner, A. Hamilton, J.A. Covington, C. Fulvi-Mari, T.J. Koickal, S.L. Tan, ***Silicon Olfactory System Implementation***, http://www.le.ac.uk/engineering/tcp1/avlsi/, March 2003.

[9.9] T.C. Pearce, C.F. Mari, J.A. Covington, S.L. Tan, J.W. Gardner, T.J. Koickal, A. Hamilton, ***Silicon-based neuromorphic implementation of the olfactory pathway***, The 2nd International IEEE EMBS Conference on Neural Engineering, Pentagon City, Arlington, USA, March 16-19, 2005.

[9.10] H-J. Chang, W.J. Freeman, B.C. Burke, ***Optimization of olfactory model in software to give 1/f power spectra reveals numerical instabilities in solutions governed by aperiodic (chaotic) attractors***, Neural Networks 11, pp. 449–466, 1998.

[9.11] J. White, S. Mall, J.S. Kauer, ***Using Biology to Guide Development of an Artificial Olfactory System***, Neurotechnology for Biomimetic Robots. Eds. Ayers, J., Davis, J., Rudolph, A. MIT Press, August 2002.

[9.12] Z-P. Li, J. Hertz, ***Odour recognition and segmentation by a model olfactory bulb and cortex***, Computation in Neural Systems 11, pp. 83-102, 2000.

Appendix A

Finite element simulation of microchannel GC using FEMLAB

Sources

[A1] FEMLAB version 2.3 revision b
COMSOL Ltd.
Shepherds Building
Rockley Road
London W14 0DA
UK
http://www.uk.comsol.com/

[A2] MATLAB Version 6.0.0.88 Release 12
The MathWorks UK
Matrix House
Cambridge Business Park
Cambridge CB4 0HH
UK
http://www.mathworks.co.uk/

Finite element simulation of microchannel GC using FEMLAB

There are several steps necessary to create a geometry model representing the physical system. Here, a brief outline of the procedures used to create a model for the microchannel GC system will be depicted. Other models with normal microchannels are less complex as they only require two multi-physics modes. The first step towards creating a model is to determine the physical/chemical process occurring in the system. In this case, the microchannel GC has very well established theories defining the three processes occurring within it. The carrier gas transport in the microchannel can be modelled with Navier-Stokes (*NS*) equation; Convection and Diffusion (*CD*) is used to model the analyte pulse broadening within the microchannel. In the stationary phase, Diffusion (*DI*) is the only dominating process.

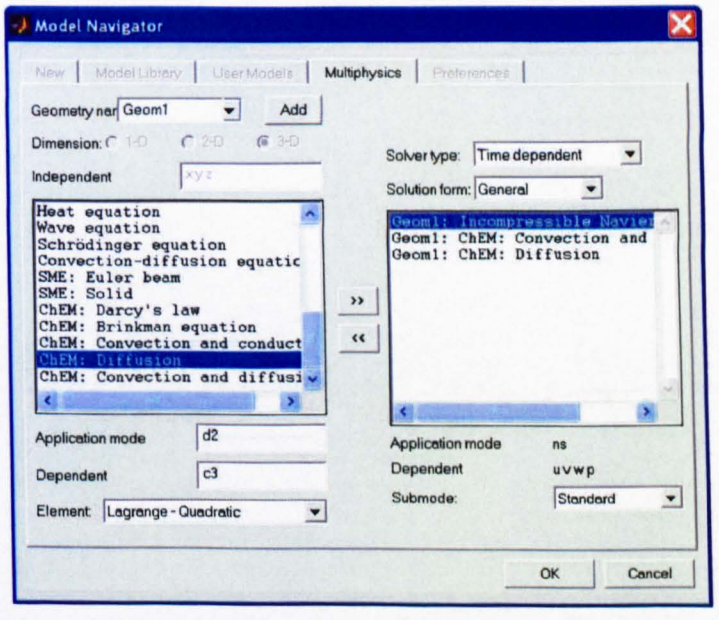

Figure A1: Creating a multi-physics model (*Multiphysics -> Add/Edit modes...*).

In FEMLAB [A1], various add-on modules are available to model different categories of phenomena. Here, the three processes (*NS*, *CD*, and *DI*) are available under "chemical engineering modules". Figure A1 shows a snapshot of the procedure of adding multi-physic modes. The next step is to create the geometry model by either using the "geometry creater" shown in figure A2 or importing the model from other standard CAD models (*DXF* and *IGES* file format supported).

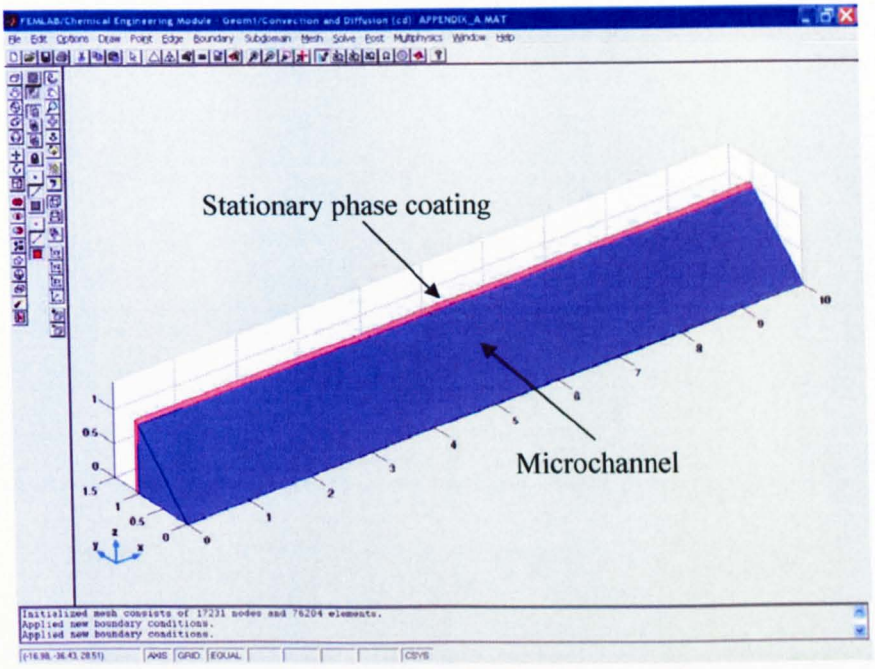

Figure A2: Creating a geometry model (*Draw -> Draw Mode*).

Figure A2 shows an example of a geometry created to model a microchannel GC with 8 fold symmetry along its central axis to reduce the computation complexity. The thin layer of pink slat represents the stationary phase coating on the microchannel GC.

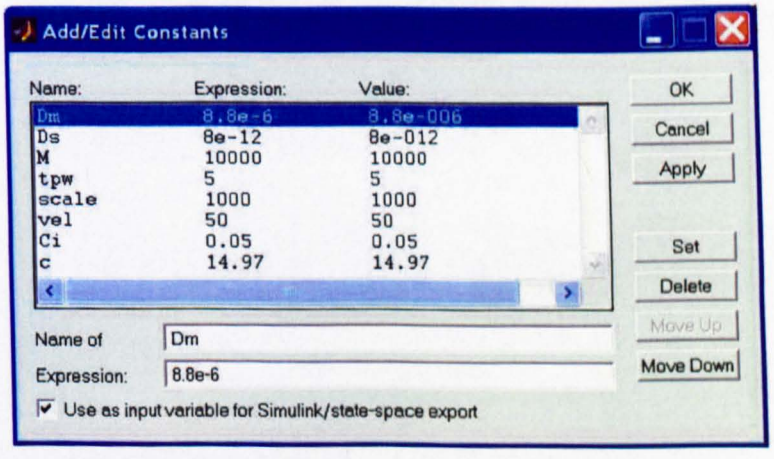

Figure A3: Constant definition (*Option -> Add/Edit Constants...*).

Figure A3 shows a snapshot of the constant definition entry table. The constant parameters used throughout the simulation can be entered here to avoid re-defining them. In addition, it also facilitate automated rerun using MATLAB [A2] scripts to simulate the model under different operating conditions.

The next step is to enter the boundary conditions as described in Chapter 3. As there are three multi-physics modes, there will be three sets of boundary conditions corresponding to each mode. The user is required to first select the desired physic mode (for e.g. *Multiphysics -> Diffusion (DI)*) before proceeding to configure their corresponding boundary conditions. Each boundary (surface) will be numbered automatically and as the user move along each boundary, the corresponding surface will be highlighted to denote the selection. The user then enters the boundary conditions for each surface as shown in Figure A4. As briefly described in Chapter 3, the Dirichlet boundary condition specifies the values a solution of the PDE is to take on the boundary condition of the domain. In addition, it also allows the velocity at the boundary to be specified.

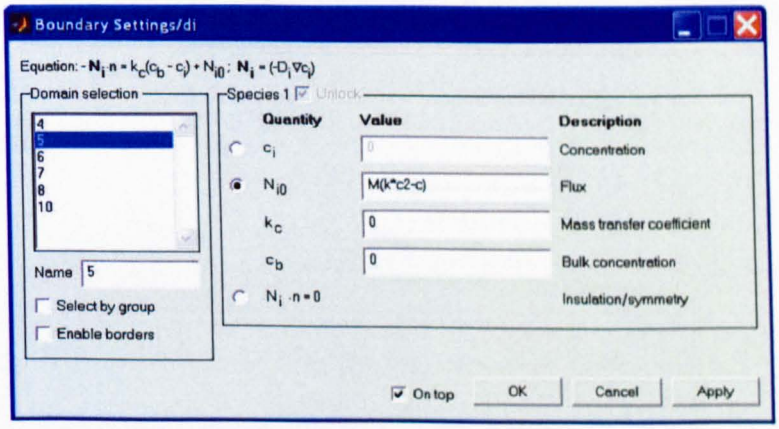

Figure A4: Boundary setting for Diffusion mode (*Boundary -> Boundary Settings*).

Similarly for the *NS* mode and *CD* mode, their boundary conditions are specified as shown in Figure A5 and A6 respectively.

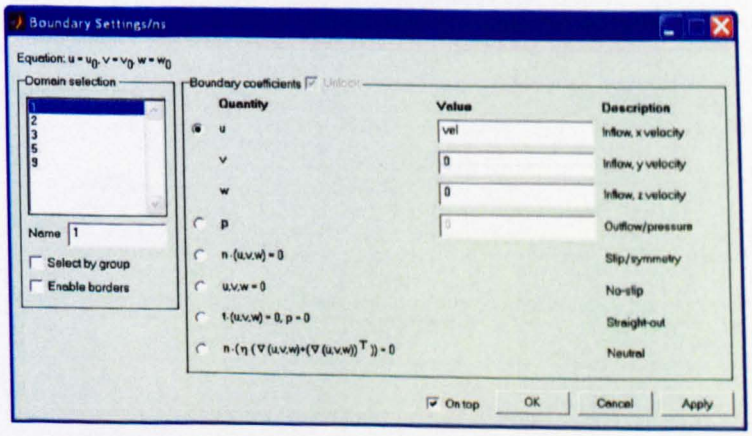

Figure A5: Boundary setting for Navier-Stokes mode (*Boundary -> Boundary Settings*).

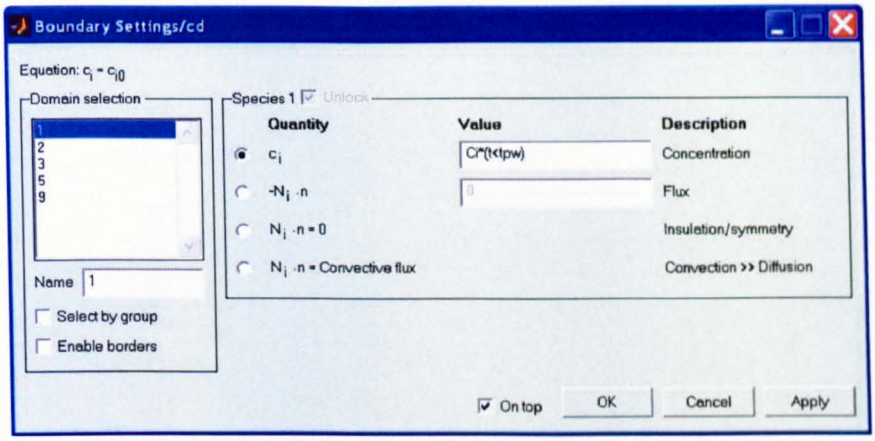

Figure A6: Boundary setting for Convection and Diffusion mode (*Boundary -> Boundary Settings*).

Figure A7 shows an example to configure the symmetry surface of the *NS* boundary condition. When surface number 3 is selected, the corresponding surface is highlighted as shown in Figure A7. The user then selects the appropriate description for that boundary.

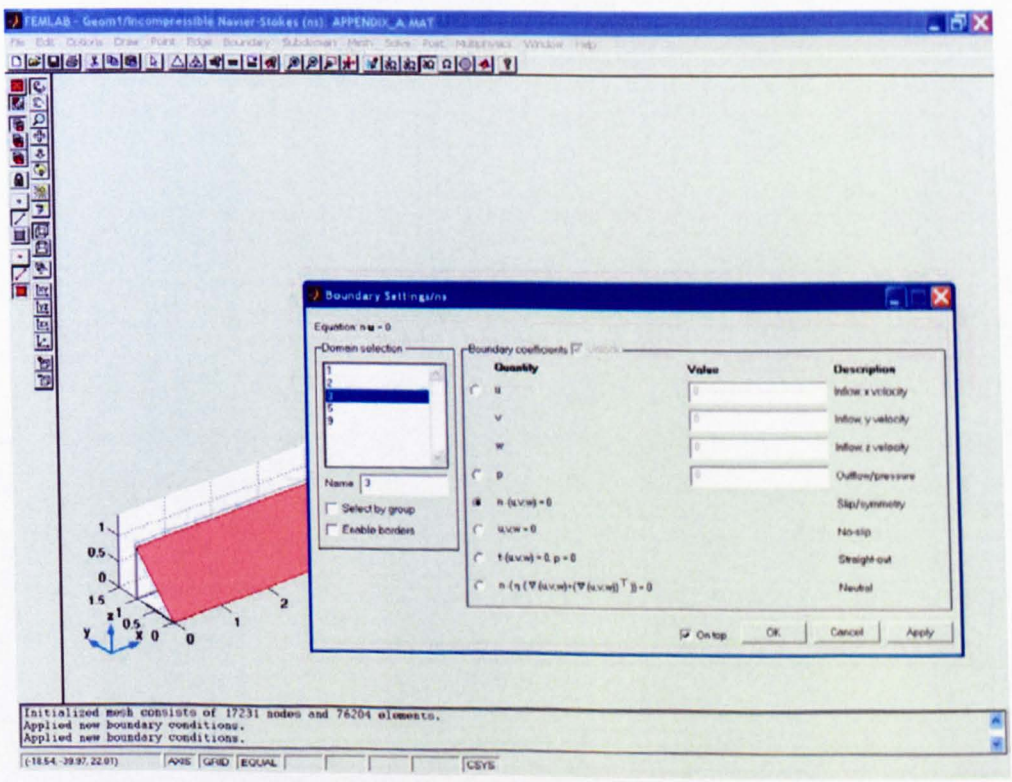

Figure A7: Boundary setting for Navier-Stokes mode (*Boundary -> Boundary Settings*).

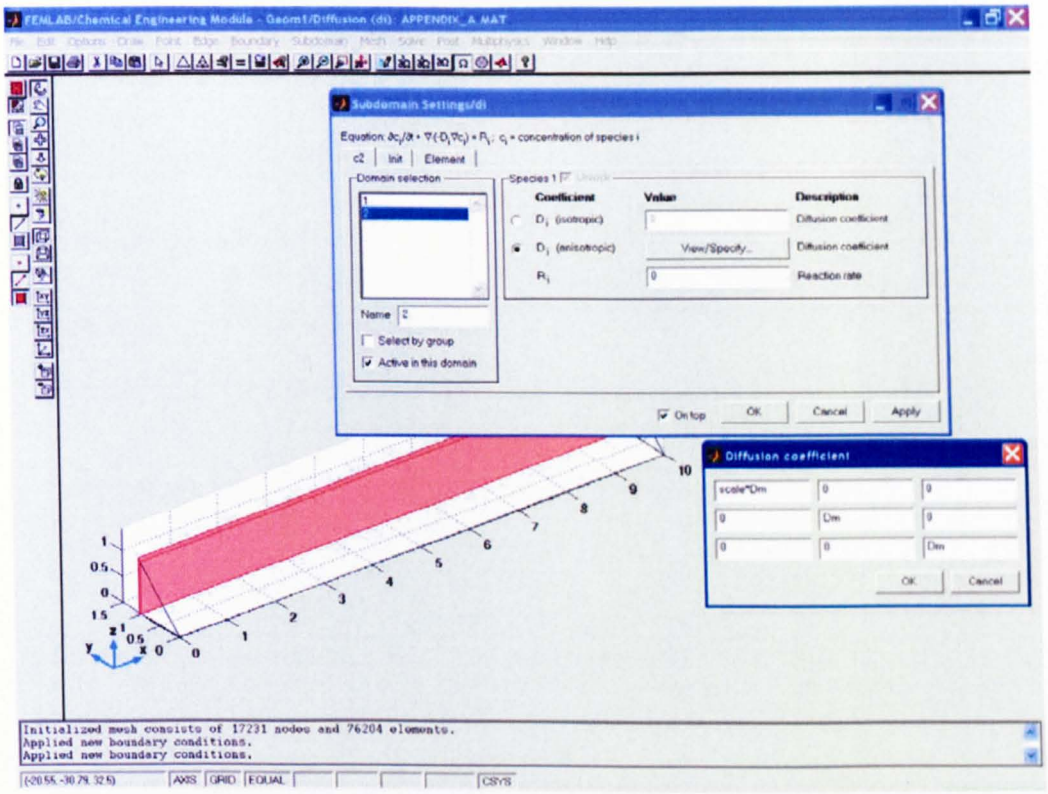

Figure A8: Subdomain setting for Diffusion mode (*Subdomain -> Subdomain Settings*).

Once the boundary conditions are set, the next step is to define the sub-domain setting (the physic(s) mode in each geometry). Here, there are two geometries; the microchannel and the stationary phase coating. As discussed earlier, the microchannel exhibits *NS* and *CD* while the stationary phase only exhibits *DI*. By selecting the appropriate mode (for e.g. *Multiphysics -> Diffusion* (*DI*)), the user can activate the corresponding physic mode by enabling the "Active in this subdomain" tick box shown in the bottom left of the second window as shown in Figure A8. The diffusion coefficient for the *Diffusion* mode can then be specified. In this case, as the geometry is scaled along the X-axis, an anisotropic diffusion coefficient must be defined. A scaling factor is specified only in the X-axis for both the diffusion coefficient in the stationary phase (coating) and mobile phase (microchannel) as shown in Figure A9 and A10 respectively.

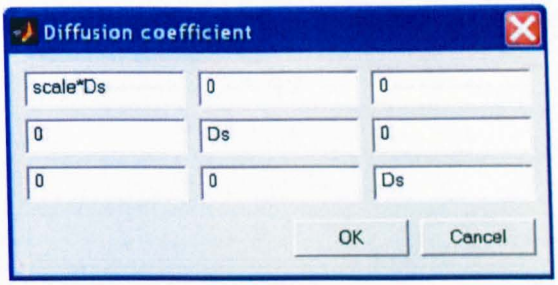

Figure A9: Scaling of diffusion coefficient in stationary phase.

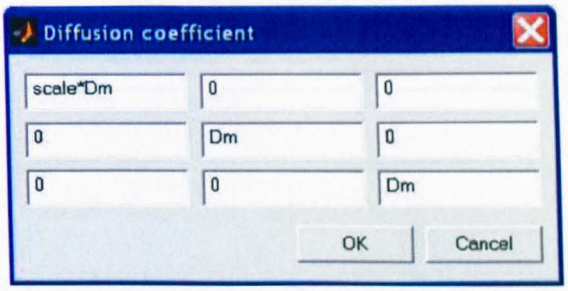

Figure A10: Scaling of diffusion coefficient in mobile phase.

Next, the geometry has to be "mesh" (triangulated) to create finite points (finite elements) within the geometry. The *PDEs* (partial differential equations) representing the phenomena are then solved at these points. This can easily be accomplished with the automatic mesh generator. Figure A11 shows a mesh generated for the microchannel GC.

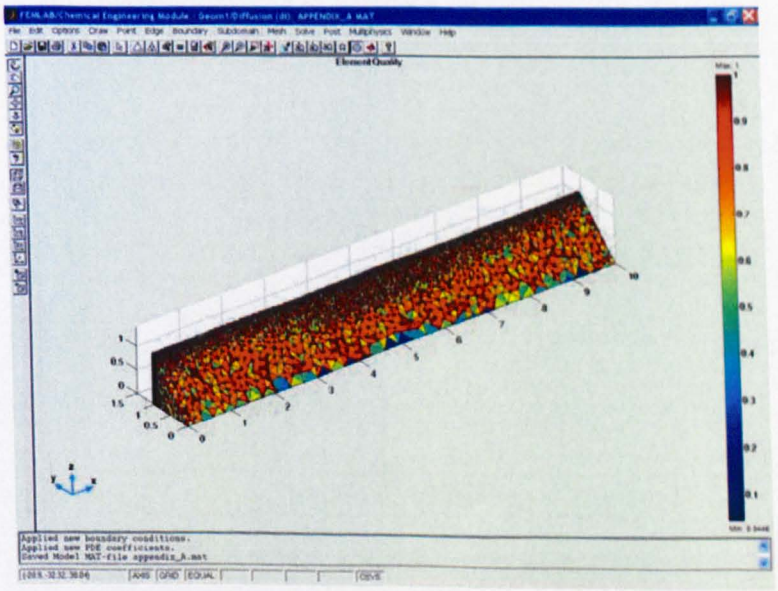

Figure A11: Meshing of geometry (*Mesh -> Initialize Mesh*).

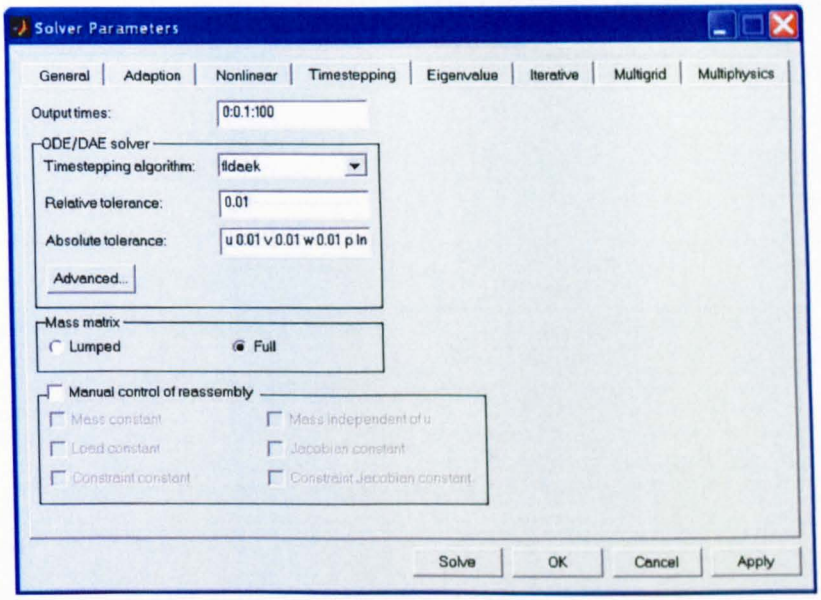

Figure A12: Solving of geometry (*Solve -> Solve problem*).

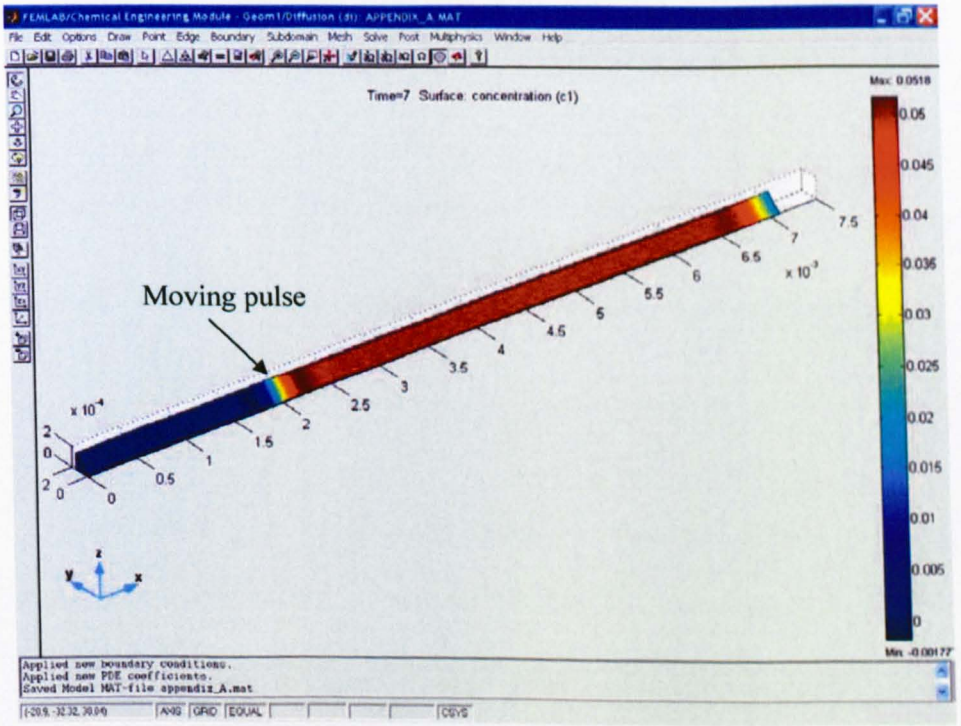

Figure A13: A solved geometry depicting the surface concentration profile at t = 7 s..

The geometry is then ready to be solved by invoking the solver's menu. Here, the user can specify the solving duration (output times), time steps and tolerance of the solver as shown in Figure A12. Once the simulation is completed, it will resemble that of Figure

A13. There are several ways to analyse the results. Figure A13 shows the surface concentration profile of the microchannel at time step = 7 s. The analyte pulse can be clearly observed to be traversing along the microchannel and it is located at approximately 20 cm from the inlet of the microchannel at this instant (t = 7 s). The cross-sectional velocity profile, pressure, and other variables defined by the 3 *PDEs* can be extracted for further analysis. As FEMLAB is closely coupled with MATLAB, the results can readily be exported to MATLAB where more complex signal processing operations can be performed by invoking the various library routines available in MATLAB. The results presented in this thesis were obtained using both techniques.

Appendix B

Estimation of partition coefficient using
linear solvation energy relationship (LSER) equations

Estimation of partition coefficient using linear solvation energy relationship (LSER) equations

The most important factor determining the separability of two analytes lies in their difference in partition coefficient with the stationary phase coating. It is therefore crucial to determine this value accurately to predict the response correctly. Numerous researches conducted by Abraham *et al.* [B1-B2] demonstrate the ability to predict the partition coefficient of various analytes in different stationary phases using the linear solvation energy relationship (LSER).

$$\log k = c + rR_2 + s\pi_2^H + a\alpha_2^H + b\beta_2^H + \ell \log L^{16} \qquad \text{(B-1)}$$

In Equation (B-1) the parameters R_2, π_2^H, α_2^H, β_2^H and L^{16} depends on the analyte, whereas the coefficients c, r, s, a, b and ℓ depend on the stationary phase coating. The parameter R_2 describes the polarizability of the n- and π-electrons in the analyte; π_2^H the dipolarity; α_2^H the hydrogen-bond acidity; β_2^H the hydrogen-bond basicity; L^{16} the gas-liquid partition coefficient in hexadecane. For the stationary phase coating, c is the constant which describes the partition of an analyte with no interactions of the types described by the other parameters (an ideal gas atom such as krypton would approximate to such an analyte); r describes the polarizability of the coating; s the dipolarity; a the hydrogen-bond basicity of the coating; b its hydrogen-bond acidity; and ℓ reflects the ability of the coating to distinguish between members of a homologous series of compounds [B3].

Abraham *et al.* compiled a comprehensive list of commonly used stationary phases and test analytes. Unfortunately, not all the desired types of stationary phase and test analytes parameters are available. Hence, similar types are used for the simulations instead. The diffusion coefficient in the mobile phase (D_M) is also required for the simulation, and Equation (B-2) can be used to estimate the diffusion coefficient of different test analytes in air.

The *Fuller-Schettler-Giddings* equation

$$D_M = \frac{0.001\ T^{1.75}\sqrt{(1/M_a + 1/M_g)}}{P\ [\ \sqrt[3]{\sum v_a} + \sqrt[3]{\sum v_g}\ ]^2} \qquad \text{(B-2)}$$

where M = molecular weight, T = temperature (K), P = pressure (atm), and Σv = sum of atomic volume increments [B4].

The most common basis for estimating diffusion coefficients in stationary phase (D_S) is the Stokes-Einstein Equation (B-3). Coefficients calculated from this equation are accurate to only about 20 %. Nonetheless, it remains the standard against which alternative correlations are compared.

The *Stokes-Einstein* equation

$$D_S = \frac{k_B T}{f} = \frac{k_B T}{6\pi\mu R_o} \qquad \text{(B-3)}$$

where f is the frictional coefficient of the solute, k_B is Boltzmann's constant, μ is the solvent viscosity, and R_o is the solute radius [B4].

Table B1 shows the list of diffusion coefficient for various analytes in air as used in the simulation.

Table B1: Diffusion coefficient of various analytes in air.

Analyte	Diffusion coefficient in air, D_m
Toluene	0.086 $cm^2\ s^{-1}$
Ethanol	0.132 $cm^2\ s^{-1}$

Table B2: Test analytes used in simulation and their parameters.

Analyte	R_2	π_2^H	β_2^H	α_2^H	$\log L^{16}$
Ethanol	0.246	0.42	0.37	0.48	1.485
Toluene	0.601	0.52	0.00	0.14	3.325

Table B3: Stationary phases used in simulation and their parameters.

Stationary phase	*c*	*r*	*s*	*a*	*b*	*ℓ*
SE-30 Poly (dimethylsiloxane)	-0.194	0.024	0.190	0.125	0	0.498
OV-11 Poly (dimethyl-methyl-phenyl-siloxane) 35% mol phenyl groups	-0.303	0.097	0.544	0.174	0	0.516
EGAD Poly (ethylene glycol adipate)	-0.688	0.132	1.394	1.720	0	0.410
H10 Bis (3-allyl-4-hydroxy-phenyl) sulfone	-0.568	-0.051	1.323	1.266	1.457	0.418
QF1 Poly (trifluoro-propyl-methyl-siloxane)	-0.269	-0.449	1.157	0.187	0	0.419

Table B4: Partition coefficients derived using parameters from Table B3.

Stationary phase	Analyte	*k*
SP1 SE-30 Poly (dimethylsiloxane)	Ethanol	4.76
	Toluene	37.59
SP2 OV-11 Poly (dimethylmethylphenylsiloxane) 35% mol phenyl groups	Ethanol	6.03
	Toluene	56.74
SP3 EGAD Poly (ethylene glycol adipate)	Ethanol	14.97
	Toluene	170.70
SP4 H10 Bis (3-allyl-4-hydroxyphenyl) sulfone	Ethanol	58.03
	Toluene	48.21
SP5 QF1 Poly (trifluoropropylmethylsiloxane)	Ethanol	6.28
	Toluene	28.57

References

[B1] M.H. Abraham, ***Scales of solute hydrogen-bonding: Their construction and application to physicochemical and biochemical processes***, Chemical Society Reviews, pp. 73-83, 1993.

[B2] M.H. Abraham, C.F. Poole, S.K. Poole, ***Classifications of stationary phases and other materials by gas chromatography***, Journal of Chromatography A, 842, pp. 79-114, 1999.

[B3] J.W. Gardner, P.N. Bartlett, ***Electronic noses: Principles and Applications***, Oxford University Press, Inc, New York, 1999.

[B4] E.L. Cussler, ***Diffusion: Mass Transfer in Fluid Systems***, Cambridge University Press, New York, 1984.

Appendix C

Stereolithography and microstereolithography resin properties

1. SL5510 (Renshape, Switzerland) Resin Properties [C1]
2. SL5220 (Renshape, Switzerland) Resin Properties [C1]
3. Orange Methacrylate Resin (EnvisionTec) [C2]

Sources

[C1] **RenShape Solutions**
Huntsman Advanced Materials
Ickleton Road
Duxford, Cambridge
CB2 4QA
UK
http://www.huntsman.com/renshape/

[C2] **Envisiontec Ltd**
Spedding Road
Stoke-on-Trent
ST4 2ST
UK
http://www.envisiontec.com/21hdesca.htm

Stereolithography Materials

SL DIRECT

for use on

RenShape™ SL 5510

SLA® 350/3500/5000 system

Highest Accuracy Stereolithography Material

- Ultimate accuracy
- Excellent sidewall quality
- Humidity resistant
- Low viscosity
- Ideal for master patterns
- Ideal for QuickCast™ applications

Liquid Material

MEASUREMENT	CONDITION	VALUE
Appearance		Clear Amber
Density	@ 25°C (77°F)	1.13 g/cm³
Viscosity	@ 28°C (82°F)	230 cps
Viscosity	@ 30°C (86°F)	180 cps
Penetration depth (Dp)		4.1 mils (4.3 mils on SLA 5000 system)
Critical exposure (Ec)		11.4 mJ/cm² (11.2 mJ/cm² SLA 5000 system)
Part building layer thickness*		0.05 mm (0.002 in) 0.10 mm (0.004 in) 0.15 mm (0.006 in)

*Dependent upon part geometry and build parameters.

Post-Cured Material

MEASUREMENT	TEST METHOD	VALUE	VALUE
		90-minute UV post-cure	90-minute UV + 2 hours @ 80° thermal post-cure
Hardness, Shore D	ASTM D 2240	86	
Flexural modulus	ASTM D 790	3,054 MPa (443 KSI)	
Flexural strength	ASTM D 790	99 MPa (14,400 PSI)	
Tensile modulus	ASTM D 638	3,296 MPa (478 KSI)	
Tensile strength	ASTM D 638	77 MPa (11,100 PSI)	
Elongation at break	ASTM D 638	5.4%	
Impact strength, notched Izod	ASTM D 256	27 J/m (0.5 ft - lbs/in)	
Heat deflection temperature	ASTM D 648 @ 66 PSI @ 264 PSI	62°C (144°F) 53°C (127°F)	87°C (189°F) 76°C (169°F)
Glass transition, Tg	DMA, E" peak	68°C (154°F)	
Coefficient of thermal expansion	TMA (T<Tg) TMA (T>Tg)	84 x 10⁻⁶/°C 182 x 10⁻⁶/°C	79 x 10⁻⁶/°C 184 x 10⁻⁶/°C
Thermal conductivity		0.181 W/m °K 4.33 x 10⁻⁴ cal/sec cm °C	
Density		1.23 g/cm³	

Protected by one or more of the following patents: US 5,476,748; US 6,100,007; US 6,136,497; US 5,972,563

For SL Technical Support: Tel: 866-288-3554 (Toll Free), Fax: 517-324-1416. Email: slmaterials@vantico.com

www.renshape.com

Vantico A&T US, Inc. 4917 Dawn Ave, E. Lansing, MI 48823 USA Tel: 800-285-4784 Fax: 517-351-6256

RenShape solutions vantico

Stereolithography Materials

SL DIRECT

for use on **SLA® 250** system

RenShape® SL 5220

Fast Multi-Functional Stereolithography Material

- Fast material
- Excellent sidewalls
- Humidity resistant
- Ideal for master patterns
- Suitable for tooling inserts
- Suitable for QuickCast™ applications

Liquid Material

MEASUREMENT	CONDITION	VALUE
Appearance		Clear Amber
Density	@ 25°C (77°F)	1.14 g/cm³
Viscosity	@ 28°C (82°F)	340 cps
Viscosity	@ 30°C (86°F)	275 cps
Penetration depth (Dp)		5.6 mils
Critical exposure (Ec)		9.0 mJ/cm²
Part building layer thickness*		0.10 mm (0.004 in) 0.15 mm (0.006 in)

*Dependent upon part geometry and build parameters.

Post-Cured Material

** The values are based on UV post cure times of 90 minutes. Higher values are obtained with longer UV post cure times.

MEASUREMENT	TEST METHOD	**VALUE	VALUE
		90-minute UV post-cure	90-minute UV + 2 hours @ 80°C thermal post-cure
Hardness, Shore D	ASTM D 2240	86	
Flexural modulus	ASTM D 790	2,951 MPa (428 KSI)	
Flexural strength	ASTM D 790	94 MPa (13,700 PSI)	
Tensile modulus	ASTM D 638	2,703 MPa (392 KSI)	
Tensile strength	ASTM D 638	62 MPa (9,000 PSI)	
Elongation at break	ASTM D 638	8.3 %	
Impact strength, notched Izod	ASTM D 256	37 J/m (0.7 ft-lbs/in)	
Heat deflection temperature	ASTM D 648 @66 PSI @264 PSI	46°C (115°F) 42°C (108°F)	76°C (169°F) 62°C (144°F)
Glass transition, Tg	DMA, E" peak	53°C (127°F)	
Coefficient of thermal expansion	TMA (T<Tg) TMA (T>Tg)	96 x 10^{-6}/°C 186 x 10^{-6}/°C	
Thermal conductivity	ASTM E1225	0.156 W/m °K (3.37 x 10^{-4} cal/sec.cm.°C)	
Density		1.18 g/cm³	

Protected by one or more of the following patents: US 5,476,748; US 6,100,007; US 6,136,497; US 5,972,563

For SL Technical Support: Tel: +44 1223 493 391. Fax: +44 1223 493 392. Email: slmaterials@huntsman.com

www.renshape.com

Huntsman Advanced Materials (UK) Limited. Tel: +44 1223 493 000, Fax: +44 1223 493 002

RenShape solutions HUNTSMAN

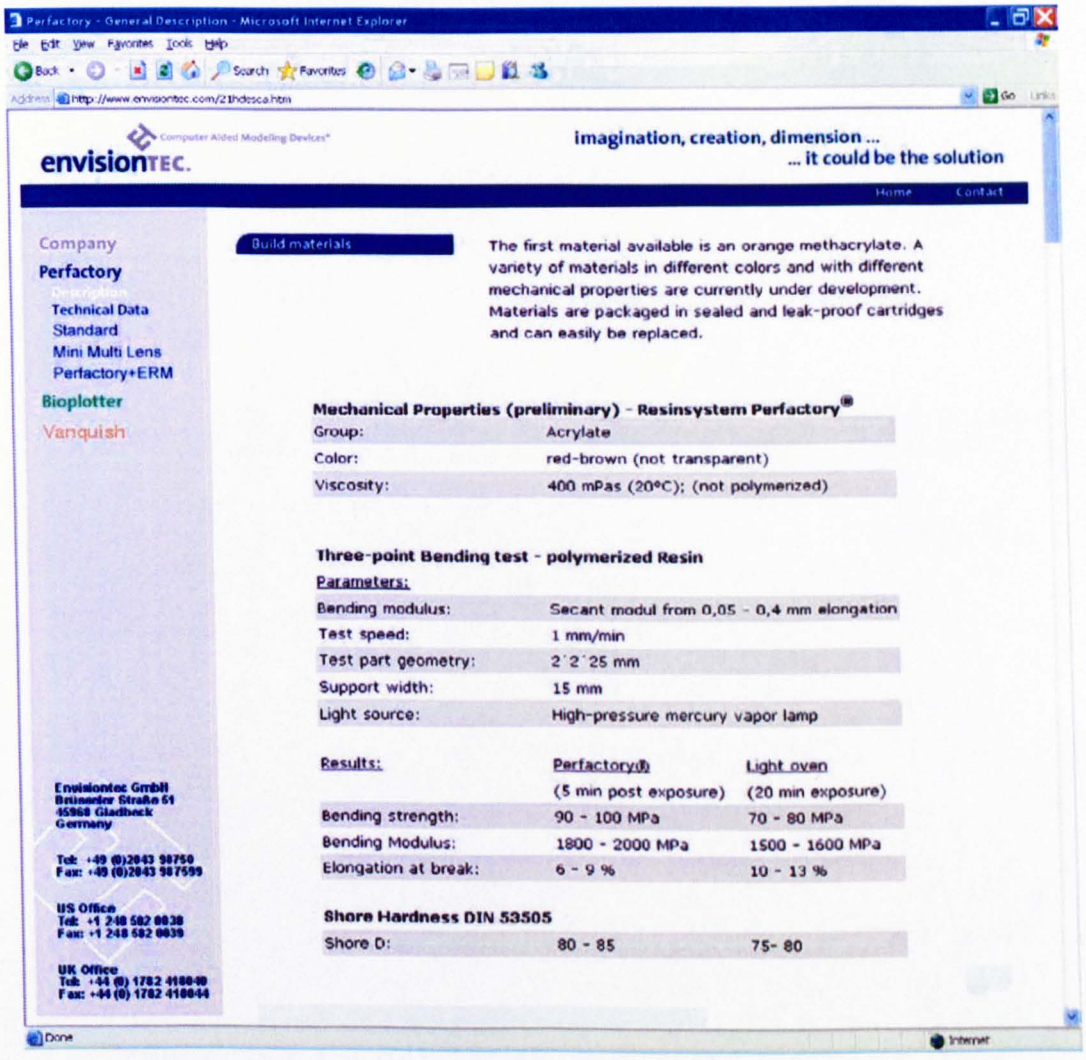

Perfactory - General Description - Microsoft Internet Explorer

File Edit View Favorites Tools Help

Back Search Favorites

Address http://www.envisiontec.com/21bdesca.htm

envisionTEC. Computer Aided Modeling Devices®

imagination, creation, dimension ...
... it could be the solution

Home Contact

Company
Perfactory
Description
Technical Data
Standard
Mini Multi Lens
Perfactory+ERM
Bioplotter
Vanquish

Envisiontec GmbH
Brüsseler Straße 61
45968 Gladbeck
Germany
Tel: +49 (0)2043 98750
Fax: +49 (0)2043 987599

US Office
Tel: +1 248 582 0038
Fax: +1 248 582 0039

UK Office
Tel: +44 (0) 1782 418040
Fax: +44 (0) 1782 418044

Build materials

The first material available is an orange methacrylate. A variety of materials in different colors and with different mechanical properties are currently under development. Materials are packaged in sealed and leak-proof cartridges and can easily be replaced.

Mechanical Properties (preliminary) - Resinsystem Perfactory®

Group:	Acrylate
Color:	red-brown (not transparent)
Viscosity:	400 mPas (20°C); (not polymerized)

Three-point Bending test - polymerized Resin

Parameters:

Bending modulus:	Secant modul from 0,05 - 0,4 mm elongation
Test speed:	1 mm/min
Test part geometry:	2*2*25 mm
Support width:	15 mm
Light source:	High-pressure mercury vapor lamp

Results:	Perfactory® (5 min post exposure)	Light oven (20 min exposure)
Bending strength:	90 - 100 MPa	70 - 80 MPa
Bending Modulus:	1800 - 2000 MPa	1500 - 1600 MPa
Elongation at break:	6 - 9 %	10 - 13 %

Shore Hardness DIN 53505

Shore D:	80 - 85	75- 80

Done Internet

Appendix D

Schematic diagrams

1. Data acquisition and vapour test station circuit (Figure D1-D6)
2. Proto-nose interface circuit (Figure D7)
3. Fast-nose interface circuit (Figure D8)
4. Hybrid-nose interface circuit (Figure D9-D11)
5. aVLSI-nose interface circuit (Figure D12-D14)

Note

The data acquisition boards were designed using Cadstar (Zuken Ltd, USA) while the rest were designed using Protel (Altium Limited, USA), hence the slight difference in their schematic.

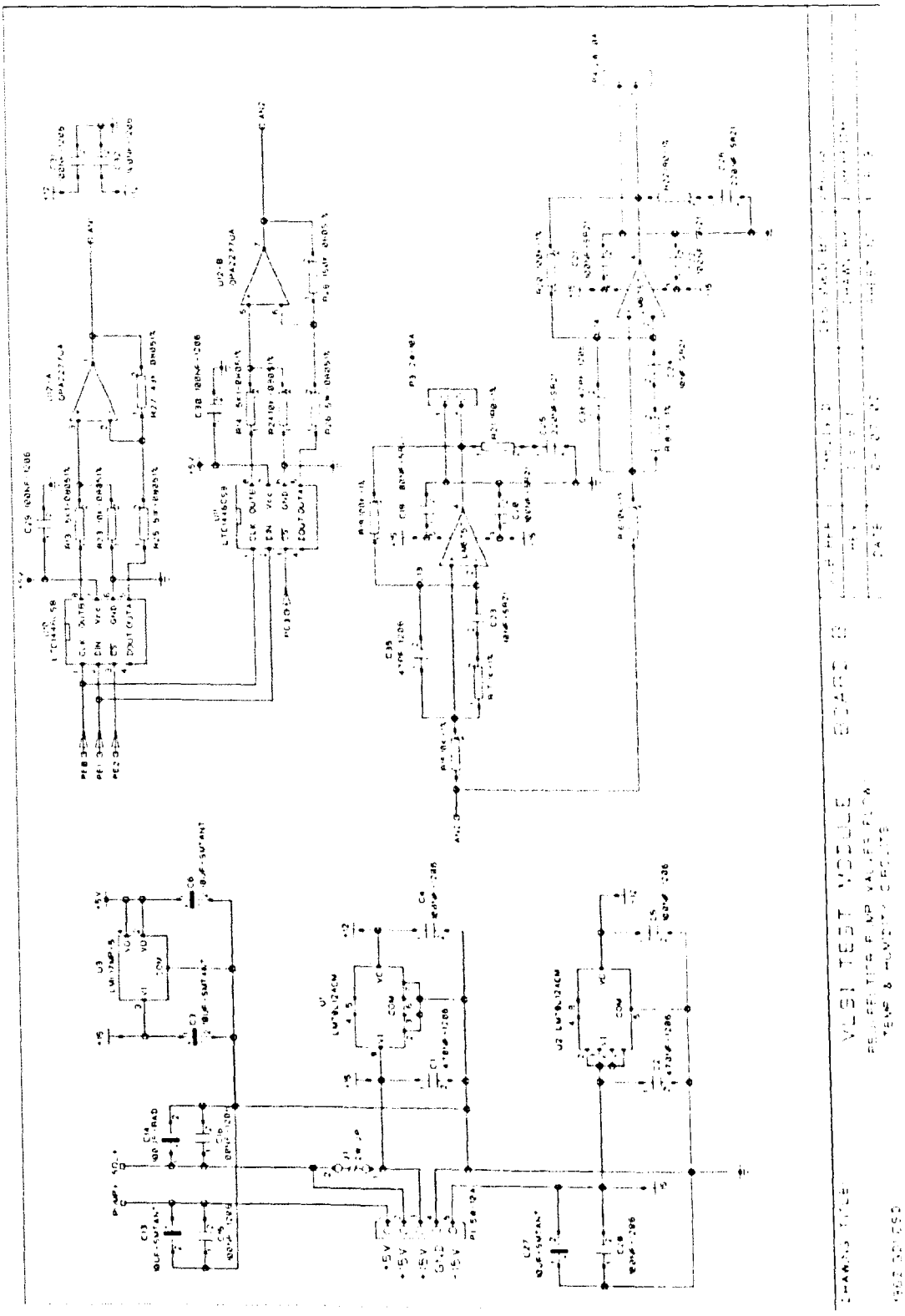

Figure D1: Data acquisition and vapour test station circuit 1.

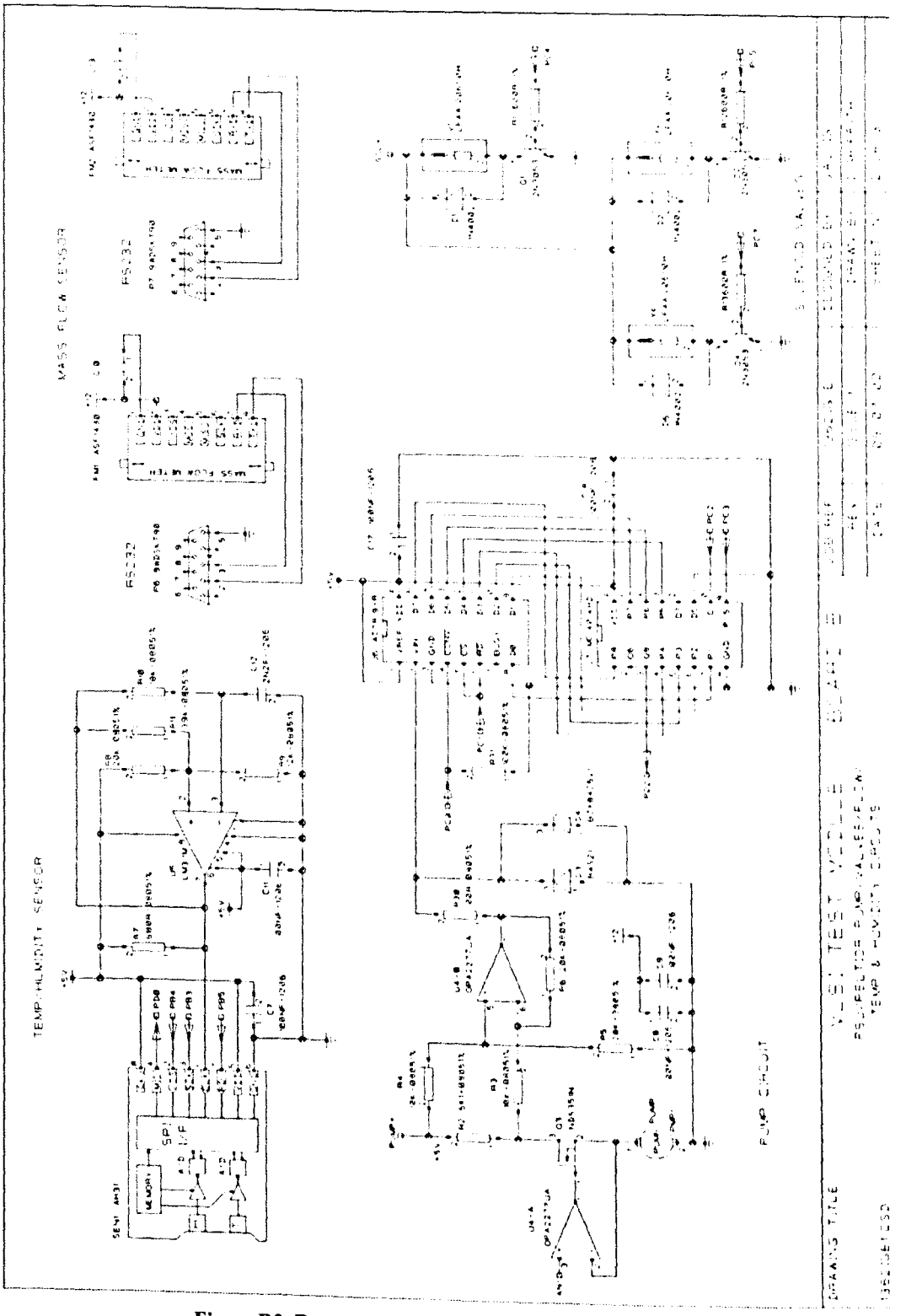

Figure D2: Data acquisition and vapour test station circuit 2.

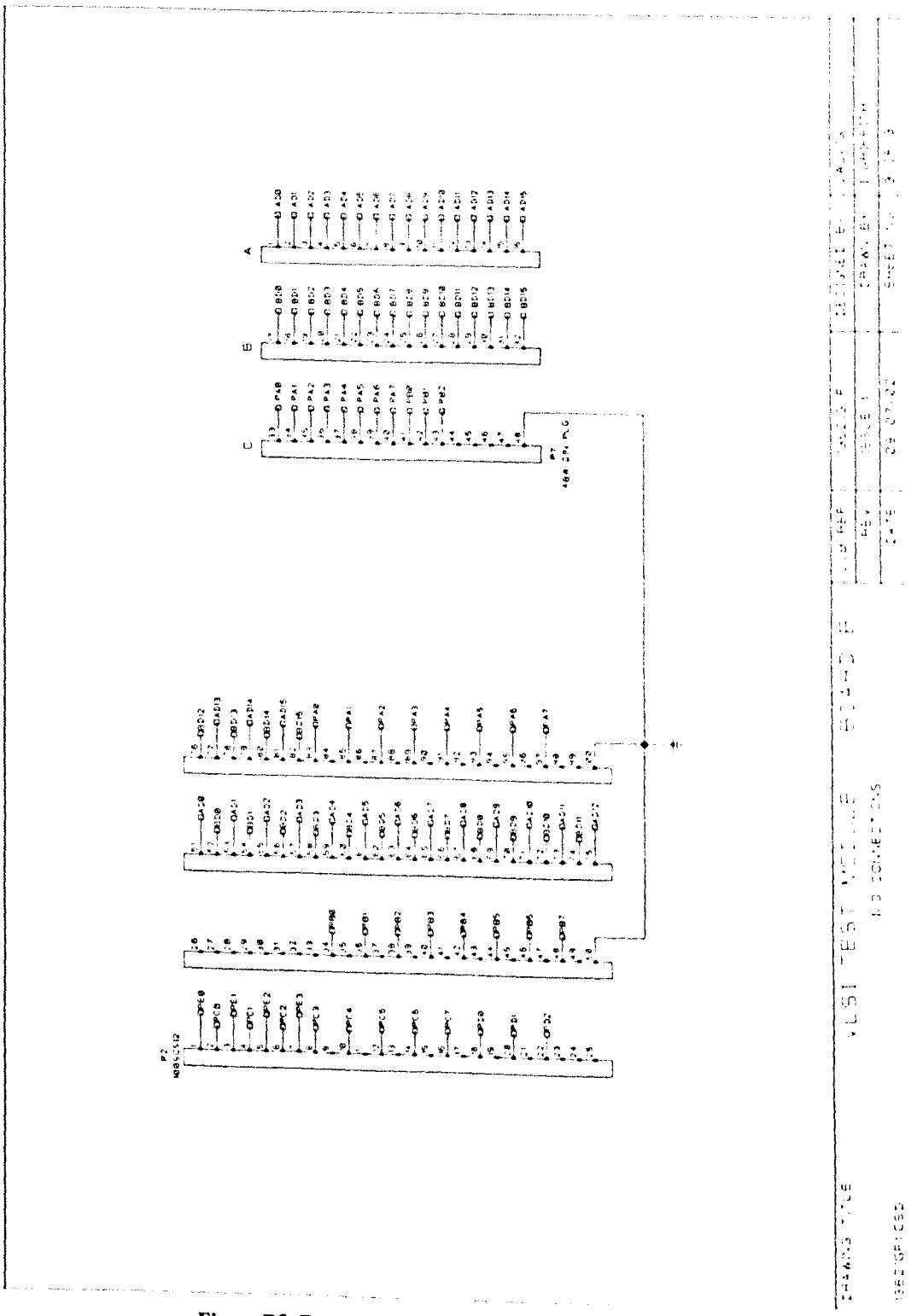

Figure D3: Data acquisition and vapour test station circuit 3.

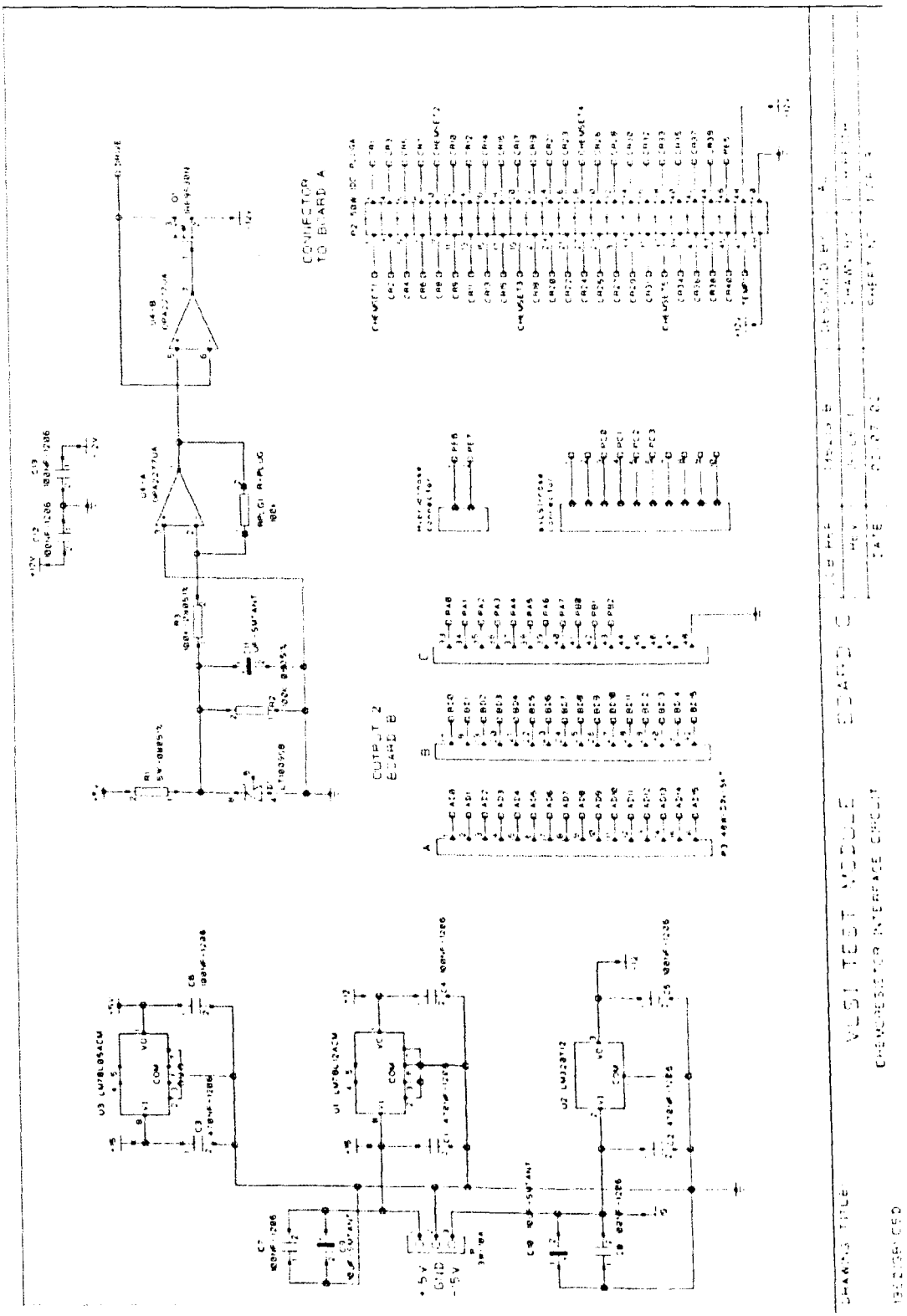

Figure D4: Data acquisition and vapour test station circuit 4.

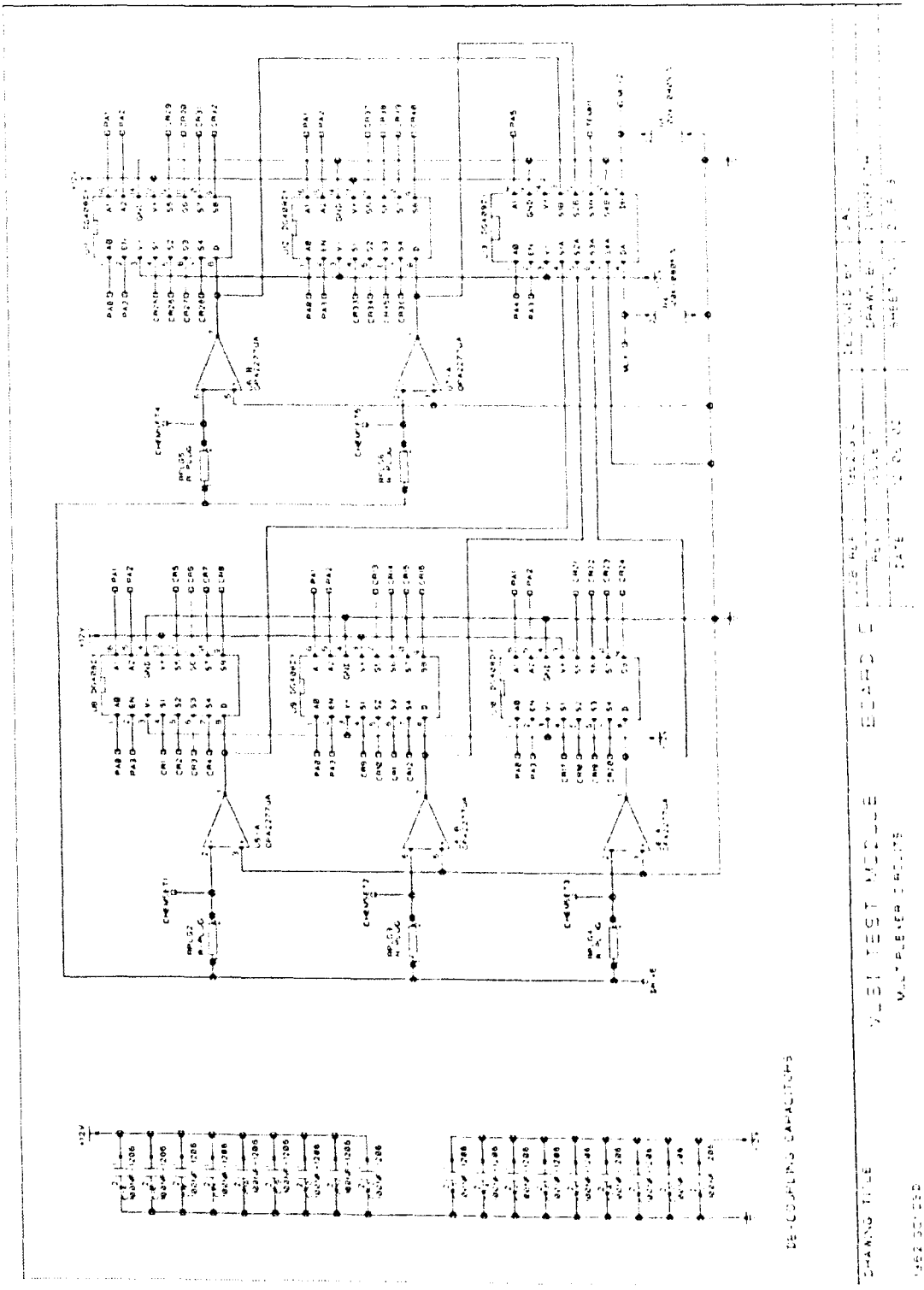

Figure D5: Data acquisition and vapour test station circuit 5.

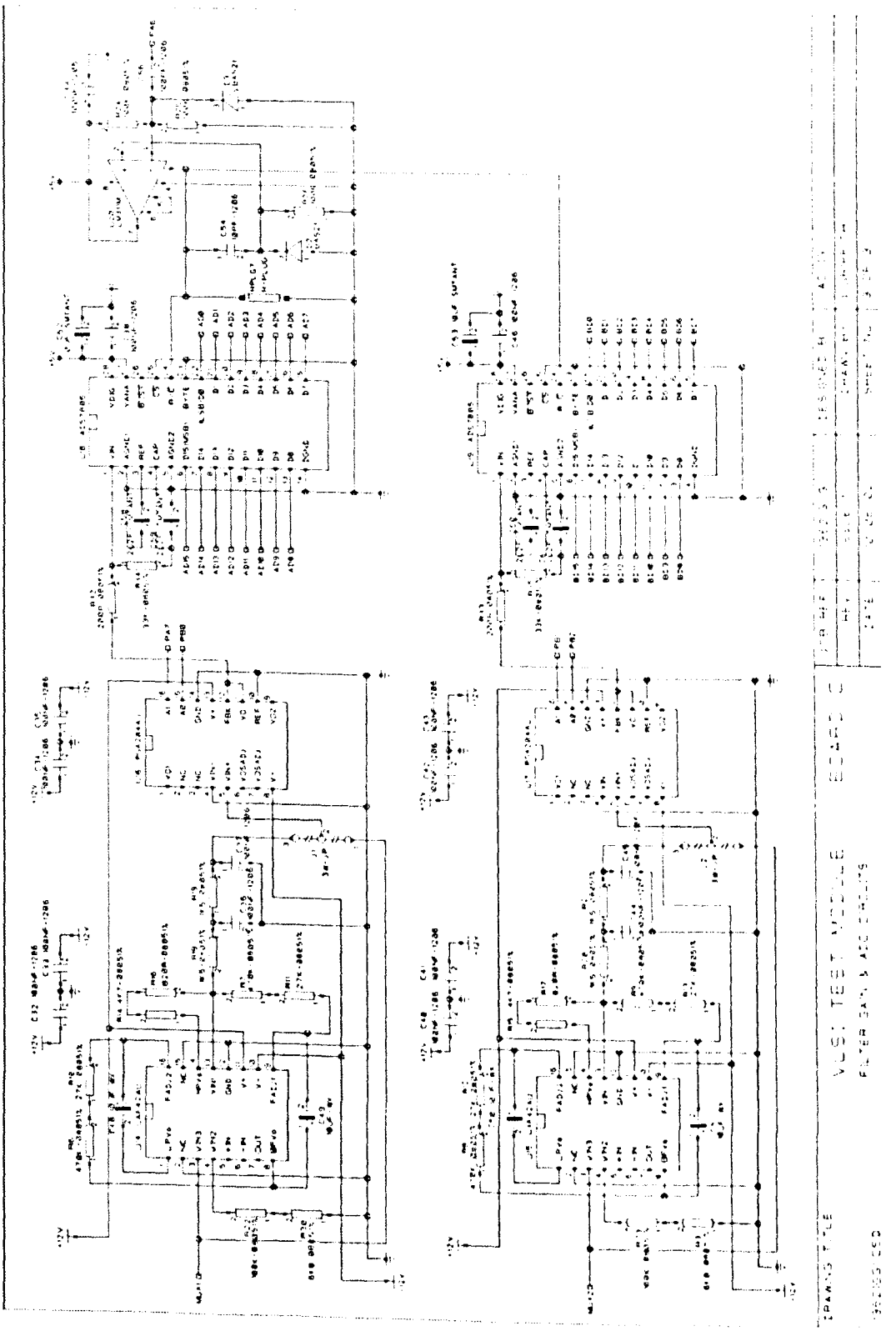

Figure D6: Data acquisition and vapour test station circuit 6.

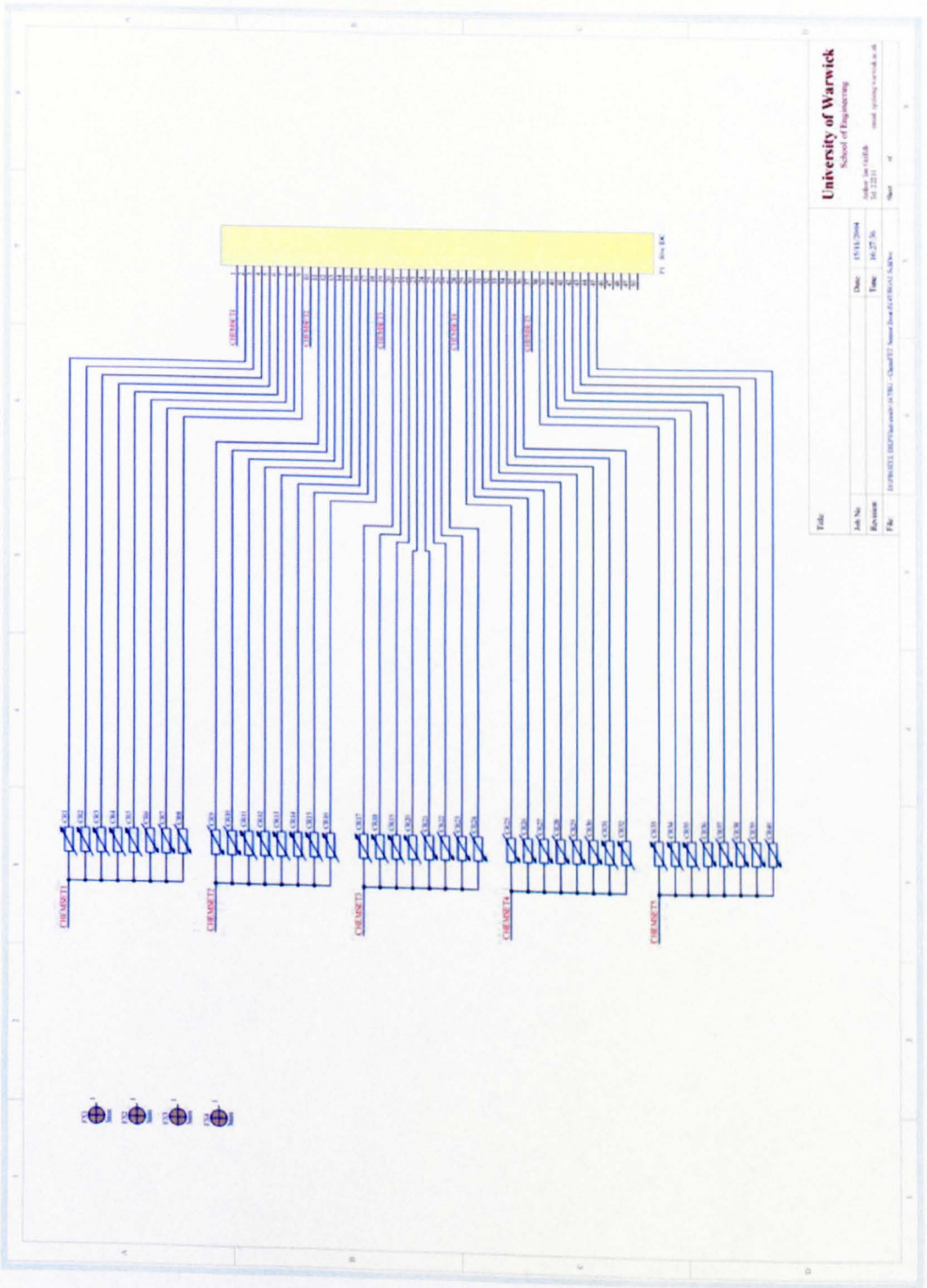

Figure D7: Proto-nose interface circuit.

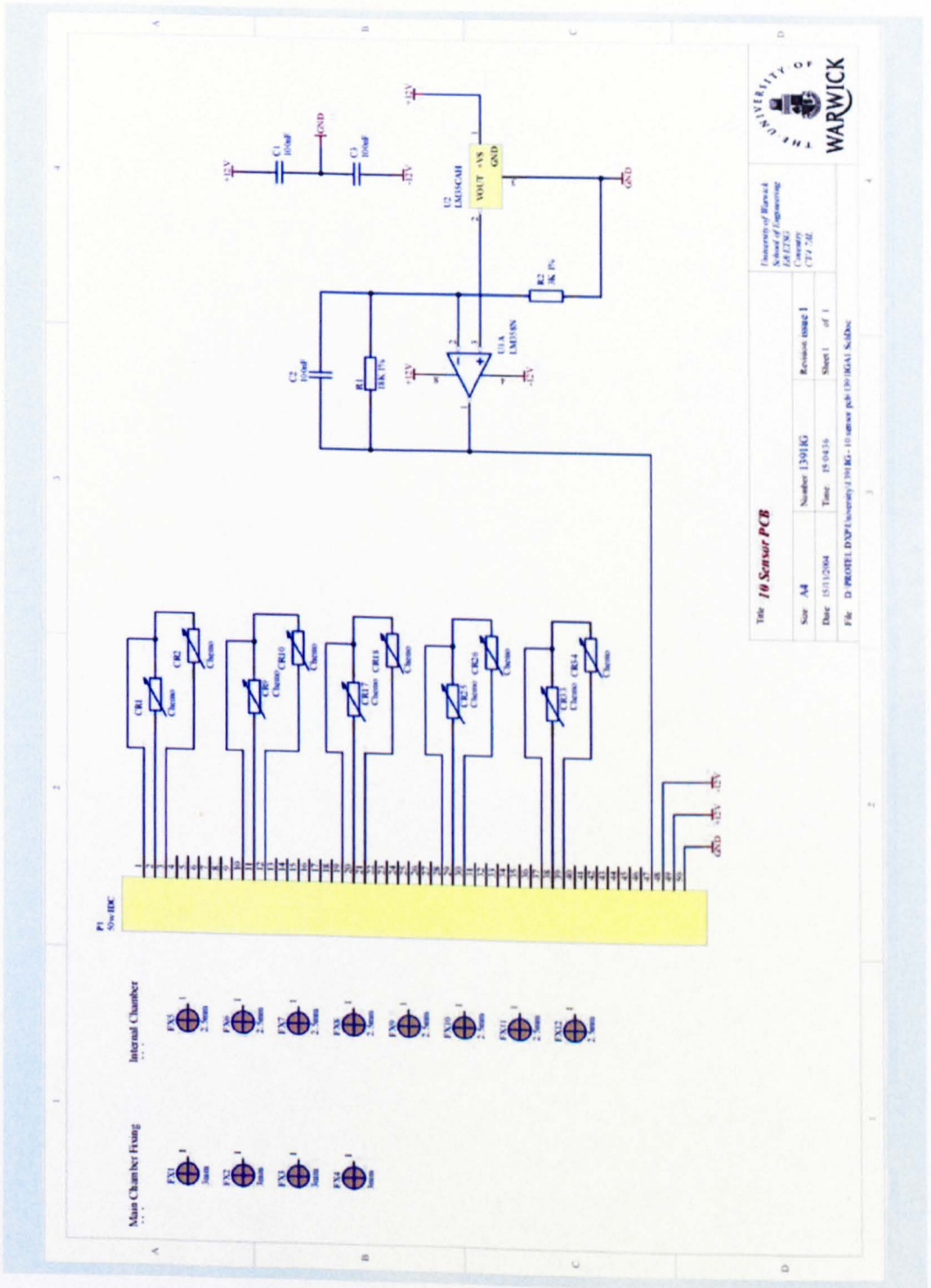

Figure D8: Fast-nose interface circuit.

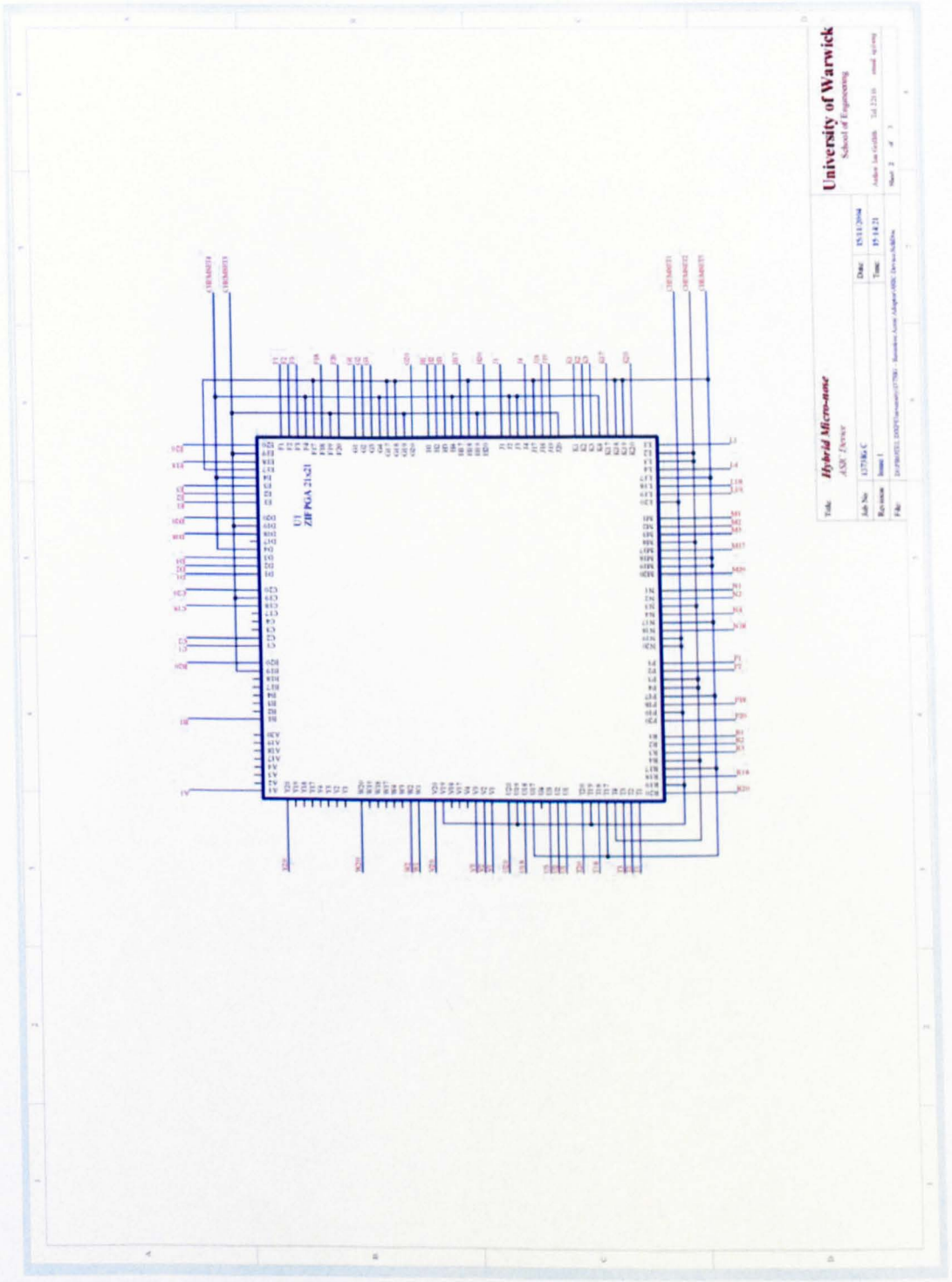

Figure D9: Hybrid-nose interface circuit 1.

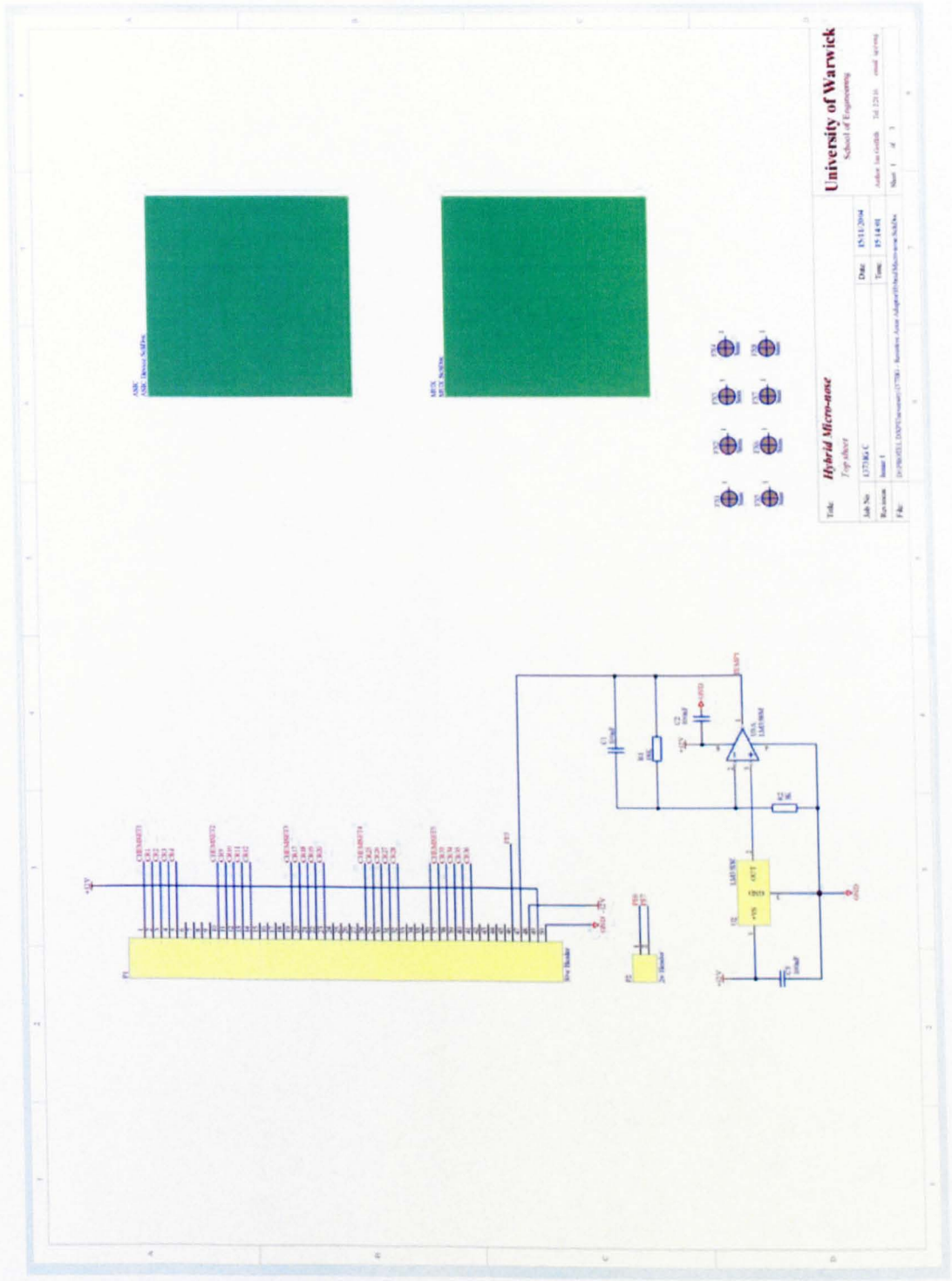

Figure D10: Hybrid-nose interface circuit 2.

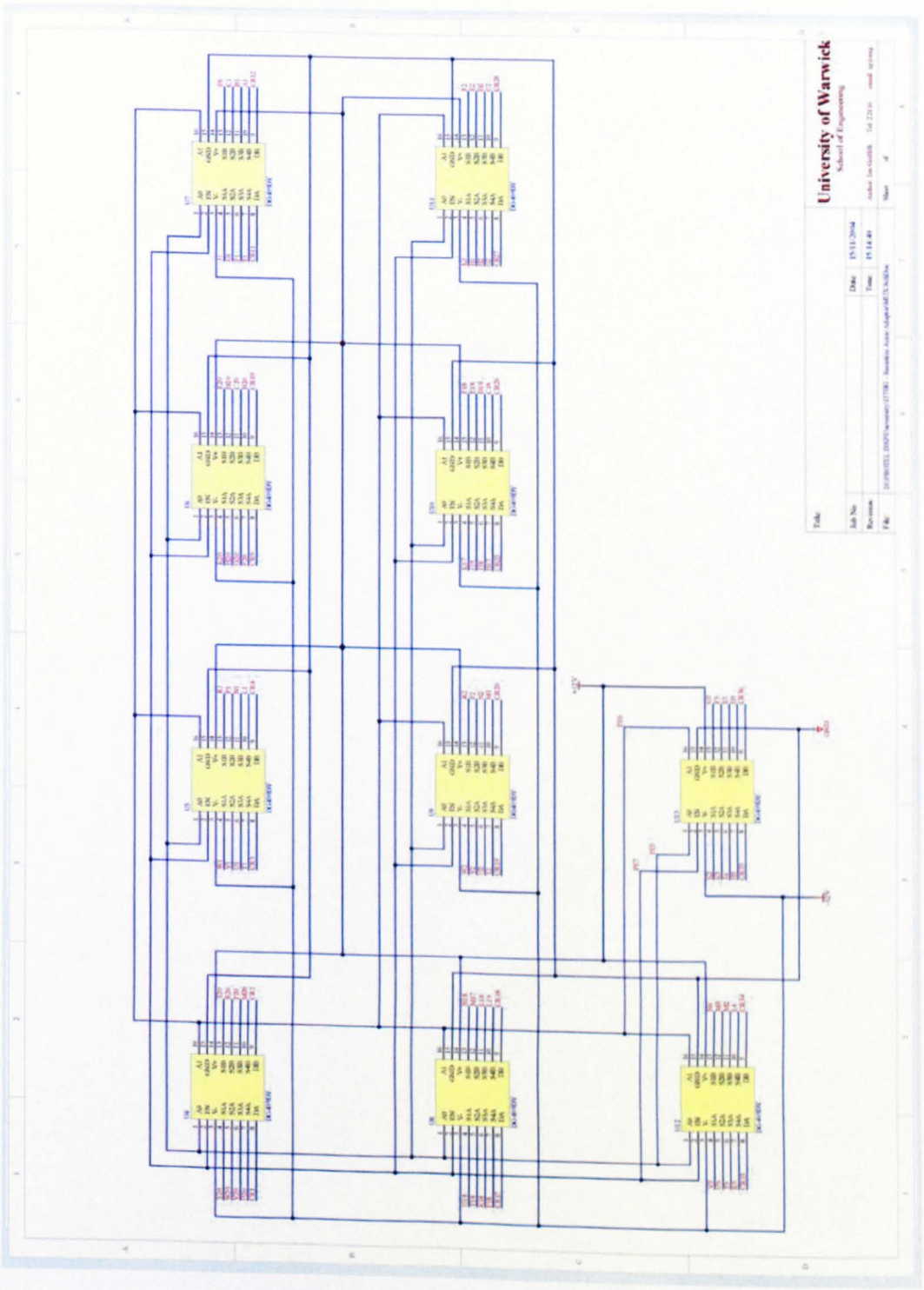

Figure D11: Hybrid-nose interface circuit 3.

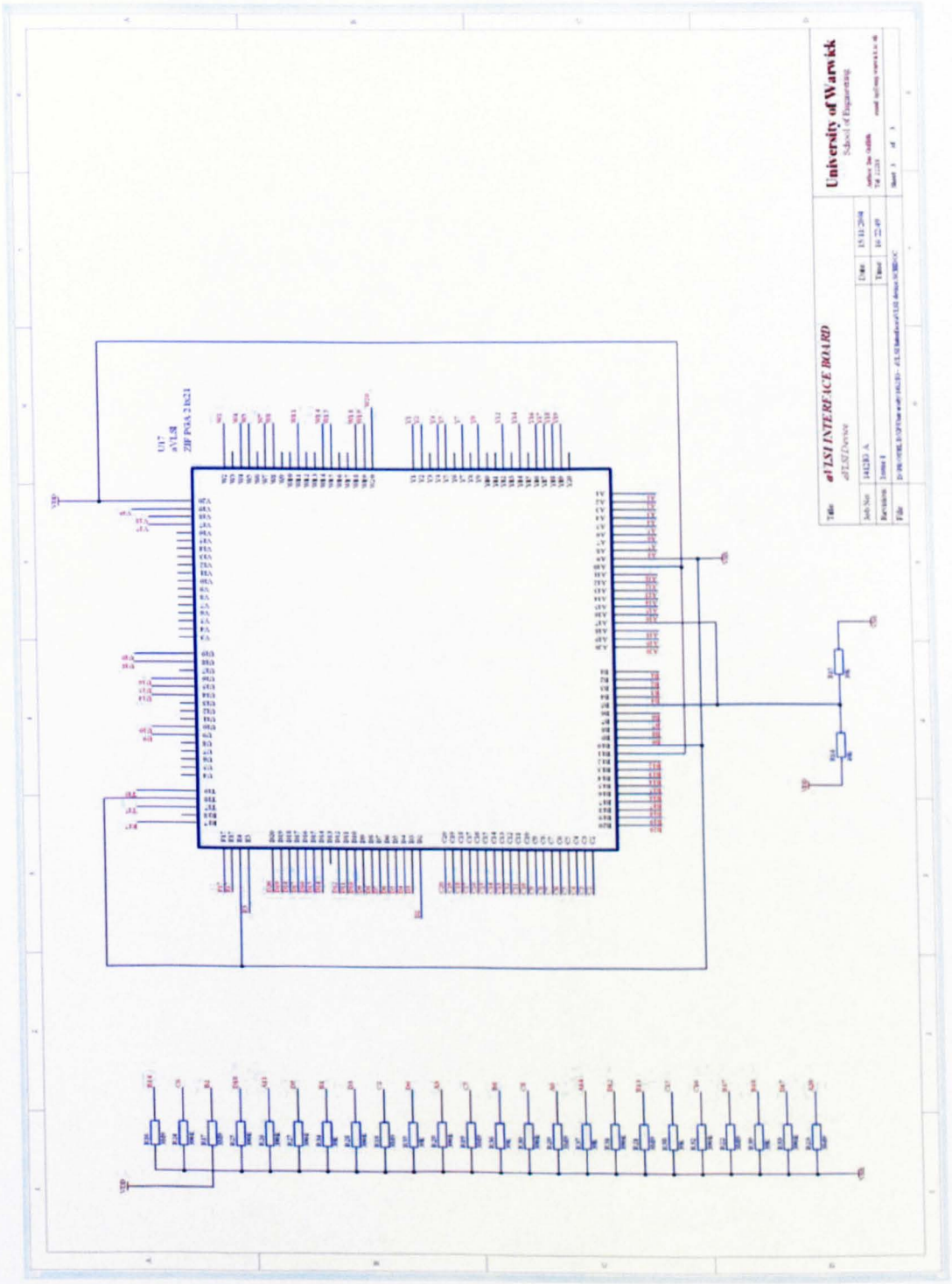

Figure D12: aVLSI-nose interface circuit 1.

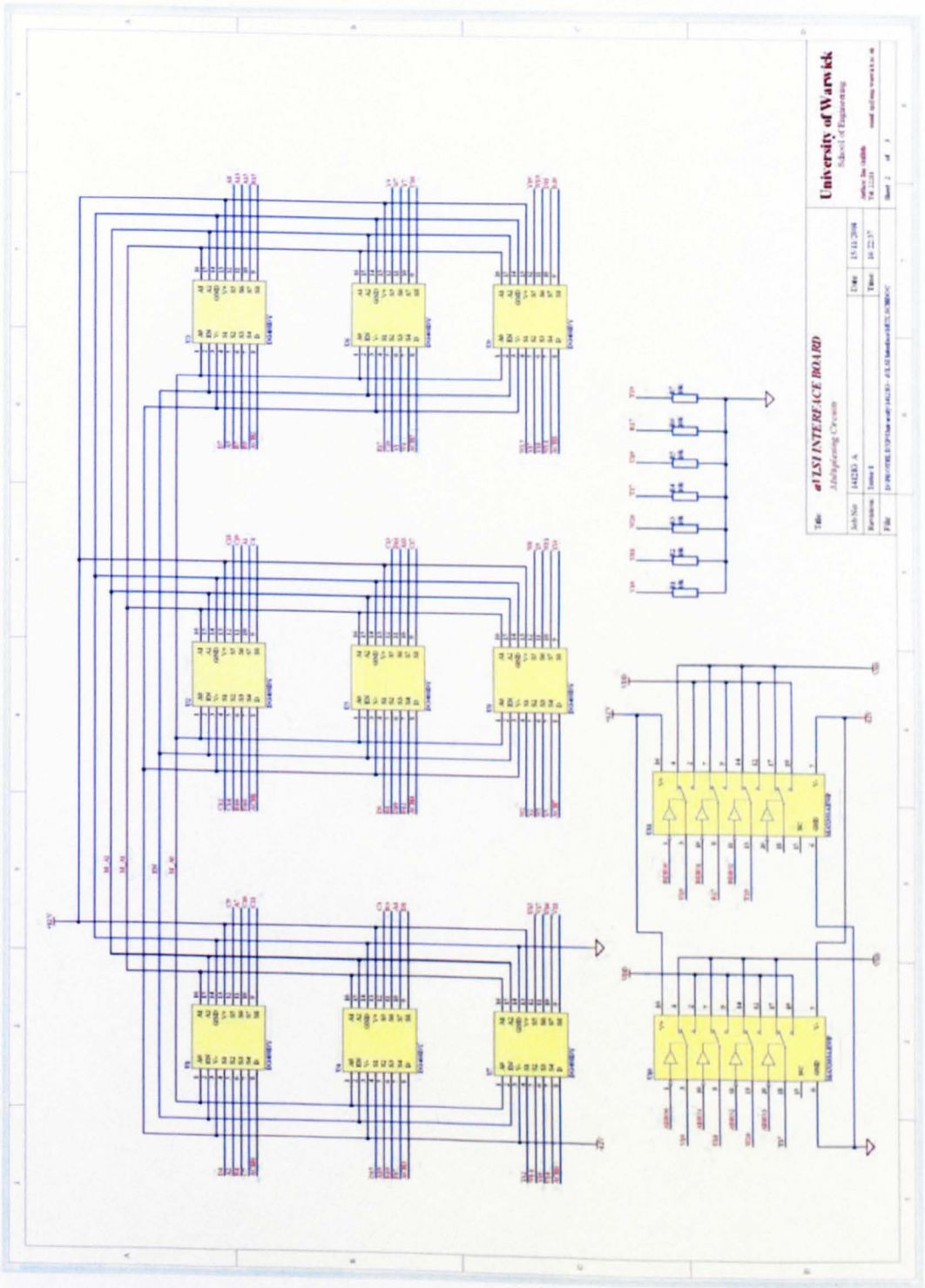

Figure D13: aVLSI-nose interface circuit 2.

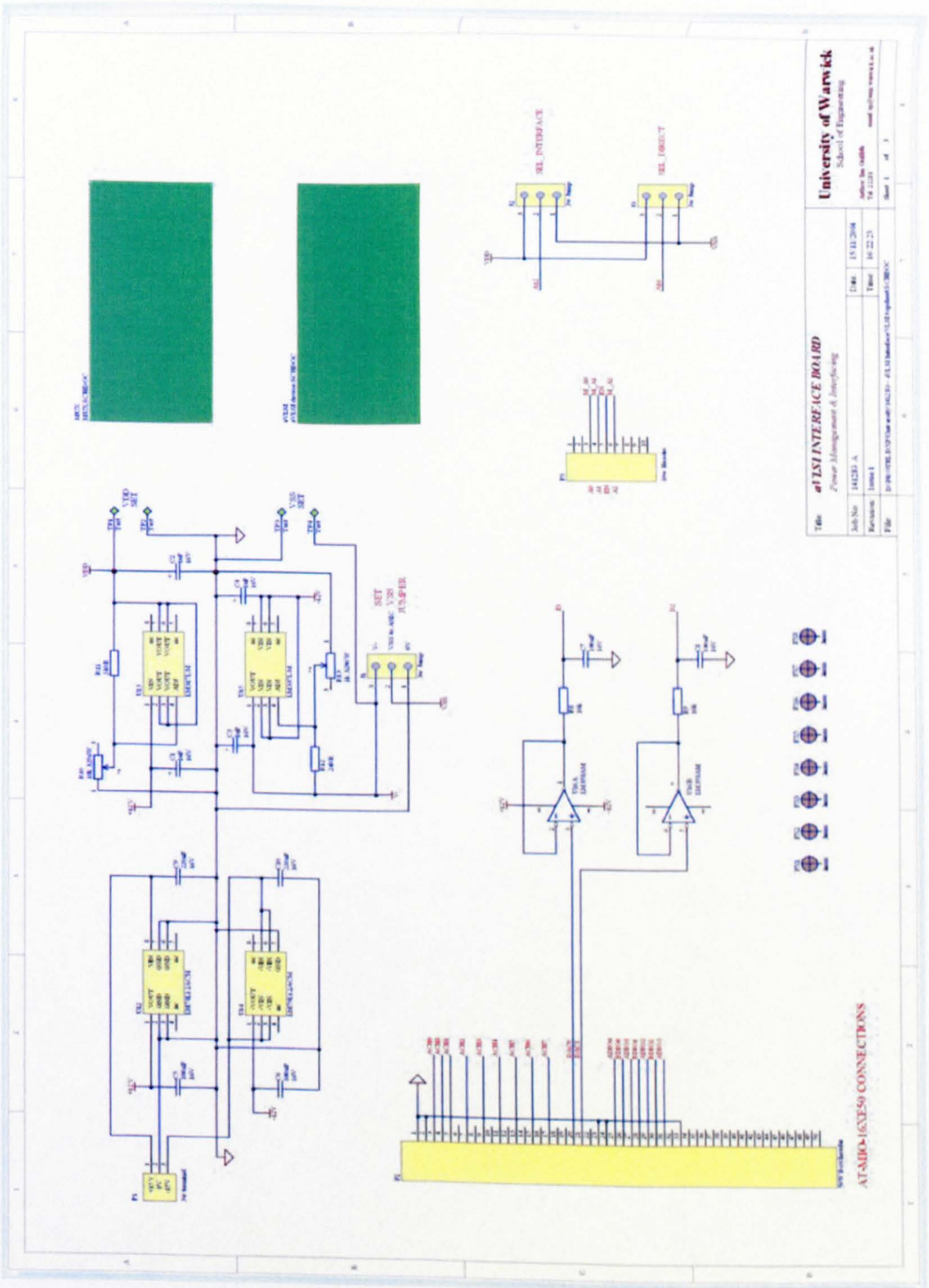

Figure D14: aVLSI-nose interface circuit 3.